

UNIVERSITY OF COPENHAGEN
FACULTY OF SCIENCE

VNIVERSITATIS HAFNIENSIS
FACVLTATIS NATVRALIS



CONNECTING THE EXTREMES

High-redshift Starbursts as Progenitors of Massive Galaxies

Dissertation submitted for the degree of

PHILOSOPHIÆ DOCTOR

to the PhD School of The Faculty of Science, University of Copenhagen

on March 31 2019, by

Carlos Gómez Guíjarro

Supervisor: *Prof. Sune Toft*

CONNECTING THE EXTREMES

High-redshift Starbursts as Progenitors of Massive Galaxies

El sistema actual está dominado por otras tres palabras mágicas: Productividad, competitividad e innovación, que deberían ser sustituidas por repartición, cooperación y recreación.

— José Luis Sampedro

Abstract

From our planet Earth, we have always been fascinated by the vastness of the cosmos. For centuries we have tried to unveil its nature, the physical laws, the origin of everything, and how we came to exist. The universe appears dark to our eyes with glimpses of light from distant stars like our Sun. Stellar diffuse conglomerations were revealed to be even more distant worlds, galaxies like our Milky Way. As the timescales of galaxy formation and evolution are much longer than our lifespan, we cannot witness the evolution of galaxies directly. Fortunately, the finite speed of light allows us to observe how the universe looked like at different epochs just by observing at larger distances. Like the photograms of a movie we can reconstruct the evolution of galaxies. In our galactic neighborhood there is one type of galaxies that encodes the richest information of the evolution of galaxies in the universe, the giant elliptical galaxies. They are the most massive and largest galaxies known, void of star formation, so-called quiescent. Besides, they are the oldest. Their formation traces back to the earliest epochs of the universe. Understanding their origins and evolutionary sequence lead to the comprehension of the history of structures in the universe over 13 billion years. In my thesis, I studied distant galaxies characterized for their vigorous star formation, so-called starbursts, aiming at unveiling their roles as progenitors of massive galaxies and providing insight in the physical processes shaping galaxy formation and evolution. First, I discovered that these starbursts are capable of assembling large amounts of stars very rapidly in compact, dust-enshrouded regions. This matches with the physical characteristics of distant massive quiescent galaxies, establishing an evolutionary connection between them. Second, I peered into the origin of the galaxy clusters where elliptical galaxies live in our nearby universe, tracing them back to their plausible progenitors as conglomerations of gas-rich, dusty star-forming galaxies. Third, I explored the transition between star-forming to quiescent galaxies, classifying galaxies based on fundamental star-forming and structural relations and applying physical diagnostics to assess their burstiness. I discovered that compact star-forming galaxies are consistent with being old starbursts on its way to quiescence. The work presented in this dissertation contributes to widening our understanding of the evolution of massive galaxies.

Resumé på Dansk

Fra vores planet Jorden har vi altid været fascineret af det enorme kosmos. I århundreder har vi prøvet at afsløre dets natur, de fysiske love, oprindelsen af alting samt hvordan vi blev til. I vores øjne fremstår universet mørkt med glimt af lys fra fjerne stjerner som vores egen Sol. Flere af de lyssvage stjernelignende lyspletter viste sig sidenhen at være endnu fjernere verdener; galakser som vores Mælkevej. Da galaksers tilblivelse samt udvikling involverer tidsskalaer betydeligt længere end vores levetid, har vi ikke mulighed for direkte at overvære, hvordan de dannes og udvikles. Heldigvis kan vi, grundet lysets konstante hastighed, observere hvordan universet så ud i forskellige perioder, blot ved at observere på større og større afstande. På samme måde som vi kan forstå handlingen af en film baseret på stillbilleder, kan vi rekonstruere udviklingen af galakser ved at observere dem i forskellige faser af deres liv. I vores galaktiske nabolag findes der en type galakser, der er indkodet med de mest betydningsfulde oplysninger om galakseudvikling i universet, nemlig de enorme elliptiske galakser. De er de tungeste og største galakser, vi kender til, og kendetegnes som værende "quiescent", da de ikke længere danner stjerner. De er derudover de ældste galakser, der findes. Dannelsen af disse galakser kan spores helt tilbage til de tidligste perioder af universets historie, og forståelsen af deres oprindelse og evolutionære sekvens giver indsigt i dannelsen af strukturer i universet over de sidste 13 milliarder år. Jeg har i min afhandling undersøgt fjerne galakser, som er karakteriseret ud fra deres kraftige stjernedannelse, såkaldte starburst-galakser, for at besvare, om disse galakser er forfædre til de enorme elliptiske galakser, og for at opnå indsigt i de fysiske processer, som former galaksedannelse og -evolution. For det første opdagede jeg, at disse starburst-galakser er i stand til at ansamle store mængder stjerner meget hurtigt i kompakte, støv-indhyllede områder. Dette stemmer overens med de fysiske karaktertræk, man har observeret i de fjerne, tunge, inaktive galakser, hvilket etablerer en evolutionær sekvens mellem dem. For det andet undersøgte jeg oprindelsen af galaksehobe, som i vores lokale univers huser de elliptiske galakser, for at undersøge, om de kan være efterkommerne af de gas-rige, støvede, stjernedannende galakser. For det tredje undersøgte jeg overgangen mellem stjernedannende og inaktive galakser, hvor jeg klassificerede galakser baseret på grundlæggende stjernedannende og strukturelle relationer og anvendte fysiske diagnoser til at vurdere kraften af stjernedannelses-udbruddet. Jeg opdagede, at kompakte stjernedannende galakser er i overensstemmelse med at være gamle starburst-galakser, som er på vej til at blive inaktive. Forskningen i denne Ph.D.-afhandling bidrager til at udvide vores forståelse af udviklingen af tunge galakser.

Resumen en Español

Desde nuestro planeta Tierra siempre hemos estado fascinados por la inmensidad del cosmos. Durante siglos hemos tratado de revelar su naturaleza, las leyes físicas, el origen de todo y cómo llegamos a existir. El universo se muestra oscuro ante nuestros ojos con destellos de luz de estrellas distantes similares a nuestro Sol. Descubrimos que las difusas nebulosidades estelares eran mundos aún más distantes, galaxias como nuestra Vía Láctea. Debido a que las escalas de tiempo relacionadas con la formación y evolución de galaxias son mucho más largas que nuestra vida, no podemos presenciar su evolución directamente. Afortunadamente, la naturaleza finita de la velocidad de la luz nos permite saber cómo era el universo en diferentes épocas simplemente observando a distancias más lejanas. Al igual que los fotogramas de una película podemos reconstruir la evolución de galaxias. En nuestro vecindario galáctico hay un tipo de ellas que contiene la información más rica acerca de la evolución de galaxias en el universo, las elípticas gigantes. Son las más masivas y grandes que se conocen, carentes de formación estelar, conocidas como quiescentes. Además son las más antiguas. Su formación se remonta a las primeras épocas del universo. Entender su origen y secuencia evolutiva nos lleva a la comprensión de la historia de las estructuras en el universo a lo largo de 13 mil millones de años. En mi tesis, he estudiado galaxias distantes caracterizadas por su vigorosa formación estelar con el objetivo de desvelar su rol como progenitores de galaxias masivas y de proporcionar información sobre los procesos físicos que dan forma a la formación y evolución de galaxias. Primero, descubrí que estos estallidos estelares son capaces de ensamblar grandes cantidades de estrellas muy rápidamente en regiones compactas envueltas de polvo. Esto coincide con las características físicas de galaxias quiescentes masivas y distantes, estableciendo una conexión evolutiva entre ellas. En segundo lugar, he observado el origen de los cúmulos de galaxias, donde las elípticas viven en nuestro universo cercano, rastreándolos hasta sus posibles progenitores como conglomerados de galaxias polvorientas y ricas en gas. En tercer lugar, he explorado la transición entre galaxias con formación estelar activa a galaxias inactivas, clasificándolas en base a relaciones fundamentales sobre su estructura y formación de estelar y aplicando diagnósticos físicos para evaluar su grado de intensidad de formación estelar. Descubrí que las galaxias compactas con formación estelar son consistentes con viejas explosiones de estrellas en su camino a la inactividad. El trabajo presentado en esta tesis doctoral contribuye a ampliar nuestro conocimiento sobre la evolución de las galaxias masivas.

Acknowledgments

First and foremost, my deepest gratitude goes to my wonderful family, my parents Eduardo and Pilar, my sister Alicia, and my grandparents Antonio, Matilde, Eduardo, and Encarna. Thanks for all you gave me, for supporting me during all my life in whatever it was that I was pursuing, in the good and bad times, for encouraging my curiosity and creativity, for always understanding and caring, for your true love and devotion.

Thanks to all my friends, so supportive along these years. Thanks for your camaraderie, for always welcome me and making me feel at home like the time had never passed, no matter whether there were thousands of kilometers between us or when I was back to Spain. You are all truly awesome.

Sune, thank you as my PhD supervisor for giving me the chance to work in an amazing science framework and within an amazing team, for your passion, for showing me how to think wider, for getting all those big grants that allowed me to travel anywhere I wanted. During these years I have been able to end up pursuing my ideas and your door has always been open. Georgios, my deepest gratitude because without you I would be lost. Besides being one of the top and most complete scientists I have ever met, you are a wonderful person, do not change. To the person I owe that I have carried out a PhD in Copenhagen, thanks Pablo, without you I would not have started this amazing journey, I have always and will always remember what you did. My gratitude to the UCM and all the astronomy department where I learnt so much and started doing research with you Jesús. Thank you Omaira and Cris for such a wonderful summer in the IAC, for inviting me to Morelia, I think I have never enjoyed science more than working with you.

To DARK and DAWN that with such a great atmosphere made my time so delightful, inspiring creativity. Keep up the good work Jens and Sune. Thanks to all the people I have shared my life with at DARK and DAWN, you guys have been my family in Copenhagen: Johannes, Nick, Francesco, Henrik, Mikkel, Isabella, Maren (special acknowledgment to you two for your last minute help with the local language), Matteo, Jonatan (special acknowledgment too for saving me a lot of time in the last month), Daniele, Bo, Mario, Sandra, Raoul, Vera, and many others, for badminton and football sessions, lunches, dinners, parties, and, of course, the foosball games.

My appreciation to my colleagues in Bonn for our work together in amazing projects, for welcoming me, to you Alex always so attentive to make work carried out by students world-wide visible. Thanks Dominik for hosting me at Cornell for my stay abroad, and deep thanks to Riccardo and Daisy who are responsible that now I know something about interferometry. To all the crew

in Ithaca. Big thanks to the COSMOS team and all our meetings, for being wonderful and crazy astronomers. To Allison, without whom I would have never started getting conference talks or job interviews.

Thanks to all those that visited me these years in The Wall, Jorge, Nerea, Alfonso, José, Nushkia. Thanks to Alex and Alex, the OGT Team, for their vital human and technical support. To the Tenerife summer crew and all our meetings. To all of you in Madrid and outside, in Copenhagen, Bianca and the salsa people. You are all wonderful. My watch has ended.

Contents

Abstract	iii
Resumé på Dansk	iv
Resumen en Español	v
Acknowledgments	vi
Contents	viii
1 Introduction	1
1.1 The Standard Cosmological Model and The Formation of Structures in the Universe	1
1.2 Types of Galaxies and Their Formation	2
1.3 Elliptical galaxies	5
1.4 Formation Scenarios of Elliptical Galaxies	7
1.4.1 Optically-selected High-redshift Galaxies	10
1.4.2 Compact Quiescent Galaxies	10
1.4.3 Submillimeter Galaxies	13
1.5 A Unified Picture of Massive Galaxy Formation	16
1.6 Objectives and Thesis Structure	16
2 Connecting Submillimeter and Quiescent Galaxies	19
2.1 Introduction	20
2.2 Sample and Data	22
2.2.1 COSMOS SMGs Sample	22
2.2.2 HST Data	22
2.2.3 ALMA Data	23
2.2.4 PSF Matching	24
2.2.5 Adaptive Smoothing	25
2.2.6 Additional Photometric Data	25
2.3 Morphology	26
2.3.1 UV Stellar Components	28
2.3.2 SED Fitting	29

2.4	Dust Absorption and Emission	33
2.4.1	Spatially Resolved UV Slopes	33
2.4.2	FIR Sizes	35
2.4.3	UV/FIR Spatial Disconnection	37
2.4.4	IRX- β Plane	38
2.5	Stellar Masses and Merger Ratios	41
2.5.1	What Triggers $z > 4$ Starbursts?	41
2.5.2	Comparison to Previous Stellar Mass Estimates	42
2.5.3	Stellar Mass Uncertainties and Caveats	43
2.6	Stellar Mass-Size Plane: Evolution to Compact Quiescent Galaxies	45
2.7	Discussion	47
2.8	Summary and Conclusions	50
3	Exploring the Origins of Galaxy Clusters	53
3.1	Introduction	54
3.2	Sample and Data	56
3.2.1	<i>Herschel</i> Candidate Protoclusters	56
3.2.2	ALMA Observations	57
3.2.3	VLA Observations	58
3.2.4	CARMA and NOEMA Observations	60
3.3	Confirmation of Protocluster Cores	60
3.3.1	HELAISS02	60
3.3.2	HXMM20	63
3.3.3	HCOSMOS02	65
3.4	Gas, Dust and Stellar Properties	71
3.4.1	CO-based Estimates of M_{H_2}	71
3.4.2	FIR Properties	71
3.4.3	Dust-based Estimates of M_{H_2}	74
3.4.4	Stellar Masses	76
3.5	Discussion	79
3.5.1	Blends of DSFGs from Single-dish Selected Sources	79
3.5.2	Gas Fractions and Star Formation Efficiencies	79
3.6	Summary and Conclusions	85
4	Investigating the Transition from Star-forming to Quiescent Galaxies	88
4.1	Introduction	89
4.2	Selection of Compact Star-Forming Galaxies	90

4.2.1	Optical Sample	90
4.2.2	Far-Infrared Sample	92
4.2.3	Active Galactic Nuclei Flagging	93
4.3	Compactness and Star Formation	94
4.3.1	General Trends	94
4.3.2	Redshift Dependence	96
4.3.3	Trends for Massive Galaxies	97
4.4	Are Compact Star-Forming Galaxies Normal Star-Forming Galaxies or Starbursts?	97
4.4.1	Diagnostic 1: Star Formation Efficiency	98
4.4.2	Diagnostic 2: Interstellar Medium	99
4.4.3	Diagnostic 3: Radio Emission	103
4.5	Discussion	106
4.5.1	Star Formation Efficiency and Selection Limits	106
4.5.2	Diagnostics of Burstiness	107
4.6	Summary and Conclusions	109
5	Conclusions and Future Research	111
	List of Publications	114
	Bibliography	116

1

Introduction

The overall theme of this thesis is the study of galaxy formation and evolution. In particular, the formation and evolution of massive galaxies that in the local universe have giant elliptical galaxies as their most representative examples. In this chapter I provide a general introduction to the current knowledge of the formation of massive elliptical galaxies and their evolutionary sequence from the highest redshifts to the local universe.

1.1 The Standard Cosmological Model and The Formation of Structures in the Universe

The Hot Big Bang model is the starting point of our knowledge about the formation and evolution of structures in the universe. According to this model, at the earliest times our universe was in a very dense and hot state. This conception of the beginning of everything came from one of the most fundamental discoveries in cosmology, the expansion of the universe. George Lemaître and Edwin Hubble discovered independently that the recession velocity of galaxies correlates linearly with their distances, proving the expansion of the universe ([Lemaître 1927](#); [Hubble 1929](#); [Hubble & Humason 1931](#); [Lemaître 1931](#)). Albert Einstein's general relativity was published in 1916 ([Einstein 1916](#)) and shortly after Alexander Friedmann derived expanding solutions of the field equations ([Friedmann 1922](#)), also worked out independently by George Lemaître reaching the same solutions ([Lemaître 1927](#); [Hubble & Humason 1931](#)). The observational discovery of an expanding universe plus the theory of gravitation that allows expanding solutions led to the idea that in the past the universe was contracted to a denser and hotter state.

Ralph Alpher and George Gamow proposed a model in which a dense and hot universe at early times was able to produce the known chemical elements in a primordial nucleosynthesis ([Alpher et al. 1948](#)). A prediction of this model is a residual radiation from that hot epoch that could be observed at microwave wavelengths at the present-day stage of the universe ([Alpher & Herman 1948](#)). This cosmic microwave background (CMB) was discovered ([Penzias & Wilson 1965](#); [Dicke et al. 1965](#)) and it constitutes one of the fundamental observational tests of the Hot Big Bang model, along with the observed abundances of light elements up to lithium that were also proven to appear from the Hot Big Bang primordial nucleosynthesis ([Hoyle & Tayler 1964](#);

Wagoner et al. 1967). The CMB was shown to be homogeneous and isotropic at a temperature of 2.7 K. How did structures emerge in such uniform conditions?

The Cosmic Background Explorer (COBE) discovered anisotropies in the CMB (Smoot et al. 1992). It provided an image of the density fluctuations at the time of photon decoupling from matter, when the universe was only $\sim 380,000$ yr old. These density fluctuations were proposed to emerge from quantum fluctuations in the field driving inflation (Hawking 1982; Guth & Pi 1982; Starobinsky 1982; Bardeen et al. 1983), a period of rapid exponential expansion of the universe shortly after the Big Bang (Guth 1981). These small initial perturbations would be the seeds of the structures formed later on. How did structures like galaxies in the present-day universe form from these initial perturbations?

The growth of structures from small initial density perturbations responds to the concept of gravitational instability. Density perturbations grow when gravity overcomes the pressure that supports them. The requirement for a density perturbation to grow is that it should be heavier than a characteristic mass known as the Jeans mass (Jeans 1902). In top-down models, galaxies formed from the fragmentation and collapse of large perturbations. In bottom-up models, galaxies formed from the hierarchical assembly of small perturbations.

The standard paradigm of structure formation is the Lambda cold dark matter model (Λ CDM). In this model, the universe is mainly composed of a cosmological constant associated with dark energy (Λ) and cold dark matter (CDM), both of yet unknown nature. It was established as the concordance model of cosmology since it was able to explain observations that other models could not explain simultaneously before. Particularly, it allows structures to start forming early enough to become present-day galaxies, reproduces the structure of the CMB, or explains the large-scale galaxy clustering. It was finally accepted upon the discovery of the accelerating expansion of the universe (Riess et al. 1998; Perlmutter et al. 1999). The cosmological parameters are now well constrained, e.g., the matter density is $\Omega_m = 0.3153 \pm 0.0073$, where $\sim 16\%$ corresponds to ordinary baryonic matter (protons, neutrons, and also electrons by convention although they are not baryons) and $\sim 84\%$ corresponds to non-baryonic dark matter; the dark energy density is $\Omega_\Lambda = 0.6847 \pm 0.0073$, in a flat universe with $\Omega_{\text{tot}} = 1$ and age 13.797 Gyr (Planck Collaboration et al. 2018) (see Figure 1.1).

1.2 Types of Galaxies and Their Formation

Observations of the nearby universe revealed two very distinct types of galaxies: ellipticals and spirals. Elliptical galaxies are ellipsoids mainly supported by random stellar motions. Spiral galaxies are characterized by a flat disk that often exhibits a well-defined spiral pattern. They are disk galaxies mainly supported by rotation. For historical reason ellipticals are also referred as early-type galaxies, while spirals are also referred as late-type galaxies. These two main categories

1. INTRODUCTION

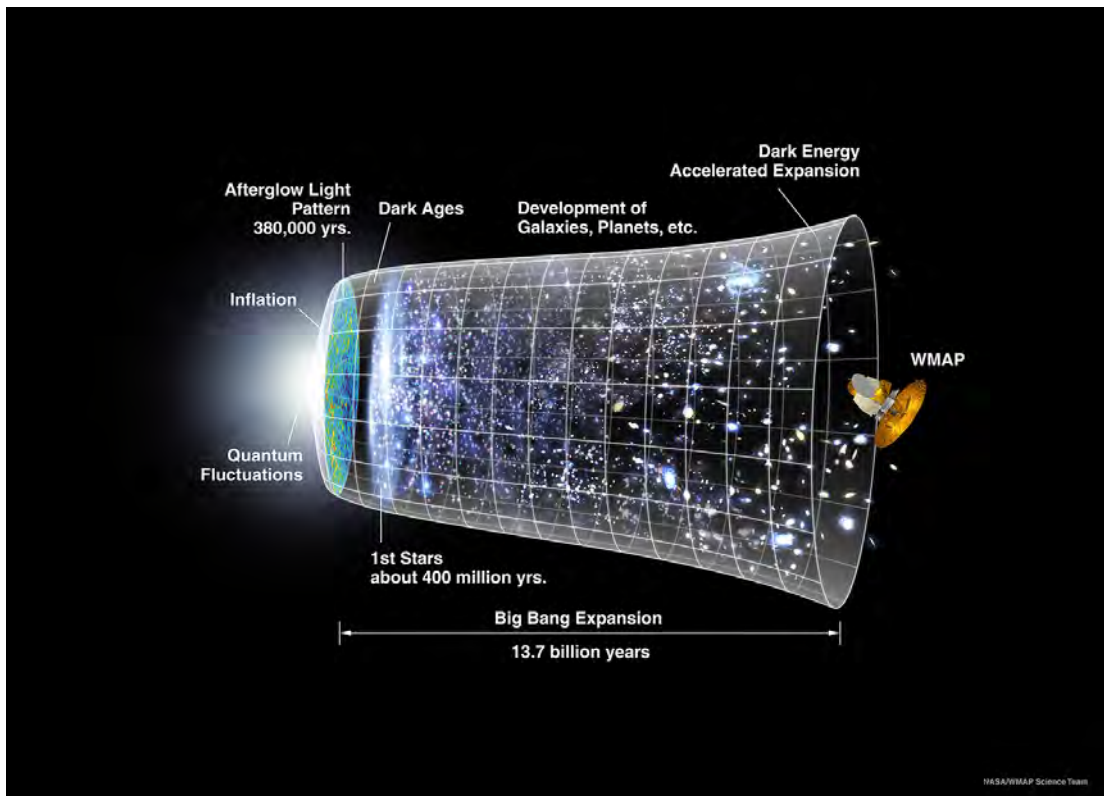


Figure 1.1: Timeline of the history of the universe illustrating its creation, expansion, and structure formation and evolution based on the standard cosmological model and observations. Credit: WMAP Science Team.

combined in different proportions describe the morphology of most of the nearby galaxies. The Hubble sequence is a morphological classification scheme of galaxies that describes the mixture of ellipsoidal and disk components leading to the broad variety of observed nearby galaxies (see Figure 1.2).

Of course, not all the galaxies in the universe can be described along the Hubble sequence. The galaxies that do not fit in the scheme are typically referred as irregulars. The Hubble sequence is a categorization that applies to the brightest galaxies, the visual morphology at optical wavelengths, and the nearby universe. In the nearby universe there are also fainter galaxies, so-called dwarf galaxies, which do not fit in the scheme. The morphology is heavily dependent on the wavelength of observation, although for historical reasons and technology development it usually alludes to the optical wavelengths, galaxies look different at different wavelengths. Finally, structures in the nearby (low-redshift) universe can be better characterized than structures in the distant (high-redshift) universe. In the high-redshift universe structures are not only more difficult to characterized due to their far distances, requiring more powerful instruments, but also because they are intrinsically different, less well-defined, clumpier, reflecting a less developed stage of galaxy evolution. It is also important to note that when observing more and more distant galaxies their light gets redshifted due to the expansion of the universe and to characterize the same visual

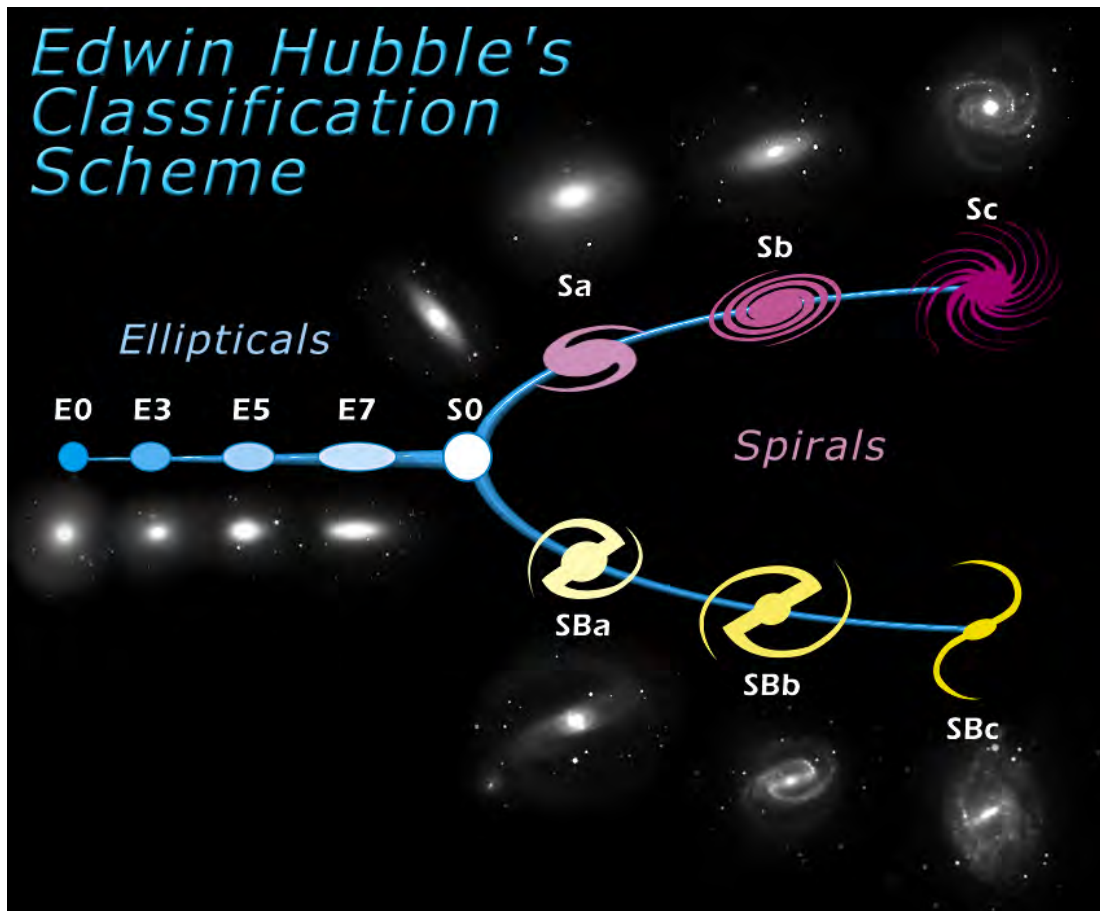


Figure 1.2: Hubble tuning fork diagram illustrating the Hubble sequence, a morphological classification scheme for galaxies invented by Edwin Hubble (Hubble 1926).

morphology as in the nearby universe their light has to be captured at redder wavelengths. How did galaxies with such different morphologies form?

The first models of galaxy formation postulated that galaxies formed from the collapse of gas clouds (monolithic collapse, top-down models), being elliptical and spiral galaxies a different product depending on how rapidly stars formed during this collapse. The gas forms stars as it collapses, if the star formation is rapid enough the process is essentially dissipationless as the stars would form before the system collapses and will result in random stellar motions that are able to generate ellipsoids typical of elliptical galaxies. On the other hand, if the star formation is slower the gas has time to collapse before forming most of the stars, gets supported by angular momentum, and forms a rotationally-supported gas disk which after forming stars will result in a stellar disk typical of spiral galaxies (Eggen et al. 1962). Conversely, other models proposed that elliptical galaxies could be merger remnants (Toomre & Toomre 1972). In these models, all galaxies would form in gas disks and would merge afterwards. Elliptical galaxies could be generated via mergers of two spheroids or two disks (e.g., White 1978; Gerhard 1981).

1. INTRODUCTION

The observations of rotation curves of spiral galaxies showed that they are embedded in dark matter haloes that extend further away than the stars (Rubin et al. 1978, 1980). Accounting the dark matter component it was proposed that galaxies formed in two stages (White & Rees 1978). In the first stage dark matter haloes formed via hierarchical clustering. Then, gas cooled down and condensed forming the stellar component within the potential wells of the dark matter haloes (hierarchical assembly, bottom-up models). In these models, spiral galaxies could be associated with the peaks of the dark matter density field, while elliptical galaxies could be linked to the highest of these density peaks (Blumenthal et al. 1984). Dark matter haloes allow mergers to be more likely, making the merger scenario for the origin of elliptical galaxies feasible (Efstathiou & Silk 1983).

The formation of galaxies in a Λ CDM hierarchical assembly paradigm implies several processes (see Figure 1.3, for a summary). First, the virialization and collapse of the dark matter halo. Second, the cooling and condensation of the gas clouds inside the dark matter halo potential well. Third, the conversion of cold gas into stars. Additionally, the formation of a central supermassive black hole (SMBH). As a galaxy forms and evolves its stars evolve as well and the SMBH grows accreting material, becoming an active galactic nuclei (AGN). Both stars, some of which explode as supernovae, and AGN inject energy, mass, and heavy chemical elements into the interstellar medium (ISM). They are even capable of generating outflowing winds that expel gaseous material away from the galaxy. These stellar and AGN feedback heavily influence the structure of a galaxy. They can aid further star formation in some regions of the galaxy by compressing the gas increasing its density, but they can also prevent star formation by heating up the gas. Finally, galaxies are not isolated systems; they are typically located around other galaxies and group together in larger systems like galaxy clusters. They interact and merge forming new systems, triggering new episodes of star formation and AGN activity, reshaping their morphology and kinematics. Overall, the properties of galaxies reflected in the different galaxy types along the cosmic history are determined by the interplay between all these physical mechanisms and the time scales they involve.

1.3 Elliptical galaxies

Elliptical galaxies exhibit ellipsoidal shapes and are mainly supported by random stellar motions. They are the most massive, largest, and oldest galaxies. They do not show recent star formation, so-called quiescent galaxies (QGs). Furthermore, they are primarily located in high-density environments such as galaxy clusters (see Figure 1.4, for example images of ellipticals).

Ellipticals follow tight scaling relations in their physical properties, e.g., the red sequence (Baum 1959; de Vaucouleurs 1961; Strateva et al. 2001; Bell et al. 2004), a sequence described by red galaxies in the galaxy color-magnitude diagram; the Faber-Jackson relation (Faber & Jackson

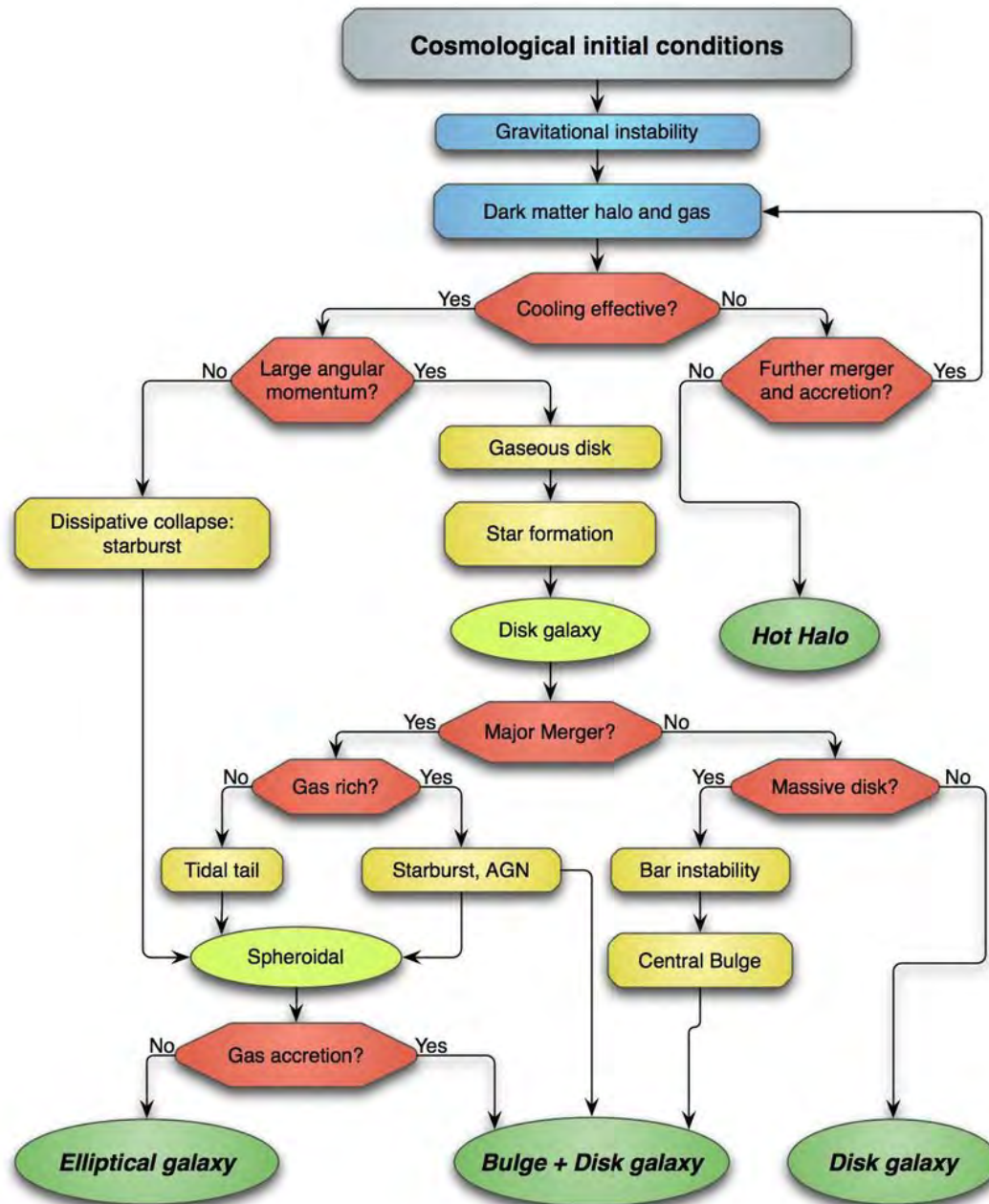


Figure 1.3: From Niemi (2011), who adapted it from Mo et al. (2010). Logic flow chart for a simplified view of galaxy formation. The cosmological framework defines the initial and boundary conditions. Paths of galaxy formation with the physical processes that lead to the formation of different galaxy types are shown.

1976), a power-law relation between the total luminosity and the central velocity dispersion; the fundamental plane (Djorgovski & Davis 1987; Dressler et al. 1987), a relation between the effective radius, the average surface brightness within the effective radius, and the central velocity dispersion, that fall in a three-dimensional plane; the mass-metallicity relation (Faber & Jackson 1976; Tremonti et al. 2004; Gallazzi et al. 2005); or the mass-size relation (Shen et al. 2003).

1. INTRODUCTION

Studies of elliptical galaxies in the distant universe showed that they appear to be already in place at least at redshift $z \sim 1$, when the universe was approximately half of its age (e.g., [Daddi et al. 2000](#); [Collins et al. 2009](#)). Overall, ellipticals have very old stellar populations with an average age of ~ 10 Gyr, implying that their formation occurred at $z \geq 2$ and their stars passively evolved since then (e.g., [Stanford et al. 1998](#)). They are thought to be the final stages of galaxy evolution.

1.4 Formation Scenarios of Elliptical Galaxies

It was the fact that elliptical galaxies show homogeneously old stellar populations that led to first propose their formation through a monolithic collapse top-down scenario as introduced in Section 1.2. In this scenario, elliptical galaxies formed at high redshift in a single burst of intense star formation followed by aging of their stellar populations ([Larson 1975](#)). However, this scenario has several problems. In such a rapid formation ellipticals would have assembled most of their stellar mass very early, while our current understanding of star formation through the cosmic history indicates that only a small fraction of the total amount of stars in the universe formed at $z > 6$ (e.g., [Madau & Dickinson 2014](#)). In addition, in the violent relaxation of the dissipationless collapse both the dark matter and stellar components follow each other and end up occupying the same region, while observations indicate that the dark matter component extends further away than the stellar component and only a small fraction of the total amount of dark matter is located within the stars region (e.g., [Gerhard et al. 2001](#); [Cappellari et al. 2006](#)). Therefore, some dissipation is required, but if this is the case the collapse time becomes more similar to that of disk galaxies, which implies the acquisition of large angular momentum.

An alternative is the merger scenario ([Toomre & Toomre 1972](#); [Toomre 1977](#)) as introduced in Section 1.2. It assumes that star formation only occurs in disks that merge later on forming systems with different morphology and kinematics. The first simulations of disks mergers produced merger remnants with large angular momentum that rotated too fast in comparison with observations of ellipticals (e.g., [Gerhard 1981](#); [Farouki & Shapiro 1981](#)). A step forward was simulations that incorporated heavy dark matter haloes. In these, dynamical friction transports angular momentum from the orbital motions of the merging disks to the dark matter halo, resulting in a slow rotating merger remnant in better agreement with observations of ellipticals ([Barnes 1988](#)). However, the merger remnants produced by pure stellar disks are not as centrally concentrated as ellipticals. Hydrodynamical simulations demonstrated that gas-rich mergers are dissipative processes capable of funneling down the gas towards the center of the system. Then, the gas compresses and a starburst triggers, forming a more concentrated merger remnant in better agreement with observations of ellipticals (e.g., [Hernquist 1989](#); [Barnes & Hernquist 1991](#); [Mihos & Hernquist 1996](#); [Naab et al. 2006](#)). In favor of this picture are the observations of galaxies

1.4. FORMATION SCENARIOS OF ELLIPTICAL GALAXIES



Figure 1.4: Top panel: Deep image of the Virgo Cluster obtained by Chris Mihos and his colleagues using the Burrell Schmidt telescope. The dark spots indicate where bright foreground stars were removed from the image. Messier 87 (M87), located at the bottom left of the image, is a giant elliptical galaxy and one of the most massive galaxies in the local universe. Credit: Chris Mihos (Case Western Reserve University)/ESO (<https://www.eso.org/public/images/eso0919a/>). Bottom left panel: Shallow image of M87 from *HST*. Its whole extension and outer diffuse light can be better appreciated in deep images like the one above. Credit: NASA/STScI. Bottom right panel: Deep image of NGC 474. Shells and tidal tails appear in deep images of the elliptical galaxy like this one, otherwise featureless in shallower images. The origin of these features is thought to be stellar debris from absorbing numerous small galaxies in a merger-rich history. Credit: P.-A. Duc (CEA, CFHT), Atlas 3D Collaboration.

1. INTRODUCTION

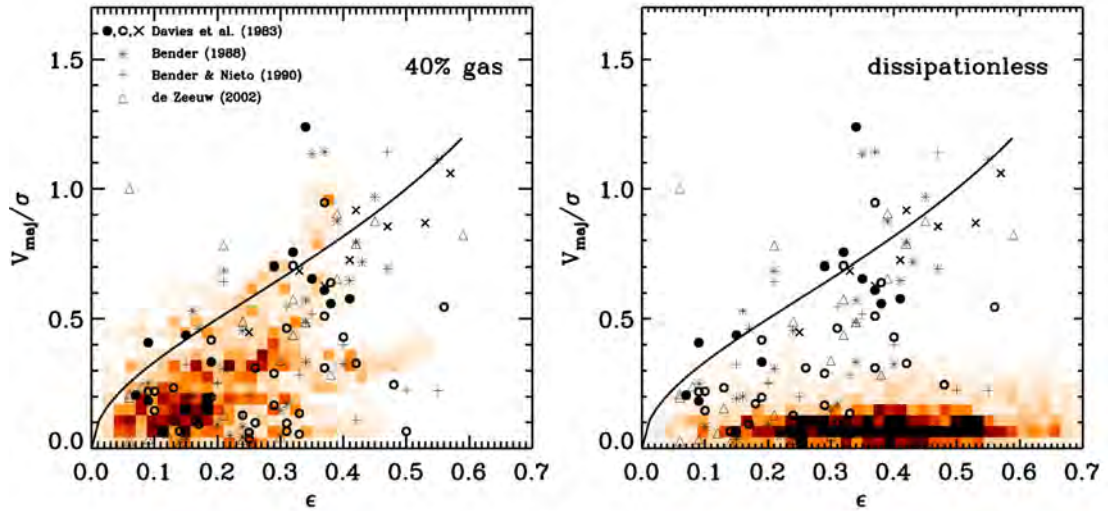


Figure 1.5: From Cox et al. (2006). V_{maj}/σ vs. ellipticity diagram for 40% gas dissipational (left panel) and dissipationless (right panel) merger remnants. The solid line in both plots is that expected for an oblate isotropic rotator (Binney 1978). Overplotted are data from observed ellipticals from Davies et al. (1983), Bender (1988), Bender & Nieto (1990), and de Zeeuw et al. (2002).

with elevated star formation rates (SFRs) that exhibit disturbed morphologies similar to those found in mergers (e.g., Joseph & Wright 1985; Kartaltepe et al. 2012). Besides, the mergers of gas-rich galaxies were likely more common at high redshift where gas fractions were larger (e.g., Tacconi et al. 2010; Daddi et al. 2010a), in agreement with the early formation of elliptical galaxies according to their ages.

Dissipationless and dissipational mergers leave behind very different merger remnants. Dissipational mergers result in compact remnants, higher rotation velocity, and higher central velocity dispersion. In Figure 1.5 it is shown the rotation velocity along the major axis over the central velocity dispersion (V_{maj}/σ) versus ellipticity (ϵ) diagram for a set of equal-mass disk galaxies dissipational and dissipationless mergers from Cox et al. (2006). Observations of elliptical galaxies indicate that they span a broad range in the parameter space, which is better reproduced by dissipational mergers. However, dissipational processes have problems producing slow rotators, such massive ellipticals. It was proposed that massive ellipticals formed via dissipationless mergers, so-called dry mergers, of elliptical progenitors (e.g., Cox et al. 2006; Naab et al. 2006). In this scenario, dissipational wet mergers would be an important in producing the wide range of properties observed in ellipticals, particularly at the less massive end, but also dissipationless dry mergers would be important as those responsible of the ellipticals at the more massive end.

In a hierarchical assembly scenario for galaxy formation smaller haloes assembled earlier than larger haloes. If the star formation history follows the halo assembly history, elliptical galaxies should have younger stellar populations than what the data indicates. The solution to this paradox

is that the halo assembly history can be different from the star formation history. The stars located in larger haloes could form earlier in smaller haloes that assembled later on to form larger haloes (e.g., [Neistein et al. 2006](#); [Li et al. 2008](#)). Therefore, elliptical galaxies could form their stars in progenitor galaxies located in smaller haloes that merged later on transforming their morphology and kinematics, in agreement with the stellar population ages of ellipticals and the hierarchical assembly scenario. Very deep observation of nearby ellipticals showed that they display remnants of a very rich merger history such as tidal tails or shells (e.g., [Duc et al. 2011, 2015](#)) (see Figure 1.4).

1.4.1 Optically-selected High-redshift Galaxies

The question that follows in this context of the formation of elliptical galaxies is then, which were the progenitor galaxies where their stars formed? First, it comes naturally to think of high-redshift star-forming galaxies (SFGs). The electromagnetic spectrum of galaxies at all wavelengths forms their spectral energy distribution (SED). Features in their SED allow the identification of certain types of galaxies. The Lyman limit ($\lambda = 912 \text{ \AA}$) is a signature that allows the identification of high-redshift SFGs. SFGs exhibit a prominent break beyond their Lyman limit owing to their stellar populations. These galaxies are called Lyman break galaxies (LBGs) and are characterized by moderately high SFRs. A LBG will appear very faint or invisible in all bands bluewards its Lyman limit and prominent again redwards its Lyman limit. The more redshifted the Lyman limit gets the more distant the galaxy is. Therefore, the Lyman break technique is an efficient way of selecting high-redshift SFGs by using just two broad bands ([Steidel et al. 1996](#)). It has been used at the highest redshifts proved with the current technology $z \sim 10$ ([Bouwens et al. 2015](#)). Of course, redshift confirmation requires spectroscopic follow-up.

Observations of $z \geq 2$ LBGs show that they have the properties expected for the progenitors of $z \leq 1$ QGs. They are blue, typically disk or irregular SFGs, sometimes exhibiting multiple components suggestive of ongoing mergers, and with stellar masses a factor of 10 lower, smaller sizes, and younger ages than ellipticals (e.g., [Pettini et al. 2001](#); [Shapley et al. 2001](#); [Giavalisco 2002](#)). These characteristics fit them qualitatively in the hierarchical assembly scenario as plausible progenitors of elliptical galaxies (e.g., [Steidel et al. 1996](#); [Baugh et al. 1998](#)).

1.4.2 Compact Quiescent Galaxies

Studies at high redshift were traditionally biased towards the detection of SFGs, brighter than QGs galaxies at rest-frame ultraviolet wavelengths that get redshifted into the observed optical bands at high redshift. Only with the development of near-infrared detectors it was feasible to study galaxy populations that, while fainter at rest-frame ultraviolet wavelengths than SFGs, are brighter at rest-frame optical wavelengths due to their large stellar content. The Faint InfraRed Extragalactic Survey (FIRES; [Franx et al. 2000](#)) was the first deep near-infrared survey of extragalactic blank

1. INTRODUCTION

fields. It discovered distant red galaxies (DRGs), a population of massive, evolved galaxies at $z \sim 2$ that dominated the massive end of the stellar mass function and were missed in previous surveys due to their faintness in the optical (rest-frame ultraviolet) wavelengths (Franx et al. 2003).

Follow-up high spatial resolution studies of DRGs with the *Hubble Space Telescope* (HST) revealed their morphology, showing that they are extremely compact objects, so-called compact quiescent galaxies (cQGs; Toft et al. 2005; Daddi et al. 2005). cQGs present stellar masses similar to the most massive local elliptical galaxies, but sizes like local dwarf galaxies (effective radius, $r_e \sim 1\text{--}2$ kpc). Therefore, cQGs have stellar densities higher than local galaxies of similar mass and comparable to those of globular clusters, but located on galactic scales. Their number densities show that at $z \sim 2$ half of the most massive galaxies were extremely compact, old, and quiescent (e.g., Brammer et al. 2011) (see Figure 1.6).

cQGs stellar masses, stellar ages, velocity dispersions, and metallicities have been revealed in detail through near-infrared spectroscopy (Toft et al. 2012; Onodera et al. 2012; van de Sande et al. 2013; Kriek et al. 2016; Belli et al. 2017). These studies revealed the post-starburst nature of cQGs with ages 1–2 Gyr, velocity dispersions $\sigma = 300\text{--}500$ km s⁻¹, rich metal content, presence of significant amounts dust with stellar extinctions $A_V = 0\text{--}1.0$, and stellar masses $\log(M_*/M_\odot) > 11.0$. In Figure 1.7 an example spectrum of a cQG characterized by typical post-starburst features is shown.

QGs at $z \sim 2$ are thus much smaller than present-day ellipticals of the same stellar mass (e.g., Toft et al. 2005; Daddi et al. 2005; Trujillo et al. 2006; Buitrago et al. 2008; van Dokkum et al. 2008) implying that strong size evolution must occur from $z = 2$ to $z = 0$. In addition, recent studies revealed that cQGs at $z \sim 2$ exhibit rotationally-supported stellar disks (e.g., Newman et al. 2015; Toft et al. 2017; Newman et al. 2018), implying that angular momentum is retained significantly in QGs after star formation is quenched (see Figure 1.8). The formation of cQGs must imply dissipational processes that leave behind compact stellar rotating disks, followed by size increase and kinematical transformation from fast to slow rotators, while the stellar populations evolve passively. Dry minor mergers were proposed as the most plausible mechanism driving the size and kinematical transformation of cQGs (e.g., Bezanson et al. 2009; Oser et al. 2012; Newman et al. 2012; Toft et al. 2012). However, the merger rate of massive galaxies with redshift posed a major problem, since mergers do not seem enough to fully explain the observed size evolution (e.g., Man et al. 2016). Dilution was suggested as an additional mechanism to solve the discrepancy. In this scenario, galaxies that get incorporated to the quiescent population with decreasing redshift are increasingly larger (e.g., Carollo et al. 2013; Krogager et al. 2014). Furthermore, other recent studies revealed more distant QGs, extending the population up to at least $z \sim 4$ (e.g., Straatman et al. 2015; Glazebrook et al. 2017; Schreiber et al. 2018a), although spectroscopic confirmation and verification of their true passive nature are still challenging (Simpson et al. 2017; Schreiber

1.4. FORMATION SCENARIOS OF ELLIPTICAL GALAXIES

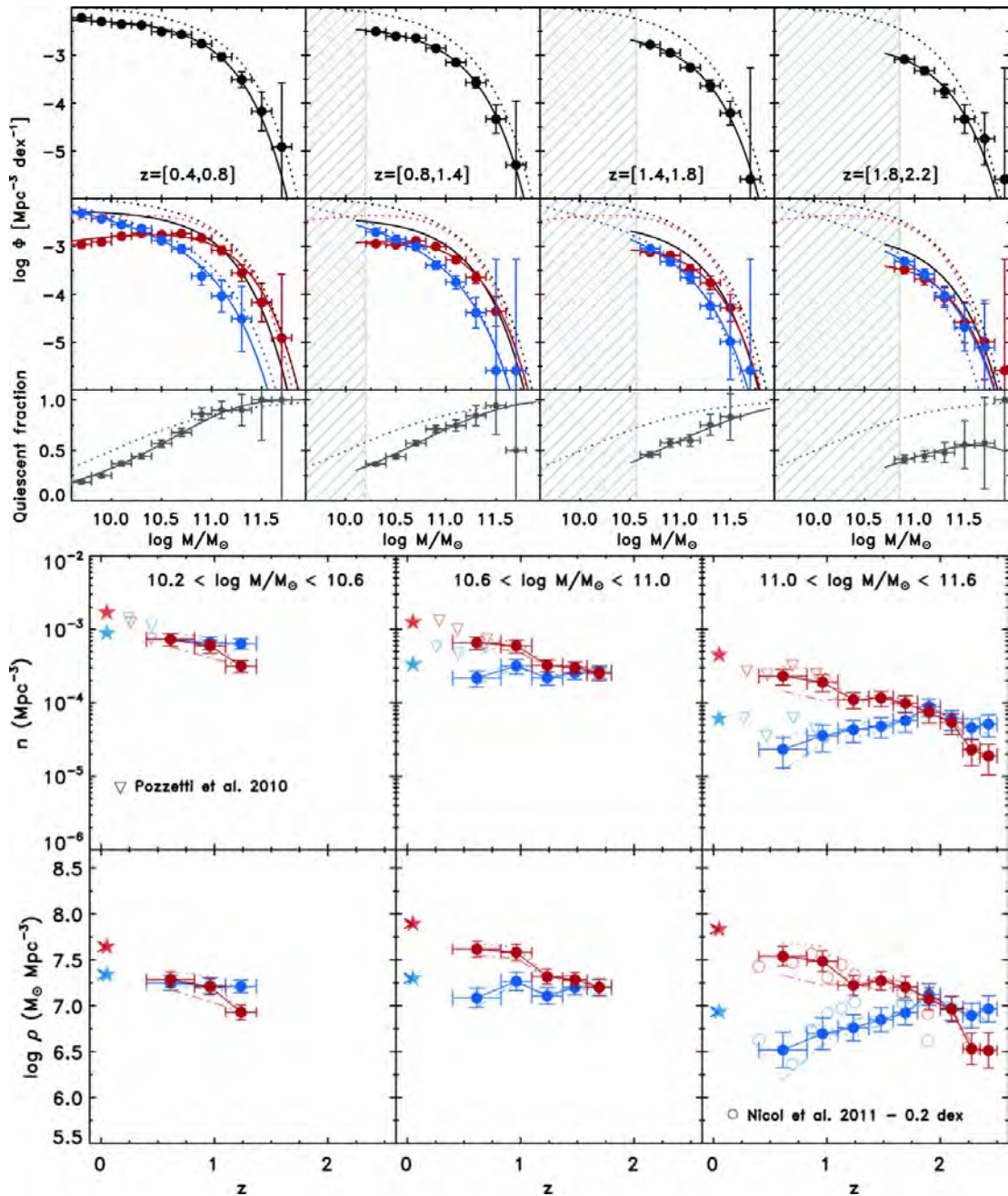


Figure 1.6: From Brammer et al. (2011). Top panel: Stellar mass function evolution for all galaxies (black), QGs (red), and SFGs (blue). The bottom row shows the fraction of QGs as a function of stellar mass and redshift. QGs evolve more rapidly than SFGs and drive the evolution of the stellar mass function at the high-mass end. Bottom panel: Number and mass density evolution for QGs (red) and SFGs (blue) for three stellar mass bins. Note that at $z \sim 2$ half of the galaxies in the most massive stellar bin are already quiescent, given the similar number densities of QGs and SFGs.

et al. 2018b; Santini et al. 2019). The estimated ages of the most distant QGs discovered so far are on the range 0.25–0.5 Gyr, with formation timescales of ~ 250 Myr. QGs present even smaller sizes with increasing redshift, extending the scenario of size evolution via dry minor mergers to earlier epochs (e.g., Kubo et al. 2018) (see Figure 1.9). At $z \sim 4$ the universe is only ~ 1.5 Gyr.

1. INTRODUCTION

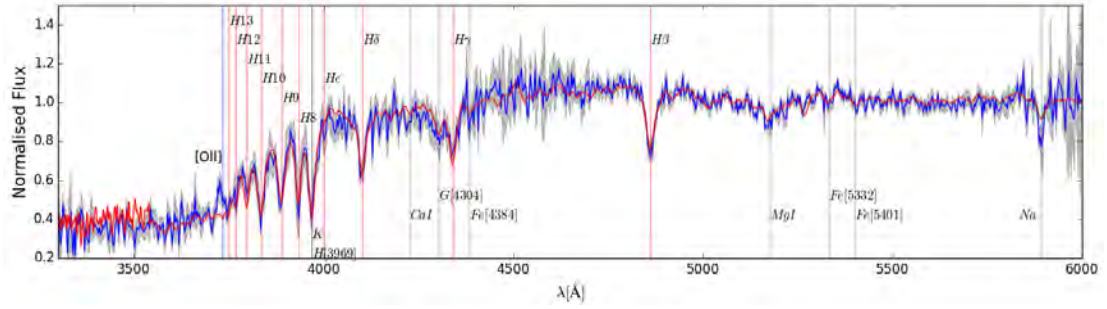


Figure 1.7: Composite spectrum of a sample of $z \sim 2$ cQGs courtesy of M. Stockmann. The spectrum is shown in blue with the 1σ confidence interval in gray. Best-fit model is shown in red. Hydrogen Balmer absorption lines are highlighted in red, other absorption lines in grey, and emission lines in blue vertical lines. Note that the 4000 Å break is prominent as well as the Balmer absorption lines, typical features of post-starburst galaxies.

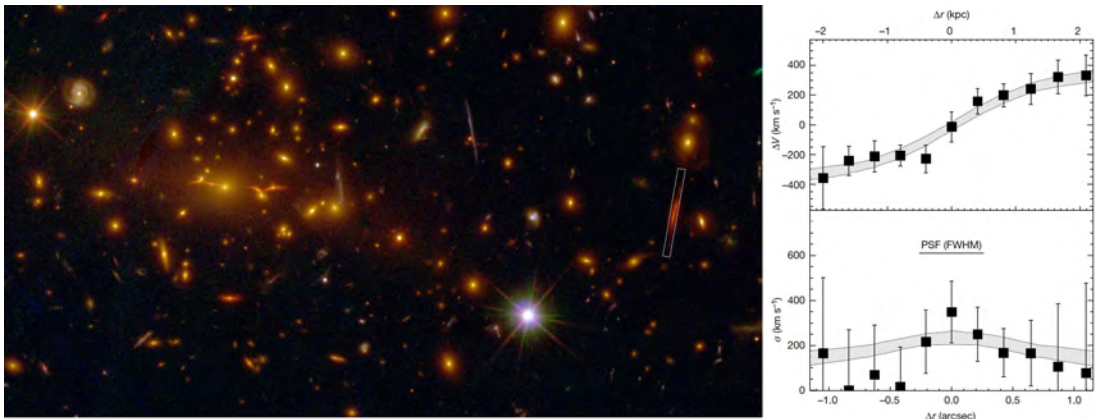


Figure 1.8: From Toft et al. (2017). Left panel: *HST* color image of the cluster MACS2129-1. The target cQG is indicated with the location of the slit during spectroscopic observations. It appears magnified and stretched by the foreground cluster. Right panel: Rotation and dispersion curve for MACS2129-1. Velocity offset (ΔV) and velocity dispersion (σ) as a function of distance from the center of the galaxy (Δr). The gray area represents the 1σ confidence interval for a thin disk model fit to the observations (black squares).

How did such a rapid and compact stellar mass assembly occur? What are the progenitors of $z \geq 4$ QGs? How did the quenching of their star formation happen?

1.4.3 Submillimeter Galaxies

In Section 1.4.1 LBGs were introduced in the context of plausible progenitors of elliptical galaxies. LBGs have moderately high SFRs, but still relatively low dust content, which make them appear bright at ultraviolet wavelengths. However, strong star formation is associated with the production of large amounts of dust. Dust absorbs ultraviolet photons and re-emits them at far-infrared wavelengths. Therefore, galaxies with strong star formation are typically dust obscured and not as bright as LBGs at ultraviolet wavelengths.

Normal SFGs are characterized by formation timescales comparable to the age of the universe as given by their specific star formation rates, i.e., the current SFR over the stellar mass ($\text{sSFR} =$

1.4. FORMATION SCENARIOS OF ELLIPTICAL GALAXIES

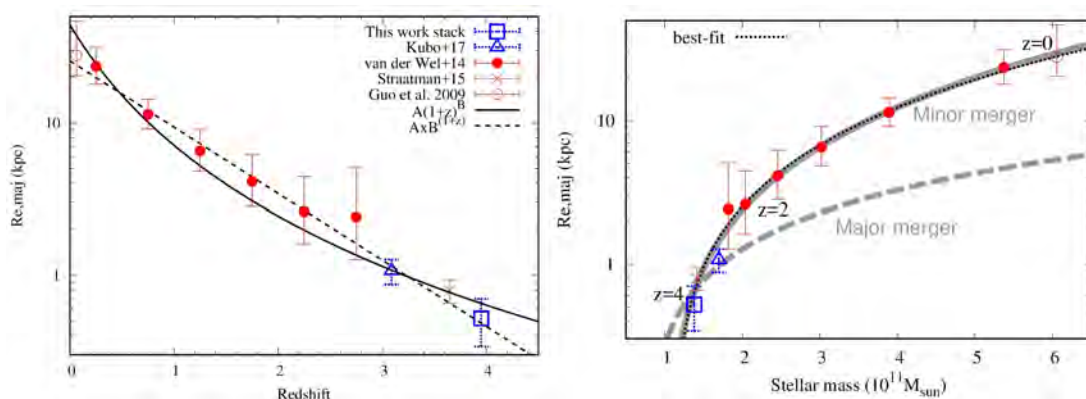


Figure 1.9: From Kubo et al. (2018). Left panel: Size-redshift relation of massive QGs taking the stellar mass evolution into account based on Marchesini et al. (2014). The data points are QGs at $z = 0$ from Guo et al. (2009), at $0.75 \leq z \leq 2.75$ from van der Wel et al. (2014), at $z = 3.1$ from Kubo et al. (2017), at $z \sim 3.7$ from Straatman et al. (2015), and at $z \sim 4$ from Kubo et al. (2018) referred as "this work/study". The black solid curve and dashed line show the best-fit curves to the functional forms shown in the legend. Right panel: Size-stellar mass growth from massive QGs at $z = 4$ taking the stellar mass evolution into account. The black dotted curve shows the best fit. The gray solid and dashed curves show toy models of size-stellar mass growth in cases of minor mergers ($r_{e,\text{maj}} \propto M_*^2$) and major mergers ($r_{e,\text{maj}} \propto M_*$).

SFR/ M_*). Galaxies with shorter formation timescales exist, so-called starburst galaxies, on the order of $\text{sSFR} \sim 100 \text{ Myr}$ (note that there is not a unique definition of starbursts in studies of galaxies). Owing to their strong SFRs, most of the starbursts belong to the population of galaxies that are dust obscured and not always directly visible at ultraviolet wavelengths.

In the nearby universe there are galaxies with large amounts of dust, emitting most of their light in the far-infrared, so-called luminous infrared galaxies (LIRGs) or even ultra-luminous infrared galaxies (ULIRGs) if their infrared luminosities exceed $L_{\text{IR}} > 10^{12} L_{\odot}$ (e.g., Sanders & Mirabel 1996). In these galaxies most of the star formation is confined to very small regions on the order of $\sim 1 \text{ kpc}$ (e.g., Lutz et al. 2016). Galaxies such luminous in the far-infrared are almost exclusively associated to mergers or interacting systems (e.g., Joseph & Wright 1985; Kartaltepe et al. 2012), indicating that mergers are likely their triggering mechanism. Furthermore, simulations showed that gas-rich mergers are capable of originating these strong nuclear starbursts (e.g., Hernquist 1989; Barnes & Hernquist 1991; Mihos & Hernquist 1996; Naab et al. 2006). At high redshift, deep surveys at submillimeter wavelengths began with the Submillimeter Common-User Bolometer Array (SCUBA; Holland et al. 1999), uncovering a population of submillimeter-bright sources, so-called submillimeter galaxies (SMGs; Smail et al. 1997; Blain et al. 2002). Most of the SMGs are associated with major mergers, strong dust-enshrouded star formation and high central concentrations of molecular gas (e.g., Greve et al. 2005; Tacconi et al. 2006, 2008; Michałowski et al. 2012; Wiklind et al. 2014). Locally, luminous infrared galaxies are rare, but at $z > 1$ their contribution to the total infrared energy and total SFR density is significant (e.g., Pérez-González et al. 2005; Magnelli et al. 2009, 2011). All dust-rich SFGs are named as dusty star-forming galaxies

1. INTRODUCTION

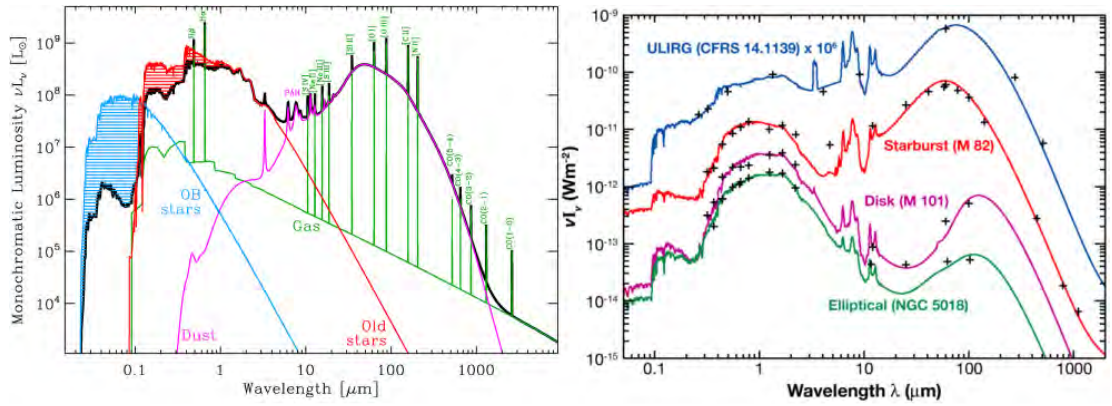


Figure 1.10: Left panel: From Galliano (2017). Contribution to the SED of a dust-rich galaxy from different components, i.e., young OB stars (blue), old stars (red), atomic and ionized gas with characteristic emission lines (green), and dust (magenta). Right panel: From Galliano (2004). A comparison between SEDs of different types of galaxies. The ULIRG represented in the rest-frame as is located at $z = 0.66$.

(DSFGs; Casey et al. 2014a). In Figure 1.10 a detail of the different components that contribute to the SED of a dust-rich galaxy and a comparison between SEDs of different types of galaxies are shown.

SMGs were proposed as progenitors of massive elliptical galaxies (e.g., Cimatti et al. 2008; Ricciardelli et al. 2010; Ivison et al. 2013; Toft et al. 2014; Simpson et al. 2014). At $z \sim 2$ QGs were compact post-starburst galaxies with significant amounts of dust as revealed by near-infrared imaging and spectroscopy studies (Toft et al. 2005; Daddi et al. 2005; Toft et al. 2012; Onodera et al. 2012; van de Sande et al. 2013; Kriek et al. 2016; Belli et al. 2017), suggesting that they were formed in dust-enshrouded nuclear starbursts. However, an important problem establishing a connection between the two populations was that the redshift distribution of SMGs and the expected formation redshift distribution of cQGs peaked at the same redshift. As a result of the development of far-infrared/submillimeter surveys, it was discovered a high-redshift tail in the SMGs redshift distribution (e.g., Chapman et al. 2005; Capak et al. 2008; Daddi et al. 2009; Smolčić et al. 2012a; Weiß et al. 2013). Following this discovery, Toft et al. (2014) presented evidence for a direct evolutionary connection between $z \gtrsim 3$ SMGs and $z \sim 2$ cQGs based on several indicators. First, the similarity between the redshift distribution of SMGs and the formation redshift distribution of QGs. Second, the similar location of the two populations in the stellar mass-size plane (see Figure 1.11). Third, if the comoving number densities of the two populations match, the derived timescale for the starburst episode in the SMGs would be 42 Myr, in agreement with the short gas depletion timescales of SMGs (e.g., Tacconi et al. 2006, 2008). Last, the high stellar velocity dispersion and dynamical masses measured in $z \sim 2$ cQGs are similar to those measured for SMGs from molecular transitions and the SMGs SFRs are similar to the SFRs of the cQGs during their formation calculated assuming they formed in Eddington-limited maximum starbursts.

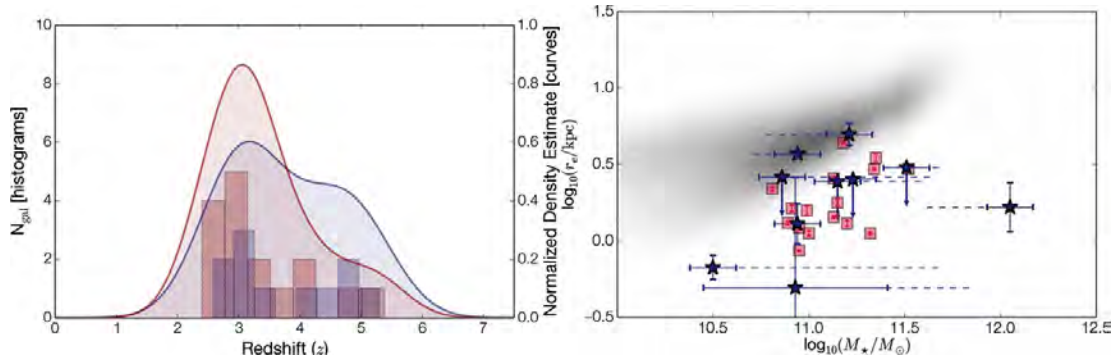


Figure 1.11: From Toft et al. (2014). Left panel: Comparison of the redshift distribution of a sample of $z \geq 3$ SMGs (blue) and the formation redshift distribution of a sample of $z \sim 2$ cQGs. Right panel: Comparison of the stellar mass-size relations of $z \sim 2$ cQGs and $z \geq 3$ SMGs. The two populations are located in the same area of the plane, significantly offset from the relation of local massive galaxies (small gray points).

1.5 A Unified Picture of Massive Galaxy Formation

A picture of the whole evolutionary sequence of massive elliptical galaxies was proposed based on the evidence given by the evolutionary connection between $z \gtrsim 3$ SMGs and $z \sim 2$ cQGs and the suggested evolution of cQGs into local ellipticals. This development sequence for massive elliptical galaxies is illustrated in Figure 1.12. At $z > 3$ a massive gas-rich merger or dynamical instability drives cold gas towards the center of the system, triggering a strong nuclear starbursts that generates large amounts of dust, being observable at submillimeter wavelengths as a SMG. After ~ 50 Myr the starburst is quenched by gas depletion or AGN feedback from the central SMBH, leaving behind a compact remnant of stars that evolves passively into a cQG observed ~ 1 Gyr later at $z \sim 2$. Over the following 10 Gyr up to $z = 0$, its structure evolve mainly due to dry minor mergers, establishing the scaling relations, and evolving its stellar population passively. The final product of this evolutionary sequence is a giant elliptical galaxy.

1.6 Objectives and Thesis Structure

The overall goal of this thesis is to test the outlined evolutionary sequence of massive elliptical galaxies. In particular, the study of the high-redshift starburst stage and its connection with the quenching of star formation and the origin of the quiescent population of galaxies.

The emerged picture of massive galaxy formation is a simple representation of the state-of-the-art in the formation and evolution of massive elliptical galaxies at the time I began my doctorate. My thesis aims at improving our understanding about the details and physical mechanisms of this picture. There are key questions that constitute the framework of my thesis and my future research goals. These questions aim to understand the evolutionary pathways of massive elliptical galaxies: What are the progenitors of massive elliptical galaxies? How did a rapid assembly

1. INTRODUCTION

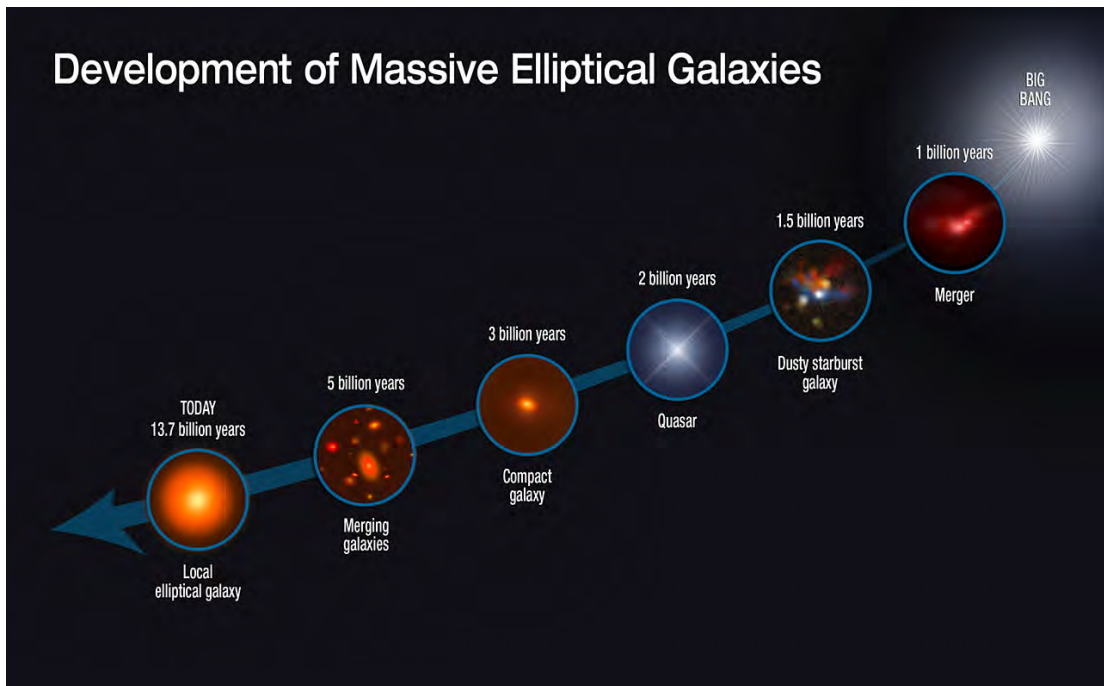


Figure 1.12: The evolutionary sequence of massive elliptical galaxies over 13 Gyr. Credit: NASA, ESA, S. Toft (Niels Bohr Institute), and A. Feild (STScI)

of their stellar mass occur? How did the quenching of their star formation happen? Also to understand more general processes about the assembly of SFGs and QGs: What are the physical processes triggering starburst galaxies? How much of the total star formation happened in a starburst mode and how much in a normal mode? What are the physical processes responsible for quenching galaxies? Did the quenching of star formation happen fast or slow? What is the dependence on the cosmic epoch of these questions? Also devoted to the overall understanding of galaxy formation and evolution: Are gravitational assembly of dark matter haloes, gas cooling and star formation, and feedback processes the basic ingredients of galaxy formation and evolution? Is galaxy formation and evolution the natural end product of a hierarchical assembly of structures in a Λ CDM cosmology?

This thesis contains the work I led during my doctorate sharing a single common narrative, the study of high-redshift starbursts in relation with the evolutionary sequence of massive elliptical galaxies. It is composed of three papers that are presented in Chapters 2, 3, and 4. For a complete list of publications see 5. The layout of the thesis is as follows:

In Chapter 1 I presented an introduction of the state-of-the-art that contextualizes the framework of my thesis. I gave an overview of the development of our current knowledge about the formation of structures in the universe. In particular, how the structure formation leads to the formation of different galaxy types. Then, I focused on the formation and evolution scenarios for massive elliptical galaxies from their early stages to the local universe.

In Chapter 2, in order to test the proposed evolutionary connection between $z \gtrsim 3$ SMGs and $z \sim 2$ cQGs, I present a deep, high resolution *HST* and Atacama Large Millimeter/submillimeter Array (ALMA) follow-up observations of six of the highest-redshift SMGs from [Toft et al. \(2014\)](#), five of which are spectroscopically confirmed at $z \sim 4.5$. A direct test for the evolutionary connection between the two populations is to compare their sizes and their location in the stellar mass-size plane as shown in Figure 1.11. However, the major roadblock in establishing such an evolutionary connection was the impossibility of deriving accurate sizes and stellar masses of $z > 3$ SMGs due to the lack of spatial resolution. The work presented in Chapter 2 solves this problem by studying both the spatially-resolved unobscured and obscured star formation, being able to measure accurate sizes of the star-forming regions and to derive accurate stellar masses that are compared with the stellar sizes and masses of cQGs at $z \sim 2$.

In Chapter 3 I present follow-up ^{12}CO line observations of three candidate protoclusters from [Bussmann et al. \(2015\)](#). Massive elliptical galaxies are located in the cores of galaxy clusters in the local universe. Clusters are gravitationally the most dominant structures in the universe. However, the origins of these systems are basically unknown. If dominated by QGs locally, at high redshift there should be a stage in which they are dominated by SFGs. The work presented in Chapter 3 aims at confirming whether the multiple ALMA $870 \mu\text{m}$ continuum sources the candidate protoclusters are composed of are located at the same redshift and likely physically associated within the same structure as protocluster core systems or are line-of-sight chance projections.

In Chapter 4 I present a study that explores the location of the general population of galaxies with respect to fundamental star-forming and structural relations, identifying compact star-forming galaxies (cSFGs), and studying diagnostics of the burstiness of star formation. SFGs spend most their time evolving as extended disks. They form a tight correlation between SFR and stellar mass, so-called main sequence (e.g., [Elbaz et al. 2007](#)). The small scatter of this relation suggests that secular evolution is their dominant mode of stellar growth. However, QGs are compact and located below the main sequence. The quenching of star formation and the departure from the main sequence must imply the build-up of a central stellar core (e.g., [Barro et al. 2017a](#)). cSFGs were proposed as immediate progenitors of QGs, although their origin and nature are debated. Were they formed in slow secular processes or in rapid merger-driven starbursts? The work presented in Chapter 4 presents three diagnostics of the burstiness of star formation: 1) Star formation efficiency, 2) ISM, and 3) radio emission, aiming at studying whether the build-up of the stellar core and subsequent quenching of star formation was the product of a slow secular evolution, as in normal SFGs, or happened rapidly, as in starburst galaxies.

I finalize my dissertation in Chapter 5 summarizing my main findings and conclusions and presenting perspectives for future research.

Connecting Submillimeter and Quiescent Galaxies

This chapter contains the following article:

**“Starburst to Quiescent from *HST*/ALMA:
Stars and Dust Unveil Minor Mergers in Submillimeter Galaxies at $z \sim 4.5$ ”**

Published in *The Astrophysical Journal*, Volume 856, Issue 2, article id. 121, 18 pp. (2018)

Authors:

C. Gómez-Guijarro, S. Toft, A. Karim, B. Magnelli, G. E. Magdis, E. F. Jiménez-Andrade, P. L. Capak, F. Fraternali, S. Fujimoto, D. A. Riechers, E. Schinnerer, V. Smolčić, M. Aravena, F. Bertoldi, I. Cortzen, G. Hasinger, E. M. Hu, G. C. Jones, A. M. Koekemoer, N. Lee, H. J. McCracken, M. J. Michałowski, F. Navarrete, M. Pović, A. Puglisi, E. Romano-Díaz, K. Sheth, J. D. Silverman, J. Staguhn, C. L. Steinhardt, M. Stockmann, M. Tanaka, F. Valentino, E. van Kampen, & A. Zirm

Dust-enshrouded, starbursting, submillimeter galaxies (SMGs) at $z \geq 3$ have been proposed as progenitors of $z \geq 2$ compact quiescent galaxies (cQGs). To test this connection, we present a detailed spatially resolved study of the stars, dust and stellar mass in a sample of six submillimeter-bright starburst galaxies at $z \sim 4.5$. The stellar UV emission probed by *HST* is extended, irregular and shows evidence of multiple components. Informed by *HST*, we deblend *Spitzer*/IRAC data at rest-frame optical finding that the systems are undergoing minor mergers, with a typical stellar mass ratio of 1:6.5. The FIR dust continuum emission traced by ALMA locates the bulk of star formation in extremely compact regions (median $r_e = 0.70 \pm 0.29$ kpc) and it is in all cases associated with the most massive component of the mergers (median $\log(M_*/M_\odot) = 10.49 \pm 0.32$). We compare spatially resolved UV slope (β) maps with the FIR dust continuum to study the infrared excess ($\text{IRX} = L_{\text{IR}}/L_{\text{UV}}$)- β relation. The SMGs display systematically higher IRX values than expected from the nominal trend, demonstrating that the FIR and UV emissions are spatially disconnected. Finally, we show that the SMGs fall on the mass-size plane at smaller stellar masses and sizes than cQGs at $z = 2$. Taking into account the expected evolution in stellar mass and size between $z = 4.5$ and $z = 2$ due to the ongoing starburst and mergers with minor companions, this is in agreement with a direct evolutionary connection between the two populations.

2.1 Introduction

Giant elliptical galaxies are the oldest, most massive galaxies in the local Universe. Understanding their formation and evolution is one of the major challenges in contemporary galaxy evolution studies. They are uniformly old, red and quiescent, i.e., void of star formation. Studies of their stellar populations suggests that they formed in violent bursts of star formation at $z \sim 3-5$ (e.g., [Thomas et al. 2005](#)). Their evolution has been traced all the way back to $z \sim 4$ through the study of mass complete samples of quiescent galaxies as a function of redshift (e.g., [Brammer et al. 2011](#); [van der Wel et al. 2014](#); [Straatman et al. 2015](#); [Davidzon et al. 2017](#)).

Compared with their lower redshift descendants, at $z \sim 2$ half of the most massive galaxies are already old, quiescent and are furthermore found to be extremely compact systems (e.g., [Toft et al. 2007](#); [van Dokkum et al. 2008](#); [Szomoru et al. 2012](#)). The brightest examples of these compact quiescent galaxies (cQGs) at $z \sim 2$ (for which follow-up spectroscopy has been possible) show clear post-starburst features, evidence of a starburst at $z > 3$ (e.g., [Toft et al. 2012](#); [van de Sande et al. 2013](#); [Kriek et al. 2016](#); [Belli et al. 2017](#); [Toft et al. 2017](#), [Stockmann et al., in prep](#)). Their subsequent evolution into local ellipticals is most likely dominated by passive aging of their stellar populations and merging with minor companions (e.g., [Bezanson et al. 2009](#); [Oser et al. 2012](#); [Newman et al. 2012](#); [Toft et al. 2012](#)).

The most intense starbursts known are the so-called dusty star-forming galaxies (DSFGs),

2. CONNECTING SUBMILLIMETER AND QUIESCENT GALAXIES

which are characterized by star formation rates of up to thousands of solar masses per year (see [Casey et al. 2014a](#), for a review). The best studied DSFGs are the submillimeter galaxies (SMGs) (e.g., [Blain et al. 2002](#)). Their high dust content absorbs the intense ultraviolet (UV) emission from the starburst and re-radiates it at far-infrared/submillimeter (FIR/sub-mm) wavelengths (e.g., [Swinbank et al. 2014](#)), making the most intense starbursts easily detectable in sub-mm surveys to the highest redshift.

Following the discovery of a high-redshift tail in the SMGs redshift distribution (e.g., [Chapman et al. 2005](#); [Capak et al. 2008, 2011](#); [Daddi et al. 2009](#); [Smolčić et al. 2012a](#); [Weiß et al. 2013](#); [Miettinen et al. 2015](#); [Strandet et al. 2016](#); [Brisbin et al. 2017](#)), [Toft et al. \(2014\)](#) presented evidence for a direct evolutionary connection between $z \gtrsim 3$ SMGs and $z \sim 2$ cQGs based on the formation redshift distribution for the quiescent galaxies, number density arguments and the similarity of the distributions of the two populations in the stellar mass-size plane (see also e.g., [Cimatti et al. 2008](#); [Simpson et al. 2014, 2015](#); [Ikarashi et al. 2015](#); [Hodge et al. 2016](#); [Oteo et al. 2016, 2017](#)). However, as the latter was based on sizes derived from low resolution data probing the rest-frame UV emission (which is likely biased towards unobscured, young stellar populations), confirmation using higher quality data is crucial.

To test the proposed evolutionary connection, we here present deep, high resolution *Hubble Space Telescope* (*HST*) and Atacama Large Millimeter/submillimeter Array (ALMA) follow-up observations of six of the highest-redshift SMGs from [Toft et al. \(2014\)](#), five of which are spectroscopically confirmed at $z \sim 4.5$. The data probe the distribution of the UV-bright stellar populations and the FIR dust continuum emission, which allows for a full characterization of the star formation and dust attenuation in the galaxies. The sources are drawn from the COSMOS field, thus a wealth of deep ground- and space-based lower resolution optical–mid-IR data are available, which we use to obtain stellar masses for the systems.

In two companion papers we will explore the gas/dust distributions and kinematics of the sample ([Karim et al.](#), in prep) and the detailed molecular gas properties of one of the sources ([Jiménez-Andrade et al. 2018](#)).

The layout of the paper is as follows. We introduce the sample, data and methodology in Section 2.2. In Section 2.3 we present the rest-frame UV/FIR morphologies of the sample. The results based on the comparison of the dust as seen in absorption and emission are shown in Section 2.4. Stellar masses are discussed in Section 2.5. We show the evolutionary connection between SMGs and cQGs in Section 2.6. Additional discussion is presented in Section 2.7. We summarize the main findings and conclusions in Section 2.8.

Throughout this work we adopted a concordance cosmology $[\Omega_\Lambda, \Omega_M, h] = [0.7, 0.3, 0.7]$ and Chabrier initial mass function (IMF) ([Chabrier 2003](#)). The AB magnitude system was employed across the whole study ([Oke 1974](#)).

Table 2.1: Sample of Targetted SMGs in COSMOS.

Source Name	Other Name	α (J2000) ^a (h:m:s)	δ (J2000) ^a (°:′:″)
AK03		10 00 18.74	+02 28 13.53
AzTEC1	AzTEC/C5	09 59 42.86	+02 29 38.2
AzTEC5	AzTEC/C42	10 00 19.75	+02 32 04.4
AzTEC/C159		09 59 30.42	+01 55 27.85
J1000+0234	AzTEC/C17	10 00 54.48	+02 34 35.73
Vd-17871		10 01 27.08	+02 08 55.60

^a From [Smolčić et al. \(2017\)](#): AK03, AzTEC/C159 and Vd-17871 refer to the VLA 3 GHz peak position ([Smolčić et al. 2015](#)); AzTEC1 and AzTEC5 refer to the SMA 890 μ m peak position ([Younger et al. 2007](#)); J1000+0234 refer to the PdBI $^{12}\text{CO}(4-3)$ emission line peak position ([Schinnerer et al. 2008](#)).

2.2 Sample and Data

2.2.1 COSMOS SMGs Sample

We selected a sample of six of the highest-redshift unlensed SMGs from [Toft et al. \(2014\)](#) (see Table 2.1), which are part of the extensive (sub)millimeter interferometric and optical/millimeter spectroscopic follow-up campaigns in the COSMOS field ([Scoville et al. 2007](#); [Younger et al. 2007, 2008](#); [Capak et al. 2008, 2011](#); [Schinnerer et al. 2008](#); [Riechers et al. 2010, 2014a](#); [Smolčić et al. 2011, 2015](#); [Yun et al. 2015](#)). All our sample sources had been spectroscopically confirmed to be at $4.3 \lesssim z \lesssim 4.8$, except AzTEC5 at a slightly lower (photometric) redshift (see Table 2.3). We refer the reader to [Smolčić et al. \(2015\)](#) for a detailed description of the selection of each source.

2.2.2 HST Data

HST WFC3/IR observations of AzTEC1, J1000+0234 and Vd-17871 were taken in the *F125W* and *F160W* bands at a 2-orbit depth on each filter (program 13294; PI: A. Karim). For AK03 and AzTEC5, WFC3 *F125W* and *F160W* imaging were taken from the CANDELS survey ([Grogin et al. 2011](#); [Koekemoer et al. 2011](#)). AzTEC/C159 was not in our *HST* program due to its faintness at near-IR wavelengths. Additionally, we included COSMOS *HST* ACS/WFC *F814W* images ([Koekemoer et al. 2007](#)) available for the full sample. At the redshift of the sources, these three bands probe the UV continuum regime in the range $\sim 140\text{--}300$ nm (175–345 nm for AzTEC5).

In order to process the *HST* observations from our program we made use of the DrizzlePac 2.0 package ([Gonzaga & et al. 2012](#)). First, we assured a good alignment between the four dithered frames on each band using the TweakReg task. Next, we combined the frames with `AstroDrizzle` employing the same parameters as used in the CANDELS reduction procedure: `final_scale = 0.06` and `final_pixfrac = 0.8` ([Koekemoer et al. 2011](#)).

2. CONNECTING SUBMILLIMETER AND QUIESCENT GALAXIES

For the purpose of this work, it is important that all three bands are properly aligned sharing a common World Coordinate System (WCS) frame with accurate absolute astrometry. In order to guarantee the absolute astrometric accuracy we chose the COSMOS ACS $F814W$ image as the reference frame. The fundamental astrometric frame for COSMOS uses the CFHT Megacam i -band image (Capak et al. 2007). The latter is tied to the USNO-B1.0 system (Monet et al. 2003), which is also tied to the VLA 1.4 GHz image (Schinnerer et al. 2004), ensuring an absolute astrometric accuracy of $0''.05$ – $0''.1$ or better, corresponding to ~ 1 – 1.5 pix for our pixel scale. To align the $F125W$ and $F160W$ images to the $F814W$ WCS, we used TweakReg along with SExtractor (Bertin & Arnouts 1996) catalogs of the three bands, with the $F814W$ catalog and frame as references. Once the three bands shared the same WCS frame, we propagated the WCS solution back to the original `flt.fits` frames using the TweakBack task, and then ran AstroDrizzle once again to produce the final drizzled images. In the case of AK03 and AzTEC5, where the $F125W$ and $F160W$ data came from CANDELS, this alignment procedure is not necessary since the images are already matched to the COSMOS WCS. The final drizzled images in the three bands were resampled to a common grid and a pixel scale of $0''.06 \text{ pix}^{-1}$ using SWarp (Bertin et al. 2002).

2.2.3 ALMA Data

Our galaxies were observed in ALMA’s Cycle-2 as part of the Cycle-1 (program 2012.1.00978.S; PI: A. Karim). We used the ALMA band-7 and tuned the correlator such that a single spectral window (SpW) would cover the [C II] line emission of our galaxies, while three adjacent SpWs with a total bandwidth of 5.7 GHz would be used for continuum detection. These continuum SpWs are those analysed in our study, while the [C II] line datacubes are presented in Karim et al. (in prep).

Observations were all taken in June 2014, using 34 12-m antennae in configuration C34-4 with a maximum baseline of ~ 650 m. For all galaxies, J1058+0133 and J1008+0621 were used as bandpass and phase calibrators, respectively. In contrast, the flux calibrator is not the same for all galaxies, varying from Titan, J1058+0133, Ceres or Pallas. Calibration was performed with the Common Astronomy Software Applications (CASA; version 4.2.2) using the scripts provided by the ALMA project. Calibrated visibilities were systematically inspected and additional flaggings were added to the original calibration scripts. Flux calibrations were validated by checking the flux density accuracies of our phase and bandpass calibrators. Continuum images were created by combining the three adjacent continuum SpWs with the CASA task CLEAN in multi-frequency synthesis imaging mode and using a standard Briggs weighting scheme with a robust parameter of -1.0. The effective observing frequencies, synthesized beams and resulting noise of these continuum images are listed in Table 2.2.

Each galaxy yields a significant continuum detection $S/N > 10$ at the phase center of our

Table 2.2: ALMA Continuum Images Properties.

Source Name	ν_{obs} (Ghz)	Beam Size ($" \times "$)	σ (mJy beam $^{-1}$)	$S_{870}^{\text{ALMA } a}$ (mJy)	$S_{850}^{\text{SCUBA2 } b}$ (mJy)
AK03	337.00	0.29 \times 0.27	0.17	2.3(2.7) \pm 0.2	2.4(1.7) \pm 0.6
AzTEC1	344.67	0.25 \times 0.22	0.47	14.5(15.7) \pm 0.2	14.8(14.3) \pm 1.2
AzTEC5	301.78	0.47 \times 0.28	0.089	7.2(12.4) \pm 0.2	13.2(13.1) \pm 0.7
AzTEC/C159	349.67	0.28 \times 0.27	0.20	6.9(7.1) \pm 0.2	6.8(5.5) \pm 1.3
J1000+0234	349.85	0.30 \times 0.23	0.11	7.6(7.8) \pm 0.2	6.7(5.8) \pm 1.0
Vd-17871	345.75	0.35 \times 0.31	0.21	5.2(5.6) \pm 0.2	4.8(3.9) \pm 0.9

^a In brackets conversion into 850 μm fluxes assuming a standard Rayleigh-Jeans slope of 3.5. ^b In brackets deboosted fluxes.

images. Their fluxes were measured via 2D Gaussian fits using the python package PyBDSF and are given in Table 2.2. These fluxes are consistent with those measured 850 μm fluxes from the S2COSMOS/SCUBA2 survey (Simpson et al., in prep). This suggests that there is not extended emission which is resolved out in the higher resolution ALMA observations.

In terms of the WCS, we do not expect a significant offset in the ALMA absolute astrometry with respect to the COSMOS WCS. The main source of uncertainty for the relative astrometry between ALMA and *HST* is the uncertainty in the *HST* absolute astrometry with respect to the COSMOS WCS, which is $< 0''.1$ as shown in the previous section. Schreiber et al. (2018b) tested the relative astrometry between an ALMA single pointing and an *HST* image tied to the COSMOS WCS. Following Schreiber et al. (2018b), at our S/N and resolution the combined pointing accuracy between our ALMA and *HST* images is $< 0''.12$, corresponding to < 2 pix for our pixel scale.

2.2.4 PSF Matching

The *HST* data span three different bands from two different instruments, so consequently, the spatial resolution is different. It is essential to compare the same physical regions when obtaining resolved color information. We therefore degraded the ACS *F814W* and WFC3 *F125W* images to the resolution of the WFC3 *F160W* data ($0''.18$ FWHM), which has the broadest point-spread function (PSF). First, we created a stacked PSF in the different bands, selecting stars that were not saturated and that did not show irregularities on their light profiles. Second, we derived the kernels to match the ACS *F814W* and WFC3 *F125W* PSFs to the PSF in the WFC3 *F160W* image using the task PSFMATCH in IRAF. We applied a cosine bell function tapered in frequency space to avoid introducing artifacts in the resulting kernel from the highest frequencies. To get the best size for the convolution box we iterated over different values. Finally, we implemented the kernel on the ACS *F814W* and WFC3 *F125W* images. The matched PSFs FWHM in the different bands deviate by less than 2%.

ALMA continuum images also show different spatial resolution compared to that in the

2. CONNECTING SUBMILLIMETER AND QUIESCENT GALAXIES

PSF-matched *HST* images (median synthesized beam size of $0''.30 \times 0''.27$ versus $0''.18$ FWHM, respectively). It is important to perform the measurements in the same physical regions when comparing *HST* and ALMA photometry as well, such as to derive rest-frame FIR/UV ratios. When this is required, we used *HST* images matched to the resolution of the ALMA continuum images constructed following the same procedure explained above. In this case the kernel was computed from the WFC3 *F160W* PSF and the ALMA clean beam, and then applied to the PSF-matched *HST* images. The matched PSFs FWHM in the *HST* and ALMA images deviate by less than 2%.

2.2.5 Adaptative Smoothing

We applied a smoothing technique to the *HST* images to enhance the signal-to-noise ratio (S/N) and improve our ability to detect low surface brightness features and color gradients between neighboring pixels.

The code employed for this purpose was ADAPTSMOOTH (Zibetti 2009), which smooths the images in an adaptative fashion, meaning that at any pixel only the minimum smoothing length to reach the S/N requested is applied. In this way the images retain the original resolution in regions where the S/N is high and only low S/N regions are smoothed.

We required a minimum $S/N = 5$ and a maximum smoothing length of two neighboring pixels in the code. The former holds true for uncorrelated noise, which is not the case for the drizzled *HST* images analyzed here. In our images the chosen value of 5 corresponds to $S/N \sim 2$ when taking into account the noise correlation and pixelation effects in the code. The chosen smoothing length prevents cross-talking between pixels, also reduced by calculating the median of the pixel distribution inside the smoothing radius as opposed to the mean. Such a smoothing length was chosen to match the resolution in the *HST* data, so the smoothing technique does not smear out the images.

We generated a smoothing mask for each band, which is a mask of the required smoothing length to reach the requested minimum S/N for each pixel. When applying a mask to the images, the pixels that do not reach the minimum S/N level are blanked out by the code. If a pixel reached the minimum S/N in at least two bands, we replaced the smoothing length in the mask by the maximum value of them. This guarantees that the same physical regions are probed in different bands, maintaining at the same time the signal if a pixel is above the minimum S/N only in one band.

2.2.6 Additional Photometric Data

A series of additional multiwavelength imaging datasets in the optical/IR were employed in this work: Subaru Hyper Suprime-Cam (HSC) from the HSC Subaru Strategic Program (SSP) team and the University of Hawaii (UH) joint dataset in g , r , i , z and y bands (Tanaka et al. 2017), with

spatial resolution (seeing FWHM) of $0''.92$, $0''.57$, $0''.63$, $0''.64$ and $0''.81$, respectively; the UltraVISTA DR3 survey (McCracken et al. 2012) covering near-IR J , H and K_s bands, which have resolution of $0''.8$, $0''.7$ and $0''.7$, respectively; and the *Spitzer* Large Area Survey with Hyper-Suprime-Cam (SPLASH; Capak et al., in prep.) mid-IR *Spitzer*/IRAC 3.6 and $4.5 \mu\text{m}$, with a PSF FWHM of $1''.66$ and $1''.72$, respectively.

2.3 Morphology

The high spatial resolution of the *HST* and ALMA data ($0''.18$ FWHM versus a median synthesized beam size of $0''.30 \times 0''.27$, respectively) allows for detailed studies of the distributions of both obscured and unobscured star formation in the galaxies. The *HST* $F814W$, $F125W$ and $F160W$ images sample the rest-frame stellar UV, which traces un-extincted to moderately extincted star formation, and ALMA band 7 ($\sim 870 \mu\text{m}$) samples the rest-frame FIR dust continuum (at $\sim 160 \mu\text{m}$ for $z = 4.5$), which traces highly obscured star formation. In Figure 2.1 we compare these two complementary probes for the objects observed in our *HST* program (all except AzTEC/C159). The *HST* images were PSF-matched and smoothed as described in Sections 2.2.4 and 2.2.5.

Qualitatively, the comparison of *HST* and ALMA images suggests important differences in the morphologies. The rest-frame UV stellar emission appears extended and irregular, whereas the rest-frame FIR dust continuum appears very compact. Recently, Hodge et al. (2016) found similar results by comparing stellar morphologies from *HST* $F160W$ and ALMA $870 \mu\text{m}$ images in a sample of 16 SMGs at a median redshift of $z \sim 2.5$. Chen et al. (2015) presented similar results regarding the stellar component at rest-frame optical in a larger sample of 48 SMGs at $z = 1-3$.

AK03, AzTEC5, J1000+0234 and Vd-17871 show evidence of two major neighboring components in the rest-frame UV. According to the available spectroscopic redshifts, or photometric redshifts compatible within the uncertainties when we lack spectroscopic confirmation, these components are consistent with being at the same redshift (see Table 2.3). They also show irregularities and features connecting them (see Figure 2.1). Therefore, it seems very plausible that they are interacting and merging. In addition, AzTEC1 displays a secondary fainter companion towards the North detected in all the three *HST* bands and *Spitzer*/IRAC. Furthermore, AK03, AzTEC5 and J1000+0234 show additional low S/N companions detected also in all the *HST* bands (marked with arrows in Figure 2.1).

All together the full sample is consistent with being multiple component interacting systems. In Section 2.5 we discuss the stellar mass estimates for the different components of each source. Being able to distinguish the components in the lower resolution datasets, specially in the case of the IRAC bands that trace the rest-frame optical, we obtain stellar masses that are large enough to support the merger scenario as opposed to patches of a single disk or other form of highly extincted single structure.

2. CONNECTING SUBMILLIMETER AND QUIESCENT GALAXIES

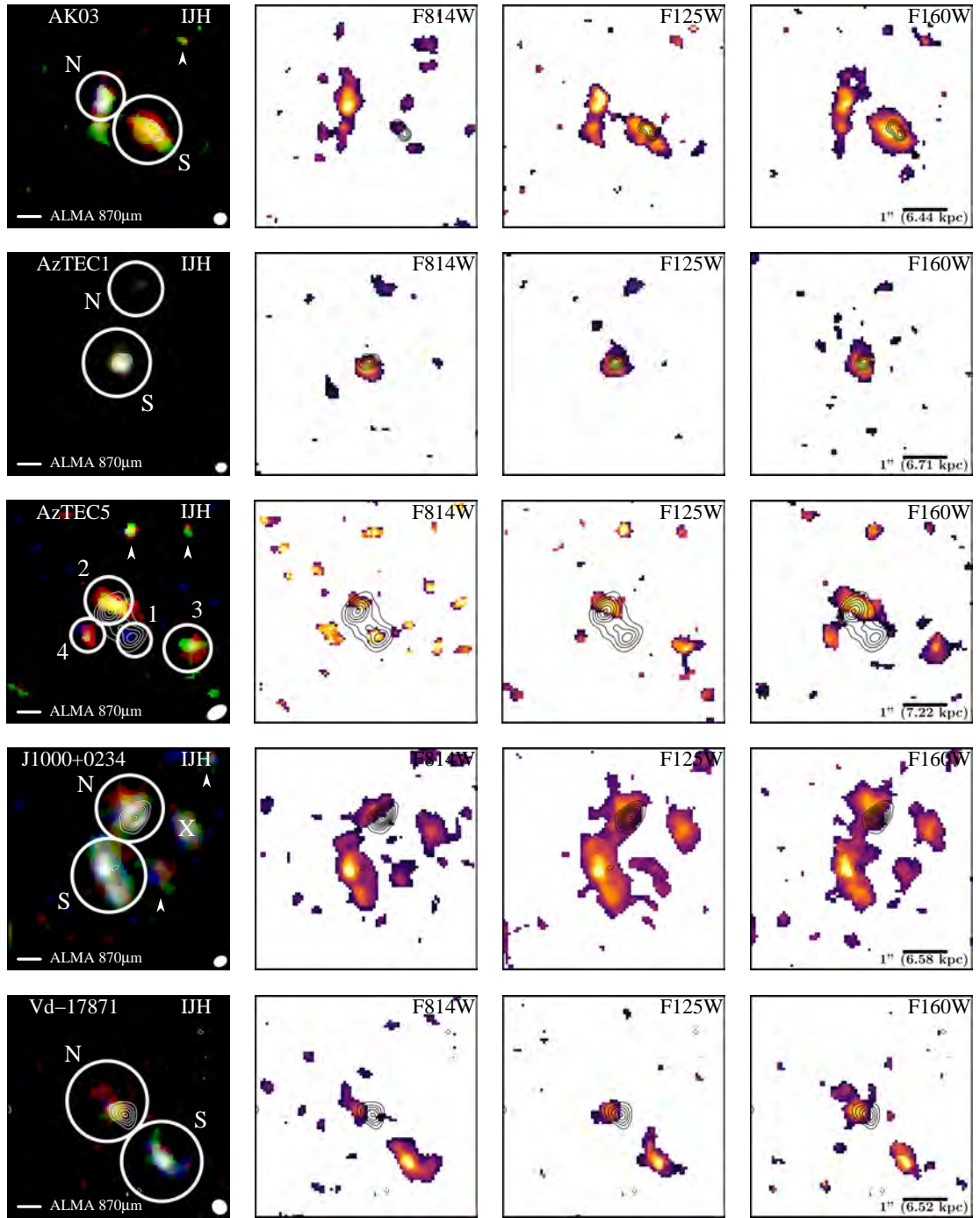


Figure 2.1: $F814W$, $F125W$ and $F160W$ images of the five sources observed with *HST*, and RGB color composite assembled from these three bands. ALMA band 7 ($\sim 870 \mu\text{m}$) contours are overlaid. The images are scaled from $S/N = 2$ to 75% of the peak value. The contours shown start at $\pm 3\sigma$ and go in steps of 1σ (AK03 and AzTEC1) or 3σ (AzTEC5, J1000+0234 and Vd-17871). Different components considered for each source are circled and labeled in the RGB image and potential additional companions are marked with an arrow. The J1000+0234 component confirmed at a lower redshift is labeled with an X. The ALMA beam size is shown at the bottom right corner. North is up, East is to the left, and the images have a size of $5'' \times 5''$.

The compact rest-frame FIR emission, tracing the bulk of the star formation in the system, is always associated with the reddest UV component, but often spatially offset, and not coinciding with the reddest part of the galaxy. This lack of spatial coincidence between the UV and FIR emission is explored further in Section 2.4.

There are no additional sub-mm detections within the ALMA primary beam at the current sensitivity, and thus, we discard equally bright (close to the phase center) or brighter (away from the phase center) companion DSFGs at distances larger than those showed in the $5'' \times 5''$ images in Figure 2.1.

2.3.1 UV Stellar Components

In this section we provide a detailed discussion of the individual systems and their subcomponents detected in the *HST* data (see Figure 2.1 and Table 2.3).

AK03: This system has two main UV components separated by $\sim 1''$ (AK03-N and AK03-S), with the *F125W* image suggesting a bridge connecting the two at an integrated $S/N = 2.4$. The spectroscopic confirmation refers to AK03-N, but AK03-S has a comparable photometric redshift (Smolčić et al. 2015, see Section 2.5.3). All these may be considered evidence for a merger. The dust continuum emission is associated with AK03-S and shows two very compact emission peaks (unresolved at the current resolution), whereas AK03-N remains undetected. Therefore, the bulk of the star formation is associated with AK03-S.

AzTEC1: The source shows a compact UV component (AzTEC1-S) and a very faint companion source $\sim 2''$ towards the North, which is detected at $2 < S/N < 3$ in all three *HST* bands (AzTEC1-N). Despite the low S/N of this companion feature, being detected in all three bands the probability of being spurious is $\sim 10^{-5}$. More importantly, it is detected at $S/N > 3$ in the HSC *r*, *i* and *z* bands, and also in *Spitzer/IRAC* data, confirming that it is a real source. We derived a photometric redshift consistent with lying at the same redshift as AzTEC1-S (Yun et al. 2015) within the uncertainties (see Section 2.5.3). The rest-frame FIR emission is also compact and centered on AzTEC1-S.

AzTEC5: For this system, three main UV components are detected in all three *HST* bands (AzTEC5-2, AzTEC5-3 and AzTEC5-4) and a fourth component is detected only in *F814W* (AzTEC5-1). AzTEC5 is the only source in our sample that lacks spectroscopic confirmation, but photometric redshift estimation indicates a plausible solution for all four components at the same redshift (see Section 2.5.3). The irregular rest-frame UV morphology of AzTEC5-2 and AzTEC5-4, with emission connecting both in *F160W*, is suggestive of an ongoing merger. The rest-frame FIR has three emission peaks. Two bright peaks associated with AzTEC5-1 and AzTEC5-2 respectively, and a fainter peak in between them, which is not detected in any *HST* bands. Besides, the FIR peaks related with AzTEC5-1 and AzTEC5-2 are aligned with the position of two peaks in the

2. CONNECTING SUBMILLIMETER AND QUIESCENT GALAXIES

IRAC images, suggesting that the bulk of the stellar mass is associated with these two components which are probably merging.

AzTEC/C159: As mentioned in Section 2.2.2 this source was excluded from the *HST* program and remains undetected in the *F814W* band image, so we do not have any constraints on its UV morphology. The rest-frame FIR emission is compact and associated with detections in the IRAC bands.

J1000+0234: This system has three main UV components. J1000+0234-N and J1000+0234-S are spectroscopically confirmed at the same redshift (Capak et al. 2008; Schinnerer et al. 2008, Karim et al., in prep). J1000+0234-X is a foreground source at $z_{\text{spec}} = 1.41$ (Capak et al. 2008). An additional companion is detected West of J1000+0234-S in all the three *HST* bands, but the HSC images show diffuse features rather than a concentrated source, consistent with Capak et al. (2008). The North and South components show a connection between them in all the three *HST* bands, suggesting a merger. The rest-frame FIR emission is compact and associated with J1000+0234-N.

Vd-17871: This system has two main UV components $\sim 1''.5$ apart (Vd-17871-N and Vd-17871-S), both with elongated morphologies. Both North and South components are spectroscopically confirmed at the same redshift (Smolčić et al. 2015, Karim et al., in prep). The compact rest-frame FIR emission is associated with the North component.

2.3.2 SED Fitting

Having disentangled different stellar components at rest-frame UV wavelengths, we performed photometry in the lower resolution datasets mentioned in Section 2.2.6, aiming at fitting the resulting spectral energy distributions (SEDs) to constrain stellar masses for every major stellar component (see Table 2.3), corresponding to those encircled in Figure 2.1. In the case of *Spitzer*/IRAC, with a significantly lower resolution, the components appear blended, so it is particularly important to know the number of them to properly deblend the fluxes.

From *g* to K_s bands the sources are resolved into the stellar components defined from the rest-frame UV *HST* data, appearing unresolved themselves but separated enough, so potential blending is not a concern. To estimate the fluxes in these bands we carried out aperture photometry. The size of the apertures varied for each component and source, being the same across bands, and correspond to those plotted in Figure 2.1. We chose the apertures in the K_s -band to be as large as possible enclosing the component we wanted to study, without overlapping with a neighboring component aperture. We performed aperture corrections for every band. In order to do so, we traced the growth curve of a PSF in the different bands and applied a correction factor to the fluxes accounting for the missing flux outside the aperture. We performed aperture corrections on each band instead of measuring in PSF-matched data to take advantage of the resolution, important for this kind of multiple component systems, that otherwise would be degraded to the

lowest-resolution band. The uncertainties in the magnitudes were derived from empty apertures measurements. To assure a good SED fit we only use detections above 3σ (upper limits are included in Figure 2.2).

For the blended *Spitzer*/IRAC 3.6 and 4.5 μm images, we employed the magnitudes from a PSF model using the two-dimensional surface brightness distribution fitting algorithm GALFIT (Peng et al. 2002). We required at least a 5σ detection to perform the fit, which was the case for all source in both 3.6 and 4.5 μm bands. The number of PSFs was set to the number of stellar components the source has as defined from the *HST* data and the PSFs centroids were placed at the positions of K_s -band centroids used as priors, allowing a shift in both X and Y axis that turn out to be < 1 pix from the initial positions (IRAC images pixel scale is $0''.6 \text{ pix}^{-1}$). The uncertainties in the photometry due to the deblending were calculated by performing a number of realizations varying the centroid coordinates randomly within 1 pix of the best fit centroid and fixing those coordinates for each realization. Additionally, we checked for detections in the IRAC 5.8 and 8.0 μm bands from the S-COSMOS survey (Sanders et al. 2007), but the sources are not detected at the required 5σ level (upper limits are included in Figure 2.2).

We fitted the resulting 13-band SEDs (g to 4.5 μm , including the three *HST* bands) using LePHARE (Arnouts et al. 1999; Ilbert et al. 2006). We adopted Bruzual & Charlot (2003) stellar population synthesis models with emission lines to account for contamination from $\text{H}\alpha$ which at the redshift probed in this work is redshifted into the IRAC 3.6 μm band. A Chabrier (2003) IMF, exponentially declining star formation histories (SFHs) and a Calzetti et al. (2000) dust law were assumed. We explored a large parameter grid in terms of SFH e-folding times (0.1 Gyr–30 Gyr), extinction ($0 < A_V < 5$), stellar age (1 Myr–age of the Universe at the source redshift) and metallicity ($Z = 0.004, 0.008$ and 0.02 , i.e., solar). The redshift was fixed to the spectroscopic redshift if available or to the photometric redshift if not (see Table 2.3). In Figure 2.2 we show the derived SEDs, with the fitted models being in good agreement with the data.

2. CONNECTING SUBMILLIMETER AND QUIESCENT GALAXIES

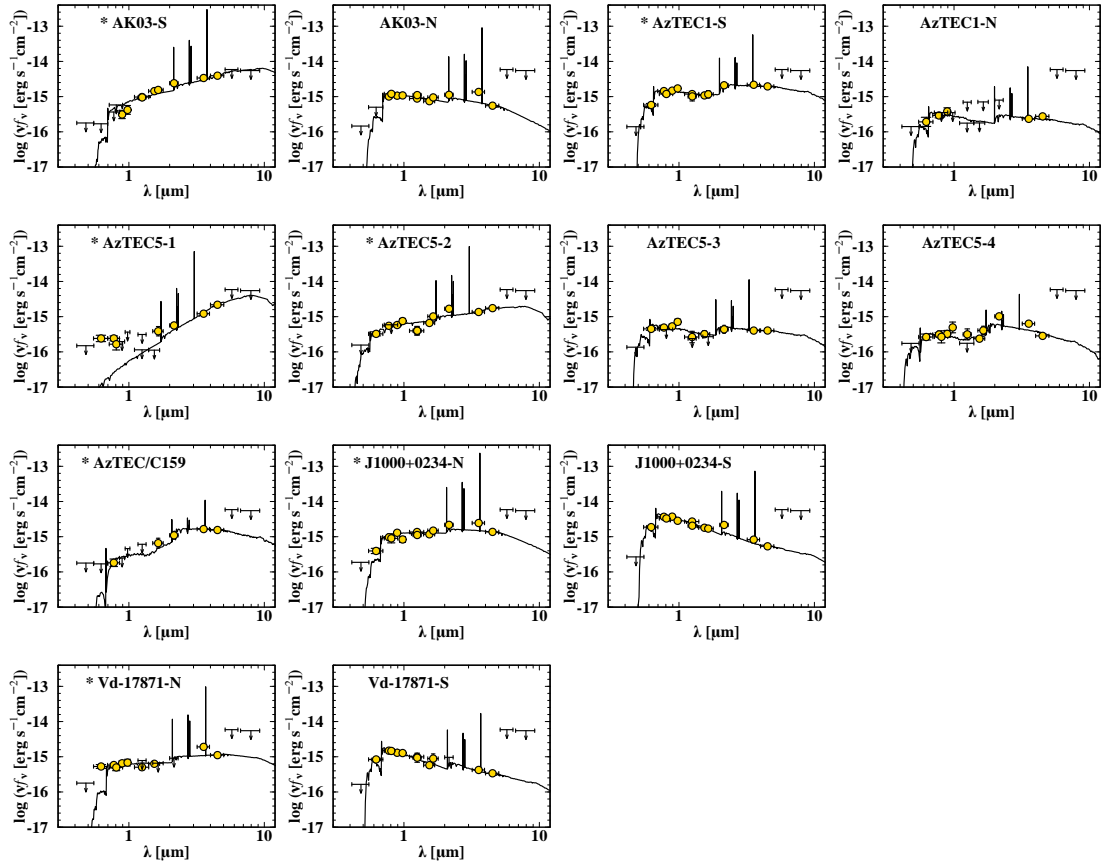


Figure 2.2: SED and best fit for the different stellar components of each object in the sample. Wavelengths are in the observer-frame. Arrows indicate 3σ upper limits (5σ for the *Spitzer* bands). Component names preceded by a star refer to those with ALMA counterpart.

Table 2.3: Properties of the Stellar Components.

Source Name	z_{spec}^a	z_{phot}^b	β	$SFR_{\text{UV}} (M_{\odot} \text{ yr}^{-1})$	$L_{\text{IR}}^c (10^{12} L_{\odot})$	$SFR_{\text{IR}}^c (M_{\odot} \text{ yr}^{-1})$	$M_{\text{dust}}^c (10^8 M_{\odot})$	$\log(M_{*}/M_{\odot})^d$	$M_{*}/M_{*,\text{prim}}^e$
* AK03-S	...	4.40 ± 0.10	$0.98^{+0.49}_{-0.39}$	25.5 ± 6.5	$1.2^{+8.1}_{-0.6}$	120^{+810}_{-60}	50^{+29}_{-35}	$10.76^{+0.08}_{-0.08}$...
AK03-N	4.747	$4.75^{+0.08}_{-0.07}$	$-1.73^{+0.16}_{-0.16}$	53.4 ± 4.1	$9.55^{+0.06}_{-0.06}$	1:16.2
* AzTEC1-S	4.3415	...	$-1.16^{+0.18}_{-0.17}$	45.0 ± 4.0	$24.0^{+8.3}_{-6.2}$	2400^{+830}_{-620}	50^{+13}_{-10}	$10.58^{+0.10}_{-0.10}$...
AzTEC1-N	...	$3.77^{+0.32}_{-0.22}$	$-2.6^{+1.0}_{-1.1}$	8.5 ± 3.3	$9.56^{+0.16}_{-0.20}$	1:10.5
* AzTEC5-1	< -3.2	> 4.2	$7.9^{+1.6}_{-2.0} h$	$790^{+160}_{-200} h$	$9.5^{+2.0}_{-2.5} h$	$10.40^{+0.16}_{-0.12}$...
* AzTEC5-2	...	$3.63^{+0.14}_{-0.15}$	$1.6^{+1.3}_{-1.2}$	2.1 ± 3.7	$13.2^{+2.7}_{-3.4} h$	$1320^{+270}_{-340} h$	$15.8^{+3.3}_{-4.1} h$	$9.92^{+0.10}_{-0.10}$	1:3.0
AzTEC5-3	...	$4.02^{+0.08}_{-0.08}$	$-0.25^{+1.1}_{-0.78}$	3.8 ± 2.6	$9.78^{+0.08}_{-0.10}$	1:4.2
AzTEC5-4	...	$3.66^{+0.40}_{-0.43}$	$-1.12^{+0.66}_{-0.52}$	5.2 ± 2.1	$9.59^{+0.08}_{-0.06}$	1:6.5
* AzTEC/C159	4.567	...	> -1.2	< 33	$7.4^{+2.1}_{-1.7} g$	740^{+210}_{-170}	$25.0^{+6.0}_{-5.0}$	$10.65^{+0.08}_{-0.08}$...
* J1000+0234-N	4.539	...	$-1.01^{+0.39}_{-0.32}$	52.6 ± 8.5	$4.4^{+1.7}_{-3.2}$	440^{+1200}_{-320}	50^{+110}_{-34}	$10.14^{+0.08}_{-0.08}$...
J1000+0234-S	4.547	$4.48^{+0.03}_{-0.03}$	$-2.04^{+0.12}_{-0.11}$	147.6 ± 7.4	$9.16^{+0.06}_{-0.08}$	1:9.5
* Vd-17871-N	4.621	$4.49^{+0.04}_{-0.31}$	$-0.59^{+0.35}_{-0.31}$	22.1 ± 4.0	$11.2^{+2.9}_{-2.3}$	1120^{+290}_{-230}	$12.6^{+3.2}_{-2.6}$	$10.04^{+0.10}_{-0.10}$...
Vd-17871-S	4.631	$4.41^{+0.08}_{-0.09}$	$-2.27^{+0.22}_{-0.23}$	59.3 ± 5.5	$9.49^{+0.18}_{-0.30}$	1:3.5

Component names preceded by * refer to those with ALMA counterpart. ^a Spectroscopic redshift references: AK03-N from Ly α by Smolčić et al. (2015); AzTEC1-S from [C II], also ¹²CO(4-3) and ¹²CO(5-4), by Yun et al. (2015); AzTEC/C159 from [C II] by Karim et al. (in prep), see also ¹²CO(2-1) and ¹²CO(5-4) by Jiménez-Andrade et al. (2018), and Ly α by Smolčić et al. (2015); J1000+0234-N from [C II] by Karim et al. (in prep), see also ¹²CO(4-3) by Schimmerer et al. (2008), and Ly α by Capak et al. (2008); J1000+0234-S from Ly α by Capak et al. (2008); Vd-17871-N from [C II] by Karim et al. (in prep), see also Smolčić et al. (2015); Vd-17871-S from Ly α by Karim et al. (in prep), see also Smolčić et al. (2015). ^b Photometric redshift references: AK03-S from Smolčić et al. (2015) who found a $z_{\text{phot}} = 4.40 \pm 0.10$ or $z_{\text{phot}} = 4.65 \pm 0.10$, depending on the template used; AzTEC1-N calculated in this work, where the uncertainties correspond to the 1σ percentiles of the maximum likelihood distribution and the redshift distribution spans over the range $3.2 < z < 4.7$; AK03-N, AzTEC5-2, AzTEC5-3 and AzTEC5-4 from the 3D-HST survey catalog (Momcheva et al. 2016; Brammer et al. 2012; Skelton et al. 2014); J1000+0234-S, Vd-17871-N and Vd-17871-S from the COSMOS2015 catalog (Laigle et al. 2016); AzTEC/C159, J1000+0234-N and AzTEC5-1 have no counterpart in the COSMOS2015 catalog. For both 3D-HST and COSMOS2015 estimates the listed uncertainties correspond to the 1σ percentiles. ^c From Smolčić et al. (2015) (Toft et al. (2014) for AzTEC5) FIR SEDs covering $100 \mu\text{m}-1.1 \text{mm}$ updated with new $850 \mu\text{m}$ fluxes from the S2COSMOS/SCUBA2 survey (Simpson et al., in prep). L_{IR} (integrated from rest-frame $8-1000 \mu\text{m}$) and M_{dust} are inferred using the Draine & Li (2007) dust model, then SFR_{IR} is calculated using the L_{IR} to SFR_{IR} conversion from Kennicutt (1998) for a Chabrier IMF. ^d Stellar mass uncertainties do not reflect systematics due to the SED fitting assumptions (i.e., stellar population synthesis models, IMF or SFH). ^e Stellar mass ratio between the quoted and the most massive components ($M_{*,\text{prim}}$). ^f Limits from detection in F814W and upper limits in F125W and F160W. ^g Limits from UltraVISTA DR3 photometry. ^h AzTEC5-1 accounts for 30% and AzTEC5-2 for 50% of the total values for this source following our GALFIT ALMA continuum images modeling (see Section 2.4.2).

2. CONNECTING SUBMILLIMETER AND QUIESCENT GALAXIES

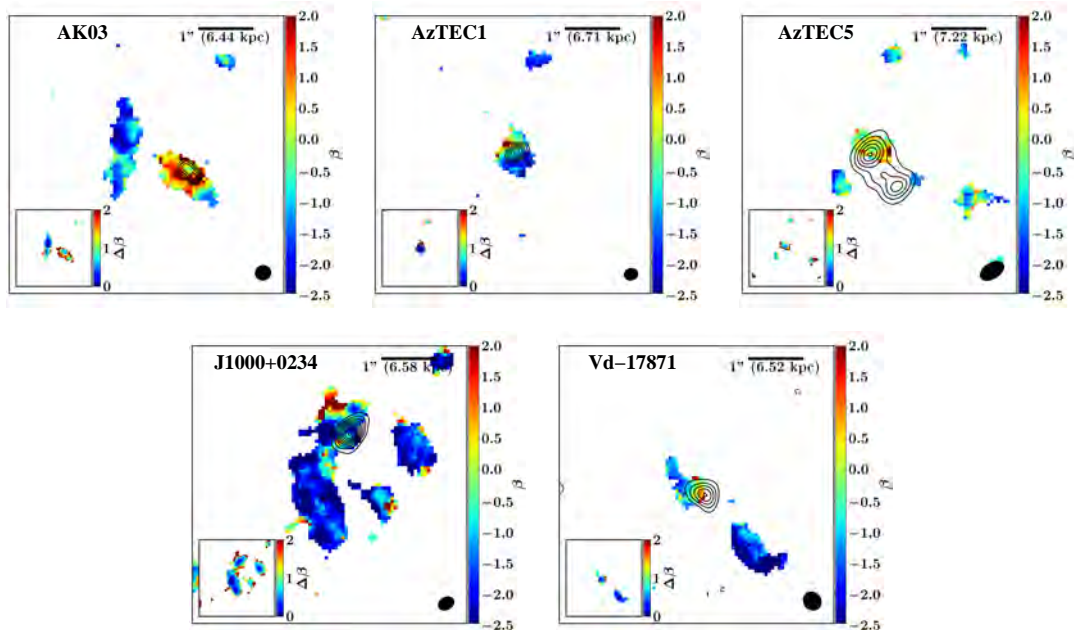


Figure 2.3: UV continuum slope maps of the five sources observed with *HST*. ALMA band 7 ($\sim 870 \mu\text{m}$) contours are overlaid starting at $\pm 3\sigma$ in steps of 1σ (AK03 and AzTEC1) or 3σ (AzTEC5, J1000+0234 and Vd-17871). The error map is shown in the bottom left corner and the ALMA beam size at the bottom right corner of each panel. North is up, East is to the left, and the images have a size of $5'' \times 5''$.

2.4 Dust Absorption and Emission

2.4.1 Spatially Resolved UV Slopes

At the redshift of the galaxies, the three *HST* bands trace the rest-frame UV continuum. This makes it possible to directly determine their spatially resolved UV slopes (β).

In Figure 2.3 we present β maps, constructed by fitting a linear slope to pixels which have $S/N > 2$ detections in at least two smoothed images (see Section 2.2.5). The 1σ uncertainty maps (inserts) were constructed by computing β -values in ~ 10000 realizations of the data, varying in each realization the measured pixel flux values within their uncertainties. Note that the pixel size is $0''.06$, but the PSF FWHM is $0''.18$. Consequently, spatially independent regions are those separated by at least 3 pixels. Since the UV slope maps were obtained using at least two detections in the *HST* bands, we see more clearly the presence of faint companions towards the North in AK03, AzTEC1, AzTEC5 and J1000+0234, as mentioned in Section 2.3.

In general, the objects present blue UV slopes, but the values are not homogeneous over the extent of the galaxies. The color gradients could be caused by structure in the distribution of dust, stellar age or metallicity. The relative importance of these cannot be disentangle with the available data but we expect a patchy dust distribution to be the dominant cause. However,

as most of the extent of the rest-frame UV emission is not detected in our ALMA observations, revealing the underlying dust structure in emission would require deeper observations.

The rest-frame FIR dust emission is in all cases associated with the reddest components. These components show evidence of gradients in their UV slopes. AK03-S is redder towards the North-East and bluer at the South-West. J1000+0234-N has an extended redder feature at the North-East. Vd-17871-N is slightly redder towards the South-West direction and bluer towards the North-East. In AzTEC1-N the red-to-blue gradient goes along the North-South axis. These color gradients may be due to a star formation gradient with higher dust content towards the redder areas. Another possibility could be close mergers between red and blue galaxies.

In AK03-S, two close FIR peaks are detected. At the current resolution and sensitivity and without dynamical information, we cannot determine whether these are part of a larger dynamical structure like a clumpy disk or remnants of a past interaction/merger. Note that in AzTEC5 we were unable to constrain the resolved UV slope of AzTEC5-1 since it is only detected in *F814W*, suggesting a extremely high extinction with strong rest-frame FIR emission, but also a very blue rest-frame UV component.

The bluer components in all five systems remain undetected in the ALMA continuum. This indicates less dusty star formation.

Spatially integrated values for the UV slopes (see Table 2.3) show a median and median absolute deviation of $\beta = -0.59 \pm 0.57$ for the components associated with the ALMA continuum emission (namely AK03-S, AzTEC1-S, AzTEC5-2, J1000+0234-N, Vd-17871-N and excluding the AzTEC5-1 and AzTEC/C159 upper limits). The rest of the components are bluer, with $\beta = -1.73 \pm 0.54$ consistent with estimates of Lyman break galaxies (LBGs) at similar redshift (e.g., Bouwens et al. 2009; Castellano et al. 2012; Finkelstein et al. 2012). By performing the photometry over larger apertures, enclosing all the components per source, we derive $\beta = -0.91 \pm 0.85$, which is in between the derived values for the red and blue components.

Having identified which UV components are associated with the dust continuum emission, we can relate the star formation rate (SFR) in the infrared (SFR_{IR}), tracing the obscured star formation, with that in the ultraviolet (SFR_{UV}), probing the unobscured star formation. The former was obtained from the FIR SEDs presented in Smolčić et al. (2015) (Toft et al. (2014) for AzTEC5) covering $100 \mu\text{m}$ – 1.1 mm updated with new $850 \mu\text{m}$ fluxes from the S2COSMOS/SCUBA2 survey (Simpson et al., in prep). The procedure is the following: The FIR SED is modeled using the Draine & Li (2007) dust model (DL07) (e.g., Magdis et al. 2012, 2017; Berta et al. 2016); L_{IR} is calculated by integrating the best fit to the SED in the range 8 – $1000 \mu\text{m}$; and then SFR_{IR} is obtained using the L_{IR} to SFR_{IR} conversion from Kennicutt (1998) for a Chabrier IMF. SFR_{UV} was calculated employing Salim et al. (2007) prescription, that relates L_{UV} to SFR_{UV} , for a Chabrier IMF. Note that SFR_{UV} derived this way corresponds to the observed value, i.e., not

2. CONNECTING SUBMILLIMETER AND QUIESCENT GALAXIES

corrected from extinction. The total SFR can be accounted by adding both infrared and ultraviolet estimates ($SFR_{\text{IR+UV}}$). Not surprisingly the star formation is dominated by SFR_{IR} , with SFR_{UV} only contributing at the level of 2–20% to the total SFR ($SFR_{\text{IR+UV}}$), in agreement with other previous works comparing obscured and unobscured star formation in starburst galaxies (e.g., [Puglisi et al. 2017](#)) and galaxies with similar stellar mass (e.g., [Whitaker et al. 2017a](#)).

In relation with the L_{IR} and SFR_{IR} estimates it is important to consider whether an important fraction of the infrared emission could be related with active galactic nuclei (AGN) activity. As reported in [Smolčić et al. \(2015\)](#), none of the sources is detected in the X-ray catalog in the COSMOS field (*Chandra* COSMOS Legacy Survey; [Civano et al. 2016](#); [Marchesi et al. 2016](#)). In terms of the radio emission [Smolčić et al. \(2015\)](#) studied the infrared-radio correlation of the sample, which show a discrepancy when compared with low-redshift star-forming galaxies due to a mild radio excess. This excess would be in line with studies showing an evolving infrared-radio ratio depending on the age on the starburst. In any case, while many SMGs host AGN, their L_{IR} is dominated by the star formation with the AGN contribution being $< 33\%$ (e.g., [Pope et al. 2008](#); [Riechers et al. 2014b](#)). This translates into a maximum overestimation in the SFR_{IR} of 33%, below the $SFR_{\text{IR+UV}}$ sample scatter.

2.4.2 FIR Sizes

We measured the sizes of the rest-frame FIR dust continuum emission by modeling the ALMA continuum images using GALFIT. Sérsic and PSF profiles were fitted to compare both resolved and unresolved modeling of the objects. The only object that was better fitted by a point source than a Sérsic model (and thus unresolved) is AK03. For this galaxy we derived an upper limit on the size from the PSF.

For the rest of the galaxies we fitted models with the Sérsic index fixed to $n = 0.5, 1$ and 4 , corresponding to a gaussian, exponential disk and de Vaucouleurs profiles, respectively, and also leaving the index free. The size of the emitting regions was obtained through the effective radius of the models (r_e). We cannot constrain which Sérsic index better explains the data at the current resolution and S/N. From higher resolution observations [Hodge et al. \(2016\)](#) found a median Sérsic index of $n = 0.9 \pm 0.2$ for a sample of 15 SMGs and concluded that the dust emission follows an exponential disk profile. Motivated by this, we fixed $n = 1$ to report the rest-frame FIR sizes for our sample in [Table 2.4](#). We also performed fits varying the axis ratio (b/a) and found that no particular value with $b/a \geq 0.3$ fitted the data better than others, so we fixed it to the circular value $b/a = 1$. We take into account the possible systematic errors associated with the assumed Sérsic index and axis ratio in the listed effective radii errors. These were computed by adding in quadrature the statistical uncertainty from GALFIT for the circular disk model and the difference between this model and the full range of models with varying n and b/a . Therefore,

Table 2.4: Rest-frame FIR Sizes.

Source Name ^a	r_e^{GALFIT}	r_e^{GALFIT}	$r_e^{\text{UVMULTIFIT}}$	$r_e^{\text{UVMULTIFIT}}$	Σ_{SFR}^b	Σ_{dust}^b
	(pc)	($''$)	(pc)	($''$)	($M_{\odot} \text{ yr}^{-1} \text{ kpc}^{-2}$)	($10^9 M_{\odot} \text{ kpc}^{-2}$)
AK03-S ^c	< 520	< 0.08	> 3.4	> 1.4
...	< 520	< 0.08	> 3.8	> 1.6
AzTEC1-S	900^{+480}_{-290}	$0.13^{+0.07}_{-0.04}$	940 ± 70	0.14 ± 0.01	480^{+540}_{-340}	$1.0^{+1.1}_{-0.7}$
AzTEC5-1 ^d	300^{+90}_{-130}	$0.04^{+0.01}_{-0.02}$	1260^{+870}_{-1200}	$1.7^{+1.1}_{-1.5}$
...	560^{+120}_{-360}	$0.08^{+0.02}_{-0.05}$	250^{+330}_{-140}	$0.33^{+0.16}_{-0.43}$
AzTEC5-2	700^{+180}_{-390}	$0.10^{+0.03}_{-0.05}$	390^{+240}_{-440}	$0.51^{+0.30}_{-0.58}$
AzTEC/C159	460^{+60}_{-240}	$0.07^{+0.01}_{-0.04}$	590 ± 70	0.09 ± 0.01	570^{+220}_{-610}	$1.9^{+2.0}_{-0.7}$
J1000+0234-N	700^{+120}_{-100}	$0.11^{+0.02}_{-0.02}$	660 ± 70	0.10 ± 0.01	150^{+380}_{-110}	$1.6^{+3.5}_{-1.2}$
Vd-17871-N	370^{+80}_{-210}	$0.06^{+0.01}_{-0.03}$	650 ± 70	0.10 ± 0.01	1300^{+670}_{-1500}	$5.8^{+4.2}_{-7.7}$

Component names preceded by * refer to those with ALMA counterpart. ^a Names refer to the stellar component associated with the FIR emission. ^b Defined as $\Sigma_{\text{SFR}} = 0.5SFR/\pi(r_{e,\text{circ}}^{\text{GALFIT}})^2$ and $\Sigma_{\text{dust}} = 0.5M_{\text{dust}}/\pi(r_{e,\text{circ}}^{\text{GALFIT}})^2$. ^c Limits from the PSF referring to each one of the two emitting regions. ^d The three values of AzTEC5 allude to the three resolved emitting regions from West to East.

the uncertainties conservatively account for the inability of the data to robustly constrain the detailed shape of the surface brightness profiles. We note that the ALMA continuum fluxes are consistent with the $850 \mu\text{m}$ fluxes from the S2COSMOS/SCUBA2 survey (Simpson et al., in prep), thus there is no evidence for resolved-out or missing flux that could affect the size estimates.

Finally, we cross-checked the results analyzing the data directly in the (u, v) plane employing UVMULTIFIT (Martí-Vidal et al. 2014) following the procedure described in Fujimoto et al. (2017). In this case for a direct comparison with the GALFIT image plane fits we also assumed a circular disk model (to obtain secure results, we omit AK03 and AzTEC5 for this comparison as they show two and three components respectively in our ALMA continuum images). We find that these estimates are in agreement with the results derived in the reconstructed images using GALFIT (see Table 2.4). In the following we use the estimates derived from GALFIT for further calculations.

The median and median absolute deviation of the size estimate for our sample are then $r_e = 0.70 \pm 0.29 \text{ kpc}$ at $\sim 870 \mu\text{m}$, which corresponds $\sim 160 \mu\text{m}$ rest-frame at $z = 4.5$ (excluding AK03 upper limits and only considering the brightest peak in AzTEC5, associated with AzTEC5-2). This result is in good agreement with Ikarashi et al. (2015), who found similar compact sizes of $r_e = 0.67^{+0.13}_{-0.14} \text{ kpc}$ for a sample of 13 1.1 mm-selected SMGs at a comparable redshift $3 < z < 6$. Oteo et al. (2017) presented an average value of $r_e = 0.91 \pm 0.26 \text{ kpc}$ (converting the reported FWHM into a circularized effective radius) in a sample of 44 DSFGs at $z \sim 4-6$ observed at $\sim 870 \mu\text{m}$ and selected as *Herschel* 500 μm risers (SED rise from 250 μm to 500 μm). On the other hand, the typical sizes derived for SMGs at a median redshift of $z \sim 2.5$ were reported to be $r_e = 1.8 \pm 0.2 \text{ kpc}$ from Hodge et al. (2016) and also $r_e = 1.2 \pm 0.1 \text{ kpc}$ from Simpson et al. (2015), both targeting $\sim 870 \mu\text{m}$. This suggest that SMGs may be more compact at $z > 3$ than at $z < 3$ (e.g., Fujimoto et al. 2017; Oteo et al. 2017). Other individual sources at $z > 4$ also point

2. CONNECTING SUBMILLIMETER AND QUIESCENT GALAXIES

towards very compact dust continuum emission (e.g., [Riechers et al. 2013, 2014a](#); [Díaz-Santos et al. 2016](#)) and also pairs of compact interacting starburst galaxies detected in gas and dust continuum which suggests a gas-rich major merger (e.g., [Oteo et al. 2016](#); [Riechers et al. 2017](#)). [Spilker et al. \(2016b\)](#) found no evidence for a difference in the size distribution of lensed DSFGs compared to unlensed samples from a sample of 47 DSFGs at $z = 1.9$ – 5.7 . Our results are also similar to the compact morphologies of local ULIRGs ($r_e = 0.5$ kpc, [Lutz et al. 2016](#)) at $70 \mu\text{m}$ rest-frame. We note that caution should be exercised when comparing samples tracing different rest-frame FIR wavelengths and based on different selection methods. Another caveat for a fair comparison is the stellar mass, since more massive galaxies are typically larger (e.g., [van der Wel et al. 2014](#)).

From the SFR_{IR} obtained for these sources (see [Table 2.3](#)) and their rest-frame FIR sizes, we calculated the SFR surface density ($\Sigma_{\text{SFR}} = 0.5 SFR / \pi r_{\text{e,circ}}^2$, see [Table 2.4](#)). Ranging from $\Sigma_{\text{SFR}} = 150$ – $1300 M_{\odot} \text{ yr}^{-1} \text{ kpc}^{-2}$ (excluding AK03 lower limits), the most extreme cases are AzTEC1, AzTEC5-1 and Vd-17871-N, but the last two are poorly constrained due to the large uncertainty on their sizes. At such extreme values, they are candidates for Eddington-limited starbursts ($\Sigma_{\text{SFR}} \sim 1000 M_{\odot} \text{ yr}^{-1} \text{ kpc}^{-2}$, [Andrews & Thompson 2011](#); [Simpson et al. 2015](#)).

2.4.3 UV/FIR Spatial Disconnection

The dust masses derived for this sample are very high at $\sim 10^9 M_{\odot}$ (see [Table 2.3](#)). Dust masses are a free parameter in the DL07 model employed, controlling the normalization of the SED. In terms of the dust opacity, DL07 assumes optically thin dust ($\tau \ll 1$) at all wavelengths (e.g., [Magdis et al. 2012, 2017](#); [Berta et al. 2016](#)). Very high dust masses combined with the small sizes derived for the dust emitting regions implies very high dust mass surface densities ($\Sigma_{\text{dust}} = 0.5 M_{\text{dust}} / \pi r_{\text{e,circ}}^2$), with values ranging $\Sigma_{\text{dust}} = 0.33$ – $5.8 \times 10^9 M_{\odot} \text{ kpc}^{-2}$ (see [Table 2.4](#)), and consequently, very high extinction.

We calculated the expected extinction assuming that the dust is distributed in a sheet with uniform density. We inferred the mean extinction from the dust mass surface density-to-extinction ratio (Σ_{dust}/A_V). To calculate Σ_{dust}/A_V we assumed a gas-to-dust mass ratio (GDR) appropriate for SMGs of $\text{GDR} = 90$ ([Swinbank et al. 2014](#)), and the gas surface number density-to-extinction ratio $N_{\text{H}}/A_V = 2.2 \times 10^{21} \text{ cm}^{-2} \text{ mag}^{-1}$ ([Watson 2011](#)). Therefore, $\Sigma_{\text{dust}}/A_V = (N_{\text{H}}/A_V) \cdot m_{\text{H}}/\text{GDR} = 2.44 M_{\odot} \text{ pc}^{-2} \text{ mag}^{-1}$. With this number the mean extinction is $\langle A_V \rangle = \Sigma_{\text{dust}}/2.44$. The values for our sample are extreme $\langle A_V \rangle = 130$ – 2400 mag , even when the numbers are halved to account for the dust behind the sources (see also [Simpson et al. 2017](#)).

Comparing [Figures 2.1 and 2.3](#) we see that while the dust emission is always associated with the reddest (likely most dust-extincted) component, in most cases it is not centered on the reddest part of that component (with the possible exception of Vd-17871). This suggests that the extinction seen in emission and absorption are disconnected, consistent with the expected extreme A_V

which implies that no emission can escape at any wavelength.

The fact that we do see blue UV emission at the peak of the dust emission suggests that a fraction of the light is able to escape due to a clumpy dust distribution and/or that the dust and stars are seen in different projections, e.g., the stars responsible for the UV emission could be in front of the dusty starbursts.

In any case it is clear that the rest-frame UV and FIR emissions are spatially disconnected and originate from a different physical region. This implies that the dust as seen in absorption from the UV slope inhomogeneities in Figure 2.3 is not tracing the dust seen in emission from the ALMA continuum.

2.4.4 IRX- β Plane

The infrared-to-ultraviolet luminosity ratio, commonly referred as infrared excess ($\text{IRX} = L_{\text{IR}}/L_{\text{UV}}$), is known to correlate with the UV continuum slope (β). This so-called Meurer relation (Meurer et al. 1999, M99 relation hereafter) is well established for normal star-forming galaxies (e.g., Overzier et al. 2011; Takeuchi et al. 2012; Casey et al. 2014b). Its origin is thought to be that galaxies get redder as the dust absorbs the rest-frame UV emission and re-radiates it at infrared wavelengths. For galaxies on the relation, the amount of dust absorption can thus be directly inferred from the UV slope. Therefore, in the absence of FIR data, the relation can be used to obtain total extinction-corrected SFR from UV data (e.g., Bouwens et al. 2009). Furthermore, this relation physically motivates energy balance codes which require that dust extinction inferred from rest-frame UV–optical SED fits must match the observed emission measured at infrared wavelengths (e.g., da Cunha et al. 2008).

Spatially unresolved observations have shown that DSFGs do not follow the M99 relation (e.g., Buat et al. 2005; Howell et al. 2010; Casey et al. 2014b). Excess of dust and UV/FIR decoupling have been suggested as a possible origin of the offsets by Howell et al. (2010) who showed that the deviation from the nominal M99 relation (ΔIRX) increases with L_{IR} , but does not correlate with L_{UV} . Following this argument the authors postulated that a concentration parameter might correlate with ΔIRX as an indicator of the decoupled UV/FIR. Casey et al. (2014b) reinforced these results showing also that the deviation from the M99 relation increases with L_{IR} above a threshold of $\log(L_{\text{IR}}/L_{\odot}) > 11.0$. Faisst et al. (2017b) proposed that the blue colors of sources with high IRX values could be due to holes in the dust cover, tidally stripped young stars or faint blue satellite galaxies. In addition, simulations propose recent star formation in the outskirts and low optical depths in UV-bright regions as plausible explanations of the offset (Safarzadeh et al. 2017; Narayanan et al. 2018). Simple models placing a dust screen in front of a starburst have been studied to provide a detailed explanation of all the possible effects that might lead to a deviation in the IRX- β plane (Popping et al. 2017a).

2. CONNECTING SUBMILLIMETER AND QUIESCENT GALAXIES

The sample studied here have infrared luminosities ranging $\log(L_{\text{IR}}/L_{\odot}) = 12.1\text{--}13.4$, above the mentioned threshold $\log(L_{\text{IR}}/L_{\odot}) > 11.0$, and the spatially resolved rest-frame UV/FIR data make it possible to study the origin of the DSFGs offsets in the IRX- β plane (see Figure 2.4).

To confirm that the galaxies in this sample are representative of previous DSFGs studies in spatially unresolved data, we first derived ultraviolet and infrared luminosities in large apertures enclosing all the components of each source. In Figure 2.4 these measurements are plotted as large open symbols, confirming that the sample does not follow the M99 relation and it is located in the same region as previous spatially unresolved measurements for DSFGs (e.g., Casey et al. 2014a, at $z > 2$). Second, we take advantage of the spatial resolution to pinpoint the origin of the FIR emission and recalculate the UV luminosity in smaller apertures defined by the 3σ contour in the ALMA images (ALMA apertures). In this case both *HST* and ALMA images were PSF-matched as described in Section 2.2.4.

In Figure 2.4 we plot the sample of DSFGs at $z > 2$ from Casey et al. (2014b) for comparison. Note that this study employed similar methods to obtain L_{IR} , L_{UV} and the UV slopes as we did: L_{IR} by integrating over the wavelength range 8–1000 μm and using a single temperature modified greybody plus mid-IR power law, which properly accounts for the warm dust contribution as the DL07 dust model; L_{UV} by interpolating the observed photometry to rest-frame 1600 \AA ; and the UV slopes by fitting a power law to the photometry, which is equivalent to our linear fit in magnitude space. Additionally, we include other IRX- β relations from the literature: the original M99 and follow-up corrections (e.g., Overzier et al. 2011; Takeuchi et al. 2012), although the methodology they followed to obtain the quantities shown in the IRX- β diagram slightly differ from Casey et al. (2014b) and ours.

All the galaxies have higher IRX in the ALMA aperture than in the large aperture. This is expected from their smaller extent in the rest-frame FIR compared to that in the rest-frame UV, which effectively lowers the L_{UV} contribution to the $L_{\text{IR}}/L_{\text{UV}}$ ratio. Furthermore, three of the galaxies have redder UV slopes and two have similar UV slopes in the ALMA apertures compared with the large apertures. Again this can be understood as a result of removing the contribution from the extended irregular UV features and companion satellite galaxies that appear bluer than the dust emitting region detected in ALMA. These results agree with the model proposed in Faisst et al. (2017b) to explain blue colors of DSFGs with high IRX.

On the other hand, even after accounting for the correction that implies going from the large to the ALMA aperture, our sample does not follow the M99 relation and lies 1.75 dex (median) above it. However, while the rest-frame FIR dust continuum emission is associated with the reddest component in the mergers, it is in general not centered on the reddest part of the component, and the component is too blue to be consistent with a physical connection between the dust seen in emission and absorption, suggesting that the UV and FIR emissions of DSFGs are spatially

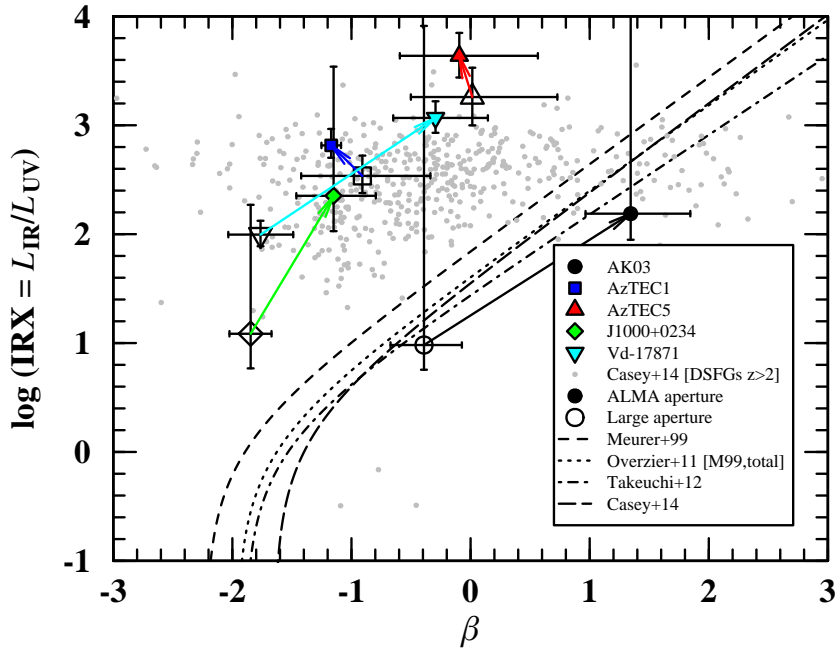


Figure 2.4: IRX- β plane. Small filled symbols indicate *HST* photometry performed over the region above the 3σ contour in the ALMA image. Large open symbols refer to *HST* photometry performed over a large aperture enclosing all the components of each source. Both small and large symbols are linked with an arrow of the color associated to each object. Small gray dots indicate the Casey et al. (2014b) sample of DSFGs at $z > 2$. IRX- β relations from the literature include: Meurer et al. (1999) (dashed line), corrected M99 relation referred as “M99, total” in Overzier et al. (2011) (dotted line), Takeuchi et al. (2012) (dashed-dotted line), Casey et al. (2014b) (long-dashed line). Our sample does not follow the M99 relation which, together with their rest-frame UV and FIR morphologies, suggests that the UV and FIR emissions of DSFGs are spatially disconnected.

disconnected.

This provides morphological and geometrical evidence for the origin of the DSFGs offsets from the M99 relation (see also Chen et al. 2017), being consistent with the extreme extinction expected from the compact and intense dust emission for this sample (see Section 2.4.3), implying that UV emission should be expected not to escape the starbursts.

A possible scenario for the origin of the UV and FIR emissions could be a patchy dust distribution causing some of the UV to be completely extinguished and some to leak relatively un-extinguished, in a similar way as proposed by the holes in the dust cover by Faisst et al. (2017b).

The UV/FIR lack of spatial coincidence has important implications for energy balance codes as noted by Hodge et al. (2016), where the detected stellar light will have no information about the obscured starburst (Simpson et al. 2015).

Therefore, the results here support that IRX and β are unrelated for such FIR-bright sources and that extinction correction prescriptions based on the nominal IRX- β relation are inappropriate for DSFGs.

In Section 2.4.1 we interpreted the UV slope differences over the source extent as variations in

2. CONNECTING SUBMILLIMETER AND QUIESCENT GALAXIES

the dust content not detected in emission in the ALMA observations. It is possible that this regime of star formation is compatible with the M99 relation. In order to check this, we calculated the expected L_{IR} below the 3σ dust continuum detection limit over the components detected in the rest-frame UV for each source, by rescaling their FIR SEDs (Smolčić et al. 2015; Toft et al. 2014). The resulting upper limits lie above the M99 relation for all cases, not being useful on putting constraints about whether these galaxies follow M99 or lie above or below it, a subject of main focus in current studies (e.g., Capak et al. 2015; Barisic et al. 2017; Faisst et al. 2017b; Fudamoto et al. 2017).

2.5 Stellar Masses and Merger Ratios

2.5.1 What Triggers $z > 4$ Starbursts?

Major mergers between gas-rich galaxies are often assumed to be the triggering mechanism for starburst galaxies, as local Universe infrared-luminous galaxies are exclusively associated with major mergers with $L_{\text{IR}} > 10^{11.5} L_{\odot}$ (e.g., Sanders & Mirabel 1996). The multiplicity of close, approximately equally-bright galaxies in the *HST* images studied here would naively support a similar triggering mechanism at $z > 4$. However, as the images trace the rest-frame UV, a stellar mass analysis of the individual merging components is needed to test this picture.

In Table 2.3 we list the stellar masses of the stellar components of each system derived from the SED fits described in Section 2.3.2. Also listed is the stellar mass ratio relative to the most massive component in the system ($M_{*,\text{prim}}$).

The median stellar mass of the most massive component is $\log(M_*/M_{\odot}) = 10.49 \pm 0.32$ (where the uncertainty is the median absolute deviation). For the remaining less massive components the median is $\log(M_*/M_{\odot}) = 9.56 \pm 0.10$. A stellar mass ratio of 1:3–4 is often adopted to distinguish between major and minor mergers (e.g., Conselice et al. 2003; Tacconi et al. 2008; Kaviraj et al. 2009; Lotz et al. 2011; Man et al. 2016). Adopting this definition, AzTEC5 is formally classified as major merger, with a stellar mass ratio for the two most massive components (AzTEC5-1 and AzTEC5-2) of $M_*/M_{*,\text{prim}} = 3.0$. Vd-17871 could be classified as a major or minor merger depending on the exact distinction ratio ($M_*/M_{*,\text{prim}} = 3.5$). The rest of the systems are consistent with undergoing at least one minor merger (also including AzTEC5 which might undergo minor merging with AzTEC5-3 and AzTEC5-4). Furthermore, it is important to note that regardless of the precise distinction between major and minor mergers, the components detected in dust continuum with ALMA are undergoing starbursts with SFRs that overwhelm those of the companions, and therefore, the stellar mass ratios are expected to decrease. Taking this into account all systems could be classified as minor mergers (except AzTEC5-1 and AzTEC5-2, both starbursting systems).

In addition to the components which were bright enough to estimate stellar masses, AK03, AzTEC5 and J1000+0234 present additional low S/N companions detected in one or more of the *HST* images (marked with arrows in Figure 2.1), which may be additional minor merger components if they are at the same redshift. The residuals in the modeling of the *Spitzer*/IRAC images do not show significant detections at their positions, and thus, they must be less massive than the detected companions. In fact, the *HST* images display $2 < S/N < 3$ potential additional low-mass components in the case of *F814W* particularly, as expected if they are small, blue star-forming galaxies. If their redshifts are confirmed, it would be further evidence for the starbursts in $z \sim 4.5$ SMGs being triggered by multiple minor mergers. A picture consistent with living in overdense environments (e.g., Blain et al. 2004; Smolčić et al. 2017). Indeed Smolčić et al. (2017) showed evidence that AzTEC1, AzTEC5, J1000+0234 and Vd-17871 have statistically significant small-scale overdensities.

Note, however, that these results do not rule out that major mergers played a role in triggering these starbursts, if they have already coalesced, or if they are so close that they are not resolved in the *HST* and ALMA data. Indeed the multiple FIR peaks in AK03 and AzTEC5, and the color gradients observed in the most massive components of the systems (most prominently in AzTEC1, J1000+0234 and Vd-17871), are consistent with such a picture.

2.5.2 Comparison to Previous Stellar Mass Estimates

Previous estimates of the stellar mass of the galaxies in this sample, derived using MAGPHYS (da Cunha et al. 2008), led to a median value of $\log(M_*/M_\odot) = 10.92 \pm 0.13$ (Smolčić et al. 2015; Toft et al. 2014). This is ~ 0.4 dex higher than our derived median value for the most massive component. Adding up all the components per source the median total stellar mass would be slightly higher $\log(M_*/M_\odot) = 10.63 \pm 0.11$, but still ~ 0.3 dex lower than the previous estimates for this sample. Recent results from Miettinen et al. (2017), also employing MAGPHYS, are also systematically higher by at least 0.3 dex for the sources in common with our sample (AzTEC1, AzTEC5 and J1000+0234). Such systematic discrepancies are consistent with the expected overestimation of MAGPHYS-derived stellar masses and slight underestimate of exponentially declining models employed here, according to Michałowski et al. (2014) SMGs stellar masses studies from simulated datasets.

We also compared our stellar mass estimates with those listed in the 3D-*HST* survey catalog (Momcheva et al. 2016; Brammer et al. 2012; Skelton et al. 2014) for the sources covered in the CANDELS fields (e.g., AK03 and AzTEC5) and the COSMOS2015 catalog (Laigle et al. 2016). In general the catalogs successfully extract the majority of the components for these complex objects and lists photometric redshifts consistent with the available spectroscopic redshifts (see Table 2.3). However, for a subset we found significant discrepancies in the derived stellar masses.

2. CONNECTING SUBMILLIMETER AND QUIESCENT GALAXIES

The discrepancy might be due to the different approach in the photometry measurements. While we measured fluxes in apertures carefully chosen to minimize the effect of blending and applied aperture corrections, COSMOS2015 employs automated PSF-matched photometry, which can be more contaminated by blending of close objects.

Furthermore, J1000+0234-N is not in the COSMOS2015 catalog, and the bulk of its stellar mass is associated to J1000+0234-S (likely due to a mismatch between the *Spitzer*/IRAC and optical/near-IR data). AzTEC/C159 is also missing from the catalog, due to its extreme faintness in the optical/near-IR. Similarly, there is no entry corresponding to the location of AzTEC5-1 in either 3D-*HST* or COSMOS2015. The absence and mis-identifications of massive and optically faint sources could affect the photometry, and thus, the stellar mass estimates. It could also affect the stellar mass functions at high redshifts (e.g., [Davidzon et al. 2017](#)).

J1000+0234 is also present in the recent work by [Brisbin et al. \(2017\)](#) and the assigned shorter wavelength counterpart to the ALMA detection is also J1000+0234-S, since J1000+0234-N remains undetected. This indicates that significant offsets between sub-mm/radio sources and UV/optical/near-IR counterparts could be indeed due to the presence of multiple blended, and perhaps merging, components if the depth and resolution of the data are not enough to detect all those components (provided a good relative astrometry between the different instruments).

Compared with previous estimates of the average stellar masses of SMGs, our results are in line with studies indicating that most SMGs have $M_* < 10^{11} M_\odot$ (e.g., [Wardlow et al. 2011](#); [Hainline et al. 2011](#); [Casey et al. 2013](#); [Simpson et al. 2014](#)). Other studies report higher values $M_* > 10^{11} M_\odot$ also for $z \sim 4.5$ sources ([Michałowski et al. 2010, 2012, 2017](#)). The median stellar mass of the satellite galaxies is consistent with estimates for faint LBGs at similar redshifts ([Magdis et al. 2010](#)).

2.5.3 Stellar Mass Uncertainties and Caveats

Stellar masses of highly obscured starburst galaxies are notoriously difficult to estimate. In this work we took advantage of high resolution *HST* imaging to identify the positions of multiple stellar components in the systems, which in turn was used to deblend the rest-frame optical *Spitzer*/IRAC fluxes that are tracing the stellar mass available for these high-redshift systems. However, our stellar mass estimates are potentially subject to a number of additional systematic uncertainties.

One caveat is that some of the components lack spectroscopic confirmation. That is the case of AK03-S, AzTEC1-N and all components of AzTEC5. When possible we assumed that these components were at the same redshift as their spectroscopically confirmed companions. For AK03-S [Smolčić et al. \(2015\)](#) found a $z_{\text{phot}} = 4.40 \pm 0.10$ or $z_{\text{phot}} = 4.65 \pm 0.10$, depending on the template used. Therefore, the two components are likely at the same redshift. AzTEC1-N is a

very faint component with $S/N < 3$ in all the *HST* bands, but it is detected above this threshold in HSC r , i and z bands, and in the IRAC bands, where the residuals from AzTEC1-S fitting showed that there is indeed a secondary component towards the North. We derived a photometric redshift consistent with being at the same redshift than AzTEC1-S within the uncertainties. Its probability distribution peaks at $3.77^{+0.32}_{-0.22}$ (where the uncertainties are the 1σ percentiles of the maximum likelihood distribution), being not null in the redshift range $3.2 < z < 4.7$). In the case of AzTEC5 none of the components have spectroscopic redshifts, but the 3D-*HST* survey catalog (Momcheva et al. 2016; Brammer et al. 2012; Skelton et al. 2014) lists $z_{\text{phot}} = 3.63^{+0.14}_{-0.15}$ for AzTEC5-2, $z_{\text{phot}} = 4.02^{+0.08}_{-0.08}$ for AzTEC5-3 and $z_{\text{phot}} = 3.66^{+0.40}_{-0.43}$ for AzTEC5-4. Therefore, it seems plausible that all components in AzTEC5 lie at the same redshift within the uncertainties.

Another caveat in the stellar mass estimates come from the assumptions made in the SED fits. Michałowski et al. (2014) studied the importance of the assumed SFHs (see also Hainline et al. 2011) over several SED fitting codes, concluding that the exponentially declining SFHs used here are able to recover the stellar masses of their simulated SMGs, with slight underestimation and significant scatter. Regardless of the model employed, the derived photometry and the color of the sources already indicates that there is a component more massive than the other. The most massive components have higher IRAC fluxes and they are also redder than their fainter IRAC companions.

Given the extreme dust mass surface densities derived for this sample (see Table 2.4), if the stars formed in-situ in the starburst that created the dust it is possible that some stellar mass is so obscured that it is not detectable even by IRAC, and thus, not accounted for in the SED fitting. Higher spatial resolution rest-frame FIR continuum observations would be needed to disentangle the underlying structure of the dust emitting region and measure its degree of homogeneity or clumpiness. This could reveal how much of the stellar light is completely obscured beneath the dust and the implied systematic error in the derived stellar masses. To estimate how big this effect could be, using the empirical dust-to-stellar-mass ratio (DTS) for local ULIRGs in Calura et al. (2017) $\log \text{DTS} = -2.83$, the median stellar mass of this sample would increase to $\log(M_*/M_\odot) \sim 11.6$. However, assuming the ratio from simulations in Popping et al. (2017b) $\log \text{DTS} \sim -1.8$ the effect would not be that significant, increasing to $\log(M_*/M_\odot) \sim 10.9$.

Over the last decade, several studies have uncovered a tight correlation between the SFR and the stellar mass of star-forming galaxies, the so-called main sequence (MS) of star formation (e.g., Noeske et al. 2007; Elbaz et al. 2007; Daddi et al. 2007). Strong outliers to the MS are present at all redshifts and this is often used as a formal definition of starburst galaxies. These systems exhibit elevated specific star formation rates ($sSFR$) compared with typical MS galaxies. For the components with ALMA detection, from the total $SFR_{\text{IR+UV}}$ and stellar masses, we obtain $sSFR = 2.5\text{--}100 \text{ Gyr}^{-1}$. Considering the MS as defined in Schreiber et al. (2015), the distance to

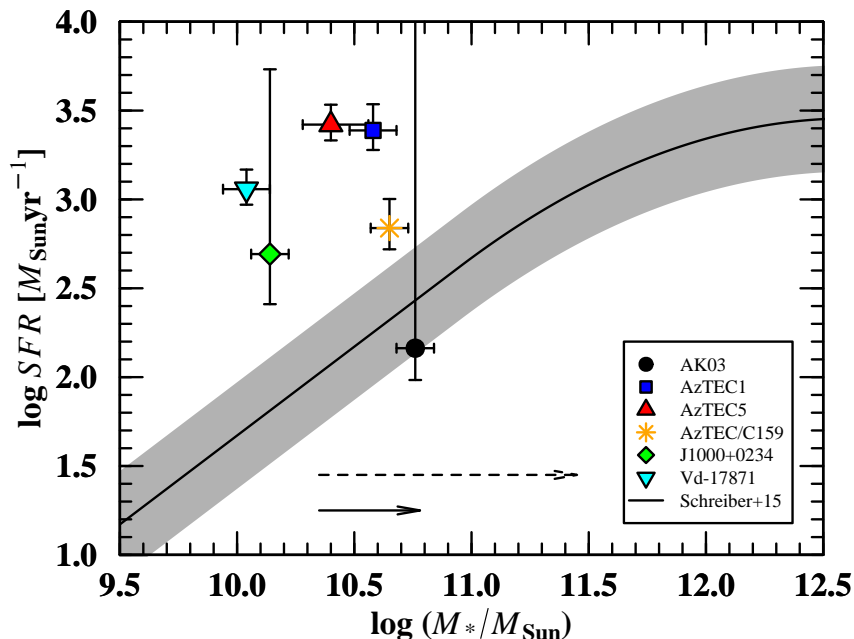


Figure 2.5: $SFR - M_*$ plane. Our sample (colored symbols) lies above the main sequence of star-forming galaxies as defined by Schreiber et al. (2015) (plotted at $z = 4.5$ for reference and converted from Salpeter to Chabrier IMF). A 0.3 dex (2 times) scatter around the MS is represented by a gray shadowed region. Bottom arrows indicate the estimated increase in the derived stellar masses if a fraction is obscured by the dust ($\log DTS \sim -1.8$ from Popping et al. (2017b), solid arrow, and $\log DTS = -2.83$ Calura et al. (2017), dashed arrow).

the MS ranges $sSFR/sSFR_{MS} = 0.5-22$, calculated at the redshift of each source. Consequently, all the sources studied here would formally fall into the starburst regime, with AK03 on the MS but also consistent with the starburst region given its large SFR uncertainty (see Figure 2.5). If an important fraction of the stellar mass is undetectable hidden beneath the dust, the objects would move towards smaller distances to the MS, as represented by the bottom arrows in Figure 2.5.

2.6 Stellar Mass-Size Plane: Evolution to Compact Quiescent Galaxies

The similar stellar mass and rest-frame optical/UV size distribution of $z > 3$ SMGs and cQGs at $z \sim 2$ has been used to argue for a direct evolutionary connection between the two populations (Toft et al. 2014). However, the stellar mass builds up in the nuclear starburst. At the derived SFR and stellar mass for our sample, approximately half of the descendant stellar mass would be formed during the starburst phase. The FIR size traces the region where the starburst is taking place, and thus, it is the relevant measurement to compare to the optical size in the descendant 1–2 Gyr later, as it is the best proxy for the location of the bulk of the stellar mass once the

2.6. STELLAR MASS-SIZE PLANE: EVOLUTION TO COMPACT QUIESCENT GALAXIES

starburst is finished.

In Figure 2.6 we compare the stellar masses and rest-frame FIR effective radii for our sample of SMGs to the stellar masses and rest-frame optical effective radii measured for spectroscopically confirmed cQGs at $1.8 < z < 2.5$ (samples from, [van de Sande et al. 2013](#); [Krogager et al. 2014](#); [Belli et al. 2017](#)). Note that the optical sizes in these cQGs comparison samples were also obtained by fitting the two-dimensional surface brightness distribution with GALFIT, as we did for the FIR sizes of our SMGs sample.

The SMGs appear offset to smaller stellar masses and sizes than cQGs, with approximately the same scatter. The median stellar mass of our SMGs is $\log(M_*/M_\odot) = 10.49 \pm 0.32$ compared to $\log(M_*/M_\odot) = 11.07 \pm 0.08$ for the cQGs. The median rest-frame FIR size for the SMGs is $r_e = 0.70 \pm 0.29$ kpc, compared to rest-frame optical sizes of $r_e = 1.61 \pm 0.68$ kpc for the cQGs. The SMGs would have to increase both in stellar mass and size to evolve into $z \sim 2$ cQGs.

In the following we discuss if such an evolution is plausible, given the observed properties of the SMG sample.

As the galaxies are undergoing starbursts, they will grow significantly in stellar mass before quenching. [Toft et al. \(2014\)](#) derived a depletion time-scale of $\tau_{\text{gas}} = 42^{+0.40}_{-0.29}$ Myr for the number density of $z \gtrsim 3$ SMGs and cQGs at $z \sim 2$ to match. Assuming this number, at their current median $SFR_{\text{IR+UV}} = 920 M_\odot \text{ yr}^{-1}$, the stellar mass is expected to increase by a factor of ~ 2.24 (~ 0.35 dex). Star formation is not expected to increase the sizes significantly. The sizes of the remnants are, however, foreseen to grow due to ongoing minor mergers.

The median stellar mass ratio of the ongoing minor mergers is 6.5 and the average number of them is 1.2. Taking into account these mergers, the expected increase in stellar mass is ~ 2.43 (~ 0.39 dex). Adopting the simple models of [Bezanson et al. \(2009\)](#) for size growth due to minor mergers, the remnants are expected to grow by a factor of ~ 1.39 (~ 0.14 dex).

Simulations suggest a typical minor merger time-scale of 0.49 ± 0.24 Gyr ([Lotz et al. 2010](#)). This provides sufficient time for the mergers to complete between $z \sim 4.5$ – 3.5 while not violating the stellar ages of 1–2 Gyr derived for $z \sim 2.5$ – 2.0 cQGs ([Toft et al. 2012](#)).

The combined average stellar mass and size growth anticipated from completion of the starburst and the minor mergers is shown as the bottom-right solid arrow in Figure 2.6. The SMGs would grow to a stellar mass of $\log(M_*/M_\odot) = 10.88 \pm 0.32$ and a size of $r_e = 0.98 \pm 0.29$ kpc, bringing the two populations into agreement within the uncertainties.

The scenario laid out here is in line with recent theoretical work by [Faisst et al. \(2017a\)](#), which suggests that models with starburst-induced compaction followed by minor merger growth better reproduces the sizes of the quenched remnants than models without structural changes.

In order to provide the stellar mass increase the SMGs need enough gas reservoir to fuel the star formation. The median gas mass for our sample calculated from M_{dust} using a GDR = 90

2. CONNECTING SUBMILLIMETER AND QUIESCENT GALAXIES

is $3.7 \times 10^{11} M_{\odot}$. The factor ~ 2.24 mentioned above means the creation of $3.8 \times 10^{10} M_{\odot}$, which would be achieved with a $\sim 10\%$ efficiency of converting gas into stars. The available molecular gas estimates derived from ^{12}CO measurements in the literature for our sample are: AzTEC1, $M_{\text{H}_2} = 1.4 \pm 0.2 \times 10^{11} M_{\odot}$, with $\tau_{\text{gas}} \sim 200$ Myr (Yun et al. 2015); AzTEC/C159, $M_{\text{H}_2} = 1.5 \pm 0.3 \times 10^{11} M_{\odot}$, with $\tau_{\text{gas}} = 200 \pm 100$ Myr (Jiménez-Andrade et al. 2018); and J1000+0234, $M_{\text{H}_2} = 2.6 \times 10^{10} M_{\odot}$, with $\tau_{\text{gas}} \sim 30$ Myr (Schinnerer et al. 2008). The amount of gas available to form stars seems enough to account for the expected increase in stellar mass and the short depletion time-scale match the short duration of the SMG phase of ~ 100 Myr (e.g., Tacconi et al. 2006, 2008).

In the propose scenario we assume that the rest-frame FIR dust continuum is a reasonable proxy for the effective star-forming region. [C II] size estimates for a subset of our sample (Karim et al. in prep) are typically two times larger, which is in agreement with other studies finding larger [C II] sizes compared with dust continuum sizes (e.g., Riechers et al. 2014a; Díaz-Santos et al. 2016; Oteo et al. 2016). Considering a scenario with $\tau_{\text{gas}} = 100$ Myr and [C II] sizes would mean a factor of ~ 3.96 (~ 0.60 dex) change in stellar mass and ~ 2.78 (~ 0.44 dex) in size, still suitable for the two populations to match, with the SMGs having a final stellar mass of $\log(M_*/M_{\odot}) = 11.09 \pm 0.32$ and size of $r_e = 1.95 \pm 0.29$ kpc.

2.7 Discussion

In this work we present detailed observations of a small sample of $z \sim 4.5$ – 3.5 SMGs and argue that their properties are consistent with being progenitors of ~ 2.5 – 2.0 cQGs.

We demonstrated that the distribution of the two populations in the stellar mass-size plane are consistent when accounting for stellar mass and size growth expected from the completion of the ongoing starbursts and subsequent merging with minor companions.

These conclusions are based on small samples for both the SMGs and cQGs, possibly subject to selection biases, and apply only in two broad redshift intervals. To further explore the evolutionary connection between the two populations, larger uniform samples, with a finer redshift sampling are needed. For example, cQGs are now being identified out to $z \sim 4$ (Straatman et al. 2015), although confirming quiescent galaxies at this high redshift can be challenging (Glazebrook et al. 2017; Simpson et al. 2017; Schreiber et al. 2018b). If the proposed connection holds at all redshifts, the properties of these should match those of SMGs at $z > 6$ (e.g., Riechers et al. 2013; Decarli et al. 2017; Strandet et al. 2017; Riechers et al. 2017). Similarly, the properties of $z \sim 2$ SMGs should match those of 1 Gyr old quiescent galaxies at $z \sim 1.5$.

A crucial measure placing starburst galaxies in a cosmic evolution context is their stellar mass. Unfortunately, it is a very difficult to derive due to large amounts of dust, that may prevent an unknown fraction of the stellar light to escape, even at rest-frame near-IR wavelengths. Perhaps

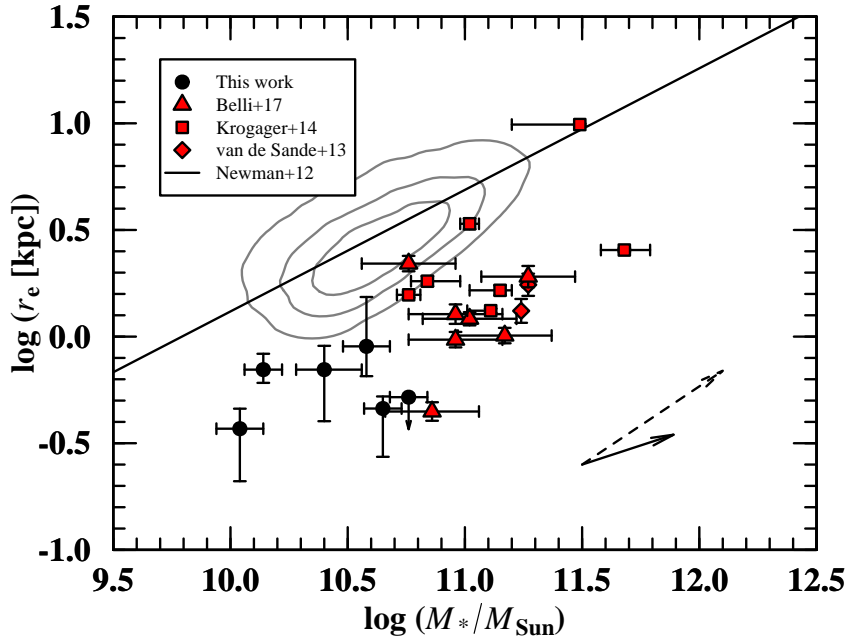


Figure 2.6: Stellar mass-size plane location of the SMG sample in this work (black filled circles), along with $z \sim 2$ CQGs (red filled symbols) from van de Sande et al. (2013) (diamonds), Krogager et al. (2014) (squares) and Belli et al. (2017) (triangles). The bottom-right black solid arrow indicates the expected evolution of the SMG sample, accounting for the stellar mass growth through the derived $SFR_{\text{IR+UV}}$ over a duty cycle of 42 Myr and minor merger contribution, and in size via minor mergers. Above a dashed arrow indicating the predicted evolution from a potential scenario with longer depletion time-scales of 100 Myr and larger sizes assuming a [C II] size proxy for the effective star-forming region. For comparison, the local mass-size relation from Newman et al. (2012) is shown as a solid line, along with SDSS local massive quiescent galaxies as gray contours (Shen et al. 2003). All plotted data were converted to a concordance cosmology $[\Omega_{\Lambda}, \Omega_M, h] = [0.7, 0.3, 0.7]$ and Chabrier initial mass function (IMF) when needed.

the best way forward is to measure it indirectly, as the difference between the total dynamical mass and the gas mass (and dark matter), both of which can be estimated from molecular line observations with ALMA (Karim et al., in prep).

What triggers high-redshift starbursts remains unclear. All of the galaxies studied here showed evidence of ongoing minor mergers and this could be the process responsible of igniting the starburst, while only one showed evidence of an ongoing major merger. Bustamante et al. (2018) have recently stated that while strong starbursts are likely to occur in a major merger, they can also originate from minor mergers if more than two galaxies interact. This suggests that the triggering processes at high redshift are different from low redshift, where the most luminous starburst galaxies are almost exclusively associated with major mergers, which would also be in agreement with recent theoretical work (Narayanan et al. 2015). Nevertheless, low-redshift lower luminosity LIRGs are also found to be associated with minor mergers. The difference could actually be due to the gas fraction of the most massive component in the interaction, which is higher at high redshift than at low redshift, and thus, it may allow for a relatively more intense

2. CONNECTING SUBMILLIMETER AND QUIESCENT GALAXIES

starburst to occur in the presence of a minor merger at high redshift than at low redshift.

However, even at the relatively high spatial resolution obtained in this study, we are not able to rule out close ongoing major mergers. As an example, the nucleus of the archetypical starburst galaxy Arp 220 breaks into two components separated by ~ 350 pc (Scoville et al. 2017a). At $z = 4.5$ this corresponds to an angular separation of $\sim 0''.05$, and thus, we would not be able to resolve this particular case at our current resolution (median synthesized beam size $0''.30 \times 0''.27$). However, the nearby FIR peaks in two of our systems that we are able to resolve and the color gradients over all the galaxies would be consistent with such a picture.

An alternative plausible scenario would be that the starburst episode we are witnessing would be indeed triggered by previous minor or major mergers that we are currently unable to detect. The minor companions we detect here would be mergers in an early phase prior to coalescence, but not responsible for the observed starburst episode. Gas dynamics in these systems show evidence for rotationally supported star-forming disks (Jones et al. 2017; Jiménez-Andrade et al. 2018, Karim et al., in prep), which would have to be triggered either by gravitational instabilities or highly dissipational mergers that quickly set into a disk configuration. Smooth accretion can also trigger high SFR while still maintaining a rotationally supported disk (e.g., Romano-Díaz et al. 2014). Some simulations of galaxy formation at high redshift have also shown that gas and stellar disks already exist at $z \gtrsim 6$ (e.g., Pawlik et al. 2011; Romano-Díaz et al. 2011; Feng et al. 2015; Pallottini et al. 2017).

Recently, a population of compact star-forming galaxies (cSFGs) at $2.0 < z < 3.0$ have been suggested as progenitors for cQGs (e.g., Barro et al. 2013; van Dokkum et al. 2015; Barro et al. 2016). Two different progenitor populations are not necessarily mutually exclusive. Both SMGs and cSFGs could be part of the same global population but observed in a different phase or intensity of the stellar mass assembly, with the SMGs reflecting the peak of the process and the cSFGs being a later stage. cSFGs are consistent with an intermediate population between $z > 3$ SMGs and $z \sim 2$ cQGs, caught in a phase where the star formation is winding down and a compact remnant is emerging, transitioning from the region above the MS of star-forming galaxies (Barro et al. 2017b) to the MS (Popping et al. 2017c), and eventually below it. In fact Elbaz et al. (2018) have recently shown that starburst galaxies exist both above and within the MS. The increased AGN fraction in cSFGs suggest that they are entering a AGN/QSO quenching phase, which could be responsible for shutting down the residual star formation, leaving behind compact stellar remnants to develop into $z \sim 2$ cQGs (Barro et al. 2013) (see also Sanders et al. 1988; Hopkins et al. 2006; Hickox et al. 2012; Wilkinson et al. 2017).

In order to further explore the evolutionary connection between SMGs, cSFGs and cQGs, larger spectroscopic samples are needed. High spatial resolution rest-frame optical/FIR observations are paramount to unveil their different subcomponents and measure accurate optical/FIR sizes, stellar

masses and uncover the underlying structure of the dust. In this context *JWST* observations of DSFGs at high redshift will revolutionize our understanding of galaxy mass assembly through cosmic time.

2.8 Summary and Conclusions

A sample of six SMGs, five of which are spectroscopically confirmed to be at $z \sim 4.5$, were imaged at high spatial resolution with *HST*, probing rest-frame UV stellar emission, and with ALMA, probing the rest-frame FIR dust continuum emission. We find that:

- The rest-frame UV emission appears irregular and more extended than the very compact rest-frame FIR emission, which exhibits a median physical size of $r_e = 0.70 \pm 0.29$ kpc.
- The *HST* images reveal that the systems are composed of multiple merging components. The dust emission pinpointing the bulk of star formation is associated with the reddest and most massive component of the merger. The companions are bluer, lower mass galaxies, with properties typical of normal star-forming galaxies at similar redshifts.
- We find morphological evidence suggesting that the lack of spatial coincidence between the rest-frame UV and FIR emissions is the primary cause for the elevated position of DSFGs in the IRX- β plane. This has consequences for energy balance modelling efforts, which must account for the implied high extinction.
- A stellar mass analysis reveals that only one of the systems is undergoing a major merger. On the other hand all the systems are undergoing at least one minor merger with a median stellar mass ratio of 1:6.5. In addition, the *HST* images hint the presence of additional nearby low-mass systems.
- The stellar masses and rest-frame FIR sizes of the $z \sim 4.5$ SMGs fall on the stellar mass-rest-frame optical size relation of $z \sim 2$ cQGs, but spanning lower stellar masses and smaller sizes. To evolve into $z \sim 2$ cQGs, the SMGs must increase both in stellar mass and size. We show that the expected growth due to the ongoing starburst and minor mergers can account for such evolution.

Minor merging thus appear to play a pivotal role in the evolution of massive elliptical galaxies throughout their full cosmic history. Both for their size evolution from $z = 2$ to $z = 0$ (e.g., [Naab et al. 2009](#); [Newman et al. 2012](#)), but also for their formation at higher redshifts.

Acknowledgments

We thank I. Smail for his detailed comments and suggestion that help on improving this manuscript; J. M. Simpson for providing the SCUBA2 data; C. Y. Peng and G. Barro for their advice on GALFIT; S. Zibetti for his support with ADAPTSMOOTH; C. M. Casey for providing the DSFGs comparison data plotted in Figure 2.4; and D. Watson, J. Hjorth, I. Davidzon, H. Rhodin, K. K. Knudsen, P. Laursen, D. B. Sanders, M. P. Haynes, R. Pavesi, T. K. D. Leung and S. Martín-Álvarez for helpful comments and suggestions. We are grateful to the anonymous referee, whose comments have been very useful to improve our work.

CGG and ST acknowledge support from the European Research Council (ERC) Consolidator Grant funding scheme (project ConTEExt, grant number: 648179). AK, EJA and FB acknowledge support by the Collaborative Research Centre 956, sub-project A1, funded by the Deutsche Forschungsgemeinschaft (DFG). Support for BM was provided by the DFG priority program 1573 "The physics of the interstellar medium". DR acknowledges support from the National Science Foundation under grant number AST-1614213. VS acknowledges support from the European Union's Seventh Frame-work program under grant agreement 337595 (ERC Starting Grant, "CoSMass"). MA acknowledges partial support from FONDECYT through grant 1140099. ERD also acknowledge support by the Collaborative Research Centre 956, sub-project C4, funded by the DFG. MJM acknowledges the support of the National Science Centre, Poland, through the POLONEZ grant 2015/19/P/ST9/04010; this project has received funding from the European Union's Horizon 2020 research and innovation programme under the Marie Skłodowska-Curie grant agreement No. 665778.

Based on observations made with the NASA/ESA *Hubble Space Telescope*, obtained at the Space Telescope Science Institute, which is operated by the Association of Universities for Research in Astronomy, Inc., under NASA contract NAS 5-26555. These observations are associated with program #13294. Support for program #13294 was provided by NASA through a grant from the Space Telescope Science Institute, which is operated by the Association of Universities for Research in Astronomy, Inc., under NASA contract NAS 5-26555.

This research made use of the following ALMA data: ADS/JAO.ALMA#2012.1.00978.S. ALMA is a partnership of ESO (representing its member states), NSF (USA) and NINS (Japan), together with NRC (Canada) and NSC and ASIAA (Taiwan), in cooperation with the Republic of Chile. The Joint ALMA Observatory is operated by ESO, AUI/NRAO and NAOJ.

This paper employed `Astropy`, a community-developed core Python package for Astronomy (Astropy Collaboration et al. 2013); `APLpy`, an open-source plotting package for Python (Robitaille & Bressert 2012); `CASA` (McMullin et al. 2007); `Matplotlib` (Hunter 2007); `Numpy`; `Photutils` (Bradley et al. 2016); `PyBDSF`; `R`, a language and environment for statistical

2.8. SUMMARY AND CONCLUSIONS

computing (R Foundation for Statistical Computing, Vienna, Austria) ([R Core Team 2015](#)).

3

Exploring the Origins of Galaxy Clusters

This chapter contains the following article:

“Confirming *Herschel* Candidate Protoclusters from ALMA/VLA CO Observations”

Published in *The Astrophysical Journal*, Volume 872, Issue 2, article id. 117, 21 pp. (2019)

Authors:

C. Gómez-Guijarro, D. A. Riechers, R. Pavesi, G. E. Magdis, T. K. D. Leung, F. Valentino, S. Toft, M. Aravena, S. C. Chapman, D. L. Clements, H. Dannerbauer, S. J. Oliver, I. Pérez-Fournon, & I. Valtchanov

ALMA 870 μm continuum imaging has uncovered a population of blends of multiple dusty star-forming galaxies (DSFGs) in sources originally detected with the *Herschel Space Observatory*. However, their pairwise separations are much smaller than what is found by ALMA follow-up of other single-dish surveys or expected from theoretical simulations. Using ALMA and VLA, we have targeted three of these systems to confirm whether the multiple 870 μm continuum sources lie at the same redshift, successfully detecting $^{12}\text{CO}(J = 3-2)$ and $^{12}\text{CO}(J = 1-0)$ lines and being able to confirm that in the three cases all the multiple DSFGs are likely physically associated within the same structure. Therefore, we report the discovery of two new gas-rich dusty protocluster cores (HELAISS02, $z = 2.171 \pm 0.004$; HXMM20, $z = 2.602 \pm 0.002$). The third target is located in the well known COSMOS overdensity at $z = 2.51$ (named CL J1001+0220 in the literature), for which we do not find any new secure CO(1-0) detection, although some of its members show only tentative detections and require further confirmation. From the gas, dust, and stellar properties of the two new protocluster cores, we find very large molecular gas fractions yet low stellar masses, pushing the sources above the main sequence, while not enhancing their star formation efficiency. We suggest that the sources might be newly formed galaxies migrating to the main sequence. The properties of the three systems compared to each other and to field galaxies may suggest a different evolutionary stage between systems.

3.1 Introduction

Galaxies luminous in the far-IR (FIR) and submillimeter (submm) wavelengths comprise the most intense starbursts in the universe, known as dusty star-forming galaxies (DSFGs; see [Casey et al. 2014a](#), for a review). With a redshift distribution that peaks at $z \sim 2-3$ (e.g., [Chapman et al. 2005](#)), they constitute an important component of the overall galaxy population at $z \sim 2$ (e.g., [Magnelli et al. 2011](#)). DSFGs are promising candidates to trace galaxy clusters in formation, the so-called protoclusters (see [Overzier 2016](#)). DSFGs have also been proposed as progenitors of the most massive elliptical galaxies in the local universe (e.g., [Cimatti et al. 2008](#); [Ricciardelli et al. 2010](#); [Fu et al. 2013](#); [Iverson et al. 2013](#); [Toft et al. 2014](#); [Gómez-Guijarro et al. 2018](#)).

At $z \gtrsim 4$ overdensities of galaxies with associated DSFGs have been discovered: GN20 (e.g., [Daddi et al. 2009](#)), HDF850.1 (e.g., [Walter et al. 2012](#)), AzTEC-3 (e.g., [Riechers et al. 2010](#); [Capak et al. 2011](#); [Riechers et al. 2014a](#)), CRLE and HZ10 (e.g., [Capak et al. 2015](#); [Pavesi et al. 2016, 2018a](#)), DRC (e.g., [Oteo et al. 2018](#)), SPT2349-56 (e.g., [Miller et al. 2018](#)). At $2 \lesssim z \lesssim 3$ several confirmed protoclusters containing dozens of galaxies are known to be DSFGs-rich: GOODS-N $z = 1.99$ protocluster (e.g., [Blain et al. 2004](#); [Chapman et al. 2009](#)), CL J1449+0856 (e.g., [Gobat et al. 2011](#); [Valentino et al. 2015, 2016](#); [Coogan et al. 2018](#)), COSMOS $z = 2.10$ protocluster (e.g., [Spitler et al. 2012](#); [Yuan et al. 2014](#)), MRC1138-256 (e.g., [Kurk et al. 2000](#); [Dannerbauer et al. 2014](#)), COSMOS $z = 2.51$ protocluster (e.g., [Bertoldi et al. 2007](#); [Aravena et al. 2010](#); [Casey et al. 2015](#); [Wang et al.](#)

3. EXPLORING THE ORIGINS OF GALAXY CLUSTERS

2016; Cucciati et al. 2018; Wang et al. 2018), SSA22 (e.g., Steidel et al. 1998; Umehata et al. 2015) (see also Casey 2016).

Large angular scale clusters and cluster candidates have been found by the *Herschel Space Observatory* and *Planck* satellite (e.g., Clements et al. 2014, 2016; Planck Collaboration et al. 2016; Greenslade et al. 2018; Martinache et al. 2018). In particular, *Herschel* has scanned wide fields at FIR and submm wavelengths with the Spectral and Photometric Imaging Receiver (SPIRE; Griffin et al. 2010) at 250, 350, and 500 μm (e.g., Eales et al. 2010; Oliver et al. 2012). The nature of the *Herschel*/SPIRE wide beam detections is diverse. Among them, gravitationally-lensed (e.g., Negrello et al. 2010; Bussmann et al. 2012; Wardlow et al. 2013; Bussmann et al. 2013; Cañameras et al. 2015) and $z > 4$ DSFGs (e.g., Riechers et al. 2013; Dowell et al. 2014; Donevski et al. 2018) have been identified in large numbers, with follow-up high spatial resolution observations proven to be very important to uncover their nature. Recently, *Herschel*/SPIRE detections have also found to be blends of multiple DSFGs that could constitute protoclusters (e.g., Bussmann et al. 2015) (see also Silva et al. 2015).

Bussmann et al. (2015) presented ALMA 870 μm observations of 29 bright *Herschel*/SPIRE DSFGs from the HerMES survey (Oliver et al. 2012). The ALMA imaging surprisingly showed that 20/29 objects comprise multiple DSFGs located within a few arcseconds of each other. Such a high fraction with small pairwise physical separations are almost completely unexpected from both a theoretical perspective (Hayward et al. 2013; Cowley et al. 2015; Muñoz Arancibia et al. 2015; Hayward et al. 2018) as well as previous high spatial resolution follow-up of the LARge APEX Bolometer CAmera (LABOCA) and the Submillimetre Common-User Bolometer Array (SCUBA) single-dish observations (Hodge et al. 2013; Wardlow et al. 2018), suggesting that a portion of the ALMA 870 μm counterparts are due to line-of-sight projection effects and are not physically related. In order to investigate whether they are physically associated or not it is necessary to have spectroscopic data with sufficient spatial resolution to distinguish the ALMA counterparts from each other.

In this work we present follow-up CO line observations of three *Herschel* candidate protoclusters from Bussmann et al. (2015) aiming to confirm whether the multiple ALMA 870 μm continuum sources are located at the same redshift or are line-of-sight projections. Note that we will refer to these associations of multiple DSFGs within a few arcseconds of each other as protocluster cores. It is known that the small field of view (FOV) of the ALMA observations is only able to detect the densest peaks of protocluster structures. Confirmation of a larger structure of members located at a similar redshift studying whether the structures will evolve into a cluster at $z = 0$ is required to properly establish the protocluster nature of the candidates, which is beyond the scope of this work (e.g., Chiang et al. 2013; Muldrew et al. 2015; Chiang et al. 2017).

The layout of the paper is as follows. We introduce the sample and data in Section 3.2. In

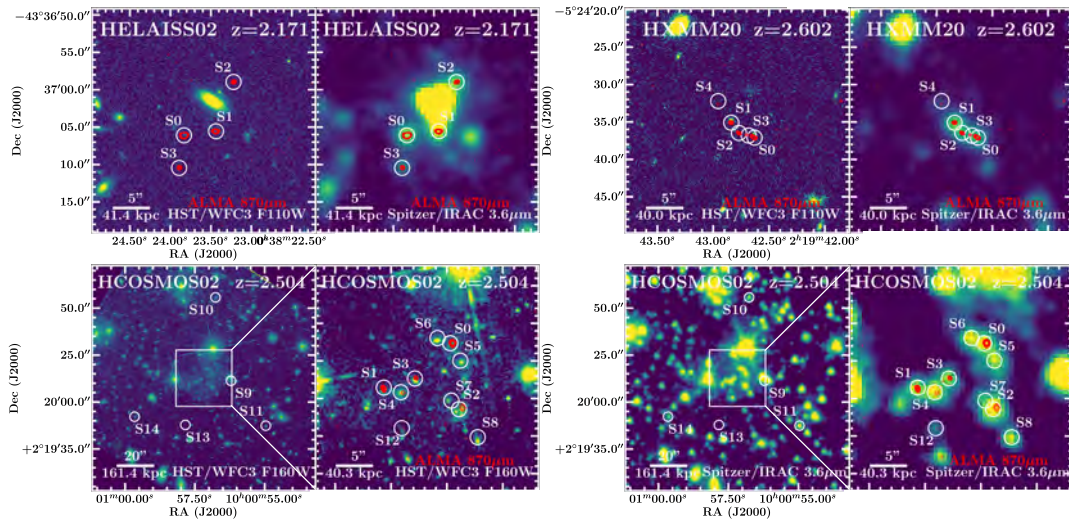


Figure 3.1: Overview of the sample. Top row: HELAISS02 and HXMM20 $30'' \times 30''$ *HST*/WFC3 F160W and *Spitzer*/IRAC $3.6 \mu\text{m}$ images. Bottom row: HCOSMOS02 $120'' \times 120''$ and $30'' \times 30''$ zoom-in of the central region *HST*/WFC3 F160W and *Spitzer*/IRAC $3.6 \mu\text{m}$ images. ALMA $870 \mu\text{m}$ contours are overlaid in red (starting at $\pm 1 \sigma$ and growing in steps of $\pm 1 \sigma$, where positive contours are solid and negative contours dotted). CO(1-0) detections presented in Section 3.3 are encircled and labeled in white.

Section 3.3 we present the analysis of the observations. Gas, dust and stellar properties of the targets are explored in Section 3.4. We discuss the results, comparing with field galaxies and protoclusters in Section 3.5. Summary of the main findings and conclusions are in Section 3.6.

Throughout this work we adopted a concordance cosmology $[\Omega_\Lambda, \Omega_M, h] = [0.7, 0.3, 0.7]$ and Chabrier initial mass function (IMF) (Chabrier 2003).

3.2 Sample and Data

3.2.1 *Herschel* Candidate Protoclusters

We followed up the three sources in the original *Herschel*-ALMA sample from Bussmann et al. (2015) with the highest multiplicity rate. Each target has at least four ALMA $870 \mu\text{m}$ counterparts (see Figure 3.1 for an overview of the sample). Briefly, the original sample of 29 *Herschel*/SPIRE DSFGs in Bussmann et al. (2015) was selected to be the brightest set of targets in the ALMA-accessible portion of HerMES (Oliver et al. 2012) available at the time of the Cycle 0 deadline. The intention was to assemble the largest sample of lenses possible, but a comparison of optical imaging with the ALMA imaging surprisingly showed that most of the objects in this subset comprise multiple DSFGs located within a few arcseconds of each other.

The targets HELAISS02 and HXMM20 are new protoclusters candidates. HCOSMOS02 was originally reported in the literature as COSBO-3 by Bertoldi et al. (2007) and shown to be an

3. EXPLORING THE ORIGINS OF GALAXY CLUSTERS

overdense region with a photometric redshift $z \sim 2.2\text{--}2.4$ in [Aravena et al. \(2010\)](#) (see also [Smolčić et al. 2012b](#)). Several works have been recently focused on this source. [Casey et al. \(2015\)](#) spectroscopically confirmed some galaxies in HCOSMOS02 using Keck/MOSFIRE. [Wang et al. \(2016\)](#) (source named CL J1001+0220) reported that there is evidence of virialization and define it as a cluster (see also [Daddi et al. 2017](#); [Wang et al. 2018](#)). It also appears to be related with a larger structure composed of several density peaks spanning $2.42 < z < 2.51$ ([Diener et al. 2013, 2015](#); [Chiang et al. 2015](#); [Casey et al. 2015](#); [Lee et al. 2016](#); [Cucciati et al. 2018](#)). We carried out a redshift search for $^{12}\text{CO}(J = 3\text{--}2)$ for HELAISS02 and HXMM20 and $^{12}\text{CO}(J = 1\text{--}0)$ for HXMM20 using prior photometric information that placed our targets at $1.5 < z < 3.5$ with high certainty. In the case of HCOSMOS02, the redshift was established from our Combined Array for Research in Millimeter-wave Astronomy (CARMA) 3 mm observations targeting $^{12}\text{CO}(J = 3\text{--}2)$ (see Section 3.2.4), independently from the Keck/MOSFIRE $\text{H}\alpha$ detections in [Casey et al. \(2015\)](#) and the NOthern Extended Millimeter Array (NOEMA) $^{12}\text{CO}(J = 5\text{--}4)$ confirmed with NSF’s Karl G. Jansky Very Large Array (VLA) $^{12}\text{CO}(J = 1\text{--}0)$ observations in [Wang et al. \(2016\)](#). Knowing the redshift of HCOSMOS02, we performed $^{12}\text{CO}(J = 1\text{--}0)$ and $^{12}\text{CO}(J = 4\text{--}3)$ observations.

3.2.2 ALMA Observations

We carried out a spectral scan of the 3 mm band with ALMA band 3 during Cycle 3 (program 2015.1.00752.S; PI: R. S. Bussmann) targeting $^{12}\text{CO}(J = 3\text{--}2)$ transition line ($\nu_{\text{rest}} = 345.79599$ GHz) for HELAISS02 and HXMM20.

Observations of HELAISS02 were executed between 2016 May 27 and June 17 with 46 usable 12-m antennae. The shortest and longest baselines were 12 m and 741 m, respectively. The resulting on-source spectral scan integration time was 25.5 min. The correlator was set up in five different tunings every one containing four spectral windows of 1.875 GHz each at 31.25 MHz (94.95 km s^{-1} at 98.664 GHz) resolution in dual polarization, covering the frequency range 84–113.2 GHz. The radio quasar J2357-5311 was observed as bandpass and secondary flux calibrator and the radio quasar J0030-4224 as amplitude and phase calibrator. Pallas was set to the primary flux calibrator, but it was not observed in the first tuning, so we substituted it for our secondary flux calibrator J2357-5311 in all tunings to be consistent. The flux calibration using J2357-5311 is 15% lower than using Pallas.

HXMM20 observations were taken on 2016 June 12 with 38 usable 12-m antennae. The shortest and longest baselines were 13 m and 704 m, respectively. The on-source spectral scan integration time was 11.6 min. The correlator configuration was identical to that of HELAISS02. The radio quasars J0006-0623 and J0238+1636 were observed as bandpass and flux calibrators, the first object for the first tuning and the second object for the rest of the tunings. The radio quasar J0209-0438 was observed for amplitude and phase calibration of all the tunings. Pallas was also

part of the observations, but the QA assessed a discrepancy of 30% between the model and the calibrator catalogue; therefore, it was rejected as flux calibrator.

The Common Astronomy Software Applications (CASA; McMullin et al. 2007, version 4.6.0 for HELAISS02 and version 4.5.6 for HXMM20) packages were employed for data reduction and analysis. HELAISS02 and HXMM20 data were mapped using the CLEAN algorithm with natural weighting to get the best point source sensitivity. We used custom masks enclosing the emitting regions in each channel, cleaning down to a 2σ threshold. For HELAISS02, the resulting synthesized beam size is $1''.36 \times 1''.14$ and the primary beam half power beam width (HPBW) $53''.4$ at 108.9655 GHz. For HXMM20, the synthesized beam size is $1''.50 \times 1''.27$ and the primary beam HPBW $60''.6$ at 96.11968 GHz. The rms noise per 94.95 km s^{-1} channel at 108.96550 GHz is $\sim 0.38 \text{ mJy beam}^{-1}$ for HELAISS02 and $\sim 0.54 \text{ mJy beam}^{-1}$ per 94.95 km s^{-1} channel at 96.11968 GHz for HXMM20, measured at the phase center.

Line free channels were combined to measure the continuum at $\sim 3 \text{ mm}$ (see Table 3.1 and Figure 3.2), resulting in a rms noise of $\sim 13 \mu\text{Jy beam}^{-1}$ for HELAISS02 and $\sim 22 \mu\text{Jy beam}^{-1}$ for HXMM20, at the phase center. Continuum subtraction is not needed since the continuum level is negligible at the rms noise of the line channels.

3.2.3 VLA Observations

A spectral scan was also carried out with VLA, Ka and Q bands during Cycle 15 semester B (program 15B-065; PI: R. S. Bussmann). We targeted $^{12}\text{CO}(J = 1-0)$ transition line ($\nu_{\text{rest}} = 115.27120 \text{ GHz}$) for HXMM20 and HCOSMOS02.

Observations of HXMM20 were taken between 2015 Oct 22 and Nov 14 in D array configuration (shortest baseline 31 m, longest baseline 997 m). Total on-source spectral scan integration time was 6.7 h. We configured three correlator tunings covering Ka and Q band frequencies, each one containing four basebands of 2 GHz using the 3-bit sampler that provides 2 MHz channels in dual polarization, covering the frequency range 26.5–48 GHz. The radio quasars 3C 147 and J0215-0222 acted as flux/bandpass and amplitude/phase calibrators, respectively.

HCOSMOS02 was observed between 2015 Oct 24 and Nov 6 in D array configuration (shortest baseline 34 m, longest baseline 922 m). Given the known redshift of this source from our CARMA observations targeting CO(3-2) (see Section 3.2.4) and independently found by Wang et al. (2016) from CO(1-0), we selected Ka band with the correlator set up covering the frequency range 31.5–33.5 GHz using the 3-bit sampler providing 2 MHz channels in dual polarization. The radio quasars 3C 147 and J1018+0530 were used as flux/bandpass and amplitude/phase calibrators, respectively. Additional data is available for HCOSMOS02 from two archival programs (program 15B-210; PI: C. Casey, and program 15B-290; PI: T. Wang. For an upcoming independent analysis of the archival data, see J. Champagne et al., in prep.) We concatenated all three programs, for

3. EXPLORING THE ORIGINS OF GALAXY CLUSTERS

Table 3.1: Continuum Measurements

Name	$S_{870\mu\text{m}}^a$ (mJy beam ⁻¹)	$S_{3\text{mm}}$ ($\mu\text{Jy beam}^{-1}$)	$S_{32\text{GHz}}$ ($\mu\text{Jy beam}^{-1}$)
HELAISS02			
S0	9.22 ± 0.17	104 ± 13	...
S1	4.34 ± 0.16	51 ± 12	...
S2	4.16 ± 0.32	42 ± 11	...
S3	2.40 ± 0.19	43 ± 12	...
HXMM20			
S0	7.15 ± 0.44	130 ± 22	21.1 ± 3.5
S1	3.52 ± 0.41	65 ± 22	...
S2	3.42 ± 0.26
S3	2.46 ± 0.47
S4	0.94 ± 0.18
HCOSMOS02			
S0	5.26 ± 0.26	...	6.4 ± 1.9
S1	3.77 ± 0.32
S2	1.69 ± 0.25	...	8.9 ± 1.9
S3	1.66 ± 0.21
S4	2.23 ± 0.41	...	6.0 ± 1.9

^a From [Bussmann et al. \(2015\)](#).

a total on-source integration time of 33.3 h. Together the programs cover the frequency range 31.5–34.2 GHz, but overlap just at 32.2–33.4 GHz.

CASA (version 4.5.0) was employed for reduction and analysis. We imaged HXMM20 using a robust = 0.5 Briggs weighting scheme ([Briggs 1995](#)) as it gave the best compromise between the spatial resolution required to deblend the different ALMA counterparts and the sensitivity to detect them. For HCOSMOS02 we used a natural weighting scheme to achieve the best point source sensitivity possible. For HXMM20, the resulting synthesized beam size is $2''.37 \times 1''.92$ and the primary beam HPBW $84''.3$ at 32.04105 GHz. For HCOSMOS02, the synthesized beam size is $2''.88 \times 2''.49$ and the primary beam HPBW $82''.1$ at 32.86889 GHz. The rms noise in a 50 km s^{-1} channel at 32.04105 GHz is $\sim 0.12 \text{ mJy beam}^{-1}$ for HXMM20 and $\sim 31 \mu\text{Jy beam}^{-1}$ in a 50 km s^{-1} channel at 32.86889 GHz for HCOSMOS02, measured at the phase center.

Line free channels were combined to search for continuum emission at $\sim 32 \text{ GHz}$ (see [Table 3.1](#) and [Figure 3.2](#)), resulting in a rms noise of $\sim 3.5 \mu\text{Jy beam}^{-1}$ for HXMM20 and $\sim 1.9 \mu\text{Jy beam}^{-1}$ for HCOSMOS02, at the phase center. Continuum subtraction is not needed since the continuum level is negligible at the rms noise of the line channels.

3.3. CONFIRMATION OF PROTOCLUSTER CORES

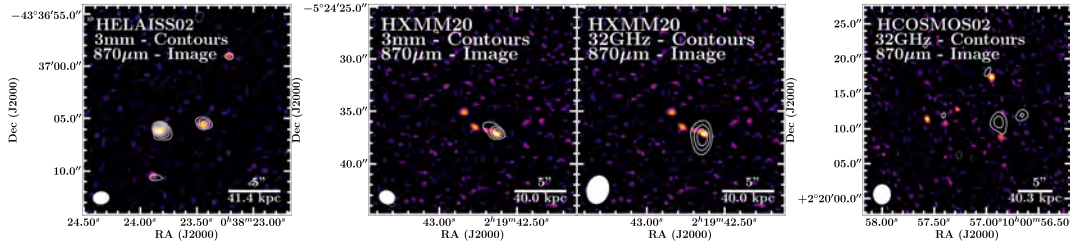


Figure 3.2: From left to right: HELAISS02 3 mm continuum, HXMM20 3 mm, 32 GHz and HCOSMOS02 32 GHz continuum emission on top of the $870\ \mu\text{m}$ continuum image. Contours start at $\pm 3\sigma$ and grow in steps of $\pm 1\sigma$ (HELAISS02 3 mm $\sigma = 13\ \mu\text{Jy beam}^{-1}$; HXMM20 3 mm $\sigma = 22\ \mu\text{Jy beam}^{-1}$; HXMM20 32 GHz $\sigma = 3.5\ \mu\text{Jy beam}^{-1}$; HCOSMOS02 32 GHz $\sigma = 1.9\ \mu\text{Jy beam}^{-1}$). Positive contours are solid and negative contours dotted.

3.2.4 CARMA and NOEMA Observations

A spectral scan was carried out with CARMA during 2011 (projects cx322 and c0673; PI: D. A. Riechers) targeting $^{12}\text{CO}(J = 3-2)$ for HCOSMOS02, since the redshift of this source was unknown at that time. Once the redshift was secured, we targeted $^{12}\text{CO}(J = 4-3)$ transition line ($\nu_{\text{rest}} = 461.04077\ \text{GHz}$) with NOEMA, formerly known as the Plateau de Bure Interferometer (PdBI), for HCOSMOS02 (project W0AB; PI: D. A. Riechers).

CARMA observations were executed in seven tracks in E configuration between 2011 January 23 and February 10, plus one track in D configuration in 2011 May 25, using 10–15 antennas. Four regular tunings were set up covering 85.48–111.48 GHz at 5.208 MHz resolution for the E configuration tracks and one custom tuning, within the frequency range of the four regular tunings, for the D configuration track. The resulting on-source spectral scan integration time was 11.9 h. The radio quasars J0927+390 and 3C273 were observed as bandpass calibrators and the radio quasar J1058+015 as phase calibrator. The radio quasars 3C84 and 3C273 were the flux calibrators. We employed MIRIAD for reduction and imaging. The resulting synthesized beam size at 100 GHz is $4''.47 \times 2''.80$ (primary beam HPBW $60''.6$).

NOEMA observations were carried out in two tracks in D configuration observed on 2013 April 10 and 13 using 6 antennas. The tuning frequency was set at 131.139 GHz. We employed GILDAS for reduction and imaging. The resulting synthesized beam size at the tuning frequency is $3''.10 \times 1''.77$ (primary beam HPBW $38''.4$).

3.3 Confirmation of Protocluster Cores

3.3.1 HELAISS02

Our ALMA spectral scan targeting CO(3-2) for HELAISS02 successfully detected significant emission in all four ALMA $870\ \mu\text{m}$ counterparts presented in [Bussmann et al. \(2015\)](#). Therefore,

3. EXPLORING THE ORIGINS OF GALAXY CLUSTERS

we confirmed that they are located at the same redshift at a median value $z = 2.171 \pm 0.004$.

We computed the moment-0 maps for each source, which represent the total intensity integrated over the velocity axis (see Figure 3.3). The velocity channels selected for integration were the line channels that maximize the signal-to-noise ratio (S/N). In Figure 3.4 we present the spectra extracted at the pixel located at the peak of the $870 \mu\text{m}$ continuum emission. S0, S2 and S3 detections are secure, while S1 appears tentatively detected at $S/N < 3$ with its spectrum showing a symmetric negative peak in adjacent channels to the line due to potential sidelobe residuals. We measured centroids, widths and peak fluxes using the CASA task `specfit` fitting a single Gaussian component. The results are presented in Table 3.2. In order to calculate the integrated line fluxes we performed a 2D Gaussian fit per source and per velocity channel in the spectral cube using the CASA task `imfit`. For each source we selected the channels used to create their respective moment-0 maps as those to be fitted. No significant emission was detected in the residuals beyond a point source fit; thus, we fixed the Gaussian width and position angle to those of the clean beam and the position to the $870 \mu\text{m}$ peak. The uncertainties in `imfit` are known to be too small when using fixed parameters, so the quoted uncertainties in Table 3.2 are the 1σ noise from the moment-0 maps instead. In addition, we calculated the line luminosity expressed in terms of the surface integrated brightness temperature (L'_{CO} ; Solomon et al. 1992).

3 mm continuum emission was detected at $S/N > 3$ for all four ALMA counterparts as well (see Figure 3.2). Measurements were also extracted at the pixel located at the peak of the $870 \mu\text{m}$ continuum emission (see Table 3.1).

Table 3.2: HELAISS02 CO(3-2) Line Measurements

Name ^a	α (J2000) ^b (h:m:s)	δ (J2000) ^b (°:′:″)	$v_{0,\text{CO}(3-2)}$ ^c (km s ⁻¹)	$dv_{\text{CO}(3-2)}$ (km s ⁻¹)	$S_{\text{CO}(3-2)}$ (mJy beam ⁻¹)	$I_{\text{CO}(3-2)}$ (Jy km s ⁻¹)	$S/N_{\text{CO}(3-2)}$	$\log L'_{\text{CO}(3-2)}$ (K km s ⁻¹ pc ⁻²)
HELAISS02	00 38 23.59	-43 37 04.15	2.171 ± 0.004					
S0	00 38 23.76	-43 37 06.10	236 ± 25	931 ± 58	2.93 ± 0.24	3.13 ± 0.30	11.8	10.90 ± 0.04
S1*	00 38 23.48	-43 37 05.56	-630 ± 100	910 ± 230	0.54 ± 0.14	0.53 ± 0.21	2.79*	10.13 ± 0.17
S2	00 38 23.31	-43 36 58.97	-236 ± 33	575 ± 78	1.70 ± 0.27	0.91 ± 0.16	7.38	10.36 ± 0.08
S3	00 38 23.80	-43 37 10.46	281 ± 66	610 ± 160	0.83 ± 0.19	0.51 ± 0.19	3.48	10.11 ± 0.16
Total						5.08 ± 0.44		11.11 ± 0.04

^a Source names correspond to those originally reported in [Bussmann et al. \(2015\)](#). ^b Coordinates correspond to those of the ALMA 870 μm continuum sources as originally reported in [Bussmann et al. \(2015\)](#). ^c Velocity offset is centered at the median redshift of the four sources. * Tentative detection.

3. EXPLORING THE ORIGINS OF GALAXY CLUSTERS

3.3.2 HXMM20

The ALMA and VLA spectral scans targeted CO(3-2) and CO(1-0) for HXMM20, respectively. We detected significant emission in all the five ALMA 870 μm counterparts in [Bussmann et al. \(2015\)](#). Therefore, we also confirmed that they are located at the same redshift at a median value $z = 2.602 \pm 0.002$.

The moment-0 maps in [Figure 3.3](#) show secure detections of S1 and a blend of S0, S2 and S3. S4 is securely detected in the ALMA CO(3-2) observations, although it is only tentatively detected at $S/N < 3$ in the VLA CO(1-0) observations. In [Figure 3.4](#) we present the spectra extracted at the pixel located at the peak of the 870 μm continuum emission. We collect the line measurements in [Table 3.3](#), obtained following the same method as in HELAISS02. For HXMM20-S4 we fixed the centroid and width of CO(1-0) line to that of the CO(3-2), since due to the low S/N part of the emission was not properly accounted in a regular Gaussian fit with free parameters. In the case of HXMM20 the 2D Gaussian fit to calculate the integrated line fluxes is particularly important to properly deblend the emission of S0, S2 and S3, since it operates on each channel taking advantage of the variation of the spatial location of the emission that moves across the different sources in velocity space. For consistency, we checked that the recovered fluxes in these blended sources are consistent with that measured in a moment-0 map created by collapsing over the line channels of the three sources in an aperture enclosing all of them. Therefore, we are not double-counting flux in the blended sources. No significant emission was detected in the residuals beyond the point source fit.

We measured the line brightness temperature ratio $r_{31} = L'_{\text{CO}(3-2)} / L'_{\text{CO}(1-0)}$, resulting in high values as observed in starburst galaxies such as submillimeter galaxies (SMGs; e.g., [Bothwell et al. 2013](#)). In the case of S1 is also consistent with thermalized level populations (see [Table 3.3](#)).

3 mm and 32 GHz continuum emission was detected for S0 and 3 mm for S3 (see [Figure 3.2](#)). Measurements were also extracted at the pixel located at the peak of the 870 μm continuum emission (see [Table 3.1](#)).

Table 3.3: HXMM20 CO(1-0) and CO(3-2) Line Measurements

Name ^a	α (J2000) ^b (hr:m:s)	δ (J2000) ^b ($^{\circ}$: $'$: $''$)	v_0 , CO(1-0) ^c (km s ⁻¹)	v_0 , CO(3-2) ^c (km s ⁻¹)	dt ^b CO(1-0) (km s ⁻¹)	dt ^b CO(3-2) (km s ⁻¹)	$S_{\text{CO}(1-0)}$ (mJy beam ⁻¹)	$S_{\text{CO}(3-2)}$ (mJy beam ⁻¹)	$I_{\text{CO}(1-0)}$ (Jy km s ⁻¹)	$I_{\text{CO}(3-2)}$ (Jy km s ⁻¹)	$S/N_{\text{CO}(1-0)}$	$S/N_{\text{CO}(3-2)}$	$\log L_{\text{CO}(1-0)}$ (K km s ⁻¹ pc ⁻²)	$\log L_{\text{CO}(3-2)}$ (K km s ⁻¹ pc ⁻²)	r31
HXMM20	02 19 42 78	-05 24 34.84	22 ± 34	2.602 ± 0.002	688 ± 81	803 ± 98	0.44 ± 0.04	2.38 ± 0.25	0.32 ± 0.05	2.00 ± 0.25	1.15	9.30	11.00 ± 0.07	10.84 ± 0.05	0.69 ± 0.14
S0	02 19 42 63	-05 24 37.11	-369 ± 27	0 ± 42	278 ± 63	241 ± 30	0.42 ± 0.08	4.11 ± 0.45	0.12 ± 0.04	1.24 ± 0.17	6.15	6.74	10.57 ± 0.14	10.63 ± 0.06	1.15 ± 0.41
S1	02 19 42 84	-05 24 35.11	1 ± 46	-389 ± 13	409 ± 110	319 ± 56	0.31 ± 0.06	2.15 ± 0.32	0.16 ± 0.05	0.83 ± 0.22	4.23	4.05	10.70 ± 0.14	10.46 ± 0.12	0.57 ± 0.24
S2	02 19 42 77	-05 24 36.48	-10 ± 25	91 ± 24	490 ± 110	319 ± 56	0.31 ± 0.06	2.15 ± 0.32	0.16 ± 0.05	0.83 ± 0.22	4.23	4.05	10.70 ± 0.14	10.46 ± 0.12	0.57 ± 0.24
S3	02 19 42 66	-05 24 36.82	-10 ± 25	91 ± 24	473 ± 58	484 ± 45	0.49 ± 0.05	3.70 ± 0.30	0.25 ± 0.04	1.37 ± 0.21	9.04*	8.86	10.69 ± 0.07	10.75 ± 0.06	0.70 ± 0.14
S4*	02 19 42 96	-05 24 32.22	-431 ± 99	-431 ± 99	590 ± 230	590 ± 230	0.25 ± 0.07	0.88 ± 0.30	0.15 ± 0.05	0.35 ± 0.18	2.71*	3.12	10.67 ± 0.14	10.28 ± 0.14	0.41 ± 0.19
Total									1.00 ± 0.10	6.19 ± 0.47			11.49 ± 0.04	11.08 ± 0.03	0.69 ± 0.09

^a Source names correspond to those originally reported in Bussmann et al. (2015). ^b Coordinates correspond to those of the ALMA 870 μ m continuum sources as originally reported in Bussmann et al. (2015). ^c Velocity offset is centered at the median CO(3-2) redshift of the five sources. * Tentative CO(1-0) detection. Centroid and width were fixed to that of CO(3-2).

3. EXPLORING THE ORIGINS OF GALAXY CLUSTERS

3.3.3 HCOSMOS02

The combined VLA programs for HCOSMOS02 (see Section 3.2¹) targeted CO(1-0) at the redshift of the source ($z = 2.506$, found by Wang et al. 2016, and in our CARMA 3 mm data). We analyzed the ALMA 870 μm counterparts reported in Bussmann et al. (2015) (namely HCOSMOS02-S0, S1, S2, S3, and S4).

We carried out a line blind search over the whole frequency range covered by the combination of VLA programs in a FOV as large as the ALMA pipeline allows by default. The sensitivity decays as we move away from the phase center, following the primary beam response, and the pipeline masked regions below 10% of the phase center sensitivity. This corresponds to a FOV $1.6 \times \text{HPBW} = 132''$. The blind search was performed on the final image cube using MF3D² (Pavesi et al. 2018b). This algorithm implements a Matched Filtering in 3D line search, which is optimized for Gaussian line profiles and either spatially unresolved or slightly resolved emission (see Pavesi et al. 2018b, for details). The purities analysis revealed that $S/N > 5.8$ is the threshold above which the ratio of spurious negative detections over positive detections is 0. At $5.0 < S/N < 5.8$ we found 12 negative detections and 14 positive detections. We checked all the $5.0 < S/N < 5.8$ sources. The line extraction showed symmetric negative peaks, or just consistent on spikes of two or three channels. Besides, they did not show an optical/near-IR counterpart. Therefore, we ended up discarding the sources in the range $5.0 < S/N < 5.8$ since they were not reliable. We detected eight sources at $S/N > 5.8$ (namely S0, S1, S2, S4, S9, S11, S13, and S14).

Additionally, we analyzed the sources in Table 1 from Wang et al. (2016) and in Table 1 from Wang et al. (2018) that fall within our FOV, comprising all the sources in the tables except for those with the IDs 128484, 129305, 129444, 132636, 132627 that fall outside our FOV and, thus, below 10% of the primary beam sensitivity.

We show the moment-0 maps for each source in Figure 3.5 and their spectra in Figure 3.6. Measurements were performed following the same method as in HELAISS02 and HXMM20. Spectra were extracted at the pixel peak of the 870 μm continuum emission for Bussmann et al. (2015) sources. In the case of the sources from the blind search the spectra were extracted at the position of the detection given by the code, which are consistent with the coordinates in Wang et al. (2016) for the sources that appear in this previous study. The spectra were binned at 100 km s^{-1} for the sources with $S/N < 3$. All measurements are collected in Table 3.4.

The moment-0 maps show that S0, S1 and S2 look extended. However, checking the *Spitzer*/IRAC 3.6 μm (SPLASH; Capak et al., in prep.) image we found that both S0 and S2 are associated with two IRAC counterparts each. In the case of S1 there is no additional IRAC counterpart at the

¹For an upcoming independent analysis of the archival data, see J. Champagne et al., in prep.

²Code available at <https://github.com/pavesiriccardo/MF3D>

3.3. CONFIRMATION OF PROTOCLUSTER CORES

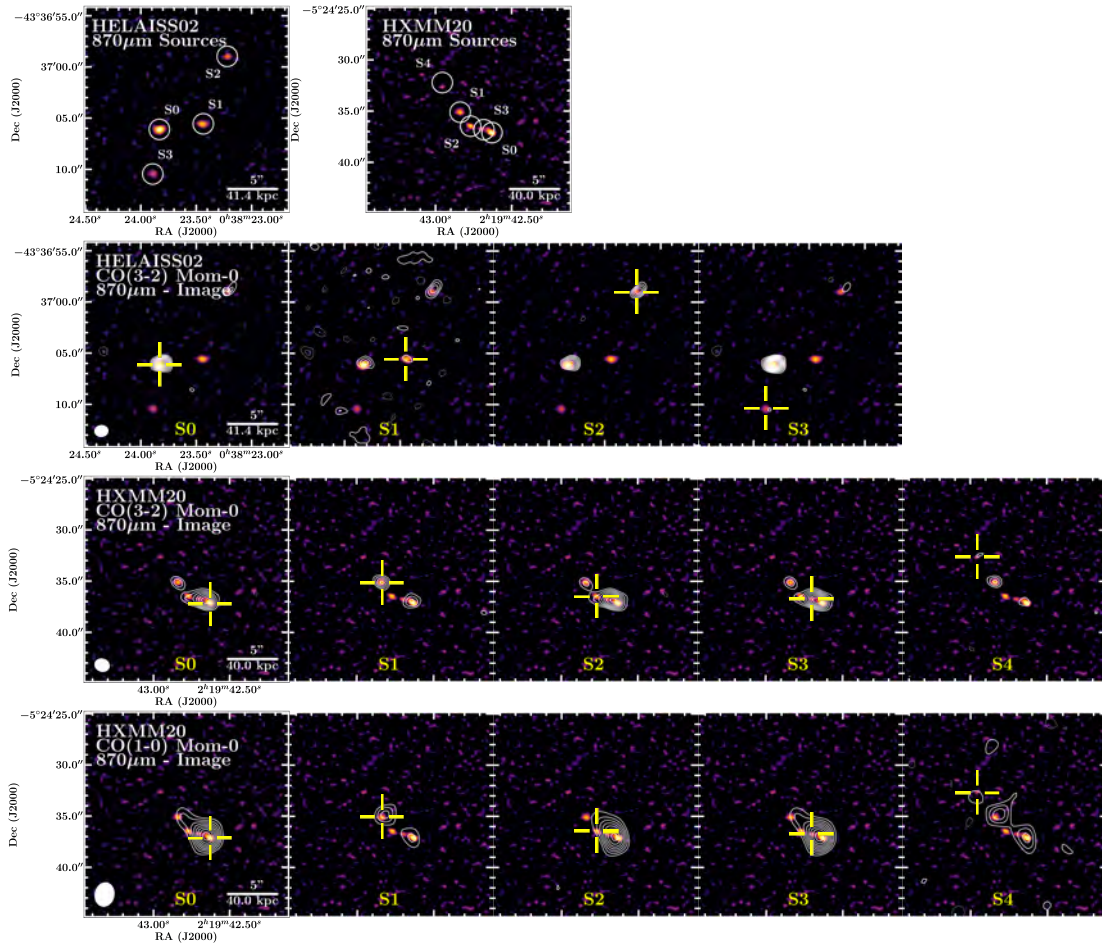


Figure 3.3: HELAISS02 and HXMM20 moment-0 maps. First row: Overview of the ALMA $870\ \mu\text{m}$ continuum sources reported in [Bussmann et al. \(2015\)](#). Second row: HELAISS02 CO(3-2) moment-0 maps of the $870\ \mu\text{m}$ continuum sources in [Bussmann et al. \(2015\)](#) represented as contours on top of the $870\ \mu\text{m}$ continuum maps. Third row: HXMM20 CO(3-2) moment-0 maps of the $870\ \mu\text{m}$ continuum sources in [Bussmann et al. \(2015\)](#) on top of the $870\ \mu\text{m}$ continuum image. Fourth row: HXMM20 CO(1-0) moment-0 maps of the $870\ \mu\text{m}$ continuum sources in [Bussmann et al. \(2015\)](#) on top of the $870\ \mu\text{m}$ continuum image. The source to which each panel refers to is marked with a yellow cross (note that sources spanning a similar velocity range appear also in the panel by construction of a moment-0 map). Contours start at $\pm 3\sigma$ and grow in steps of $\pm 1\sigma$, except for HELAISS02 CO(3-2) S1 and HXMM20 CO(1-0) S4 that start at $\pm 2\sigma$. Positive contours are solid and negative contours dotted.

northeast where the excess of CO emission is located, but this excess can be well modeled by an additional component covering a frequency range that is narrower and blueshifted respect to S1. The 2D Gaussian fit for S0, S1 and S2 was performed using an extra component on each source centered at the coordinates of the additional IRAC counterparts for S0 (namely S6), S2 (namely S7), and northeast of S1 with no additional IRAC counterpart (we included its flux contribution in S1). No significant emission was detected beyond the point source fit with the extra components. For consistency, we checked that the recovered fluxes in these blended sources are consistent with that measured in a moment-0 map created by collapsing over the line channels of the blended

3. EXPLORING THE ORIGINS OF GALAXY CLUSTERS

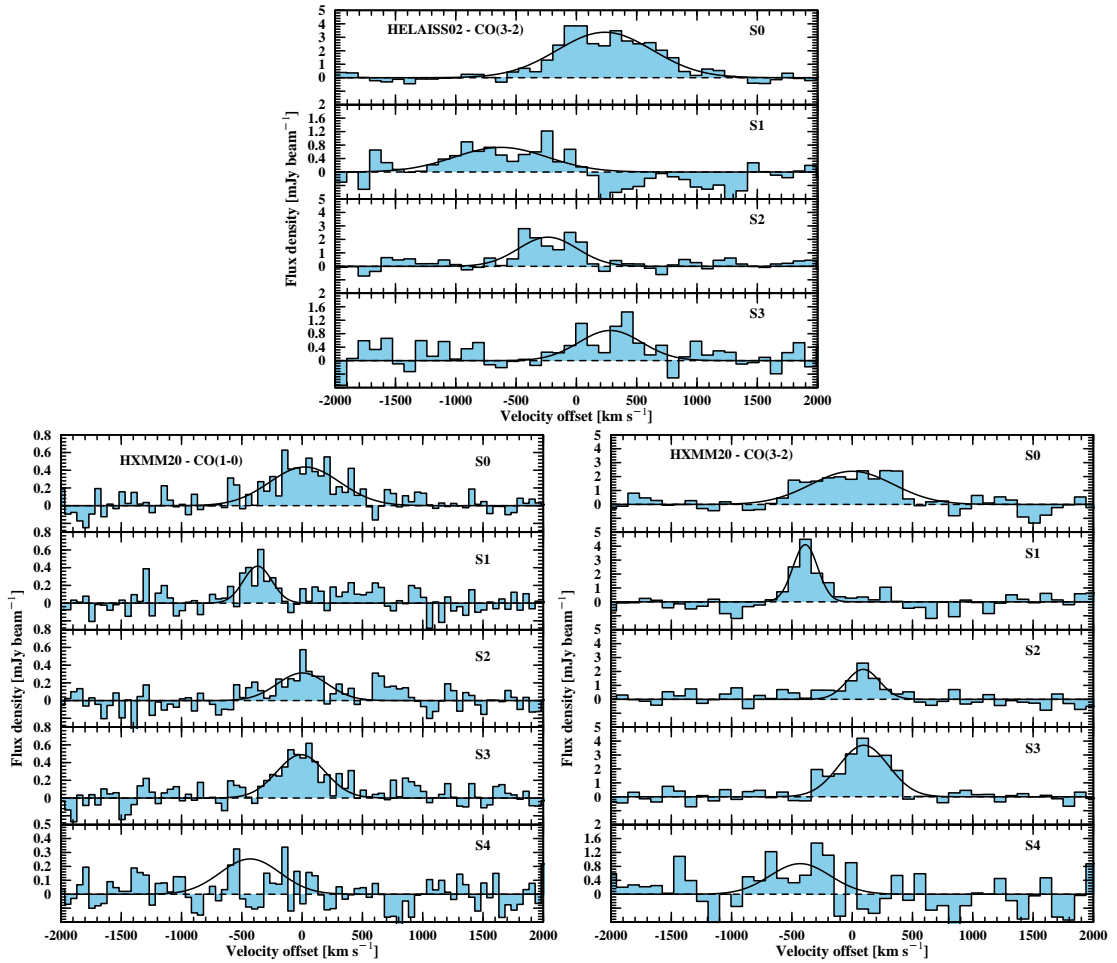


Figure 3.4: HELAISS02 CO(3-2), HXMM20 CO(3-2), and CO(1-0) spectra of the $870 \mu\text{m}$ continuum sources reported in [Bussmann et al. \(2015\)](#). The spectra are ordered according to that nomenclature. Velocity offset for each protocluster core is centered at the median redshift of their sources given by the CO(3-2) transition.

sources in an aperture enclosing all of them and, thus, we are not double-counting flux (as done for HXMM20 in Section 3.3.2).

All the [Bussmann et al. \(2015\)](#) sources were securely detected, except for S3, which was only tentatively detected containing potential sidelobe residuals and a symmetric negative peak in the adjacent line channels. S3 is known for displaying prominent stellar, $870 \mu\text{m}$, and 1.4 GHz continuum emission, hosting a radio loud AGN ([Wang et al. 2016](#); [Daddi et al. 2017](#)). In the case of the sources from [Wang et al. \(2016\)](#) and [Wang et al. \(2018\)](#) we detected the same sources except for those with the IDs 132044 and 131661, at which position we did not retrieve significant emission at $S/N > 2$. Note that we also report S6, additional IRAC counterpart next to S0, and also S8 and S12, both of which have IRAC counterparts, but detected at $S/N < 3$ and also showing possible sidelobe residuals, which we classify as tentative. The blind search arose a tentative detection

3.3. CONFIRMATION OF PROTOCLUSTER CORES

for an extra source namely S13 and an extra secure source namely S14 part of the structure encompassing a larger redshift range (Diener et al. 2013, 2015; Chiang et al. 2015; Casey et al. 2015; Lee et al. 2016; Cucciati et al. 2018). Note that the sources with IDs 132617 and 129444 in Wang et al. (2016) and Wang et al. (2018) were not covered by our FOV that stops at 10% of the sensitivity at the phase center.

All the tentative sources with $S/N < 4$ and affected by potential sidelobe contamination need further observations to be securely confirmed.

Additionally, our CARMA program searched for CO(3-2) and our NOEMA program targeted CO(4-3) (see Section 3.2.4). S0 and S2 are detected in CO(3-2) and S0, S1, and S2 in CO(4-3). Note that the beam size is larger in these observations than in VLA, especially in the case of CARMA. Therefore, CO(3-2) and CO(4-3) could come from several or different neighboring sources. The case of S2 is particularly clear, since CO(3-2) and CO(4-3) line detections are offset in velocity from that of CO(1-0), but also the spatial location of the CO(3-2) and CO(4-3) emissions point towards a contribution from S7, which CO(1-0) is slightly broader and offset from that of S2. The line ratios are unphysical when considering that the CO(3-2) and CO(4-3) are associated to a single source. However, they become physical when adding up the CO(1-0) contribution from S5 and S6 to S0 and the CO(1-0) contribution from S7 to S2.

33 GHz continuum emission was detected at $S/N > 3$ slightly offset from S0, S2 and S4 (see Figure 3.2).

Table 3.4: H COSMOS02 CO(1-0) Line Measurements

Name ^a	Other Name ^b	α (J2000) ^a (h:m:s)	δ (J2000) ^a (°:':")	$v_{0, \text{CO}(1-0)}$ ^c (km s ⁻¹)	$dv_{\text{CO}(1-0)}$ (km s ⁻¹)	$S_{\text{CO}(1-0)}$ (mJy beam ⁻¹)	$I_{\text{CO}(1-0)}$ (Jy km s ⁻¹)	$S/N_{\text{CO}(1-0)}$	$\log L'_{\text{CO}(1-0)}$ (K km s ⁻¹ pc ⁻²)
H COSMOS02	CL J1001+0220	10 00 57.18	+02 20 12.70	2.504 ± 0.005					
S0	131077	10 00 56.95	+02 20 17.35	-833 ± 26	534 ± 61	0.167 ± 0.017	0.105 ± 0.007	15.7	10.48 ± 0.03
S1	130891	10 00 57.57	+02 20 11.26	748 ± 27	404 ± 63	0.122 ± 0.016	0.129 ± 0.013	6.93	10.58 ± 0.04
S2	130949	10 00 56.86	+02 20 08.93	-74 ± 24	358 ± 57	0.131 ± 0.018	0.032 ± 0.006	10.29	9.97 ± 0.08
S3*	130933	10 00 57.27	+02 20 12.66	-230 ± 170	830 ± 390	0.025 ± 0.010	0.022 ± 0.014	3.85*	9.81 ± 0.28
S4	130901	10 00 57.40	+02 20 10.83	384 ± 86	860 ± 210	0.058 ± 0.012	0.065 ± 0.014	5.13	10.28 ± 0.09
S5*	131079	10 00 56.88	+02 20 14.93	-874 ± 64	630 ± 150	0.051 ± 0.011	0.034 ± 0.011	2.37*	9.99 ± 0.14
S6	...	10 00 57.06	+02 20 18.40	-863 ± 30	519 ± 71	0.121 ± 0.014	0.078 ± 0.006	8.74	10.35 ± 0.03
S7	130842	10 00 56.90	+02 20 09.70	-34 ± 26	479 ± 61	0.139 ± 0.015	0.073 ± 0.007	8.98	10.33 ± 0.04
S8*	...	10 00 56.70	+02 20 05.20	0 ± 43	370 ± 100	0.063 ± 0.015	0.025 ± 0.009	2.22*	9.86 ± 0.16
S9	no-ID	10 00 56.32	+02 20 11.50	8 ± 61	700 ± 140	0.063 ± 0.011	0.046 ± 0.013	5.27	10.13 ± 0.12
S10*	132044	10 00 56.76	+02 20 55.72	271 ± 46	310 ± 110	0.117 ± 0.035	0.039 ± 0.018	2.59*	10.06 ± 0.20
S11	130359	10 00 54.96	+02 19 48.10	284 ± 27	234 ± 63	0.192 ± 0.044	0.048 ± 0.017	4.26	10.15 ± 0.15
S12*	...	10 00 57.38	+02 20 06.40	706 ± 96	720 ± 230	0.040 ± 0.011	0.031 ± 0.013	2.57*	9.96 ± 0.18
H COSMOS02 -									
OTHER									
S13*	...	10 00 57.84	+02 19 47.80	-7428 ± 12	105 ± 27	0.414 ± 0.094	0.046 ± 0.016	3.00*	...
S14	...	10 00 59.66	+02 19 52.90	-3029 ± 74	630 ± 170	0.119 ± 0.029	0.080 ± 0.030	4.66	...

^a Source names and coordinates correspond to those originally reported in [Busmann et al. \(2015\)](#) for S0 to S4. The rest of sources are named subsequently with increasing velocity and their coordinates correspond to the position where the spectrum was extracted as explained in Section 3.3.3. ^b From [Wang et al. \(2016\)](#). ^c Velocity offset is centered at the median redshift of sources. * Tentative detection.

Table 3.5: HCOSMOS02 CO(3-2) and CO(4-3) Line Measurements

Name	$v_{0, \text{CO}(3-2)}^a$ (km s^{-1})	$v_{0, \text{CO}(4-3)}^a$ (km s^{-1})	$\text{dv}_{\text{CO}(3-2)}$ (km s^{-1})	$\text{dv}_{\text{CO}(4-3)}$ (km s^{-1})	$S_{\text{CO}(3-2)}$ (mJy beam^{-1})	$S_{\text{CO}(4-3)}$ (mJy beam^{-1})	$I_{\text{CO}(3-2)}$ (Jy km s^{-1})	$I_{\text{CO}(4-3)}$ (Jy km s^{-1})	$S/N_{\text{CO}(3-2)}$	$S/N_{\text{CO}(4-3)}$	$\log L_{\text{CO}(3-2)}$ ($\text{K km s}^{-1} \text{pc}^{-2}$)	$\log L_{\text{CO}(4-3)}$ ($\text{K km s}^{-1} \text{pc}^{-2}$)	r_{31}	r_{41}
HCOSMOS02														
S0	-923 ± 41	-828 ± 77	442 ± 98	710 ± 180	3.84 ± 0.72	3.56 ± 0.80	1.70 ± 0.31	2.51 ± 0.57	5.48	4.40	10.74 ± 0.08	10.66 ± 0.10	$1.18 \pm 0.24^*$	$0.97 \pm 0.23^*$
S1	...	810 ± 50	...	400 ± 120	...	4.6 ± 1.2	...	1.84 ± 0.30	...	6.13	...	10.53 ± 0.07	...	0.89 ± 0.17
S2	149 ± 31	87 ± 31	225 ± 73	181 ± 74	3.7 ± 1.0	4.6 ± 1.6	0.84 ± 0.25	0.83 ± 0.19	3.36	4.37	10.44 ± 0.13	10.18 ± 0.10	$0.86 \pm 0.26^*$	$0.48 \pm 0.12^*$

^a Velocity offset is centered at the median redshift as quoted in Table 3.4. * CO(1-0) contribution from S5 and S6 added up to S0 and CO(1-0) contribution from S7 added up to S2.

3.4 Gas, Dust and Stellar Properties

In this section we derive the gas, dust and stellar properties of the confirmed new protoclusters cores HELAISS02 and HXMM20. Particularly, we calculated the molecular gas masses, infrared luminosities, star formation rates, and stellar masses. Note that in the case of HCOSMOS02 these properties have been well studied in Wang et al. (2016) and Wang et al. (2018); therefore, we use the values obtained in those works, with updated molecular gas masses based on our CO observations. We compared our CO(1-0) line luminosity values with those in Wang et al. (2018). The median of the relative difference between the two estimates is $\sim 7\%$ and, thus, we argue that there are no systematics between the two works. Individually, the estimates are in good agreement within a factor of two (for the comparison we added up S6 to S0 to be compared with 131077 in Wang et al. (2018) and added up S8 to S2 to be compared with 130949 in Wang et al. (2018)).

3.4.1 CO-based Estimates of M_{H_2}

One of the most commonly used methods to derive the molecular gas mass (M_{H_2}) is by measuring the CO(1-0) line luminosity ($L'_{\text{CO}(1-0)}$) and assuming an α_{CO} conversion factor that relates them through $M_{\text{H}_2} = \alpha_{\text{CO}} L'_{\text{CO}(1-0)}$, α_{CO} depends on metallicity and likely on the mode of star formation. In the absence of direct gas-phase metallicities and since the majority of our targets are massive ($M_* > 10^{10} M_{\odot}$, Table 3.6), we assumed a solar metallicity for all sources. Then, we adopted $\alpha_{\text{CO}} = 3.5$ as reported in Magdis et al. (2017) for normal SFGs at solar metallicity, calculated as an average value from $\alpha_{\text{CO}}-Z$ relations in the literature (Leroy et al. 2011; Genzel et al. 2012; Magdis et al. 2012). In the case of HELAISS02 we also converted the CO(3-2) measurements into a CO(1-0) line luminosity. For this conversion we used the line ratio $r_{31} = 0.69 \pm 0.09$ derived for HXMM20 from our data (see Table 3.3), assuming that the sample selection criteria are leading to a similar excitation. The $M_{\text{H}_2}^{\text{CO}}$ results are collected in Table 3.6.

3.4.2 FIR Properties

The available photometry from mid-IR to sub-millimeter can be fitted to derive the dust mass (M_{dust}) and infrared luminosity (L_{IR}) estimates of the different ALMA 870 μm continuum sources of each protocluster core. We acquired *Spitzer*/MIPS 24 μm measurements using the images publicly available from the *Spitzer* Wide-area Infrared Extragalactic Survey (SWIRE; Lonsdale et al. 2003) in the ELAIS-S1 and XMM-LSS fields, where our protocluster cores are located. Since the sources are blended, following Gómez-Guijarro et al. (2018), we got the fluxes by fitting a PSF model using GALFIT (Peng et al. 2002). We required at least a 5σ detection to perform the fit. The number of PSFs and the PSFs centroids were set to the number and positions of the 870 μm

3.4. GAS, DUST AND STELLAR PROPERTIES

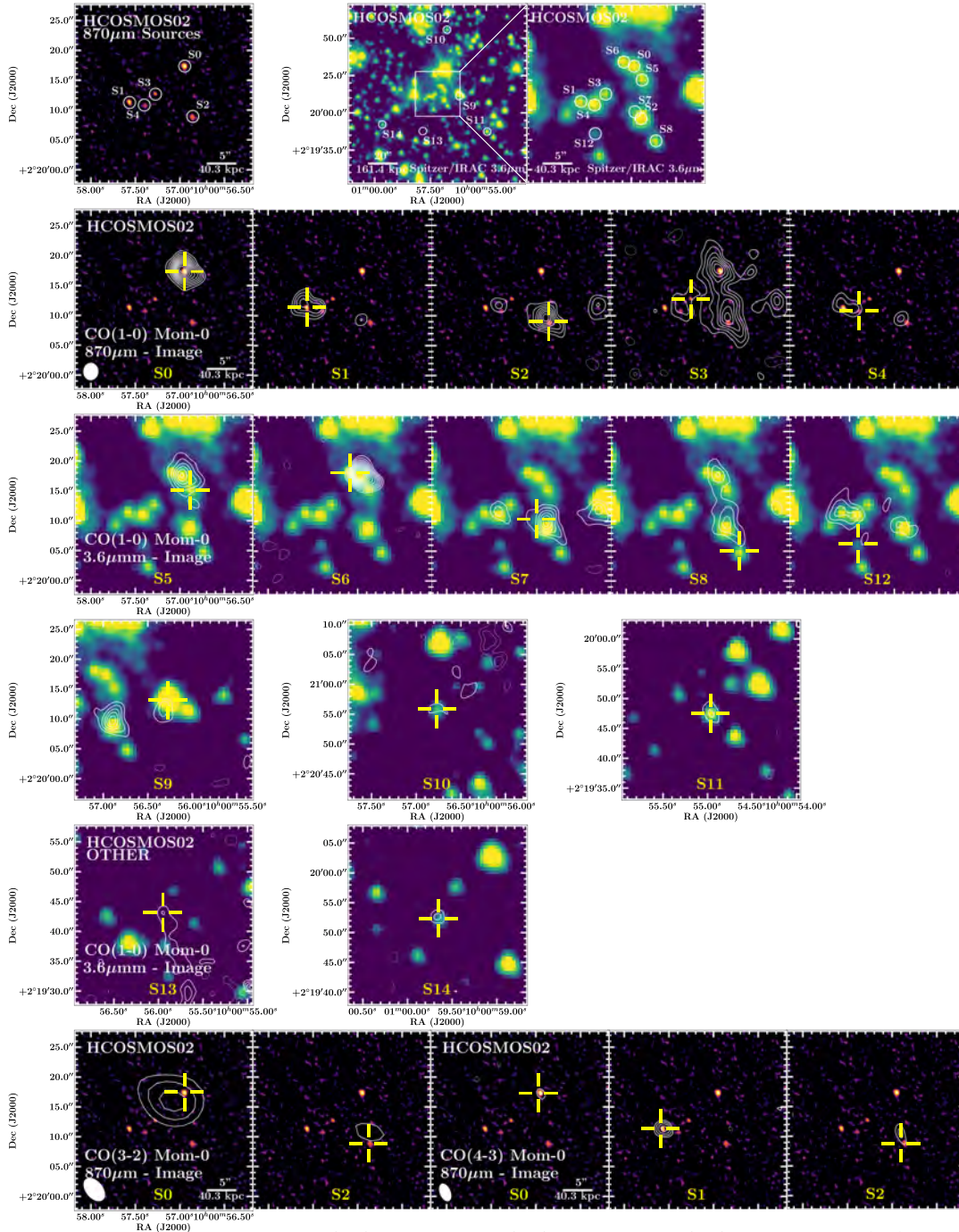


Figure 3.5: HCOSMOS02 moment-0 maps. First row: Overview of the sources. Second row: CO(1-0) moment-0 maps of the $870\ \mu\text{m}$ continuum sources in [Bussmann et al. \(2015\)](#) represented as contours on top of the $870\ \mu\text{m}$ continuum image. Third row: CO(1-0) moment-0 maps of the detections in the $30'' \times 30''$ central region on top of the IRAC $3.6\ \mu\text{m}$ image. Fourth row: CO(1-0) moment-0 maps of the detections outside the $30'' \times 30''$ central region. Fifth row: Moment-0 maps of the line detections outside the $30'' \times 30''$ central region not part of the HCOSMOS02 structure. Sixth row: CO(3-2) from CARMA and CO(4-3) from NOEMA moment-0 maps of the detected $870\ \mu\text{m}$ continuum sources. The source to which each panel refers to is marked with a yellow cross (note that sources spanning a similar velocity range appear also in the panel by construction of a moment-0 map). Contours start at $\pm 3\sigma$ and grow in steps of $\pm 1\sigma$, except for CO(1-0) S3, S5, S8, S10, S12 and S13 that start at $\pm 2\sigma$. Positive contours are solid and negative contours dotted.

3. EXPLORING THE ORIGINS OF GALAXY CLUSTERS

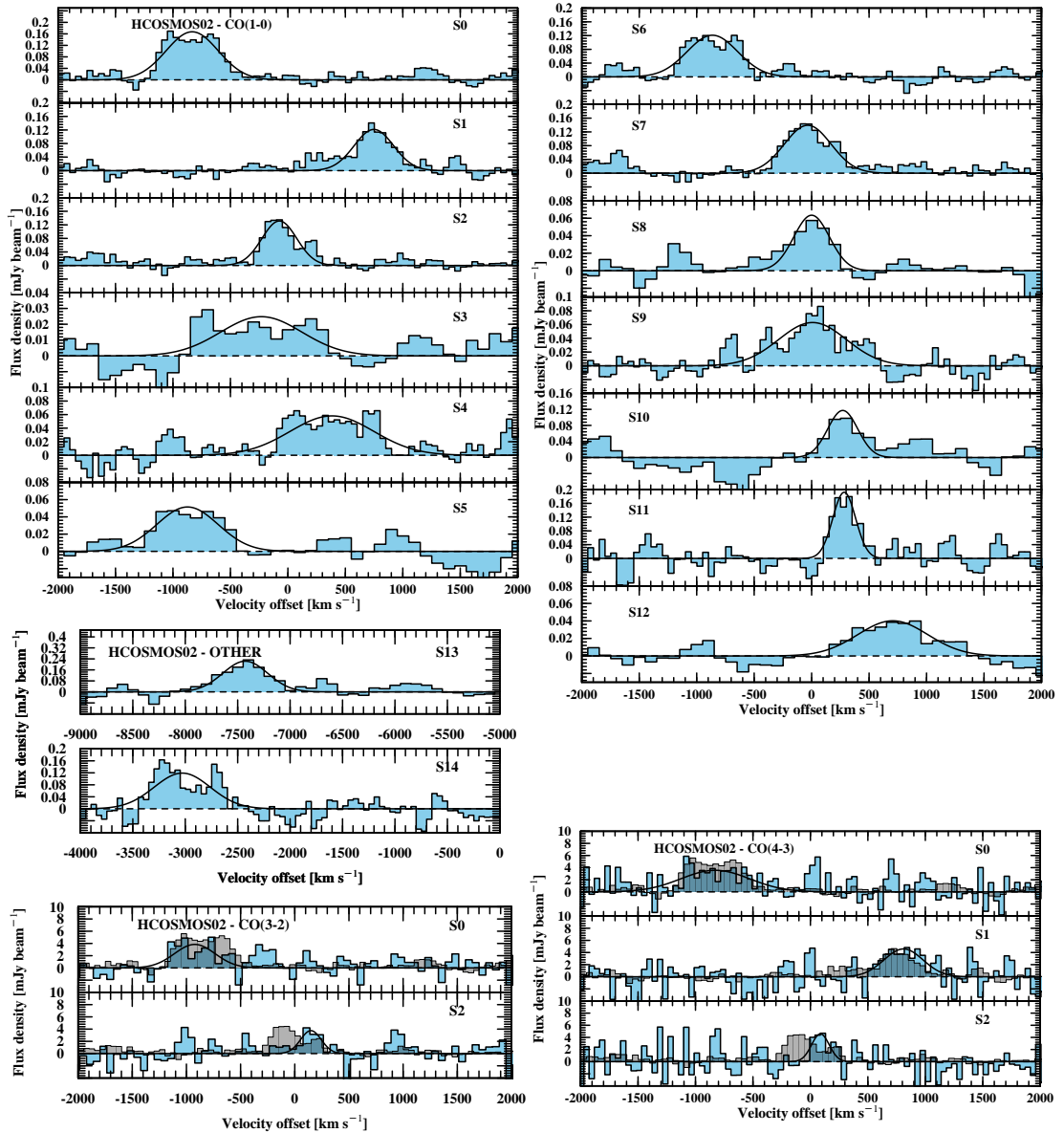


Figure 3.6: HCOSMOS02 CO(1-0), CO(3-2), and CO(4-3) spectra. Source names are those originally reported in [Bussmann et al. \(2015\)](#) for S0 to S4. The rest are named subsequently with increasing velocity. The spectra are ordered according to the nomenclature. Velocity offset is centered at the median redshift of the sources given by the CO(1-0) transition. Scaled CO(1-0) spectra are overlaid on top of the CO(3-2) and CO(4-3) in gray.

continuum sources, allowing a shift in both the X and Y < 1 pixel from the initial positions. The sources are not detected in *Spitzer*/MIPS 70 μm or *Herschel*/PACS 100 and 160 μm imaging. In the case of *Herschel*/SPIRE 250, 350, and 500 μm we scaled the total fluxes presented in [Bussmann et al. \(2015\)](#) using the ratio of the 870 μm fluxes of each ALMA continuum source by the total 870 μm flux also presented in [Bussmann et al. \(2015\)](#). Finally, we employed 3 mm fluxes presented in Table 3.1.

We fitted the mid-IR to sub-millimeter spectral energy distribution (SED) with the [Draine & Li \(2007\)](#) models (DL07). The methodology has been presented in detail in various previous studies (e.g., [Magdis et al. 2012](#); [Berta et al. 2016](#)). In brief, DL07 models describe the mid-IR to sub-millimeter spectrum of a galaxy by a linear combination of two dust components, one arising from dust in the diffuse interstellar medium (ISM), heated by a minimum radiation field U_{\min} ("diffuse ISM" component) and the other from dust heated by a power-law distribution of starlight, $dM/dU \propto U^{-\alpha}$ extending from U_{\min} to U_{\max} , associated with the intense photodissociation regions (PDRs, "PDR" component). The relative contribution of the two components is quantified by the parameter γ that yields the fraction of the dust exposed to starlight with intensities ranging from U_{\min} to U_{\max} . Finally, the properties of the grains in the dust models are parameterized by the polycyclic aromatic hydrocarbon (PAH) index, q_{PAH} , defined as the fraction of the dust mass in the form of PAH grains. Each observed SED is fitted with a wide range of models generated by combinations of different set of parameters. For our case we considered models with $q_{\text{PAH}} = 0.4\text{--}4.6\%$, $U_{\min} = 0.7\text{--}25$, $\gamma = 0.0\text{--}0.8$, while following [Draine et al. \(2007\)](#), we fixed $U_{\max} = 10^6$, and $\alpha = 2$. The best fit were derived through χ^2 minimization yielding to M_{dust} , U_{\min} , γ and q_{PAH} estimates. L_{IR} was calculated by integrating the best fit to the SED in the range 8–1000 μm . To estimate the uncertainties of the parameters we created 1000 realizations of the observed SEDs by perturbing the photometry within the errors and repeating the fit. The corresponding uncertainties are defined by the standard deviation of the distribution of the derived quantities. The L_{IR} and M_{dust} estimates along with their uncertainties are listed in Table 3.6, where SFR_{IR} estimates were obtained using the L_{IR} to SFR_{IR} conversion from [Kennicutt \(1998\)](#) for a Chabrier IMF. In Figure 3.7 we present the observed SEDs along with best fit models as derived from our analysis.

3.4.3 Dust-based Estimates of M_{H_2}

A very efficient way to determine the molecular gas reservoir of the galaxies is through their dust emission, either using the metallicity-dependent gas-to-dust mass ratio technique (δ_{GD}) (e.g., [Magdis et al. 2012](#); [Berta et al. 2016](#)), which converts the M_{dust} estimates to M_{gas} through the well established, almost linear, gas-to-dust mass ratio vs gas-phase metallicity relation ($M_{\text{gas}}/M_{\text{dust}} - Z$); or through the single band measurement of the dust emission flux on the Rayleigh-Jeans (R-J) side of the SED (e.g., [Scoville et al. 2014](#); [Groves et al. 2015](#); [Schinnerer et al. 2016](#)). Here, and thanks to the detailed coverage of the IR part of the spectrum of our objects, including the R-J tail of the SED, we are in position to use both techniques. We refer to these estimates as $M_{\text{gas}}^{\text{GD}}$ and $M_{\text{gas}}^{\text{RJ}}$, respectively.

First, we converted the M_{dust} estimates, derived as described in the previous section, to M_{gas} by adopting the $M_{\text{gas}}/M_{\text{dust}} - Z$ relation of [Magdis et al. \(2012\)](#) ($\log(M_{\text{dust}}/M_{\text{gas}}) = (10.54 \pm$

3. EXPLORING THE ORIGINS OF GALAXY CLUSTERS

$1.0) - (0.99 \pm 0.12) \times (12 + \log(O/H))$), where the metallicity is calibrated using the [Pettini & Pagel \(2004\)](#) scale. We assumed a solar metallicity for all sources that corresponds to a $M_{\text{gas}}/M_{\text{dust}} \sim 90$. The corresponding uncertainties take into quadrature the uncertainties in M_{dust} and adopting a 0.2 dex uncertainty in Z . Similarly, we converted the ALMA 3 mm (rest-frame $\sim 950 \mu\text{m}$ for HELAISS02 and $\sim 830 \mu\text{m}$ for HXMM20) flux densities of each source (except for HXMM20-S2, S3 and S4 that are not detected at 3 mm) to M_{gas} through the equation 12 of [Scoville et al. \(2014\)](#). The M_{gas} estimates derived by the two approaches are in excellent agreement, compatible within the uncertainties, with an average ratio of 1.24 ± 0.23 . This is not surprising given the implicit assumption of solar gas-phase metallicity in both approaches. The values are summarized in [Table 3.6](#). Finally, we note that these estimates yield the total gas budget of the galaxies, including contributions from the molecular (M_{H_2}) and the atomic phase (M_{H_I}). However, assuming that for high-redshift relatively massive galaxies the molecular gas dominates over the atomic gas within the physical scale probed by the dust continuum observations, $M_{\text{H}_2} \gg M_{\text{H}_\text{I}}$ (e.g., [Blitz & Rosolowsky 2006](#); [Bigiel et al. 2008](#); [Obreschkow et al. 2009](#); [Tacconi et al. 2010](#); [Daddi et al. 2010a](#); [Geach et al. 2011](#)), we can then write $M_{\text{gas}} = M_{\text{H}_2} + M_{\text{H}_\text{I}} \approx M_{\text{H}_2}$.

The CO-independent M_{H_2} estimates derived using the two dust-based methods allow us to explore the α_{CO} conversion factor of the different sources in each protocluster core (see [Bolatto et al. 2013](#), for a review). [Papadopoulos et al. \(2012b,a\)](#) concluded that α_{CO} is affected by gas density and temperature, but mostly by the overall dynamical state of the gas. High values are related with self-gravitating gas clouds, such as those found in local star-forming disks like the Milky Way (MW) (e.g., $\alpha_{\text{CO}} = 4.3 \text{ K km s}^{-1} \text{ pc}^{-2}$ [Strong & Mattox 1996](#); [Dame et al. 2001](#); [Abdo et al. 2010](#)). Low values are associated to gravitationally unbound gas, such as disturbed gas in local major mergers (e.g., $\alpha_{\text{CO}} = 0.8 \text{ K km s}^{-1} \text{ pc}^{-2}$ [Solomon et al. 1997](#); [Downes & Solomon 1998](#); [Tacconi et al. 2008](#)). We employed $M_{\text{H}_2}^{\text{GD}}$, that could be derived for all sources, to calculate α_{CO} . Our results in [Table 3.6](#) show that HELAISS02 sources have a high α_{CO} , while HXMM20 sources have a lower α_{CO} . The integrated measurement for HELAISS02 displays a high $\alpha_{\text{CO}} = 4.6 \pm 2.4$ consistent with those of MW-like disks, while the lower HXMM20 $\alpha_{\text{CO}} = 1.8 \pm 0.9$ resembles better those found in mergers. Although the uncertainties are large, it is also worth noting that the lowest α_{CO} are associated with the blended sources in HXMM20 (S0, S2 and S3), while the highest α_{CO} are related with HELAISS02, where all the sources are well separated from each other, and HXMM20-S1 with a large distance to another neighboring source (with the exception of HXMM-S4, but which CO(1-0) flux is poorly constrained). This agrees with the interpretation of the overall dynamical state of the gas being the major contributor to α_{CO} , with disturbed gas associated with lower α_{CO} , which is likely the case of the blended sources of HXMM20, and bound gas linked to higher α_{CO} , likely the case of the more isolated sources.

3.4.4 Stellar Masses

The ELAIS-S1 and XMM-LSS fields, where HELAISS02 and HXMM20 are respectively located, are covered by optical/IR data sets publicly available suitable to determine the stellar masses of the different optical/near-IR counterparts associated to the ALMA 870 μm continuum counterparts through SED fitting.

We employed optical/near-IR data from the VISTA Deep Extragalactic Observations (VIDEO; [Jarvis et al. 2013](#)) survey in the z , y , J , H , and K_s bands; and mid-IR coverage from the *Spitzer* Extragalactic Representative Volume Survey (SERVS; [Mauduit et al. 2012](#)) at 3.6 and 4.5 μm , and from the *Spitzer* Wide-area Infrared Extragalactic Survey (SWIRE; [Lonsdale et al. 2003](#)) at 5.8 and 8.0 μm .

The photometry was measured following the procedure described in [Gómez-Guijarro et al. \(2018\)](#) for crowded and blended objects. Briefly, from the z to the K_s bands we performed aperture photometry. The number of apertures is set to the number of 870 μm continuum sources. We excluded HXMM20-S3 because it is not clearly detected, being too faint and too close to HXMM20-S0 and HXMM20-S2 to disentangle its individual contribution. Therefore, we did not derive a stellar mass for this source. The apertures were selected in the K_s band as large as possible (typically 2" diameter) without overlapping with neighboring apertures. We applied aperture corrections for every band by deriving the growth curve of a PSF in the different bands and computing the correction factor to the fluxes to account for the missing flux outside the aperture. The flux uncertainties were derived from empty aperture measurements. We only use detections above 3σ to guarantee a good SED fit (upper limits are included in Figure 3.7). In the case of *Spitzer*/IRAC 3.6 and 4.5 μm data the sources appear blended. In this case, the fluxes were calculated from PSF fitting with GALFIT as explained in Section 3.4.2 for the *Spitzer*/MIPS 24 μm images. The 5σ detection criterion to perform the PSF fit was reached for all sources in the 3.6 and 4.5 μm bands, but not in the 5.8 and 8.0 μm and, thus, these bands were not included in the SED fit (upper limits are shown in Figure 3.7). The number of PSFs was again set to the number of 870 μm continuum sources and the PSFs centroids were placed at the positions of K_s band centroids used as priors, allowing a shift in both the X and Y < 1 pixel from the initial positions. To account the uncertainty in the photometry due to the deblending we performed a number of realizations varying the centroid coordinates randomly within 1 pixel of the best-fit centroid and fixing those coordinates for each realization.

We fitted the resulting SEDs using the code LePHARE ([Arnouts et al. 1999](#); [Ilbert et al. 2006](#)) adopting [Bruzual & Charlot \(2003\)](#) stellar population synthesis models with emission lines to account for nebular line contamination in the broad bands. We assumed a [Chabrier \(2003\)](#) IMF, exponentially declining star formation histories (SFHs) and a [Calzetti et al. \(2000\)](#) dust law. The parameter grid employed ranges SFH e-folding times 0.1 Gyr–30 Gyr, extinction $0 < A_V < 5$,

3. EXPLORING THE ORIGINS OF GALAXY CLUSTERS

stellar age 1 Myr–age of the universe at the source redshift and metallicity $Z = 0.004, 0.008$ and 0.02 (i.e., solar). The redshift was fixed to the derived CO(3-2) spectroscopic redshifts for each source (see Tables 3.2 and 3.3). The derived SEDs are shown in Figure 3.7 and the stellar masses in Table 3.6. Additionally, we explored whether the output stellar extinction A_V correlates with M_{dust} derived in Section 3.4.2. We found no correlation between them. Some studies have shown that these two quantities could be linked to different stellar populations and depend differently on the viewing angle and on the geometry of the dust distribution (e.g., Safarzadeh et al. 2017; Faisst et al. 2017b; Popping et al. 2017a; Narayanan et al. 2018; Gómez-Guijarro et al. 2018). The plausible different physical origin of the stellar and dust continuum light justifies the use of two different SED fitting techniques, one for the optical/near-IR SED and another one for the FIR SED, as opposed to employing an energy balanced solution that implies a direct relation between stars and dust.

With both the molecular gas and stellar masses we calculated the molecular gas fraction defined as $f_{\text{H}_2} = M_{\text{H}_2}/(M_* + M_{\text{H}_2})$. The values are also presented in Table 3.6.

Table 3.6: HELAISS02 and HXMM20 Gas, Dust and Stellar Properties

Name	$\log(M_{\text{H}_2}^{\text{CO}}/M_{\odot})$	$\log(M_{\text{H}_2}^{\text{GD}}/M_{\odot})$	$\log(M_{\text{H}_2}^{\text{RJ}}/M_{\odot})$	$\log(L_{\text{IR}}/L_{\odot})$	$\log(M_{\text{dust}}/M_{\odot})$	α_{CO} ($M_{\odot} \text{ K}^{-1} \text{ km}^{-1} \text{ s pc}^{-2}$)	SFR _{IR} ($M_{\odot} \text{ yr}^{-1}$)	$\log(M_{*}/M_{\odot})$	f_{H_2}
HELAISS02	11.81 ± 0.04	11.93 ± 0.22	11.82 ± 0.04	13.18 ± 0.05	9.96 ± 0.09	4.6 ± 2.4	1510 ± 170	$11.49^{+0.06}_{-0.05}$	0.68 ± 0.11
S0	11.61 ± 0.04	11.60 ± 0.23	11.45 ± 0.05	12.88 ± 0.07	9.64 ± 0.12	3.5 ± 1.9	760 ± 120	$10.48^{+0.16}_{-0.11}$	0.93 ± 0.02
S1	10.83 ± 0.09	11.27 ± 0.24	11.15 ± 0.10	12.43 ± 0.06	9.30 ± 0.12	9.7 ± 5.7	269 ± 37	$11.06^{+0.09}_{-0.11}$	0.37 ± 0.07
S2	11.07 ± 0.05	11.27 ± 0.23	11.06 ± 0.11	12.48 ± 0.07	9.30 ± 0.11	5.6 ± 3.0	302 ± 49	$11.17^{+0.08}_{-0.10}$	0.44 ± 0.05
S3	10.82 ± 0.09	11.10 ± 0.23	11.07 ± 0.12	12.30 ± 0.07	9.13 ± 0.11	6.7 ± 3.8	200 ± 32	$10.13^{+0.09}_{-0.14}$	0.83 ± 0.04
HXMM20	12.04 ± 0.04	11.75 ± 0.22	11.64 ± 0.07	13.23 ± 0.05	9.79 ± 0.09	1.8 ± 0.9	1700 ± 200	$10.81^{+0.19}_{-0.15}$	0.94 ± 0.04
S0	11.54 ± 0.07	11.46 ± 0.24	11.47 ± 0.07	12.82 ± 0.06	9.50 ± 0.14	2.9 ± 1.7	661 ± 91	$9.88^{+0.05}_{-0.04}$	0.98 ± 0.01
S1	11.11 ± 0.14	11.14 ± 0.23	11.17 ± 0.15	12.58 ± 0.05	9.18 ± 0.11	3.7 ± 2.3	380 ± 44	$10.12^{+0.09}_{-0.04}$	0.91 ± 0.03
S2	11.24 ± 0.14	11.08 ± 0.23	...	12.54 ± 0.06	9.12 ± 0.12	2.4 ± 1.5	347 ± 48	$10.04^{+0.14}_{-0.07}$	0.94 ± 0.03
S3	11.44 ± 0.07	10.96 ± 0.29	...	12.64 ± 0.29	8.99 ± 0.21	1.2 ± 0.8	440 ± 290
S4	11.21 ± 0.14	10.58 ± 0.24	...	12.00 ± 0.06	8.61 ± 0.13	0.8 ± 0.5	100 ± 14	$10.51^{+0.29}_{-0.31}$	0.83 ± 0.10

3.5 Discussion

3.5.1 Blends of DSFGs from Single-dish Selected Sources

HELAISS02 and HXMM20 are composed of four and five gas-rich DSFGs within a projected diameter of 125 kpc and 64 kpc, respectively. The HCOSMOS02 core comprises five gas-rich DSFGs within a projected diameter of 105 kpc. All the ALMA 870 μm continuum sources reported in [Bussmann et al. \(2015\)](#) for these three candidate protoclusters originally selected as single-dish *Herschel*/SPIRE sources turned out to be located at the same redshift as confirmed by the CO observations presented in our work. Such a high fraction of sources with small pairwise separations located at the same redshift are unexpected from both a theoretical perspective ([Hayward et al. 2013](#); [Cowley et al. 2015](#); [Muñoz Arancibia et al. 2015](#); [Hayward et al. 2018](#)) and previous high spatial resolution follow-up of longer wavelength single-dish observations. [Wardlow et al. \(2018\)](#) presented CO observations from six single-dish selected 870 μm continuum sources that appeared as blends of at least two individual sources, suggesting that 64% of these individual sources are unlikely to be physically associated.

Our results are in line with [Iverson et al. \(2013\)](#), that confirmed four ALMA 870 μm continuum sources across a ~ 100 kpc region at $z \sim 2.41$ through CO(4-3) and CO(1-0) observations in a *Herschel*/SPIRE-selected hyperluminous infrared galaxy. In addition, recent discoveries of $z > 4$ protoclusters with associated DSFGs resemble the result presented in our work. [Oteo et al. \(2018\)](#) discovered a protocluster of at least 10 DSFGs at $z \sim 4.002$, confirmed through [C I] and high-J CO transitions, located within a 260 kpc \times 310 kpc region. [Miller et al. \(2018\)](#) discovered a protocluster at $z \sim 4.31$ of at least 14 gas-rich sources within a projected diameter of 130 kpc, confirmed from [C II], with eight of them also detected in CO(4-3) and 12 in 1 mm continuum.

3.5.2 Gas Fractions and Star Formation Efficiencies

At $z \sim 1.5$ – 2.5 several works have studied the molecular gas content, efficiency of converting gas into stars and their relation with the specific star formation rate ($\text{sSFR} = \text{SFR}/M_*$) and with field galaxies, those that do not necessarily live in an overdense environment (e.g., [Noble et al. 2017](#); [Lee et al. 2017](#); [Rudnick et al. 2017](#); [Dannerbauer et al. 2017](#); [Hayashi et al. 2018](#); [Coogan et al. 2018](#)). In this section we explore and discuss these matters regarding our sample of protoclusters cores. We employed the properties derived for HELAISS02 and HXMM20 870 μm continuum sources in Section 3.4 and those derived in [Wang et al. \(2016\)](#) and [Wang et al. \(2018\)](#) for HCOSMOS02 for its five 870 μm continuum sources, with updated molecular gas masses based in our CO observations following the method described in Section 3.4.1.

The well studied correlation between the SFR and the stellar mass of star-forming galaxies (SFGs), so-called main sequence (MS) of star formation (e.g., [Noeske et al. 2007](#); [Elbaz et al. 2007](#);

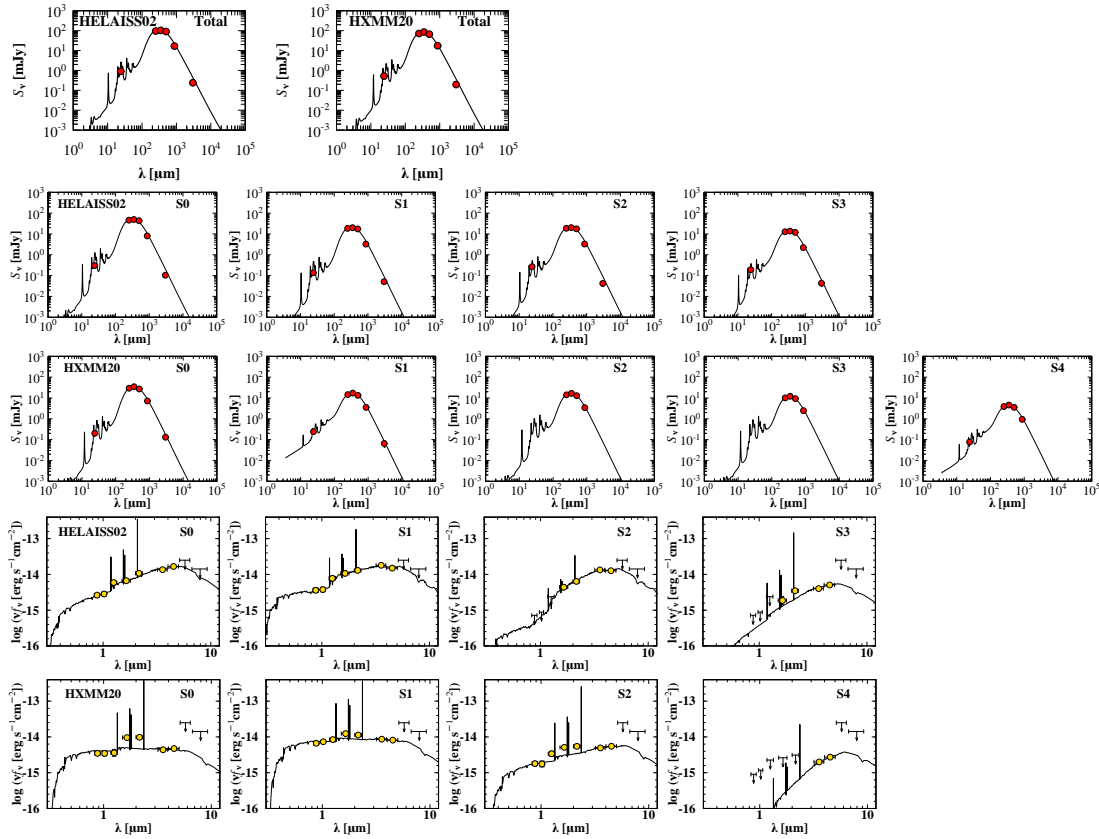


Figure 3.7: HELAISS02 and HXMM20 optical/IR and FIR SEDs. First row: HELAISS02 and HXMM20 FIR SED and best fit for the integrated values over all sources. Second row: HELAISS02 FIR SED and best fit for each $870 \mu\text{m}$ continuum source. Third row: HXMM20 FIR SED and best fit for each $870 \mu\text{m}$ continuum source. Wavelengths are in the observer-frame. Fourth row: HELAISS02 optical/IR SED and best fit for the optical/near-IR counterparts associated to each $870 \mu\text{m}$ continuum source. Fifth row: HXMM20 optical/IR SED and best fit for the optical/near-IR counterparts associated to each $870 \mu\text{m}$ continuum source. Arrows indicate 3σ upper limits (5σ for the *Spitzer* bands). Wavelengths are in the observer-frame.

Daddi et al. 2007) permits to distinguish between MS galaxies, as those located within the scatter of the MS, and starburst (SB) galaxies, outliers to the MS exhibiting an elevated sSFR compared to MS galaxies. Another correlation in SFGs arises between the observables $L'_{\text{CO}(1-0)}$ and L_{IR} and, thus, between M_{H_2} and SFR_{IR} calculated from these observables, commonly referred in the literature as the star formation law or Kennicutt-Schmidt relation (KS relation; Schmidt 1959; Kennicutt 1998, originally defined using star formation rate and gas mass surface densities). There are studies that suggest that MS and SB galaxies follow different relations between these quantities, with SB galaxies having increased star formation efficiency ($\text{SFE} = \text{SFR}/M_{\text{H}_2}$) (e.g., Daddi et al. 2010b; Genzel et al. 2010).

In Figure 3.8 we show the location of the protocluster core members in the $\text{SFR} - M_*$, $L_{\text{CO}} - L_{\text{IR}}$ and $M_{\text{H}_2} - \text{SFR}_{\text{IR}}$ planes, where M_{H_2} comes from the CO-based measurements

3. EXPLORING THE ORIGINS OF GALAXY CLUSTERS

as derived in Section 3.4.1. We can see that the integrated measurements for HELAISS02 and HXMM20 are consistent with the SB regime in $\text{SFR} - M_*$, but with the MS relation in the observables KS plane $L_{\text{CO}} - L_{\text{IR}}$. The tension is somewhat smaller in the case of HCOSMOS02, consistent with the MS scatter in $\text{SFR} - M_*$ plane. In order to explore the nature of this apparent discrepancies in Figure 3.9 we show how f_{H_2} and SFE (or depletion time-scale, $\tau_{\text{H}_2} = 1/\text{SFE}$) vary as a function of the distance to the MS (DMS), defined as the ratio of the sSFR to the sSFR of the MS at the same stellar mass and redshift ($\text{sSFR}/\text{sSFR}_{\text{MS}}$). A number of studies have revealed that the DMS scales with both f_{H_2} and SFE, with SFGs having increasing f_{H_2} and SFE (lower τ_{H_2}) as they move to higher DMS (e.g., Daddi et al. 2010b; Genzel et al. 2010; Magdis et al. 2012; Sargent et al. 2014; Genzel et al. 2015; Scoville et al. 2017b; Tacconi et al. 2018). The integrated measurements for HELAISS02, HXMM20, and HCOSMOS02 follow the expected literature trends in f_{H_2} . However, the behavior in SFE as a function of DMS is the opposite of what we know from the literature.

It is important to remember the assumptions we made when deriving M_{H_2} from CO in Section 3.4.1. The excitation conversion for HELAISS02 ($r_{31} = 0.69 \pm 0.09$) and the conversion factor $\alpha_{\text{CO}} = 3.5$. Adopting a MS-like excitation conversion $r_{31} = 0.42 \pm 0.07$ (Daddi et al. 2015) would increase the $L'_{\text{CO}(1-0)}$ measurement (and M_{H_2}) and decrease the SFE (increase τ_{H_2}) as represented by the green arrows in Figures 3.8 and 3.9. While the trend in f_{H_2} is pretty robust to a change in this assumption, HELAISS02 SFE (τ_{H_2}) would move to values similar to HXMM20 within the uncertainties. In the case of α_{CO} , the values were independently calculated for HELAISS02 and HXMM20 from M_{H_2} estimates through the δ_{GD} technique in Section 3.4.3. Wang et al. (2018) presented also individual α_{CO} values for HCOSMOS02 members. Adopting these values instead, the trend in f_{H_2} holds, but that of SFE (τ_{H_2}) is less robust (green, blue, and black arrows in Figures 3.8 and 3.9). The excitation assumption also affects the estimates of α_{CO} and the mentioned change would lower the values of HELAISS02. Another assumption that affects the α_{CO} estimates is the adoption of solar metallicity. If different from solar, we might expect that HXMM20, having lower stellar mass than HELAISS02 and HCOSMOS02, has a lower metallicity and, thus, higher α_{CO} (e.g., Genzel et al. 2012; Magdis et al. 2012; Sargent et al. 2014).

In addition to the integrated measurements, we explored the behavior of the individual $870 \mu\text{m}$ continuum sources in each protocluster core in the planes mentioned above. A caveat is the scaling assumption we used when deriving the L_{IR} and SFR_{IR} estimates for HELAISS02 and HXMM20 in Section 3.4.2. We have enough spatial resolution to get individual measurements of most of the sources in the left-hand side of the FIR SED peak through *Spitzer*/*MIPS* $24 \mu\text{m}$ and in the R-J side of the peak from ALMA $870 \mu\text{m}$ and 3 mm , but we have no constraints on the actual peak of the SED due the large beam size of *Herschel*/*SPIRE* compared to the distance between sources. Therefore, we scaled the integrated *SPIRE* fluxes to the ALMA $870 \mu\text{m}$ measurements

for the distinct individual sources. While the R-J side of the FIR SED is enough to constrain M_{gas} , from M_{dust} using the δ_{GD} technique, or through the single band measurement of the dust emission flux (see Section 3.4.3), the peak and the left-hand side are needed to constrain the overall shape of the SED and, thus, L_{IR} and SFR_{IR} . Consequently, the scaling assumption implies an almost constant SED shape that is dictated almost only based on the region sensitive to M_{dust} , varying only based on $24 \mu\text{m}$. This means an almost constant $L_{\text{IR}}/M_{\text{dust}}$ ratio and, hence, $\text{SFE} = \text{SFR}/M_{\text{H}_2} \propto L_{\text{IR}}/M_{\text{dust}} \approx \text{constant}$. The different sources or each protocluster core are by construction bound to have very similar SFE (τ_{H_2}). HCOSMOS02 $870 \mu\text{m}$ continuum sources are less affected by these caveats, since the left-hand side of the FIR SED is better constrained thanks to the *Herschel*/PACS detections (Wang et al. 2016). Additionally, the assumptions affecting the integrated measurements of the excitation conversion for HELAISS02 ($r_{31} = 0.69 \pm 0.09$) and the adopted $\alpha_{\text{CO}} = 3.5$ also applies to the individual sources.

Bearing in mind this caveats, the individual sources reproduce qualitatively the same trends of the integrated measurements. We see that our sources above the MS have higher f_{H_2} than those within the MS. Besides SFE (τ_{H_2}) seem to decrease (increase) as a function of DMS. Some of the HCOSMOS02 sources display high SFE reaching the SB regime in the observables KS plane $L_{\text{CO}} - L_{\text{IR}}$.

In summary, we see that the most massive sources of each protocluster core (HELAISS02-S1 and S2, HXMM20-S4, HCOSMOS02-S2, S3, and S4) are those located within the MS and associated with the lowest gas fraction of each protocluster core. On the other hand, the least massive sources are those located above the MS and are completely dominated by molecular gas. This is also true for the integrated values, being HXMM20 the least massive and the most gas dominated with the highest fraction of galaxies above the MS, HCOSMOS02 the most massive and the least gas dominated with the lowest fraction of galaxies above the MS, while HELAISS02 plays an intermediate role. This points towards a different evolutionary stage of the three protocluster cores. Although there could be a difference in SFE (τ_{H_2}) between the different sources as a function of DMS, our current data requires the use of assumptions that are artificially creating any trend in SFE (τ_{H_2}). Additional higher spatial resolution at the peak of the FIR SED is paramount to uncover the real SFE of HELAISS02 and HXMM20. HCOSMOS02, with less caveats, points towards a decreasing SFE with DMS.

All this suggests that the molecular gas fraction is pushing the individual sources above the MS, while maintaining a MS-like efficiency as seen for both HELAISS02 and HXMM20 in the observables $L_{\text{CO}} - L_{\text{IR}}$ plane. The latter is in agreement with Dannerbauer et al. (2017) that concludes that the SFE does not vary in dense environments compared to field galaxies. One possible explanation of why the least massive sources appear above the MS while maintaining a MS-like efficiency in forming stars could be that they are newly formed galaxies migrating to

3. EXPLORING THE ORIGINS OF GALAXY CLUSTERS

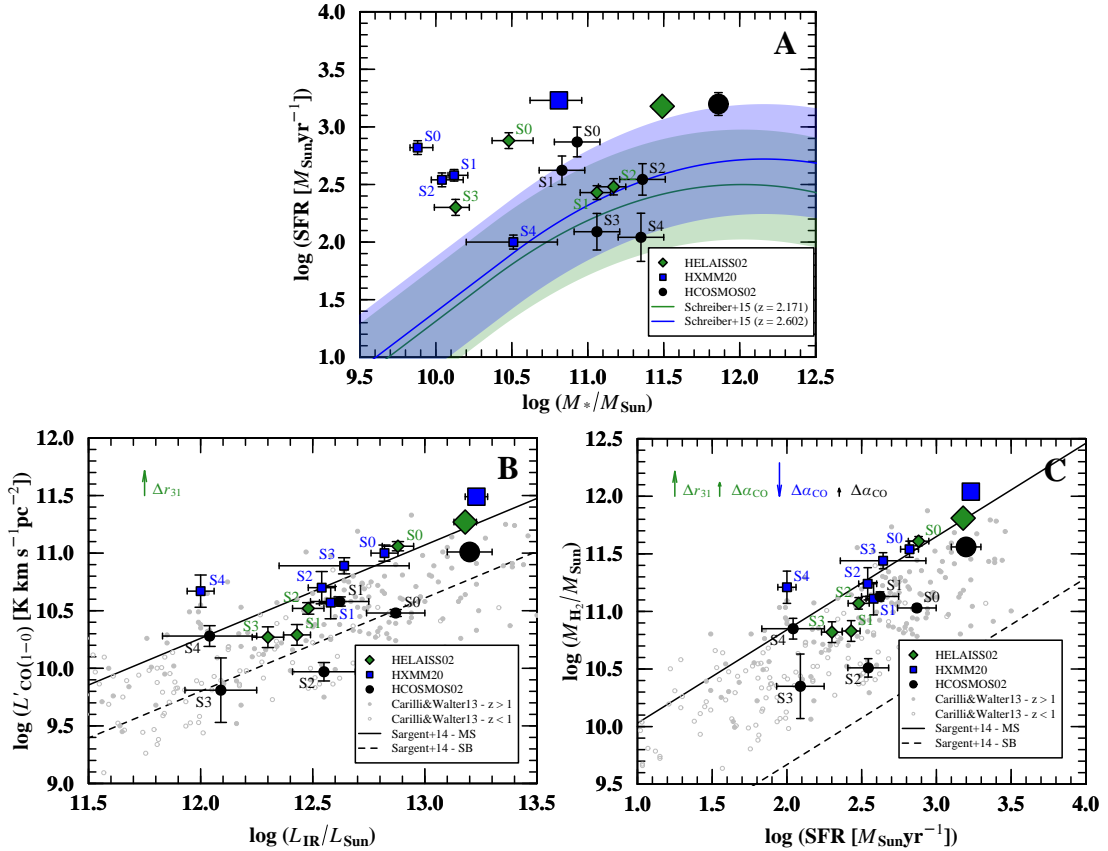


Figure 3.8: Panel A: SFR – M_* plane. The main sequence of star-forming galaxies defined by Schreiber et al. (2015) converted from Salpeter to Chabrier IMF is plotted at the highest and lowest redshifts of the sample with a 0.5 dex (3 times) scatter represented by a shadowed region. The big symbols correspond to the total values of the protoclusters. Panel B: $L_{\text{CO}} - L_{\text{IR}}$ plane. The arrows indicate the expected displacement of the total values represented with big symbols when using a MS-like excitation conversion (Δr_{31} , affecting HELAISS02). Panel C: $M_{\text{H}_2} - \text{SFR}_{\text{IR}}$ plane. The arrows indicate the expected displacement of the total values represented with big symbols when using the individual α_{CO} values ($\Delta \alpha_{\text{CO}}$). Trends for main sequence (MS, solid line) and starburst (SB, dashed line) galaxies from Sargent et al. (2014) and datapoints from Carilli & Walter (2013) are shown as reference in the B and C panels.

the MS, being the most massive sources already in place probably because they started forming earlier. For example, if the HELAISS02 and HXMM20 sources located above the MS consume half of their available molecular gas at their current SFR by $z \sim 2.00$ and $z \sim 2.37$, respectively, they will be located within the scatter of the MS.

After discussing the overall trends of the integrated and individual measurements, we compare f_{H_2} and τ_{H_2} with the gas scaling relations for field galaxies in Scoville et al. (2017b) at the same redshift, stellar mass and DMS in Table 3.7. The integrated f_{H_2} are very similar to field galaxies within the uncertainties, perhaps indicating an overall small excess for HELAISS02 and HXMM20 (1.7 and 3.0σ , respectively). The individual sources show more discrepancies, with those within the MS (HELAISS02-S1, S2, HCOSMOS02-S2, S3, and S4) having a lack of molecular gas compared to the field, especially in the case of HCOSMOS02. In terms of τ_{H_2} , the integrated measurements are

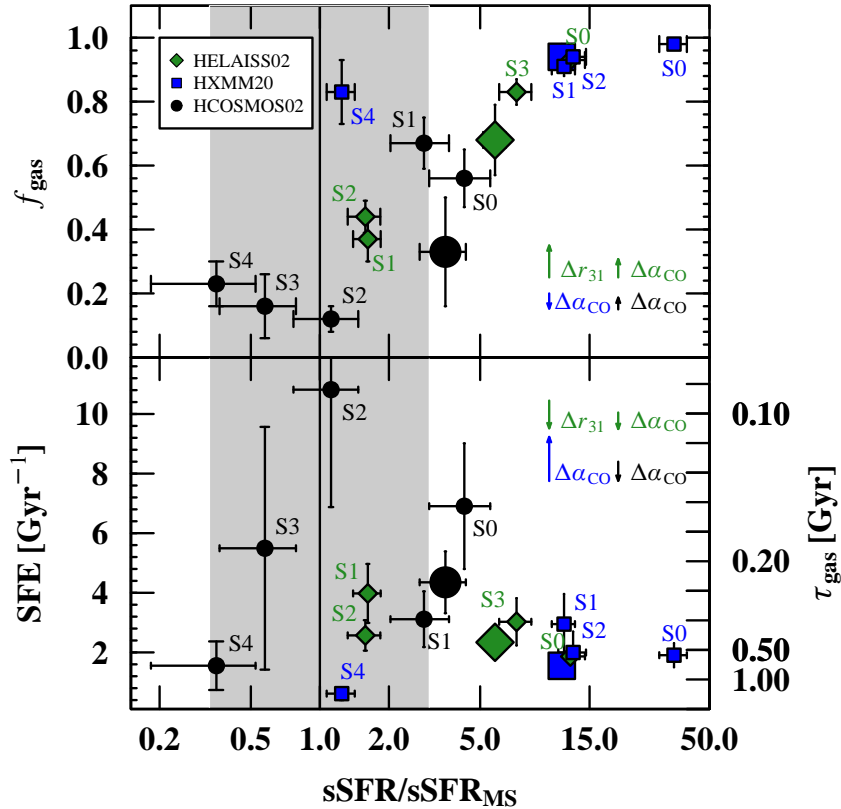


Figure 3.9: f_{H_2} (top panel), SFE and τ_{H_2} (bottom panel) vs distance to the MS. The shadowed region represents the main sequence of star-forming galaxies defined by Schreiber et al. (2015) converted from Salpeter to Chabrier IMF with a 0.5 dex (3 times) scatter. The arrows indicate the expected displacement of the total values when using a MS-like excitation conversion (Δr_{31} , affecting HELAISS02 in both panels) and when using the individual α_{CO} ($\Delta \alpha_{\text{CO}}$, affecting HELAISS02, HXMM20, and HCOSMOS02 in both panels).

larger than field galaxies for HELAISS02 and HXMM20 (2.0 and 5.1σ) and smaller for HCOSMOS02 (2.1σ). On a source-by-source basis, given the large caveats affecting the SFE (τ_{H_2}) estimates of HELAISS02 and HXMM20, it is difficult to draw conclusions. In summary, our results suggest that two of our protoclusters cores are only slightly more gas rich than field galaxies, but display higher τ_{H_2} due to their MS-like SFE, somewhat unexpected at this redshift, stellar mass and DMS, where galaxies with an enhanced SFE in the field are more common. These two are the ones with the lowest overall stellar mass, while that with the highest overall stellar mass displays lower τ_{H_2} due to some of its members having SB-like SFE and small f_{H_2} compared to the field.

In the literature the conclusions of studies that tackle gas fractions and efficiencies in protocluster galaxies compared to the field are varied. Noble et al. (2017) concluded that f_{H_2} and τ_{H_2} are higher in $z \sim 1.6$ cluster environments than in the field, from a sample of 11 MS gas-rich sources located in three different targets. Rudnick et al. (2017) observed two protoclusters members at $z = 1.62$, one of them on the MS and the other below the MS, concluding that both f_{H_2} and τ_{H_2}

3. EXPLORING THE ORIGINS OF GALAXY CLUSTERS

Table 3.7: HELAISS02 and HXMM20 Molecular Gas Fractions and Depletion Time-scales vs Field Galaxies

Name	$f_{\text{H}_2}/\langle f_{\text{H}_2} \rangle^a$	$\tau_{\text{gas}}/\langle \tau_{\text{gas}} \rangle^a$
HELAISS02	1.40 ± 0.23	1.56 ± 0.23
S0	1.08 ± 0.02	3.24 ± 0.59
S1	0.67 ± 0.13	0.37 ± 0.09
S2	0.86 ± 0.10	0.57 ± 0.11
S3	0.92 ± 0.04	1.36 ± 0.36
HXMM20	1.15 ± 0.05	4.22 ± 0.63
S0	1.01 ± 0.01	7.4 ± 1.6
S1	0.98 ± 0.03	2.22 ± 0.76
S2	1.00 ± 0.03	3.5 ± 1.2
S3
S4	1.07 ± 0.13	2.24 ± 0.79
HCOSMOS02	0.95 ± 0.49	0.66 ± 0.16
S0	0.78 ± 0.13	0.46 ± 0.14
S1	0.93 ± 0.11	0.78 ± 0.23
S2	0.27 ± 0.09	0.12 ± 0.04
S3	0.31 ± 0.19	0.14 ± 0.11
S4	0.63 ± 0.19	0.37 ± 0.19

^a $\langle f_{\text{H}_2} \rangle$ and $\langle \tau_{\text{gas}} \rangle$ from Table 2 in [Scoville et al. \(2017b\)](#) at the redshift, stellar mass and DMS of each source.

are consistent with the gas scaling relation of field galaxies. [Lee et al. \(2017\)](#) also found consistent f_{H_2} with the gas scaling relations in MS protoclusters members at $z \sim 2.49$. [Hayashi et al. \(2018\)](#) detected 17 member galaxies in CO(2-1) and eight in 870 μm dust continuum at $z = 1.46$, arguing that f_{H_2} and τ_{H_2} are larger than those from the scaling relations. The sources were located on and below the MS. The authors speculated that the environment of galaxy clusters helps feeding the gas through into the cluster members and reduces the efficiency of star formation. On the other hand, [Coogan et al. \(2018\)](#) found lower τ_{H_2} , enhanced SFE and highly excited CO SLEDs in protocluster members at $z = 1.99$, linking such activity to mergers.

The general picture of how dense environments might or not contribute to enhance or suppress the accretion of gas and affect its efficiency to form stars is still debated and unclear. From our observations and based on the literature studies it seems that the evolutionary stage at which each protocluster structure is observed might play an important role in this picture.

3.6 Summary and Conclusions

We selected three *Herschel* candidate protoclusters with multiple ALMA 870 μm continuum counterparts with small pairwise separations in order to confirm whether they are or not located

at the same redshift by using CO observations. In summary we found:

- Three out of three candidates are confirmed protocluster core systems, where all the ALMA 870 μm continuum sources previously reported are at the same redshift. We confirm the discovery of two new protocluster cores named HELAISS02 ($z = 2.171 \pm 0.004$) and HXMM20 ($z = 2.602 \pm 0.002$).
- We do not find any new secure CO(1-0) detections in the $z = 2.51$ COSMOS overdensity, in addition to the previously reported ones. Although the system consists on numerous members, some display only tentative CO(1-0) detections and they should be treated with caution requiring further confirmation.
- The physical conditions of the gas in HELAISS02 and HXMM20 reveal a star formation efficiency consistent with main sequence galaxies, although some of the sources are located in the starburst regime of the SFR – M_* plane due to high gas fractions and yet small stellar masses. We suggest that they could be newly formed galaxies moving into the main sequence.
- Overall, the three studied protocluster cores display trends when compared to each other and the field. HXMM20 is the least massive system with enhanced gas fraction with respect to the field, while HCOSMOS02 is the most massive system with depleted gas fraction with respect to the field. More precise measurements of star formation efficiencies are needed to confirm a trend in this quantity. We suggest an evolutionary sequence between the three protocluster cores and that the comparison with field galaxies depends on the evolutionary stage of the structure.

Acknowledgments

We thank R. S. Bussmann for his contributions to this project and C. M. Casey for useful discussion. We are grateful to the anonymous referee, whose comments have been very useful to improving our work.

C.G.G and S.T. acknowledge support from the European Research Council (ERC) Consolidator Grant funding scheme (project ConTExt, grant number: 648179). D.R. and R.P. acknowledge support from the National Science Foundation under grant number AST-1614213. G.M. and F.V. acknowledge the Villum Fonden research grant 13160 "Gas to stars, stars to dust: tracing star formation across cosmic time". T.K.D.L. acknowledges support by the NSF through award SOSPA4-009 from the NRAO and support by the Simons Foundation. I.P.F. acknowledges support from the Spanish research grants ESP2015-65597-C4-4-R and ESP2017-86852-C4-2-R. H.D. acknowledges

3. EXPLORING THE ORIGINS OF GALAXY CLUSTERS

financial support from the Spanish Ministry of Economy and Competitiveness (MINECO) under the 2014 Ramón y Cajal program MINECO RYC-2014-15686.

The Cosmic Dawn Center is funded by the Danish National Research Foundation.

This paper makes use of the following ALMA data: ADS/JAO.ALMA#2015.1.00752.S. ALMA is a partnership of ESO (representing its member states), NSF (USA) and NINS (Japan), together with NRC (Canada), MOST and ASIAA (Taiwan), and KASI (Republic of Korea), in cooperation with the Republic of Chile. The Joint ALMA Observatory is operated by ESO, AUI/NRAO and NAOJ.

The National Radio Astronomy Observatory is a facility of the National Science Foundation operated under cooperative agreement by Associated Universities, Inc.

This paper employed `Astropy`, a community-developed core Python package for Astronomy ([Astropy Collaboration et al. 2013](#)); `APLpy`, an open-source plotting package for Python ([Robitaille & Bressert 2012](#)); `CASA` ([McMullin et al. 2007](#)); `Matplotlib` ([Hunter 2007](#)); `Numpy`; `Photutils` ([Bradley et al. 2016](#)); R, a language and environment for statistical computing (R Foundation for Statistical Computing, Vienna, Austria).

4

Investigating the Transition from Star-forming to Quiescent Galaxies

This chapter contains the following article:

“Compact Star-Forming Galaxies as Old Starbursts Becoming Quiescent”

In preparation for *The Astrophysical Journal*, (2019)

Authors:

C. Gómez-Guijarro, G. E. Magdis, F. Valentino, S. Toft, & Others

4. INVESTIGATING THE TRANSITION FROM STAR-FORMING TO QUIESCENT GALAXIES

Compact star-forming galaxies (SFGs) have been proposed as immediate progenitors of quiescent galaxies, although their origin and nature are debated. Were they formed in slow secular processes or in rapid merger-driven starbursts? Addressing this question would provide fundamental insight in how quenching of SFGs occurs. We explore the location of the general population of galaxies with respect to fundamental star-forming and structural relations, identify compact SFGs based on their stellar core densities, and study three diagnostics of the burstiness of star formation: 1) Star formation efficiency, 2) interstellar medium (ISM), and 3) radio emission. The overall distribution of galaxies in the fundamental relations points towards a smooth transition towards quiescence while galaxies grow their stellar cores, although some galaxies significantly increase their specific star-formation rate when they become compact. From their star formation efficiencies compact and extended SFGs appear similar. In relation to the ISM diagnostic compact SFGs ISM properties resemble those of upper main sequence SFGs. Regarding the radio emission diagnostic we find that compactness grows along the expected evolution in the radio emission with the age of a starburst, implying that compact SFGs are old starbursts, while extended SFGs are young starbursts. We suggest that compact SFGs could starbursts winding down and eventually crossing the main sequence towards quiescence.

4.1 Introduction

In the past decade, various studies have revealed a tight correlation between the star-formation rate (SFR) and the stellar mass of star-forming galaxies (SFGs). The so-called main sequence (MS) of star formation (e.g., [Brinchmann et al. 2004](#); [Daddi et al. 2007](#); [Elbaz et al. 2007](#); [Noeske et al. 2007](#); [Whitaker et al. 2012](#)) exhibits a small scatter observed at least up to $z \sim 4$ (~ 0.3 dex; e.g., [Elbaz et al. 2007](#); [Noeske et al. 2007](#); [Whitaker et al. 2012](#); [Speagle et al. 2014](#); [Schreiber et al. 2015](#)) implying that secular evolution is the dominant mode of stellar growth where gas inflows, outflows, and consumption through star formation are in equilibrium (e.g., [Daddi et al. 2010a](#); [Genzel et al. 2010](#); [Tacconi et al. 2010](#); [Dekel et al. 2013](#); [Feldmann & Mayer 2015](#)). Therefore, SFGs spend most of their time evolving as extended star-forming disks. Conversely, quiescent galaxies (QGs) are located below the MS and are typically more compact than SFGs for fixed stellar mass and redshift (e.g., [van der Wel et al. 2014](#)). The quenching of star formation and the departure from the MS must imply the build-up of a central stellar core (e.g., [Kauffmann et al. 2003](#); [Lang et al. 2014](#); [van Dokkum et al. 2014](#); [Whitaker et al. 2017b](#); [Barro et al. 2017a](#)).

A population of galaxies have been proposed to be the missing link between the extended SFGs and the more compact QGs, the so-called compact star-forming galaxies (cSFGs; e.g., [Barro et al. 2013, 2014](#); [Nelson et al. 2014](#); [Williams et al. 2014](#); [van Dokkum et al. 2015](#)). cSFGs are typically located within the scatter of the MS, although their origin and nature are still debated. Given the implications of the small scatter of the MS, several studies advocated that normal SFGs

within the MS are capable of building up their stellar cores slowly in their secular evolution (e.g., [Tacchella et al. 2016](#)). However, starburst galaxies (SBs) dominated by a violent episode of star formation typical of gas-rich mergers that move well above the scatter of the MS are also capable of quickly building up compact stellar cores and have also been proposed as early progenitors of QGs (e.g., [Cimatti et al. 2008](#); [Ricciardelli et al. 2010](#); [Fu et al. 2013](#); [Ivison et al. 2013](#); [Toft et al. 2014, 2017](#); [Gómez-Guijarro et al. 2018](#)). Did the build-up of the stellar core, formation of cSFGs, and subsequent quenching of star formation happen as the product of the slow secular evolution, as in normal SFGs, or rapidly, as in SBs? Some works have recently pointed towards the starburst nature of cSFGs based on their interstellar medium (ISM) properties (e.g., [Spilker et al. 2016a](#); [Barro et al. 2017b](#); [Popping et al. 2017c](#); [Tadaki et al. 2017](#); [Talia et al. 2018](#)). However, these results are still based on a handful of cSFGs.

In this work we explore the location of extended and compact SFGs and QGs with respect to the MS and fundamental structural relations and investigate three diagnostics of the burstiness of star formation: 1) Star formation efficiency (SFE), 2) ISM, and 3) radio emission. We aim at shedding some light on how rapidly the build-up of compact stellar cores and successive quenching of SFGs takes place.

The layout of the paper is as follows. We describe the sample selection and identification of extended, compact SFGs, and QGs in Section 4.2. In Section 4.3 we explore the distribution of SFGs and QGs with respect to fundamental star-forming and structural relations. We investigate SFE, ISM, and radio emission diagnostics of the burstiness of star formation in Section 4.4, followed by a discussion in Section 4.5. We summarize the main findings and conclusions in Section 4.6.

Throughout this work we adopted a concordance cosmology $[\Omega_\Lambda, \Omega_M, h] = [0.7, 0.3, 0.7]$ and Chabrier initial mass function (IMF) ([Chabrier 2003](#)).

4.2 Selection of Compact Star-Forming Galaxies

4.2.1 Optical Sample

There are several cSFGs selection criteria in the literature. We followed [Barro et al. \(2017a\)](#) identification criteria based on structural and star-forming relations. [Barro et al. \(2017a\)](#), (see also reference therein) showed that SFGs and QGs follow distinct trends in the stellar density versus stellar mass plane, with QGs being offset to higher densities at fixed stellar mass and redshift. cSFGs are galaxies that follow the structural relation of QGs, while being star-forming. Therefore, cSFGs are more compact than regular SFG at fixed stellar mass and redshift. [Barro et al. \(2017a\)](#) proposed a compactness selection threshold in the core density ($\Sigma_1, r < 1$ kpc) as the most efficient way of selecting cSFGs, given the $\Sigma_1 - M_*$ QGs structural relation small scatter

4. INVESTIGATING THE TRANSITION FROM STAR-FORMING TO QUIESCENT GALAXIES

and mild normalization decline with redshift. This threshold is:

$$\Sigma_1 - 0.65(\log M_* - 10.5) > \log B(z) - 0.2, \quad (4.1)$$

where $\log B(z)$ have a small redshift dependence ranging between $9.5-9.8 M_* \text{ kpc}^{-2}$ (see Barro et al. 2017a, for details on its definition). For simplicity we will refer to this threshold as Σ_{QGs} hereafter. In contrast, the QGs structural relation based on the effective density ($\Sigma_e, r < r_e$, where r_e is the effective radius) would be less efficient identifying cSFGs as it shows larger scatter and variation of the normalization with redshift. By extension, other selection criteria based on a cut in stellar mass and effective radius would be also less efficient. Since by construction both cSFGs and QGs follow the same structural relation, the distinction between cSFGs and QGs is based on the distance to the main sequence of star formation (ΔMS), defined as the ratio of the specific star-formation rate (sSFR) to the sSFR of the MS at the same stellar mass and redshift ($\Delta\text{MS} = \text{sSFR}/\text{sSFR}_{\text{MS}}$). The threshold in Barro et al. (2017a) is $\Delta\text{MS} = -0.7$ dex, which corresponds to $\sim 2.5\sigma$ below the MS. cSFGs are galaxies above this threshold in star formation.

For our analysis we worked with the cosmological fields COSMOS (Scoville et al. 2007) and GOODS-North (Dickinson et al. 2003). As a starting point, we employed the 3D-*HST* survey catalogs (Brammer et al. 2012; Skelton et al. 2014; Whitaker et al. 2014; Momcheva et al. 2016) in the CANDELS (Grogin et al. 2011; Koekemoer et al. 2011) portion of COSMOS and GOODS-North, from which we collected stellar masses, SFRs, and redshifts. The structural parameters were gathered from the associated catalogs in van der Wel et al. (2014). We trimmed the catalogs following Barro et al. (2017a): 1) $0.5 < z < 3.0$, to guarantee that Barro et al. (2017a) structural relations were derived; 2) $\log M_* > 9.0$ for SFGs, $\log M_* > 10.0$ for QGs, and $H_{\text{F160W}} < 25.5$, to guarantee that the minimum requirements in the validity of the structural parameters are fulfilled (van der Wel et al. 2012, 2014), where sources flagged as catastrophic failures in the surface brightness profile fits were excluded. van der Wel et al. (2012, 2014) showed that the effective radius (r_e) and Sérsic index (n) have uncertainties $< 10\%$ for galaxies $H_{\text{F160W}} < 24.5$, and discussed that a redshift-dependent mass threshold of $\log M_* > 8.5-9.75$ for SFGs and $\log M_* > 9.0-10.3$ for QGs at $0.5 < z < 3.0$ guarantees that the galaxies are $H_{\text{F160W}} < 24.5$. Barro et al. (2017a) chose $\log M_* > 9.0$ for SFGs and $\log M_* > 10.0$ for QGs as a good compromise between dynamical range in stellar mass and accuracy in the structural parameters. To trace approximately the same rest-frame wavelength as a function of redshift we used the structural parameters derived in the J_{F125W} -band at $z < 1.5$ and H_{F160W} -band at $z \geq 1.5$. We refer to the sample resulting from this selection as our parent optical sample, which is composed of 13703 galaxies (7222 in COSMOS and 6481 in GOODS-North) with 416 cSFGs (227 in COSMOS and 189 in GOODS-North).

4.2.2 Far-Infrared Sample

The "super-deblended" far-infrared (FIR) to submillimeter photometric catalogs in COSMOS (Jin et al. 2018) and GOODS-North (Liu et al. 2018) provided fluxes from highly-confused low-resolution data to optical counterparts by using a mix of high-resolution priors (*Spitzer*/MIPS 24 μm , VLA 1.4, and 3 GHz for COSMOS; *Spitzer*/MIPS 24 μm , VLA 1.4 GHz for GOODS-North). We trimmed these catalogs to sources with a combined signal-to-noise $S/N_{\text{FIR+mm}} \geq 5$ (where $S/N_{\text{FIR+mm}}$ is the quadrature-sum of the S/N in all $\lambda \geq 100 \mu\text{m}$ bands in the catalogs (Liu et al. 2018; Jin et al. 2018)). We refer to the sample resulting from this selection as our FIR sample, which is composed of 968 galaxies (357 in COSMOS and 611 in GOODS-North) with 73 cSFGs (26 in COSMOS and 47 in GOODS-North).

Rayleigh-Jeans and Radio Subsets

We separated a subset of galaxies in the FIR sample that have at least one detection at $S/N \geq 3$ above a rest-frame wavelength of 250 μm , so-called Rayleigh-Jeans (R-J) side of the FIR spectral energy distribution (SED), required to obtain gas mass estimates (Section 4.2.2). This comprises our R-J subset of the FIR sample, composed of 59 galaxies (24 in COSMOS and 35 in GOODS-North) with 5 cSFGs (4 in COSMOS and 1 in GOODS-North).

Additionally, we cross-matched our FIR catalog with radio catalogs from the Giant Metrewave Radio Telescope (GMRT) at 325 MHz and 610 MHz in COSMOS (Tisanić et al. 2019) and at 610 MHz in GOODS-North. Besides, we substituted the COSMOS "super-deblended" FIR catalog 3 GHz measurements for those in the COSMOS-XS survey (D. van der Vlugt et al. 2019, in preparation; H. Algera et al. 2019, in preparation) for overlapping sources in both catalogs, given the increased depth of the latter survey. We looked for radio counterparts within the half power beam width (HPBW) at each frequency. We separated a subset of galaxies that have at least two $S/N \geq 5$ detections at any available radio frequency (325 MHz, 610 MHz, 1.4 GHz, and 3 GHz in COSMOS; 610 MHz, 1.4 GHz, and 3 GHz in GOODS-North), required for our radio diagnostic analysis (Section 4.4.3). This comprises our radio subset of the FIR sample, composed of 60 galaxies (23 in COSMOS and 37 in GOODS-North) with 7 cSFGs (2 in COSMOS and 5 in GOODS-North).

Far-infrared Properties

We derived infrared luminosities (L_{IR}) and infrared-based star formation rates (SFR_{IR}) for our FIR sample. In order to derive these quantities, we first fitted the mid-IR-to-millimeter SED using the Draine & Li (2007) models. These models linearly combine two dust components, one coming from the diffuse ISM and one heated by a power-law distribution of starlight associated with photodissociation regions (PDRs). The methodology was presented in detail in previous

4. INVESTIGATING THE TRANSITION FROM STAR-FORMING TO QUIESCENT GALAXIES

studies (e.g., [Magdis et al. 2012, 2017](#); [Berta et al. 2016](#)). We also included an active galactic nuclei component (AGN) to ensure that FIR properties account for star formation only. The best fit to the models were derived through χ^2 minimization and the uncertainties were calculated over 1000 realizations of the observed SED perturbing the photometry within the errors. L_{IR} was calculated integrating the best fit to the SED in the range 8–1000 μm and SFR_{IR} from the L_{IR} to SFR_{IR} conversion in [Kennicutt \(1998\)](#) for a Chabrier IMF. One of the parameters derived from the fit is the dust mass (M_{dust}), which can be used to derive gas masses (M_{gas}). In order for the M_{gas} estimates to be reliable it is required at least one detection in the R-J side of the SED. Therefore, we derive M_{gas} for our R-J subset of the FIR sample. We used the metallicity-dependent gas-to-dust mass ratio technique (δ_{GD}), adopting the $M_{\text{gas}}/M_{\text{dust}}-Z$ relation of [Magdis et al. \(2012\)](#) ($\log(M_{\text{dust}}/M_{\text{gas}}) = (10.54 \pm 1.0) - (0.99 \pm 0.12) \times (12 + \log(O/H))$), where the metallicity is calibrated using the [Pettini & Pagel \(2004\)](#) scale. We assumed a solar metallicity for all galaxies that corresponds to a $M_{\text{gas}}/M_{\text{dust}} \sim 90$. Another method to derive M_{gas} is the single band measurement of the dust continuum emission flux on the R-J side of the SED (e.g., [Scoville et al. 2014](#); [Groves et al. 2015](#); [Scoville et al. 2016](#); [Schinnerer et al. 2016](#)). Both the δ_{GD} method and the single-band measurement of the dust emission method from [Scoville et al. \(2016\)](#) yielded consistent results on average, with a median and median absolute deviation ratio of $M_{\text{gas}}^{\text{GD}}/M_{\text{gas}}^{\text{R-J}} = 0.88 \pm 0.41$. In the following we adopt M_{gas} estimates from the δ_{GD} method since it employs all datapoints in the SED and, particularly, when there are several detections in the R-J side. Note that both methods account for the total gas budget of the galaxies, including the molecular (M_{H_2}) and the atomic phases (M_{HI}).

4.2.3 Active Galactic Nuclei Flagging

AGN activity is known to follow star formation and, particularly, to be present in a large fraction of cSFGs at $2 < z < 3$ ([Barro et al. 2014](#)). We kept track of the galaxies with evidence of AGN activity from several indicators. We flagged all the galaxies for which the AGN fraction from our FIR SED modeling is $\geq 20\%$. In addition, we checked for X-ray bright AGN ($\log L_X > 42.5$, absorption-corrected soft and hard X-ray luminosity) in the COSMOS (*Chandra* COSMOS Legacy Survey; [Civano et al. 2016](#); [Marchesi et al. 2016](#)) and GOODS-North ([Xue et al. 2016](#)) X-ray catalogs. Finally, we identified radio-excess AGN as those having a significantly low FIR/radio ratio ($q < 1.68$) following [Del Moro et al. \(2013\)](#). These AGN flagging accounts for unobscured to relatively obscured bright AGN and radio loud AGN, particularly for the FIR sample for which all AGN indicators are available.

4.3 Compactness and Star Formation

In this section we explore the location of SFGs and QGs with respect to the MS of star formation and the structural relation of QGs.

For each galaxy in the parent optical sample we calculated ΔMS , adopting the MS definition of [Whitaker et al. \(2014\)](#), and the distance to the QGs structural relation ($\Delta\Sigma_{\text{QGs}} = \Sigma_1/\Sigma_{\text{QGs}}$), adopting the relation definition in [Barro et al. \(2017a\)](#), at its stellar mass and redshift. We will refer to extended SFGs as regular SFGs located at $\Delta\Sigma_{\text{QGs}} < 1.0$, as opposed to cSFGs located at $\Delta\Sigma_{\text{QGs}} > 1.0$. Similarly, extended QGs are QGs at $\Delta\Sigma_{\text{QGs}} < 1.0$ and compact QGs are QGs at $\Delta\Sigma_{\text{QGs}} > 1.0$.

Note that the SFRs in the 3D-*HST* catalogs are defined as $\text{SFR}_{\text{IR+UV}} = 1.09 \times 10^{-10}(L_{\text{IR}} + 2.2L_{\text{UV}})$, where L_{IR} is obtained through a conversion from the observed *Spitzer*/*MIPS* 24 μm flux density to L_{IR} (8–1000 μm) based on a single template. L_{UV} is the total integrated rest-frame luminosity in the range 1216–3000 Å. For the FIR sample ($\sim 7\%$ of the parent optical sample) we substituted the SFR_{IR} contribution for the one we obtained in Section 4.2.2, since it uses all the information available in the FIR SED, as opposed to a single template which could dilute galaxies that intrinsically deviate from the template. We checked that making this SFR_{IR} substitution does not introduce a systematic bias respect to [Whitaker et al. \(2014\)](#) MS definition, which could alter our ΔMS values.

4.3.1 General Trends

In Figure 4.1 we present the ΔMS - $\Delta\Sigma_{\text{QGs}}$ plane for the parent optical sample. The overall distribution reproduces the L-shape reported in [Barro et al. \(2017a\)](#), with the population of cSFGs forming the knee between extended SFGs and cQGs. This was used as an argument in favour of cSFGs as progenitors of QGs at later times, implying that SFGs become compact before they quench. Note that the majority of QGs are compact QGs.

We also explored the behaviour of the ΔMS per bins of $\Delta\Sigma_{\text{QGs}}$ (i.e., core density) in Figure 4.1. In order to do so, we draw a violin plot, a combination of a box and whiskers plot and a density plot to visualize the distribution of the data and its probability density. The box and whiskers plot represents the central value given by the median, the scatter given by the interquartile range ($\text{IQR} = Q3 - Q1$), and the extremes given by the lower and upper adjacent values ($\text{LAV} = Q1 - 1.5\text{IQR}$; $\text{UAV} = Q3 + 1.5\text{IQR}$). The density plot represents the frequency of a certain value within its bin. The median ΔMS is approximately constant up to $\Delta\Sigma_{\text{QGs}} = 0.5$, with symmetric scatter above and below the median value that slightly grows with increasing compactness. It is interesting that the median ΔMS stays systematically above the MS ($\Delta\text{MS} = 1.25$; ~ 0.1 dex). At $\Delta\Sigma_{\text{QGs}} = 0.6$ – 1.0 galaxies go systematically below the median ΔMS of the

4. INVESTIGATING THE TRANSITION FROM STAR-FORMING TO QUIESCENT GALAXIES

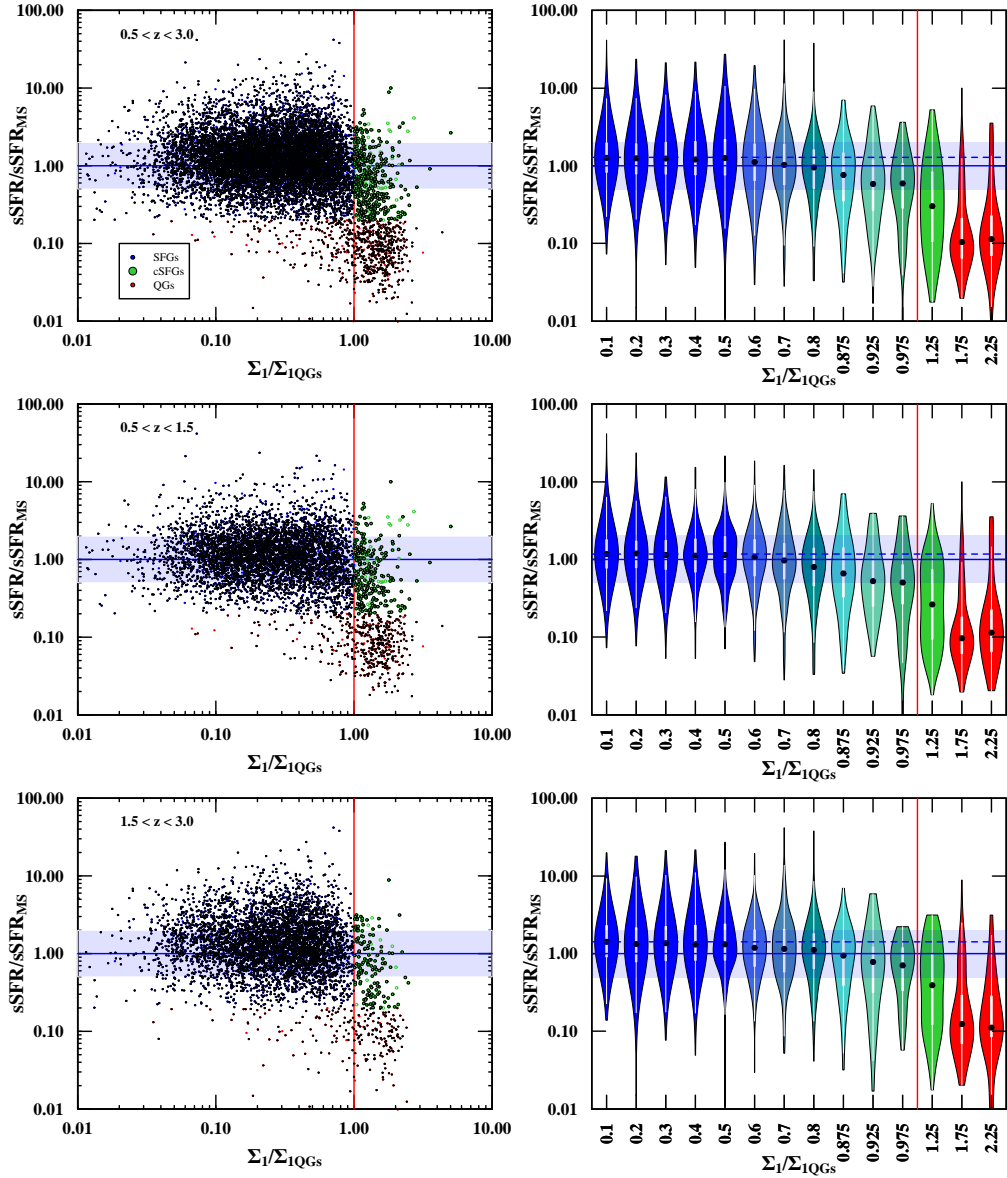


Figure 4.1: $\Delta_{\text{MS}}-\Delta\Sigma_{\text{QG}s}$ plane. First row left panel: Parent optical sample at all redshifts ($0.5 < z < 3.0$) composed of extended SFGs (blue), cSFGs (green), and QGs (red). AGN-flagged galaxies are represented with empty symbols. Right panel: Violin plot, a combination of a box and whiskers and a density plot. The black dot in the middle is the median value and the thick white bar in the centre represents the interquartile range ($\text{IQR} = Q_3 - Q_1$). The thin white line extended from it indicates the upper and lower adjacent values, defined as $\text{LAV} = Q_1 - 1.5\text{IQR}$ and $\text{UAV} = Q_3 + 1.5\text{IQR}$, respectively. The width of the colored area represents the probability density of a given value in the Y axis. Note that the colors of the violin plot are not directly linked to extended, compact SFGs, or QGs, but were chosen to be a representative color of their abundance on each bin. The MS as defined in [Whitaker et al. \(2014\)](#) is represented with a blue solid line. The 1σ scatter of the MS (~ 0.3 dex; e.g., [Whitaker et al. 2012](#); [Schreiber et al. 2015](#)) is indicated with a blue shaded region. The median $\Delta_{\text{MS}} = 1.25$ in the phase up to $\Delta\Sigma_{\text{QG}s} = 0.5$ is represented as a dashed blue line. The QGs structural relation as defined in [Barro et al. \(2017a\)](#) is represented with a red solid line. Second row: Similar to the first row for galaxies at $0.5 < z < 1.5$. Third row: Similar to the first row for galaxies at $1.5 < z < 3.0$. The typical uncertainties are 0.15 dex in the X axis and 0.1 dex in the Y axis.

previous phase, with increasing scatter, increasing lower extreme values, and decreasing upper extreme values compared to the previous phase. At $\Delta\Sigma_{\text{QGs}} = 1.0\text{--}1.5$ an abrupt decrease in the ΔMS occurs, galaxies go below the scatter of the MS, show symmetric larger scatter, and larger lower and upper extremes than in the previous phase. At $\Delta\Sigma_{\text{QGs}} > 1.5$ galaxies fall well below the MS, with the ΔMS scatter and extreme values starting to show symmetry.

Overall, the description above indicates that galaxies start to transition smoothly towards quiescence, since the median ΔMS decreases continuously for increasing $\Delta\Sigma_{\text{QGs}}$. Some extended SFGs quench smoothly forming extended QGs as they build up their stellar cores. On the other hand, the sharp transition region at $\Delta\Sigma_{\text{QGs}} \sim 1.0$ indicates that other galaxies become compact before they quench as reported in Barro et al. (2017a). Some extended SFGs become cSFGs and then compact QGs as they build up their stellar cores. The latter would be a more common track since the majority of QGs are compact QGs. Note that it has to be considered that SFGs do not evolve into QGs at the same epoch (i.e., redshift), but into QGs at later times.

The fact that the median ΔMS stays slightly above the MS up to $\Delta\Sigma_{\text{QGs}} = 0.5$ indicates that, while the MS is dominated by galaxies in this extended phase, there is a contribution from more compact galaxies in transition towards quiescence that affects the overall trend that defines the MS lowering its normalization. Another interesting fact is that extended SFGs above the scatter of the MS are far more numerous than cSFGs above the scatter of the MS. Nevertheless, it is remarkable the scatter and the presence of extreme values around the $\Delta\Sigma_{\text{QGs}} \sim 1.0$ transition threshold. At $\Delta\Sigma_{\text{QGs}} \leq 0.95$, the median ΔMS decreases smoothly, and so it does Q1. However, the next bin centered at $\Delta\Sigma_{\text{QGs}} = 0.975$ has similar median ΔMS , Q1, and lower extreme values than the previous bin centered at $\Delta\Sigma_{\text{QGs}} = 0.925$. This indicates that right before crossing the $\Delta\Sigma_{\text{QGs}} = 1.0$ threshold galaxies build up their stellar cores at approximately constant sSFR. Right after crossing the $\Delta\Sigma_{\text{QGs}} = 1.0$ threshold, while the median ΔMS , Q1, Q3, and lower extreme values decrease, the IQR and the upper extreme values increase. Even at the bin centered at $\Delta\Sigma_{\text{QGs}} = 1.75$ the upper extreme values still increase, although they are less frequent than in the previous bin. This indicates that, at least some of the galaxies make the transition by increasing their sSFR and going above the scatter of the MS.

4.3.2 Redshift Dependence

In addition to the ΔMS - $\Delta\Sigma_{\text{QGs}}$ plane for the whole redshift range studied, we also present the results in the redshift bins $0.5 < z < 1.5$ and $1.5 < z < 3.0$ in Figure 4.1. The general trends are similar at low and high redshift, although there are some important differences. At $1.5 < z < 3.0$ the median ΔMS up to $\Delta\Sigma_{\text{QGs}} = 0.5$ is higher ($\Delta\text{MS} = 1.35$) than at $0.5 < z < 1.5$ ($\Delta\text{MS} = 1.16$). This indicates that the overall trend that defines the MS is more affected at the high-redshift bin than at the low-redshift bin by galaxies that are already in transition towards

4. INVESTIGATING THE TRANSITION FROM STAR-FORMING TO QUIESCENT GALAXIES

quiescence and that lower its normalization.

4.3.3 Trends for Massive Galaxies

The $\Delta\text{MS}-\Delta\Sigma_{\text{QGs}}$ planes discussed above follow the selection criteria explained in Section 4.2.1. Particularly, the stellar mass limits are $\log M_* > 9.0$ for SFGs, $\log M_* > 10.0$ for QGs. At $\log M_* \geq 10.3$ the sample is complete for both SFGs and QGs at $z < 3.0$ (van der Wel et al. 2014) (see also Skelton et al. 2014; Tal et al. 2014; Barro et al. 2017a). Therefore, we explored the $\Delta\text{MS}-\Delta\Sigma_{\text{QGs}}$ plane for the most massive galaxies $\log M_* \geq 10.3$ in Figure 4.2.

Overall, the trends are similar than those discussed in the previous section. Note that the sample statistics are smaller in this case, which has to be taken in consideration when interpreting the plots. One important difference is that the median ΔMS is not approximately constant up to $\Delta\Sigma_{\text{QGs}} = 0.5$ anymore, but it rather starts to decay since the first bin centered at $\Delta\Sigma_{\text{QGs}} = 0.1$. This is expected as a consequence of massive galaxies being more dominated by galaxies that are already in transition towards quiescence than low-mass galaxies. In this case we do not appreciate differences in the ΔMS at $\Delta\Sigma_{\text{QGs}} = 0.1$ at low redshift ($\Delta\text{MS} = 1.27$) and high redshift ($\Delta\text{MS} = 1.25$), which indicates that the trend in Section 4.3 was dominated by low-mass galaxies. Another important difference is that the number of galaxies above the scatter of the MS respect to those within the scatter of the MS is smaller for massive galaxies. Besides, outliers are less strong (i.e., smaller ΔMS), as expected given that for the same increase in SFR the effect in sSFR is smaller as galaxies become more massive.

4.4 Are Compact Star-Forming Galaxies Normal Star-Forming Galaxies or Starbursts?

cSFGs have been proposed as a transition population between being star-forming and quiescence. Revealing their nature implies revealing whether the transition to quiescence occurred secularly or rapidly. Phases of abrupt changes in increasing sSFR are typical of SBs. The time a galaxy is detectable in such phase is short, since these are short-lived (e.g., Tacconi et al. 2008; Di Matteo et al. 2008). This means that the number of detectable SBs is small compared to the general population, but the phase can still be very relevant in terms of stellar mass assembly. We examined three diagnostics of the burstiness of star formation: 1) SFE, 2) ISM, and 3) radio emission. The aim is exploring whether cSFGs can be considered normal SFGs, pointing to a more secular evolution, or SBs, pointing to a more rapid evolution. Note that the galaxies selected for each of the three diagnostics are not the same sources as the selections do not overlap.

4.4. ARE COMPACT STAR-FORMING GALAXIES NORMAL STAR-FORMING GALAXIES OR STARBURSTS?

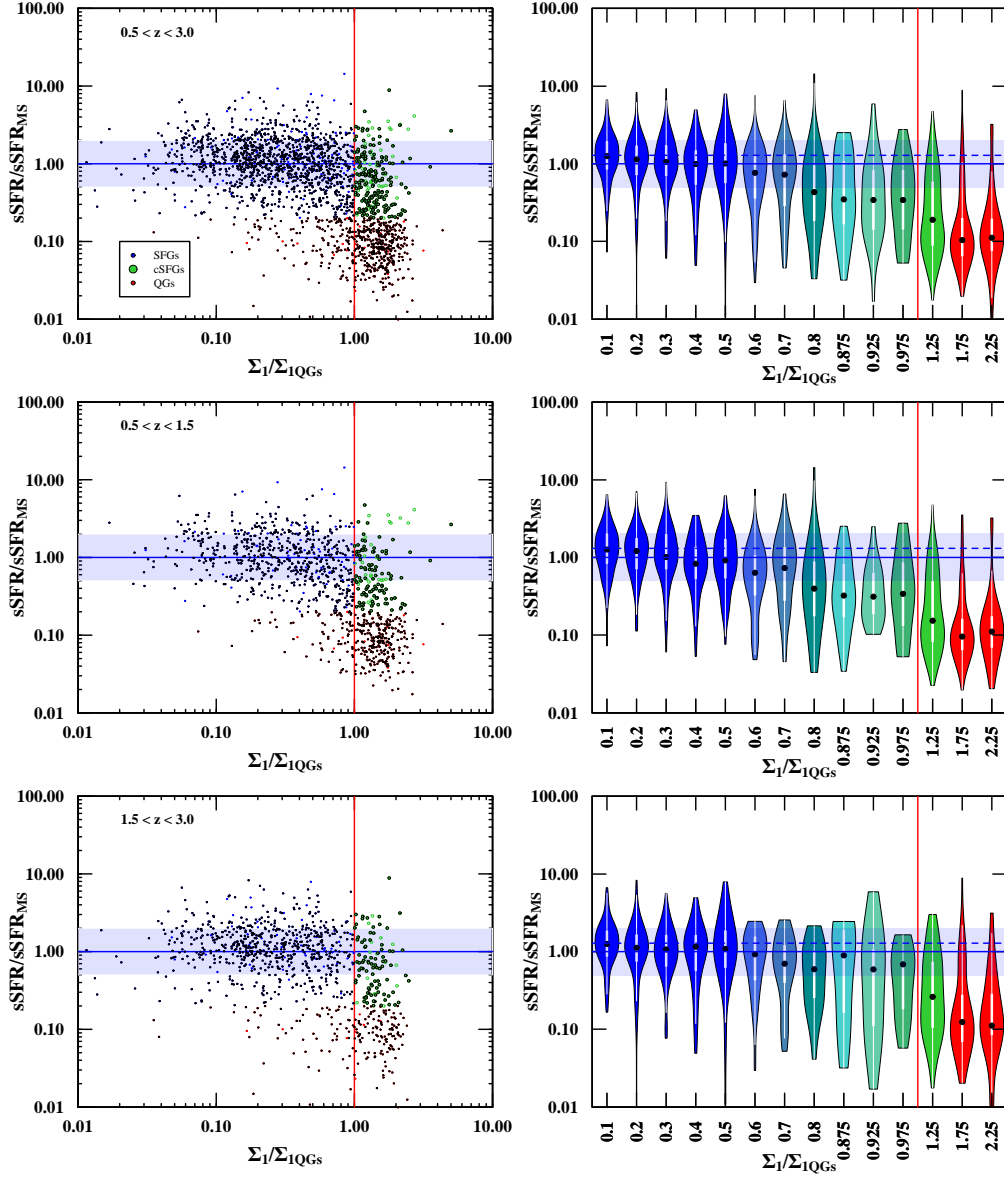


Figure 4.2: $\Delta_{\text{MS}}-\Delta\Sigma_{\text{QG}s}$ plane as presented in Figure 4.1 for galaxies at $\log M_* \geq 10.3$.

4.4.1 Diagnostic 1: Star Formation Efficiency

The star formation law or Kennicutt-Schmidt relation (KS relation; [Schmidt 1959](#); [Kennicutt 1998](#)) relates the gas mass and the SFR of SFGs (originally defined using surface densities). Several studies indicated that normal SFGs and SBs follow different trends. SBs have higher SFR per unit of gas mass and, thus, higher star formation efficiencies ($\text{SFE} = \text{SFR}/M_{\text{gas}}$) than normal SFGs (e.g., [Daddi et al. 2010b](#); [Genzel et al. 2010](#)). This distinction in SFE serves to distinguish normal SFGs from SBs, regardless of their location with respect to the MS. In this section we apply this

4. INVESTIGATING THE TRANSITION FROM STAR-FORMING TO QUIESCENT GALAXIES

SFE-based definition of normal SFGs and SBs.

In Figure 4.3 we present the locus of our R-J subset of the FIR sample in the M_{gas} -SFR plane in relation with the trends for normal SFGs and SBs in Sargent et al. (2014), where the normal SFGs trend comes from massive MS galaxies in Sargent et al. (2014). Note that we only included the most massive subset of galaxies with $\log M_* \geq 10.3$, to guarantee that the assumption of solar metallicity to derive M_{gas} is valid. We also include Elbaz et al. (2018) sample, calculating their $\Delta\Sigma_{\text{QGs}}$ and assessing whether they are extended SFGs or cSFGs, according to Barro et al. (2017a) criterion. This can be successfully done for 18/19 galaxies in Elbaz et al. (2018) as one of the galaxies has bad structural parameters in van der Wel et al. (2014) catalogs (shown with a gray symbol in Figure 4.3). In Figure 4.3 we also explore the relation between SFE, gas fraction ($f_{\text{gas}} = M_{\text{gas}}/(M_* + M_{\text{gas}})$), and ΔMS , being SFE and f_{gas} normalized to the normal SFGs trends in Sargent et al. (2014).

cSFGs in our sample are consistent with the SFE trend established for normal SFGs. Besides, the extended SFGs in our sample follow the normal SFGs SFE trend as well. Our sample is located within and above the scatter of the MS. The SFE- f_{gas} plane exhibits a tendency, being galaxies with lower SFE those with higher f_{gas} , as expected for galaxies that decrease their SFE as a consequence of increasing their gas content. On the other hand, Elbaz et al. (2018) sample occupies complementary regions in these diagrams respect to our sample, exhibiting enhanced SFE closer to those of the SBs trend due to low gas fractions.

These diagrams indicate that our cSFGs are consistent with the trends of normal SFGs with no evidence of SB-like SFE. The combination of our sample with Elbaz et al. (2018) sample indicates that there is no difference between cSFGs and extended SFGs in terms of their SFE, since both occupy the same regions in the SFE and f_{gas} parameter space. Overall, these results point towards both secular and rapid evolution processes are able to generate cSFGs.

4.4.2 Diagnostic 2: Interstellar Medium

CO Excitation

The properties of the ISM are a critical piece of information to study how star formation occurs. The excitation of the CO emission is a good tracer of the ISM properties. It is measured through the line luminosity ratio of CO lines with different rotational number (J). The CO (5 – 4)/CO (2 – 1) ratio shows the biggest discrepancy between normal SFGs and SBs excitation conditions than any other pair of CO transitions calibrated in the literature (e.g., Bothwell et al. 2013; Daddi et al. 2015). Daddi et al. (2015) established a benchmark for the excitation conditions of normal SFGs by studying a sample of BzK -selected normal SFGs at $z \sim 1.5$ located within the scatter of the MS. They found that, while less excited than typical SBs such as local ULIRGs or high-redshift SMGs, the average excitation was higher than in the Milky Way. The authors argued that the excitation

4.4. ARE COMPACT STAR-FORMING GALAXIES NORMAL STAR-FORMING GALAXIES OR STARBURSTS?

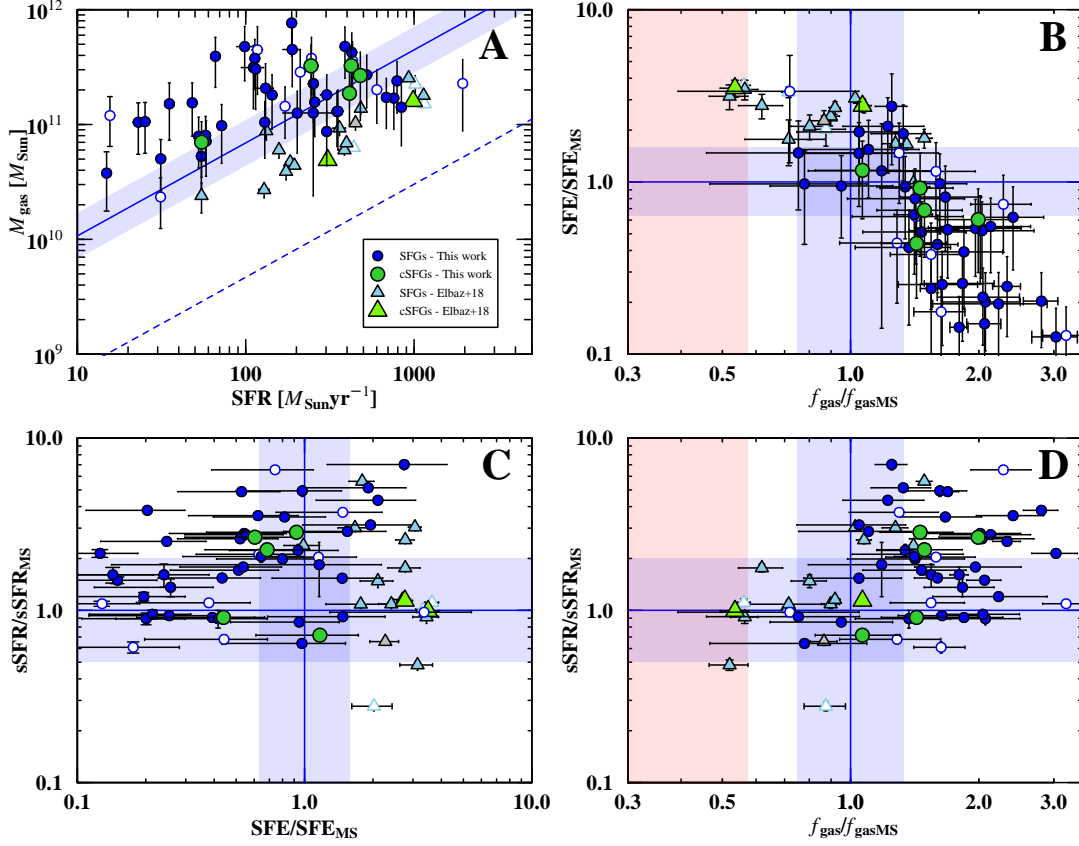


Figure 4.3: Panel A: M_{gas} -SFR plane. Trends for normal SFGs (solid line), with its 0.2 dex scatter, and SBs (dashed line) from Sargent et al. (2014) are shown as reference. Panel B: SFE- f_{gas} plane. Panel C: ΔMS -SFE plane. Panel D: ΔMS - f_{gas} plane. SFE and f_{gas} are normalized to the normal SFGs trends in Sargent et al. (2014). The 1σ scatter of the MS (~ 0.3 dex; e.g., Whitaker et al. 2012; Schreiber et al. 2015) and the normal SFGs SFE (~ 0.2 dex; Sargent et al. 2014) and f_{gas} (~ 0.125 dex; Sargent et al. 2014) trends are represented as a blue shaded region. Our sample is displayed as circles, Elbaz et al. (2018) as triangles. Both samples are classified as extended SFGs (blue) or cSFGs (green), except for one of Elbaz et al. (2018) galaxies (gray) unclassifiable due to bad structural parameters. AGN-flagged galaxies are represented with empty symbols. In panels B and D the most favorable f_{gas} limit in our selection is shown as a red shaded region as a reference of the detection threshold (see Section 4.5).

correlates with the star formation surface density. This along with the fact that the excitation varied within the sample motivated us to study whether some of Daddi et al. (2015) galaxies are cSFGs. In this section we refer to normal SFGs as those consistent with the CO spectral line energy distribution (SLED) of Daddi et al. (2015) BzK -selected MS galaxies, while we refer to SBs as those consistent with the median CO SLED of SMGs from Bothwell et al. (2013).

We cross-matched our parent optical sample with the galaxies in Daddi et al. (2015). We found three of our galaxies, namely GN2359, GN20044, and GN23304, which correspond to BzK -4171, BzK -16000, and BzK -17999 in Daddi et al. (2015), respectively. The missing galaxy BzK -21000 in Daddi et al. (2015) corresponds to GN38099. Its structural parameters are poorly constrained and, thus, it was excluded from our sample. For the analysis in this section we added it back

4. INVESTIGATING THE TRANSITION FROM STAR-FORMING TO QUIESCENT GALAXIES

bearing in mind this caveat. In Figure 4.4 we show the SLEDs in Daddi et al. (2015) for these four galaxies. In Table 4.1 we present their ΔMS and $\Delta\Sigma_{\text{QGs}}$ values.

All four galaxies are extended SFGs and not cSFGs. However, we see that the three galaxies with the highest ΔMS are the ones with the highest CO excitation (GN2359, GN23304, and GN38099), while the other galaxy located right on the MS is the one with the lowest CO excitation (GN20044).

The galaxies with the highest CO excitation are also those with the highest star formation surface density according to Daddi et al. (2015), suggesting that the scatter at higher ΔMS is linked to galaxies progressively forming compact cores.

Photodissociation Regions

Another way of studying the ISM properties is through characterizing the photodissociation regions (PDRs). PDRs are neutral gas regions dominated by far-ultraviolet (FUV) photons. PDR modeling have been used to characterize the strength of the ultraviolet radiation field (G) and the density of the neutral gas (n) (e.g., Alaghband-Zadeh et al. 2013; Popping et al. 2017c). In particular, Popping et al. (2017c) employed it to characterize the ISM properties of a cSFGs at $z = 2.225$ located within the scatter of the MS (namely GS30274). They found that the galaxy has SB-like ISM properties, low gas fraction, and high efficiency. The authors interpreted that a previous merger event triggered a central starburst that is quickly building up a dense core of stars responsible for the compact distribution of stellar light. We studied whether galaxies in our sample are similar. In this section we refer to normal SFGs as those consistent with the location of the sample of MS galaxies from Malhotra et al. (2001) in the G - n plane, while we refer to SBs as those consistent with the location of the sample of local ULIRGS from Davies et al. (2003) in the G - n plane, identical to the definition used in Alaghband-Zadeh et al. (2013); Popping et al. (2017c).

Valentino et al. (2018) presented a survey of atomic carbon [C I] of FIR-selected galaxies on the MS at $z \sim 1.2$. We cross-matched our parent optical sample with the galaxies in Valentino et al. (2018). We found that one of our extended SFGs was observed in that survey, namely COS24563 (which corresponds to 18538 in Valentino et al. (2018)). We performed PDR modeling for this galaxy and also for GS30274 in Popping et al. (2017c) for consistency in the methodology. Besides, we calculated GS30274 $\Delta\Sigma_{\text{QGs}}$ and checked that it is a cSFGs according to Barro et al. (2017a) criterion. Note that the structural parameters of GS30274 are poorly constrained, as also mentioned in Popping et al. (2017c), and do not meet the same quality criteria applied to our sample. In Figure 4.4 we locate the two modeled galaxies in the the G - n plane. In Table 4.1 we present the ΔMS and $\Delta\Sigma_{\text{QGs}}$ values for them.

We estimated the density n (in cm^{-3}) and the strength of the FUV ($6 \text{ eV} < h\nu < 13.6 \text{ eV}$)

Table 4.1: ΔMS and $\Delta\Sigma_{\text{QGs}}$ for Galaxies in Section 4.4.2

Name	ΔMS	$\Delta\Sigma_{\text{QGs}}$
COS24563	3.15 ± 0.12	0.325 ± 0.011
GN2359	2.81 ± 0.12	0.227 ± 0.012
GN20044	1.13 ± 0.09	0.394 ± 0.007
GN23304	2.37 ± 0.05	0.227 ± 0.012
GN38099	5.13 ± 0.10	0.095 ± 0.003
GS30274	2.02 ± 0.10	1.132 ± 0.011

radiation field G (in the Habing field units, $G_0 = 1.6 \times 10^{-3} \text{ erg cm}^{-2} \text{ s}^{-1}$) by comparing the available line luminosities with the 1D modeling of the PDRs by [Kaufman et al. \(1999, 2006\)](#). This modeling provides a simplified picture of the complex cold ISM phases and their interplay in high-redshift galaxies, but it is enough to capture the average properties of these unresolved systems, without introducing a large number of parameters that cannot be observationally constrained at the current stage. We downloaded the relevant line intensity maps from the online PDR TOOLBOX ([Pound & Wolfire 2008](#)), originally spanning a density interval of $1 < \log n[\text{cm}^{-3}] < 7$ and FUV intensity range of $-0.5 < \log(G/G_0) < 6.5$ and we resampled them to a 0.05 dex step grid. We then compared the models and the observations finding the combination of (n, G) that minimizes the χ^2 . We estimated the uncertainties on the best fit (n, G) both applying the criterion described in [Avni \(1976\)](#) and bootstrapping 1000 times the line luminosities and computing the 68%, 90%, and 95% confidence intervals as inter-percentile ranges. In this work we modeled the neutral atomic carbon ${}^3P_1 \rightarrow {}^3P_0$ transition ($[\text{C I}]({}^3P_1 - {}^3P_0)$, $\nu_{\text{rest}} = 492.161 \text{ GHz}$), a mid- J CO line (CO (4 – 3) or CO (5 – 4) at $\nu_{\text{rest}} = 461.0408$ and 576.2679 GHz , respectively), and the total infrared luminosity (L_{IR}) removing the possible AGN contribution due to the dusty torus around the central supermassive black hole (see Section 4.2.2). The $[\text{C I}]({}^3P_1 - {}^3P_0)/\text{mid-}J$ ratio is primarily sensitive to the density. The election of CO (4 – 3) or CO (5 – 4) as the CO mid- J transition does not affect the results on the density (F. Valentino et al. 2019, in preparation). $[\text{C I}]({}^3P_1 - {}^3P_0)/L_{\text{IR}}$ depends on G by construction ($G \propto L_{\text{IR}}$, [Kaufman et al. \(1999\)](#)). We thus have roughly perpendicular tracks to determine both (n, G) parameters (e.g., [Alaghband-Zadeh et al. 2013](#); [Popping et al. 2017c](#)).

COS24563 and GS30274 have similar properties as seen in Figure 4.4. They are both located in the intersection between normal SFGs and SBs ISM properties. COS24563 is placed at a ΔMS slightly above the scatter of the MS, suggesting that the scatter at higher ΔMS is linked to galaxies progressively forming compact cores, similar to the interpretation drawn from the CO excitation.

Overall, the ISM properties from both the CO excitation and PDR modeling suggest that extended SFGs located slightly above the MS (upper-MS galaxies) are capable of hosting an ISM

4. INVESTIGATING THE TRANSITION FROM STAR-FORMING TO QUIESCENT GALAXIES

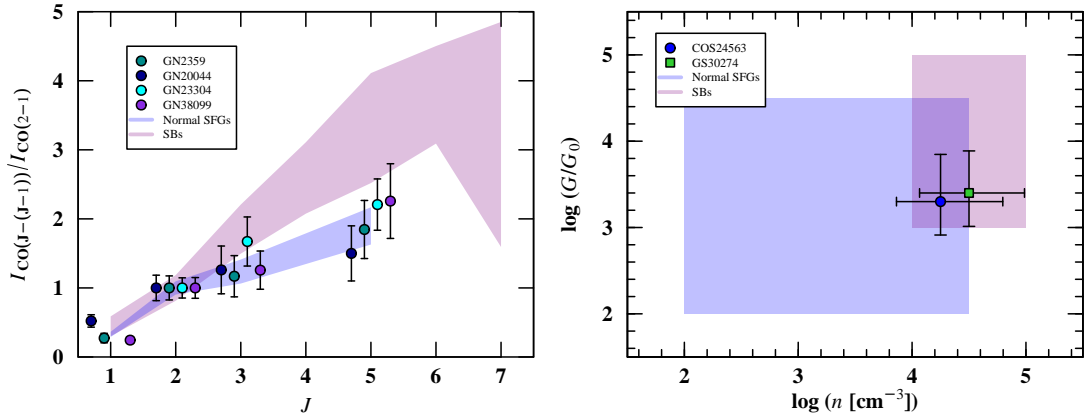


Figure 4.4: Left panel: CO SLEDs from Daddi et al. (2015) for the galaxies in our parent optical sample namely GN2359, GN20044, GN23304, and GN38099 which correspond to BzK -4171, BzK -16000, BzK -17999, and BzK -21000 in Daddi et al. (2015). The normal SFGs CO SLED is represented as a blue shaded region, corresponding to the average SLED of the sample from Daddi et al. (2015). The SBs CO SLED is represented as a purple shaded region and corresponds to the median SLED of SMGs from Bothwell et al. (2013). Right panel: G - n plane with our PDR-modeled COS24563 (18538 in Valentino et al. (2018)) and GS30274 (studied in Popping et al. (2017c)). The normal SFGs span values within the blue shaded region, which corresponds to the sample of MS galaxies from Malhotra et al. (2001). The SBs span values within the purple shaded regions, which refers to the sample of local ULIRGS from Davies et al. (2003).

that appears mildly excited and dense, populating the high-end of normal SFGs ISM properties equivalent to the low-end of SB-like ISM properties. This suggests that the build-up of a compact core leading to cSFGs could happen secularly, or at least that if coming from the product of a rapid starburst-like event the latent ISM has similar properties to that of upper-MS normal SFGs. However, given the small sample sizes and the lack of ISM characterization of cSFGs, it is still difficult to conclude whether the shown ISM properties are the product of a slow secular evolution or the final stages of SBs pointing towards a more rapid evolution.

4.4.3 Diagnostic 3: Radio Emission

The FIR/radio correlation (FRC; e.g., de Jong et al. 1985; Helou et al. 1985; Condon 1992) arises because massive stars ($M_* > 8 M_\odot$) are responsible for producing UV photons that are absorbed and re-emitted by dust at FIR wavelengths, and also responsible for accelerating cosmic ray electrons after exploding as supernovae that originate the synchrotron emission at radio wavelengths. Bressan et al. (2002) modeled the FIR and radio emission of SBs, studying the interplay between the two with the age of the starburst episode and their effect on the FIR/radio ratio ($q \propto L_{\text{IR}}/L_{\text{radio}}$) and the slope of the power law radio spectrum ($S \propto \nu^{-\alpha}$), introducing the $q_{1.4\text{GHz}}-\alpha$ diagram as a diagnostic of SBs age evolution. During the very early phase after the star formation ignites SBs are dominated by FIR emission since only thermal free-free emission from HII regions contributes to the radio emission. At this stage the radio slope is shallow ($\alpha \sim 0.2$) and

4.4. ARE COMPACT STAR-FORMING GALAXIES NORMAL STAR-FORMING GALAXIES OR STARBURSTS?

the radio output is low compared to FIR ($q_{1.4\text{GHz}} \sim 3$). Then, core-collapse supernovae explosions occur feeding relativistic electrons to the galactic magnetic fields and non-thermal synchrotron steepens the radio spectrum increasing at the same time the radio output. At this stage the radio slope progressively gets similar to the value typical of normal SFGs ($\alpha \sim 0.8$) and the FIR/radio ratio progressively decreases to a minimum value ($q_{1.4\text{GHz}} \sim 1.7$). At older ages, the FIR/radio ratio increases again at almost constant radio slope (α and $q_{1.4\text{GHz}}$ reach asymptotic values). These models were first observationally tested by Thomson et al. (2014) for 870 μm -selected SMGs. The authors found that the data populated the predicted region of the parameter space and the stellar masses tend to increase along the SBs evolutionary tracks in the $q_{1.4\text{GHz}}-\alpha$ diagram. We explored the location of our galaxies in this diagram as another diagnostic of their nature. In this section we refer to normal SFGs to the typical values of local SFGs $\alpha = 0.80 \pm 0.25$ (e.g., Condon 1992) and $q_{1.4\text{GHz}} = 2.34 \pm 0.26$ (e.g., Yun et al. 2001).

We calculated α and $q_{1.4\text{GHz}}$ for the galaxies in the radio subset of the FIR sample. α was obtained through fitting a single power law to the data (χ^2 minimization). This corresponds to the slope in the range 325 MHz–3 GHz for galaxies in COSMOS and 610 MHz–1.4 GHz for galaxies in GOODS-North. The FIR/ratio at 1.4GHz is defined as:

$$q_{1.4\text{GHz}} = \log \frac{L_{\text{IR}} [\text{W}]}{3.75 \times 10^{12} [\text{Hz}]} - \log(L_{1.4\text{GHz}} [\text{W Hz}^{-1}]), \quad (4.2)$$

(e.g., Helou et al. 1985; Yun et al. 2001; Magnelli et al. 2015). The uncertainties were calculated over 10000 realizations of the observed radio SED perturbing the photometry within the errors. In Figure 4.5 we present the locus of our radio subset of the FIR sample in the $q_{1.4\text{GHz}}-\alpha$ plane along with the SBs evolutionary tracks from Bressan et al. (2002).

The distribution of galaxies scatters around the normal SFGs values with some outliers. Among the outliers we found ultra-steep spectrum galaxies (USS; $\alpha > 1$). The nature of these galaxies is debated and beyond the scope of our work. Early-stage mergers are capable of steeping the radio spectrum enhancing the radio emission (Murphy 2013). However, we did not find signatures of mergers in the *HST* images and these galaxies have low L_{radio} . This is similar to what was found in Thomson et al. (2014), where the authors argued that an alternative scenario are galaxies with radio jet emission propagating away for the galactic center that is truncated by interactions with dense gas in their environments (O’Dea 1998).

Among the few cSFGs available, it seems that their location could be slightly biased towards Bressan et al. (2002) tracks at older ages. We checked whether there exists a trend in $\Delta\Sigma_{\text{QGs}}$ and, thus, in compactness along Bressan et al. (2002) tracks. Following Thomson et al. (2014), we divide the parameter space overlapping with Bressan et al. (2002) tracks in three boxes representing young (0–20 Myr), middle-aged (33–130 Myr), and old (220–400 Myr) SBs. First, we considered all extended SFGs and cSFGs. Second, since the scatter of normal SFGs overlaps with some regions

4. INVESTIGATING THE TRANSITION FROM STAR-FORMING TO QUIESCENT GALAXIES

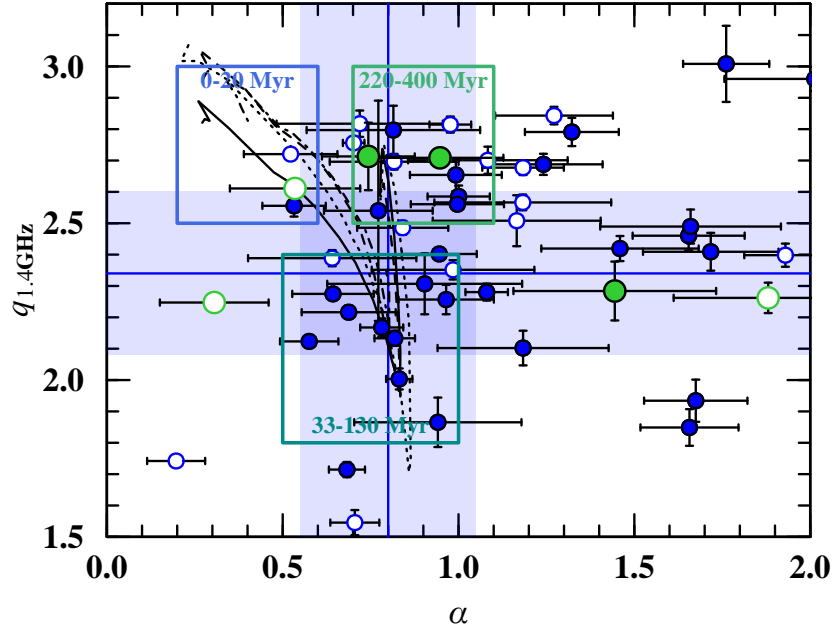


Figure 4.5: $q_{1.4\text{GHz}}-\alpha$ plane. The 1σ scatter of the normal SFGs $q_{1.4\text{GHz}}$ (0.26 dex; Yun et al. 2001) and α (~ 0.25 dex) typical values are represented as a blue shaded region. (Bressan et al. 2002) evolutionary tracks for SBs are plotted as black lines (different linetypes are examples of different t_{burst} in the models). The models run in a logarithmic step ranging $\log t[\text{yr}] = 6.3-8.6$. Following (Thomson et al. 2014) we plot three boxes where young (0–20 Myr), middle-aged (33–130 Myr), and old (220–400 Myr) SBs are expected to be located. AGN-flagged galaxies are represented with empty symbols. Note that some AGN-flagged sources fall outside the plotted region, but we zoom in the area of interest.

of the SBs tracks, we considered only galaxies at $\Delta\text{MS} \geq 3$. In both cases we removed the galaxies classified as AGN, since Bressan et al. (2002) tracks refer only to pure star formation and the contribution from the AGN to the radio spectrum could bias the interpretation. In both cases we found that $\Delta\Sigma_{\text{QG}_s}$ grows with the age of the starburst episode (see Table 4.2), growing from $\Delta\Sigma_{\text{QG}_s} = 0.137$ to $\Delta\Sigma_{\text{QG}_s} = 0.55 \pm 0.63$. These values correspond to the median and the uncertainty is given by the median absolute deviation (MAD). Note that since the increase in compactness is a continuous function, we expect the scatter of each bin given by the MAD to overlap (as in Figure 4.1). We did not find a similar trend in the case of the stellar mass as reported in Thomson et al. (2014), although to make a proper comparison it should be considered that different selections are in place.

Overall, we find a trend of increasing compactness with the age evolution of a starburst episode, leading to cSFGs at the final stages. It indicates that cSFGs are old SBs, while extended SFGs well above the MS are young SBs.

Table 4.2: Properties of Galaxies at Different Age Bins

Age (Myr)	$\log(M_*/M_\odot)$	ΔMS	$\Delta\Sigma_{\text{QG}s}$
0–20	10.67	6.44	0.137
	10.67	6.44	0.137
33–130	10.62 ± 0.37	3.5 ± 1.1	0.21 ± 0.20
	10.50 ± 0.16	3.89 ± 0.55	0.22 ± 0.22
220–400	10.66 ± 0.19	5.14 ± 0.69	0.55 ± 0.63
	10.65 ± 0.19	5.28 ± 0.66	0.50 ± 0.58

The values in the first row of each age bin correspond to the case of all extended SFGs and cSFGs. The values in the second row of each age bin correspond to the case of galaxies at $\Delta\text{MS} \geq 3$. The uncertainties refer to the MAD of the galaxies in each bin and, thus, since in the young (0–20 Myr) age bin there is just one galaxy no dispersion is shown.

4.5 Discussion

4.5.1 Star Formation Efficiency and Selection Limits

We indicated in Section 4.4.1 that the combination of our sample with [Elbaz et al. \(2018\)](#) sample implied no difference between cSFGs and extended SFGs in terms of their SFE. However, it could be the case that [Elbaz et al. \(2018\)](#) galaxies are closer to the $\Delta\Sigma_{\text{QG}s} \sim 1.0$ transition threshold, particularly for the subset with high SFE and low f_{gas} that could be on the last stage before becoming quiescent. In Figure 4.6 we show the location of both samples in the ΔMS - $\Delta\Sigma_{\text{QG}s}$ plane to explore this scenario. We did not find evidence that that is the case as we do not see any distinction between our sample and [Elbaz et al. \(2018\)](#) sample in the ΔMS - $\Delta\Sigma_{\text{QG}s}$ plane.

In Section 4.4.1 we also mentioned that our sample and [Elbaz et al. \(2018\)](#) sample are located in distinct complementary regions in the different diagrams shown Figure 4.3. For instance, we did not find galaxies with simultaneously high SFE and low f_{gas} within our sample, the galaxies described in [Elbaz et al. \(2018\)](#) as SBs that also fall within the scatter of the MS. [Elbaz et al. \(2018\)](#) galaxies occupy a parameter space offset from our sample, which made us consider the possibility that our selection is biased against the detection of SBs within the MS.

The R-J subset of the FIR sample was selected to fulfill a detection criteria in the R-J side of the FIR SED; therefore, establishing a detection limit for the different bands available in the R-J side of the "super-deblended" FIR catalogs in COSMOS and GOODS-North. For $0.5 < z < 3.0$ galaxies these bands are *Herschel*/SPIRE 500 μm , SCUBA 850 μm , AzTEC 1.1 mm, and MAMBO 1.2 mm. We explored the required fluxes in these bands as a function of redshift to be able to detect galaxies that, while located within the scatter of the MS, exhibited enhanced SFE. We employed [Scoville et al. \(2016\)](#) technique to predict the single band flux measurement of the dust continuum expected for a given M_{gas} . In Figure 4.7 we plot the predicted fluxes for the different bands as function of redshift for galaxies with a SFE three times higher (M_{gas} three times lower) than the

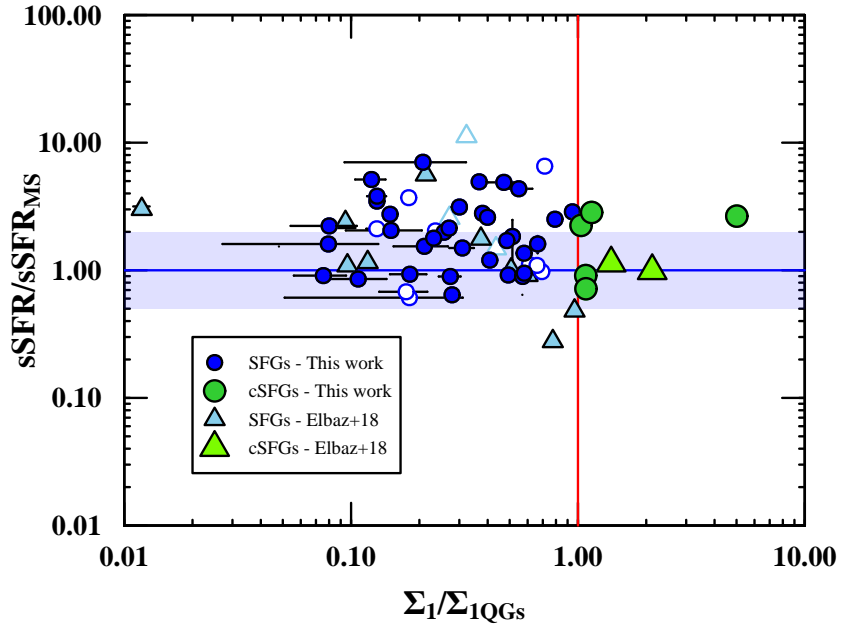


Figure 4.6: $\Delta\text{MS}-\Delta\Sigma_{\text{QGs}}$ plane as presented in Figure 4.1 for the R-J subset of the FIR sample (circles) and Elbaz et al. (2018) sample (triangles). The $\Delta\Sigma_{\text{QGs}}$ uncertainties were calculated over 1000 realizations varying the structural parameters within their uncertainties.

normal SFGs SFE trend at fixed stellar mass for a range of SFRs equivalent to $\Delta\text{MS} = 3$ both above and below the MS. Only galaxies with $M_* \geq 5 \times 10^{11} M_\odot$ start to be detectable. These detection limits are consistent with the fact that we did not detect galaxies with enhanced SFE within the scatter of the MS. In Figure 4.3 we show as a reference the most favorable f_{gas} limit, which would correspond to a galaxy that has a stellar mass as high as the highest stellar mass of the sample ($\log M_* = 11.73$) and located at a redshift such that the predicted detectable f_{gas} given the flux limits at the different bands in the two fields results in a minimum. Even in this extreme case, since there is not a galaxy in our sample that fulfills all the criteria at the same time, justifies that we missed galaxies with simultaneously high SFE and low f_{gas} , like the ones presented in Elbaz et al. (2018).

Therefore, we did not find SB-like SFE within the MS due to the detection limits in the catalogs.

4.5.2 Diagnostics of Burstiness

We examined three indicators of the burstiness of star formation: 1) SFE, 2) ISM, and 3) radio emission.

Regarding SFE there is no difference between cSFGs and extended SFGs. The similar values for cSFGs and extended SFGs extend to various regimes. There are both cSFGs and extended

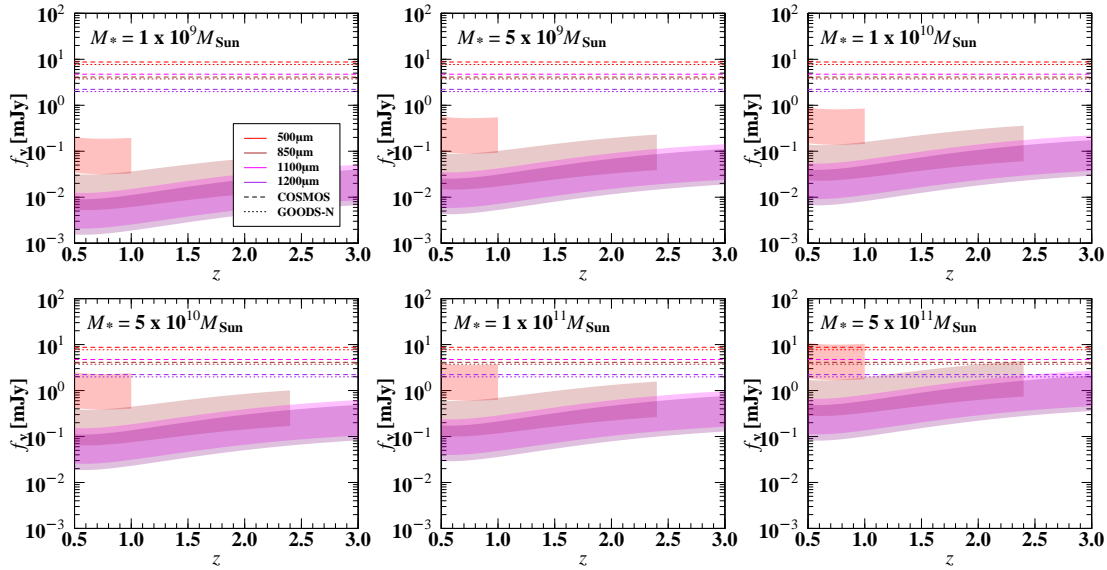


Figure 4.7: Expected flux densities as a function of redshift for a SFE three times higher (M_{gas} three times lower) than the normal SFGs SFE trend for a fixed stellar mass. The width of the shaded areas represent the SFR scatter equivalent to $\Delta\text{MS} = 3$ above and below the MS. The different bands plotted are those available in the COSMOS and GOODS-North fields at $\lambda_{\text{rest}} > 250 \mu\text{m}$ for our redshift limits. The horizontal lines represent the 3σ detection limits for the different bands (color-coded as the legend shows) for COSMOS (dashed lines) and GOODS-North (dotted lines). Note that in the case of GOODS-North the 1100 mm and 1200 mm bands are combined and, thus, the detection limit refers to 1160 mm.

SFGs with low SFE due to high gas fractions, also both cSFGs and extended SFGs with enhanced SFE, some of which have enhanced SFE due to low gas fractions (see Figure 4.3). All together, it suggests that compactness could arise from different origins, like an extended normal SFG with low efficiency and a large gas reservoir that is secularly growing its stellar core, or an extended SB with enhanced efficiency that is rapidly consuming its gas reservoir growing its stellar core.

In terms of the ISM properties, the mildly excited values for extended SFGs in the upper-MS (see Figure 4.4 and Table 4.1) are in line with Tacchella et al. (2016) scenario, that related the width of the MS to the evolution of galaxies following compaction events as part of the secular evolution of SFGs.

On the other hand, regarding the radio emission diagnostic the increasing compactness with the expected age evolution of the radio emission in SBs leads to the conclusion of cSFGs being old SBs. Note also that most of the galaxies are above the scatter of the MS in this part of the analysis, particularly in the old age bin (see Table 4.2). It suggests that the galaxies displaying high sSFR going above the scatter of the MS when becoming cSFGs (see Figure 4.1) are old SBs.

The analysis carried out in our work was performed in an unresolved fashion. This could be the reason of the apparent contradictory conclusions drawn from the SFE and ISM diagnostics

4. INVESTIGATING THE TRANSITION FROM STAR-FORMING TO QUIESCENT GALAXIES

versus the radio emission diagnostic. The conclusions drawn from the ISM and SFE diagnostics can be reconciled with that of the radio emission diagnostic if the SFE and ISM properties do not dominate the entire galaxy in an old SB phase. In that case the galaxy would not display an overall (unresolved) high SFE or SB-like ISM. This scenario would be also supported by the handful of resolved follow-up studies of the ISM of cSFGs, which indicate an undergoing nuclear starburst (e.g., [Spilker et al. 2016a](#); [Barro et al. 2017b](#); [Popping et al. 2017c](#); [Tadaki et al. 2017](#); [Talia et al. 2018](#)).

4.6 Summary and Conclusions

In this work we studied the general population of galaxies based on their location with respect to fundamental structural and star-forming relations, and classified them in extended, compact SFGs, and QGs. Based on a methodology of three diagnostics of the burstiness of star formation: 1) SFE, 2) ISM, and 3) radio emission, we aimed at studying whether cSFGs can be considered normal SFGs or SBs. As a proposed immediate transition population towards QGs, unveiling the nature of cSFGs implies understanding how the build-up of compact stellar cores and subsequent quenching of star formation happens. If cSFGs were normal SFGs it would point towards a secular transition towards quiescence and, conversely, a SB nature of cSFGs would point towards a more rapid transition towards quiescence. In summary we found:

- The distribution of galaxies in the $\Delta\text{MS}-\Delta\Sigma_{\text{QG}s}$ plane reveal that galaxies transition smoothly towards quiescence with increasing compactness. Some extended SFGs quench forming extended QGs. Most of the extended SFGs become compact before they quench, in agreement with ([Barro et al. 2017a](#)). Furthermore, at least some galaxies become compact going above the scatter of the MS.
- The MS is dominated by the most extended SFGs. However, SFGs with increasing compactness that are transitioning to quiescence contribute to lower the normalization of the overall star-forming relation that defines the MS.
- There is no evidence for a distinct SFE in cSFGs and extended SFGs, suggesting that both secular and rapid evolution processes could generate cSFGs.
- Extended SFGs in the upper-MS have ISM properties that connect with the high-end of the ISM properties of normal SFGs, equivalent to the low-end of SBs, and appear similar to those of cSFG, with the caveat of the lack of ISM characterization for cSFGs. This suggest that the growth of a compact stellar core leading to cSFGs could happen secularly. Another explanation could be that if coming from a rapid starburst event, the latent ISM in cSFGs retains similar properties to that of upper-MS normal SFGs.

- There is evidence for a trend in increasing compactness with the expected age evolution of the radio emission in SBs, indicating that cSFGs are old SBs, while extended SFGs above the MS are young SBs.

The apparent contradictory conclusions drawn from the SFE and ISM diagnostics versus the radio emission diagnostic can be reconciled if the SFE and ISM properties do not dominate the entire galaxy in an old SB phase, in agreement with resolved follow-up studies in the literature. We suggest that cSFGs could be SBs winding down and eventually crossing the main sequence towards quiescence.

Acknowledgments

We thank A. Bressan and A. P. Thomson for their support on the starburst evolutionary tracks in radio. C.G.G and S.T. acknowledge support from the European Research Council (ERC) Consolidator Grant funding scheme (project ConTExt, grant number: 648179). G.M. and F.V. acknowledge the Villum Fonden research grant 13160 "Gas to stars, stars to dust: tracing star formation across cosmic time".

The Cosmic Dawn Center is funded by the Danish National Research Foundation.

Conclusions and Future Research

In this chapter I summarize the main finding and conclusions from the work presented in this thesis, devoted to study the evolutionary sequence of massive elliptical galaxies and, particularly, high-redshift starbursts in connection with the origin of the quiescent population of galaxies.

In Chapter 2 I presented a detailed spatially resolved study of the stars and dust in a sample of six SMGs at $z \sim 4.5$. The stellar emission probed by *HST* is extended and divided into multiple merging components with stellar mass ratios typical of minor mergers. The far-infrared dust continuum probed by ALMA is extremely compact ($r_e < 1$ kpc), locating the bulk of star formation, associated with the most massive stellar component of the merger. Given the expected extinction in such compact dusty regions, the detection of stellar light implies that the stars and dust emission come from physically unrelated regions, which explains the puzzling location of SMGs in the IRX- β relation. I studied the location of the SMGs sample in comparison with their proposed cQGs descendants at $z \sim 2$ in the size-stellar mass plane. While the SMGs are less massive and even more compact than the cQGs, the difference can be explained by the growth in stellar mass through the ongoing starburst episode and in size via the minor mergers. This study furthers the grounds of $z \gtrsim 3$ SMGs as progenitors of $z \sim 2$ QGs and the importance of minor mergers in the entire evolution of giant elliptical galaxies.

In addition, part of the $z \sim 4.5$ SMGs sample analyzed in Chapter 2 have complementary [C II] and CO line observations. The analysis carried out by Jones et al. (2017) and Jiménez-Andrade et al. (2018) indicates evidence for rotationally supported star-forming disks. $z \sim 2$ cQGs exhibit rotationally-supported stellar disks (e.g., Newman et al. 2015; Toft et al. 2017; Newman et al. 2018). Therefore, considering these two complementary results the evolutionary picture of $z \gtrsim 3$ SMGs as progenitors of $z \sim 2$ QGs gains an additional kinematical evidence, i.e., SMGs form stars within gaseous disks that once quenched would leave behind rotating stellar disks to evolve morphologically and kinematically into larger slow quiescent rotators mainly via dry minor mergers.

The stellar structure at rest-frame optical/near-infrared wavelengths remains yet an unknown for SMGs at $z > 3$. The *James Webb Space Telescope (JWST)* will revolutionize our understanding of galaxy formation and evolution with unprecedented detail at near/mid-infrared wavelengths. I will request for follow-up observations of this sample of SMGs to uncover their rest-frame

optical/near-infrared stellar structure in order to fully understand the evolution of their stellar mass profiles to better establish their evolutionary connection with $z \sim 2$ QGs.

In Chapter 3 I presented a follow-up study of dust continuum ALMA $870 \mu\text{m}$ detections with pairwise separations of a few arcsec. Theoretical simulations and other follow-up studies of single-dish surveys failed to reproduce this population of multicomponent and small separation dust-rich galaxies, suggesting that a fraction should be line-of-sight projections. I studied three of these candidate protoclusters with ALMA and VLA successfully detecting CO(3-2) and CO(1-0) lines for all the $870 \mu\text{m}$ detections, locating them at the same redshift and, thus, confirming three out of three candidates as protocluster core systems. Two of these systems are newly discovered protocluster cores named HELAISS02 ($z = 2.171 \pm 0.004$) and HXMM20 ($z = 2.602 \pm 0.002$). The gas, dust, and stellar properties reveal very large molecular gas fractions, yet low stellar masses, pushing the galaxies above the main sequence of star formation, but with no enhanced star formation efficiencies. I suggested that they might be newly formed galaxies migrating into the main sequence of star formation. The properties of the three systems compared to each other and to field galaxies suggest a different evolutionary stage between systems. This study shows the existence of groups of dusty SFGs unexpected from the theory and furthers our knowledge about the first stages of galaxy clusters.

Sources with such small pairwise separations need high-resolution far-infrared observations to determine precisely their star formation efficiencies and study trends in this quantity. ALMA is perfectly suitable for this follow-up study. In addition, gas-phase metallicities could reveal the individual gas-to-dust ratios for an accurate estimation of gas masses and gas conversion factors. Finally, the confirmation of a larger structure of members located at a similar redshift could reveal whether these systems will evolve into a cluster at $z = 0$.

In Chapter 4 I studied three diagnostics of the burstiness of star formation: 1) Star formation efficiency, 2) ISM, and 3) radio emission, for galaxies classified according to their location with respect to fundamental star-forming and structural relations in extended, compact SFGs, and QGs. The star formation efficiency diagnostic shows that cSFGs and extended SFGs have no evidence for a different efficiency. The ISM diagnostic indicate that extended upper main sequence SFGs and cSFGs have analogous properties that resemble the high-end of the ISM properties of normal SFGs, equivalent to the low-end of starburst galaxies. However, the radio emission diagnostic reveals that compactness grows along the expected evolution in the radio emission with the age of a starburst, implying that cSFGs are old starbursts, while extended SFGs are young starbursts. The three diagnostics can be brought into agreement if the SFE and ISM properties do not dominate the entire galaxy in an old starburst phase, in agreement with resolved follow-up studies in the literature. I suggested that cSFGs could be old starbursts winding down and eventually crossing the main sequence towards quiescence.

5. CONCLUSIONS AND FUTURE RESEARCH

For my future research I plan to expand the diagnostics outlined in Chapter 4. In the case of the star formation efficiencies, the study would benefit from incorporating ALMA data in order to reach intrinsically fainter galaxies in the far-infrared that could indeed have enhanced star formation efficiencies. ALMA data could be gathered for the COSMOS field, but also for GOODS-South with the corresponding increase in the sample statistics by incorporating a new field. ALMA follow-up studies to characterize the ISM properties of cSFGs are also planned, since they are currently limited to a handful of sources in the literature. Finally, a selected sample to characterize simultaneously the three diagnostics would provide invaluable insight about how the build-up of compact stellar cores and subsequent quenching of star formation happens.

Together, the work presented in my Ph.D. thesis contributes towards establishing a unified picture of the progenitors of massive galaxies, linking the starburst, normal star-forming, and quiescent galaxy populations. It provides a fundamental insight in the physical processes shaping galaxy formation and evolution.

The combination of future and current facilities such as *JWST*, Euclid, ALMA, VLA, and SKA will revolutionize our understanding of galaxy formation and evolution and will provide answers in many of the fundamental questions outlined in Chapter 1: What are the physical processes triggering starburst galaxies? How much of the total star formation happened in a starburst mode and how much in a normal mode? What are the physical processes responsible for quenching galaxies? Did the quenching of star formation happen fast or slow? What is the dependence on the cosmic epoch of these questions?

List of Publications

Source (ADS) (31-03-2019)

published: 12 – first author: 4 – citations: 64

1. **Gómez-Guijarro** et al., *Confirming Herschel Candidate Protoclusters from ALMA/VLA CO Observations*, ApJ, 872, 117, 2019
2. Cortzen et al., *PAHs as tracers of the molecular gas in star-forming galaxies*, MNRAS, 482, 1618, 2019 (arXiv:1810.05178)
3. Borlaff et al., *The missing light of the Hubble Ultra Deep Field*, A&A, 621, 133, 2019 (arXiv:1810.00002)
4. Kubo et al., *The Rest-frame Optical Sizes of Massive Galaxies with Suppressed Star Formation at $z \sim 4$* , ApJ, 867, 1, 2018 (arXiv:1810.00543)
5. Fujimoto et al., *ALMA 26 Arcmin² Survey of GOODS-S at One Millimeter (ASAGAO): Average Morphology of High- z Dusty Star-forming Galaxies in an Exponential Disk ($n \simeq 1$)*, ApJ, 861, 7, 2018 (arXiv:1802.02136)
6. Jimeénez-Andrade et al., *Molecular gas in AzTEC/C159: a star-forming disk galaxy 1.3 Gyr after the Big Bang*, A&A, 615, 25, 2018 (arXiv:1710.10181)
7. **Gómez-Guijarro** et al., *Starburst to Quiescent from HST/ALMA: Stars and Dust Unveil Minor Mergers in Submillimeter Galaxies at $z \sim 4.5$* , ApJ, 856, 121, 2018, (arXiv:1802.07751)
8. Lee et al., *The fine line between normal and starburst galaxies*, MNRAS, 471, 2124, 2017 (arXiv:1710.02757)
9. **Gómez-Guijarro** et al., *A comparison between the soft X-ray and [O III] morphologies of active galactic nuclei*, MNRAS, 469, 2720, 2017 (arXiv:1705.00633)
10. Magdis et al., *Dust and gas in star-forming galaxies at $z \sim 3$. Extending galaxy uniformity to 11.5 billion years*, A&A, 603, 93, 2017 (arXiv:1705.06296)
11. Toft et al., *A massive, dead disk galaxy in the early Universe*, **Nature**, 546, 510, 2017 (arXiv:1706.07030)

List of Publications

12. **Gómez-Guijarro** et al., *Properties of galaxies at the faint end of the $H\alpha$ luminosity function at $z \sim 0.62$* , A&A, 591, 151, 2016 (arXiv:1604.04632)

Bibliography

- Abdo, A. A., Ackermann, M., Ajello, M., et al. 2010, *ApJ*, 710, 133, doi: [10.1088/0004-637X/710/1/133](https://doi.org/10.1088/0004-637X/710/1/133)
- Alaghband-Zadeh, S., Chapman, S. C., Swinbank, A. M., et al. 2013, *MNRAS*, 435, 1493, doi: [10.1093/mnras/stt1390](https://doi.org/10.1093/mnras/stt1390)
- Alpher, R. A., Bethe, H., & Gamow, G. 1948, *Physical Review*, 73, 803, doi: [10.1103/PhysRev.73.803](https://doi.org/10.1103/PhysRev.73.803)
- Alpher, R. A., & Herman, R. 1948, *Nature*, 162, 774, doi: [10.1038/162774b0](https://doi.org/10.1038/162774b0)
- Andrews, B. H., & Thompson, T. A. 2011, *ApJ*, 727, 97, doi: [10.1088/0004-637X/727/2/97](https://doi.org/10.1088/0004-637X/727/2/97)
- Aravena, M., Bertoldi, F., Carilli, C., et al. 2010, *ApJ*, 708, L36, doi: [10.1088/2041-8205/708/1/L36](https://doi.org/10.1088/2041-8205/708/1/L36)
- Arnouts, S., Cristiani, S., Moscardini, L., et al. 1999, *MNRAS*, 310, 540, doi: [10.1046/j.1365-8711.1999.02978.x](https://doi.org/10.1046/j.1365-8711.1999.02978.x)
- Astropy Collaboration, Robitaille, T. P., Tollerud, E. J., et al. 2013, *A&A*, 558, A33, doi: [10.1051/0004-6361/201322068](https://doi.org/10.1051/0004-6361/201322068)
- Avni, Y. 1976, *ApJ*, 210, 642, doi: [10.1086/154870](https://doi.org/10.1086/154870)
- Bardeen, J. M., Steinhardt, P. J., & Turner, M. S. 1983, *Phys. Rev. D*, 28, 679, doi: [10.1103/PhysRevD.28.679](https://doi.org/10.1103/PhysRevD.28.679)
- Barisic, I., Faisst, A. L., Capak, P. L., et al. 2017, *ApJ*, 845, 41, doi: [10.3847/1538-4357/aa7eda](https://doi.org/10.3847/1538-4357/aa7eda)
- Barnes, J. E. 1988, *ApJ*, 331, 699, doi: [10.1086/166593](https://doi.org/10.1086/166593)
- Barnes, J. E., & Hernquist, L. E. 1991, *ApJ*, 370, L65, doi: [10.1086/185978](https://doi.org/10.1086/185978)
- Barro, G., Faber, S. M., Pérez-González, P. G., et al. 2013, *ApJ*, 765, 104, doi: [10.1088/0004-637X/765/2/104](https://doi.org/10.1088/0004-637X/765/2/104)
- . 2014, *ApJ*, 791, 52, doi: [10.1088/0004-637X/791/1/52](https://doi.org/10.1088/0004-637X/791/1/52)
- Barro, G., Kriek, M., Pérez-González, P. G., et al. 2016, *ApJ*, 827, L32, doi: [10.3847/2041-8205/827/2/L32](https://doi.org/10.3847/2041-8205/827/2/L32)

BIBLIOGRAPHY

- Barro, G., Faber, S. M., Koo, D. C., et al. 2017a, *ApJ*, 840, 47, doi: [10.3847/1538-4357/aa6b05](https://doi.org/10.3847/1538-4357/aa6b05)
- Barro, G., Kriek, M., Pérez-González, P. G., et al. 2017b, *ApJ*, 851, L40, doi: [10.3847/2041-8213/aa9f0d](https://doi.org/10.3847/2041-8213/aa9f0d)
- Baugh, C. M., Cole, S., Frenk, C. S., & Lacey, C. G. 1998, *ApJ*, 498, 504, doi: [10.1086/305563](https://doi.org/10.1086/305563)
- Baum, W. A. 1959, *PASP*, 71, 106, doi: [10.1086/127346](https://doi.org/10.1086/127346)
- Bell, E. F., Wolf, C., Meisenheimer, K., et al. 2004, *ApJ*, 608, 752, doi: [10.1086/420778](https://doi.org/10.1086/420778)
- Belli, S., Newman, A. B., & Ellis, R. S. 2017, *ApJ*, 834, 18, doi: [10.3847/1538-4357/834/1/18](https://doi.org/10.3847/1538-4357/834/1/18)
- Bender, R. 1988, *A&A*, 202, L5
- Bender, R., & Nieto, J.-L. 1990, *A&A*, 239, 97
- Berta, S., Lutz, D., Genzel, R., Förster-Schreiber, N. M., & Tacconi, L. J. 2016, *A&A*, 587, A73, doi: [10.1051/0004-6361/201527746](https://doi.org/10.1051/0004-6361/201527746)
- Bertin, E., & Arnouts, S. 1996, *A&AS*, 117, 393, doi: [10.1051/aas:1996164](https://doi.org/10.1051/aas:1996164)
- Bertin, E., Mellier, Y., Radovich, M., et al. 2002, in *Astronomical Society of the Pacific Conference Series*, Vol. 281, *Astronomical Data Analysis Software and Systems XI*, ed. D. A. Bohlender, D. Durand, & T. H. Handley, 228
- Bertoldi, F., Carilli, C., Aravena, M., et al. 2007, *ApJS*, 172, 132, doi: [10.1086/520511](https://doi.org/10.1086/520511)
- Bezanson, R., van Dokkum, P. G., Tal, T., et al. 2009, *ApJ*, 697, 1290, doi: [10.1088/0004-637X/697/2/1290](https://doi.org/10.1088/0004-637X/697/2/1290)
- Bigiel, F., Leroy, A., Walter, F., et al. 2008, *AJ*, 136, 2846, doi: [10.1088/0004-6256/136/6/2846](https://doi.org/10.1088/0004-6256/136/6/2846)
- Binney, J. 1978, *MNRAS*, 183, 501, doi: [10.1093/mnras/183.3.501](https://doi.org/10.1093/mnras/183.3.501)
- Blain, A. W., Chapman, S. C., Smail, I., & Ivison, R. 2004, *ApJ*, 611, 725, doi: [10.1086/422353](https://doi.org/10.1086/422353)
- Blain, A. W., Smail, I., Ivison, R. J., Kneib, J.-P., & Frayer, D. T. 2002, *Phys. Rep.*, 369, 111, doi: [10.1016/S0370-1573\(02\)00134-5](https://doi.org/10.1016/S0370-1573(02)00134-5)
- Blitz, L., & Rosolowsky, E. 2006, *ApJ*, 650, 933, doi: [10.1086/505417](https://doi.org/10.1086/505417)
- Blumenthal, G. R., Faber, S. M., Primack, J. R., & Rees, M. J. 1984, *Nature*, 311, 517, doi: [10.1038/311517a0](https://doi.org/10.1038/311517a0)

- Bolatto, A. D., Wolfire, M., & Leroy, A. K. 2013, *ARA&A*, 51, 207, doi: [10.1146/annurev-astro-082812-140944](https://doi.org/10.1146/annurev-astro-082812-140944)
- Bothwell, M. S., Smail, I., Chapman, S. C., et al. 2013, *MNRAS*, 429, 3047, doi: [10.1093/mnras/sts562](https://doi.org/10.1093/mnras/sts562)
- Bouwens, R. J., Illingworth, G. D., Franx, M., et al. 2009, *ApJ*, 705, 936, doi: [10.1088/0004-637X/705/1/936](https://doi.org/10.1088/0004-637X/705/1/936)
- Bouwens, R. J., Illingworth, G. D., Oesch, P. A., et al. 2015, *ApJ*, 803, 34, doi: [10.1088/0004-637X/803/1/34](https://doi.org/10.1088/0004-637X/803/1/34)
- Bradley, L., Sipocz, B., Robitaille, T., et al. 2016, *astropy/photutils: v0.3*, doi: [10.5281/zenodo.164986](https://doi.org/10.5281/zenodo.164986). <https://doi.org/10.5281/zenodo.164986>
- Brammer, G. B., Whitaker, K. E., van Dokkum, P. G., et al. 2011, *ApJ*, 739, 24, doi: [10.1088/0004-637X/739/1/24](https://doi.org/10.1088/0004-637X/739/1/24)
- Brammer, G. B., van Dokkum, P. G., Franx, M., et al. 2012, *ApJS*, 200, 13, doi: [10.1088/0067-0049/200/2/13](https://doi.org/10.1088/0067-0049/200/2/13)
- Bressan, A., Silva, L., & Granato, G. L. 2002, *A&A*, 392, 377, doi: [10.1051/0004-6361:20020960](https://doi.org/10.1051/0004-6361:20020960)
- Briggs, D. S. 1995, PhD thesis, New Mexico Institute of Mining and Technology
- Brinchmann, J., Charlot, S., White, S. D. M., et al. 2004, *MNRAS*, 351, 1151, doi: [10.1111/j.1365-2966.2004.07881.x](https://doi.org/10.1111/j.1365-2966.2004.07881.x)
- Brisbin, D., Miettinen, O., Aravena, M., et al. 2017, *A&A*, 608, A15, doi: [10.1051/0004-6361/201730558](https://doi.org/10.1051/0004-6361/201730558)
- Bruzual, G., & Charlot, S. 2003, *MNRAS*, 344, 1000, doi: [10.1046/j.1365-8711.2003.06897.x](https://doi.org/10.1046/j.1365-8711.2003.06897.x)
- Buat, V., Iglesias-Páramo, J., Seibert, M., et al. 2005, *ApJ*, 619, L51, doi: [10.1086/423241](https://doi.org/10.1086/423241)
- Buitrago, F., Trujillo, I., Conselice, C. J., et al. 2008, *ApJ*, 687, L61, doi: [10.1086/592836](https://doi.org/10.1086/592836)
- Bussmann, R. S., Gurwell, M. A., Fu, H., et al. 2012, *ApJ*, 756, 134, doi: [10.1088/0004-637X/756/2/134](https://doi.org/10.1088/0004-637X/756/2/134)
- Bussmann, R. S., Pérez-Fournon, I., Amber, S., et al. 2013, *ApJ*, 779, 25, doi: [10.1088/0004-637X/779/1/25](https://doi.org/10.1088/0004-637X/779/1/25)

BIBLIOGRAPHY

- Bussmann, R. S., Riechers, D., Fialkov, A., et al. 2015, *ApJ*, 812, 43, doi: [10.1088/0004-637X/812/1/43](https://doi.org/10.1088/0004-637X/812/1/43)
- Bustamante, S., Sparre, M., Springel, V., & Grand, R. J. J. 2018, *MNRAS*, 479, 3381, doi: [10.1093/mnras/sty1692](https://doi.org/10.1093/mnras/sty1692)
- Cañameras, R., Nesvadba, N. P. H., Guery, D., et al. 2015, *A&A*, 581, A105, doi: [10.1051/0004-6361/201425128](https://doi.org/10.1051/0004-6361/201425128)
- Calura, F., Pozzi, F., Cresci, G., et al. 2017, *MNRAS*, 465, 54, doi: [10.1093/mnras/stw2749](https://doi.org/10.1093/mnras/stw2749)
- Calzetti, D., Armus, L., Bohlin, R. C., et al. 2000, *ApJ*, 533, 682, doi: [10.1086/308692](https://doi.org/10.1086/308692)
- Capak, P., Aussel, H., Ajiki, M., et al. 2007, *ApJS*, 172, 99, doi: [10.1086/519081](https://doi.org/10.1086/519081)
- Capak, P., Carilli, C. L., Lee, N., et al. 2008, *ApJ*, 681, L53, doi: [10.1086/590555](https://doi.org/10.1086/590555)
- Capak, P. L., Riechers, D., Scoville, N. Z., et al. 2011, *Nature*, 470, 233, doi: [10.1038/nature09681](https://doi.org/10.1038/nature09681)
- Capak, P. L., Carilli, C., Jones, G., et al. 2015, *Nature*, 522, 455, doi: [10.1038/nature14500](https://doi.org/10.1038/nature14500)
- Cappellari, M., Bacon, R., Bureau, M., et al. 2006, *MNRAS*, 366, 1126, doi: [10.1111/j.1365-2966.2005.09981.x](https://doi.org/10.1111/j.1365-2966.2005.09981.x)
- Carilli, C. L., & Walter, F. 2013, *ARA&A*, 51, 105, doi: [10.1146/annurev-astro-082812-140953](https://doi.org/10.1146/annurev-astro-082812-140953)
- Carollo, C. M., Bschorr, T. J., Renzini, A., et al. 2013, *ApJ*, 773, 112, doi: [10.1088/0004-637X/773/2/112](https://doi.org/10.1088/0004-637X/773/2/112)
- Casey, C. M. 2016, *ApJ*, 824, 36, doi: [10.3847/0004-637X/824/1/36](https://doi.org/10.3847/0004-637X/824/1/36)
- Casey, C. M., Narayanan, D., & Cooray, A. 2014a, *Phys. Rep.*, 541, 45, doi: [10.1016/j.physrep.2014.02.009](https://doi.org/10.1016/j.physrep.2014.02.009)
- Casey, C. M., Chen, C.-C., Cowie, L. L., et al. 2013, *MNRAS*, 436, 1919, doi: [10.1093/mnras/stt1673](https://doi.org/10.1093/mnras/stt1673)
- Casey, C. M., Scoville, N. Z., Sanders, D. B., et al. 2014b, *ApJ*, 796, 95, doi: [10.1088/0004-637X/796/2/95](https://doi.org/10.1088/0004-637X/796/2/95)
- Casey, C. M., Cooray, A., Capak, P., et al. 2015, *ApJ*, 808, L33, doi: [10.1088/2041-8205/808/2/L33](https://doi.org/10.1088/2041-8205/808/2/L33)

BIBLIOGRAPHY

- Castellano, M., Fontana, A., Grazian, A., et al. 2012, *A&A*, 540, A39, doi: [10.1051/0004-6361/201118050](https://doi.org/10.1051/0004-6361/201118050)
- Chabrier, G. 2003, *PASP*, 115, 763, doi: [10.1086/376392](https://doi.org/10.1086/376392)
- Chapman, S. C., Blain, A., Ibata, R., et al. 2009, *ApJ*, 691, 560, doi: [10.1088/0004-637X/691/1/560](https://doi.org/10.1088/0004-637X/691/1/560)
- Chapman, S. C., Blain, A. W., Smail, I., & Ivison, R. J. 2005, *ApJ*, 622, 772, doi: [10.1086/428082](https://doi.org/10.1086/428082)
- Chen, C.-C., Smail, I., Swinbank, A. M., et al. 2015, *ApJ*, 799, 194, doi: [10.1088/0004-637X/799/2/194](https://doi.org/10.1088/0004-637X/799/2/194)
- Chen, C.-C., Hodge, J. A., Smail, I., et al. 2017, *ApJ*, 846, 108, doi: [10.3847/1538-4357/aa863a](https://doi.org/10.3847/1538-4357/aa863a)
- Chiang, Y.-K., Overzier, R., & Gebhardt, K. 2013, *ApJ*, 779, 127, doi: [10.1088/0004-637X/779/2/127](https://doi.org/10.1088/0004-637X/779/2/127)
- Chiang, Y.-K., Overzier, R. A., Gebhardt, K., & Henriques, B. 2017, *ApJ*, 844, L23, doi: [10.3847/2041-8213/aa7e7b](https://doi.org/10.3847/2041-8213/aa7e7b)
- Chiang, Y.-K., Overzier, R. A., Gebhardt, K., et al. 2015, *ApJ*, 808, 37, doi: [10.1088/0004-637X/808/1/37](https://doi.org/10.1088/0004-637X/808/1/37)
- Cimatti, A., Cassata, P., Pozzetti, L., et al. 2008, *A&A*, 482, 21, doi: [10.1051/0004-6361:20078739](https://doi.org/10.1051/0004-6361:20078739)
- Civano, F., Marchesi, S., Comastri, A., et al. 2016, *ApJ*, 819, 62, doi: [10.3847/0004-637X/819/1/62](https://doi.org/10.3847/0004-637X/819/1/62)
- Clements, D. L., Braglia, F. G., Hyde, A. K., et al. 2014, *MNRAS*, 439, 1193, doi: [10.1093/mnras/stt2253](https://doi.org/10.1093/mnras/stt2253)
- Clements, D. L., Braglia, F., Petitpas, G., et al. 2016, *MNRAS*, 461, 1719, doi: [10.1093/mnras/stw1224](https://doi.org/10.1093/mnras/stw1224)
- Collins, C. A., Stott, J. P., Hilton, M., et al. 2009, *Nature*, 458, 603, doi: [10.1038/nature07865](https://doi.org/10.1038/nature07865)
- Condon, J. J. 1992, *ARA&A*, 30, 575, doi: [10.1146/annurev.aa.30.090192.003043](https://doi.org/10.1146/annurev.aa.30.090192.003043)
- Conselice, C. J., Bershadsky, M. A., Dickinson, M., & Papovich, C. 2003, *AJ*, 126, 1183, doi: [10.1086/377318](https://doi.org/10.1086/377318)
- Coogan, R. T., Daddi, E., Sargent, M. T., et al. 2018, *MNRAS*, 479, 703, doi: [10.1093/mnras/sty1446](https://doi.org/10.1093/mnras/sty1446)

BIBLIOGRAPHY

- Cowley, W. I., Lacey, C. G., Baugh, C. M., & Cole, S. 2015, MNRAS, 446, 1784, doi: [10.1093/mnras/stu2179](https://doi.org/10.1093/mnras/stu2179)
- Cox, T. J., Dutta, S. N., Di Matteo, T., et al. 2006, ApJ, 650, 791, doi: [10.1086/507474](https://doi.org/10.1086/507474)
- Cucciati, O., Lemaux, B. C., Zamorani, G., et al. 2018, A&A, 619, A49, doi: [10.1051/0004-6361/201833655](https://doi.org/10.1051/0004-6361/201833655)
- da Cunha, E., Charlot, S., & Elbaz, D. 2008, MNRAS, 388, 1595, doi: [10.1111/j.1365-2966.2008.13535.x](https://doi.org/10.1111/j.1365-2966.2008.13535.x)
- Daddi, E., Cimatti, A., & Renzini, A. 2000, A&A, 362, L45
- Daddi, E., Renzini, A., Pirzkal, N., et al. 2005, ApJ, 626, 680, doi: [10.1086/430104](https://doi.org/10.1086/430104)
- Daddi, E., Dickinson, M., Morrison, G., et al. 2007, ApJ, 670, 156, doi: [10.1086/521818](https://doi.org/10.1086/521818)
- Daddi, E., Dannerbauer, H., Stern, D., et al. 2009, ApJ, 694, 1517, doi: [10.1088/0004-637X/694/2/1517](https://doi.org/10.1088/0004-637X/694/2/1517)
- Daddi, E., Bournaud, F., Walter, F., et al. 2010a, ApJ, 713, 686, doi: [10.1088/0004-637X/713/1/686](https://doi.org/10.1088/0004-637X/713/1/686)
- Daddi, E., Elbaz, D., Walter, F., et al. 2010b, ApJ, 714, L118, doi: [10.1088/2041-8205/714/1/L118](https://doi.org/10.1088/2041-8205/714/1/L118)
- Daddi, E., Dannerbauer, H., Liu, D., et al. 2015, A&A, 577, A46, doi: [10.1051/0004-6361/201425043](https://doi.org/10.1051/0004-6361/201425043)
- Daddi, E., Jin, S., Strazzullo, V., et al. 2017, ApJ, 846, L31, doi: [10.3847/2041-8213/aa8808](https://doi.org/10.3847/2041-8213/aa8808)
- Dame, T. M., Hartmann, D., & Thaddeus, P. 2001, ApJ, 547, 792, doi: [10.1086/318388](https://doi.org/10.1086/318388)
- Dannerbauer, H., Kurk, J. D., De Breuck, C., et al. 2014, A&A, 570, A55, doi: [10.1051/0004-6361/201423771](https://doi.org/10.1051/0004-6361/201423771)
- Dannerbauer, H., Lehnert, M. D., Emonts, B., et al. 2017, A&A, 608, A48, doi: [10.1051/0004-6361/201730449](https://doi.org/10.1051/0004-6361/201730449)
- Davidzon, I., Ilbert, O., Laigle, C., et al. 2017, A&A, 605, A70, doi: [10.1051/0004-6361/201730419](https://doi.org/10.1051/0004-6361/201730419)
- Davies, R. I., Sternberg, A., Lehnert, M., & Tacconi-Garman, L. E. 2003, ApJ, 597, 907, doi: [10.1086/378634](https://doi.org/10.1086/378634)

- Davies, R. L., Efstathiou, G., Fall, S. M., Illingworth, G., & Schechter, P. L. 1983, *ApJ*, 266, 41, doi: [10.1086/160757](https://doi.org/10.1086/160757)
- de Jong, T., Klein, U., Wielebinski, R., & Wunderlich, E. 1985, *A&A*, 147, L6
- de Vaucouleurs, G. 1961, *ApJS*, 5, 233, doi: [10.1086/190056](https://doi.org/10.1086/190056)
- de Zeeuw, P. T., Bureau, M., Emsellem, E., et al. 2002, *MNRAS*, 329, 513, doi: [10.1046/j.1365-8711.2002.05059.x](https://doi.org/10.1046/j.1365-8711.2002.05059.x)
- Decarli, R., Walter, F., Venemans, B. P., et al. 2017, *Nature*, 545, 457, doi: [10.1038/nature22358](https://doi.org/10.1038/nature22358)
- Dekel, A., Zolotov, A., Tweed, D., et al. 2013, *MNRAS*, 435, 999, doi: [10.1093/mnras/stt1338](https://doi.org/10.1093/mnras/stt1338)
- Del Moro, A., Alexander, D. M., Mullaney, J. R., et al. 2013, *A&A*, 549, A59, doi: [10.1051/0004-6361/201219880](https://doi.org/10.1051/0004-6361/201219880)
- Di Matteo, P., Bournaud, F., Martig, M., et al. 2008, *A&A*, 492, 31, doi: [10.1051/0004-6361:200809480](https://doi.org/10.1051/0004-6361:200809480)
- Díaz-Santos, T., Assef, R. J., Blain, A. W., et al. 2016, *ApJ*, 816, L6, doi: [10.3847/2041-8205/816/1/L6](https://doi.org/10.3847/2041-8205/816/1/L6)
- Dicke, R. H., Peebles, P. J. E., Roll, P. G., & Wilkinson, D. T. 1965, *ApJ*, 142, 414, doi: [10.1086/148306](https://doi.org/10.1086/148306)
- Dickinson, M., Giavalisco, M., & GOODS Team. 2003, in *The Mass of Galaxies at Low and High Redshift*, ed. R. Bender & A. Renzini, 324
- Diener, C., Lilly, S. J., Knobel, C., et al. 2013, *ApJ*, 765, 109, doi: [10.1088/0004-637X/765/2/109](https://doi.org/10.1088/0004-637X/765/2/109)
- Diener, C., Lilly, S. J., Ledoux, C., et al. 2015, *ApJ*, 802, 31, doi: [10.1088/0004-637X/802/1/31](https://doi.org/10.1088/0004-637X/802/1/31)
- Djorgovski, S., & Davis, M. 1987, *ApJ*, 313, 59, doi: [10.1086/164948](https://doi.org/10.1086/164948)
- Donevski, D., Buat, V., Boone, F., et al. 2018, *A&A*, 614, A33, doi: [10.1051/0004-6361/201731888](https://doi.org/10.1051/0004-6361/201731888)
- Dowell, C. D., Conley, A., Glenn, J., et al. 2014, *ApJ*, 780, 75, doi: [10.1088/0004-637X/780/1/75](https://doi.org/10.1088/0004-637X/780/1/75)
- Downes, D., & Solomon, P. M. 1998, *ApJ*, 507, 615, doi: [10.1086/306339](https://doi.org/10.1086/306339)

BIBLIOGRAPHY

- Draine, B. T., & Li, A. 2007, *ApJ*, 657, 810, doi: [10.1086/511055](https://doi.org/10.1086/511055)
- Draine, B. T., Dale, D. A., Bendo, G., et al. 2007, *ApJ*, 663, 866, doi: [10.1086/518306](https://doi.org/10.1086/518306)
- Dressler, A., Lynden-Bell, D., Burstein, D., et al. 1987, *ApJ*, 313, 42, doi: [10.1086/164947](https://doi.org/10.1086/164947)
- Duc, P.-A., Cuillandre, J.-C., Serra, P., et al. 2011, *MNRAS*, 417, 863, doi: [10.1111/j.1365-2966.2011.19137.x](https://doi.org/10.1111/j.1365-2966.2011.19137.x)
- Duc, P.-A., Cuillandre, J.-C., Karabal, E., et al. 2015, *MNRAS*, 446, 120, doi: [10.1093/mnras/stu2019](https://doi.org/10.1093/mnras/stu2019)
- Eales, S., Dunne, L., Clements, D., et al. 2010, *PASP*, 122, 499, doi: [10.1086/653086](https://doi.org/10.1086/653086)
- Efstathiou, G., & Silk, J. 1983, *Fund. Cosmic Phys.*, 9, 1
- Eggen, O. J., Lynden-Bell, D., & Sandage, A. R. 1962, *ApJ*, 136, 748, doi: [10.1086/147433](https://doi.org/10.1086/147433)
- Einstein, A. 1916, *Annalen Phys.*, 49, 769, doi: [10.1002/andp.200590044](https://doi.org/10.1002/andp.200590044), [10.1002/andp.19163540702](https://doi.org/10.1002/andp.19163540702)
- Elbaz, D., Daddi, E., Le Borgne, D., et al. 2007, *A&A*, 468, 33, doi: [10.1051/0004-6361:20077525](https://doi.org/10.1051/0004-6361:20077525)
- Elbaz, D., Leiton, R., Nagar, N., et al. 2018, *A&A*, 616, A110, doi: [10.1051/0004-6361/201732370](https://doi.org/10.1051/0004-6361/201732370)
- Faber, S. M., & Jackson, R. E. 1976, *ApJ*, 204, 668, doi: [10.1086/154215](https://doi.org/10.1086/154215)
- Faisst, A. L., Carollo, C. M., Capak, P. L., et al. 2017a, *ApJ*, 839, 71, doi: [10.3847/1538-4357/aa697a](https://doi.org/10.3847/1538-4357/aa697a)
- Faisst, A. L., Capak, P. L., Yan, L., et al. 2017b, *ApJ*, 847, 21, doi: [10.3847/1538-4357/aa886c](https://doi.org/10.3847/1538-4357/aa886c)
- Farouki, R., & Shapiro, S. L. 1981, *ApJ*, 243, 32, doi: [10.1086/158563](https://doi.org/10.1086/158563)
- Feldmann, R., & Mayer, L. 2015, *MNRAS*, 446, 1939, doi: [10.1093/mnras/stu2207](https://doi.org/10.1093/mnras/stu2207)
- Feng, Y., Di Matteo, T., Croft, R., et al. 2015, *ApJ*, 808, L17, doi: [10.1088/2041-8205/808/1/L17](https://doi.org/10.1088/2041-8205/808/1/L17)
- Finkelstein, S. L., Papovich, C., Salmon, B., et al. 2012, *ApJ*, 756, 164, doi: [10.1088/0004-637X/756/2/164](https://doi.org/10.1088/0004-637X/756/2/164)
- Franx, M., Moorwood, A., Rix, H.-W., et al. 2000, *The Messenger*, 99, 20

- Franx, M., Labbé, I., Rudnick, G., et al. 2003, *ApJ*, 587, L79, doi: [10.1086/375155](https://doi.org/10.1086/375155)
- Friedmann, A. 1922, *Zeitschrift fur Physik*, 10, 377, doi: [10.1007/BF01332580](https://doi.org/10.1007/BF01332580)
- Fu, H., Cooray, A., Feruglio, C., et al. 2013, *Nature*, 498, 338, doi: [10.1038/nature12184](https://doi.org/10.1038/nature12184)
- Fudamoto, Y., Oesch, P. A., Schinnerer, E., et al. 2017, *MNRAS*, 472, 483, doi: [10.1093/mnras/stx1948](https://doi.org/10.1093/mnras/stx1948)
- Fujimoto, S., Ouchi, M., Shibuya, T., & Nagai, H. 2017, *ApJ*, 850, 83, doi: [10.3847/1538-4357/aa93e6](https://doi.org/10.3847/1538-4357/aa93e6)
- Gallazzi, A., Charlot, S., Brinchmann, J., White, S. D. M., & Tremonti, C. A. 2005, *MNRAS*, 362, 41, doi: [10.1111/j.1365-2966.2005.09321.x](https://doi.org/10.1111/j.1365-2966.2005.09321.x)
- Galliano, F. 2004, PhD thesis, Service d'Astrophysique, CEA/Saclay, L'Orme des Merisiers, 91191 Gif sur Yvette, France
- . 2017, *Planet. Space Sci.*, 149, 38, doi: [10.1016/j.pss.2017.09.006](https://doi.org/10.1016/j.pss.2017.09.006)
- Geach, J. E., Smail, I., Moran, S. M., et al. 2011, *ApJ*, 730, L19, doi: [10.1088/2041-8205/730/2/L19](https://doi.org/10.1088/2041-8205/730/2/L19)
- Genzel, R., Tacconi, L. J., Gracia-Carpio, J., et al. 2010, *MNRAS*, 407, 2091, doi: [10.1111/j.1365-2966.2010.16969.x](https://doi.org/10.1111/j.1365-2966.2010.16969.x)
- Genzel, R., Tacconi, L. J., Combes, F., et al. 2012, *ApJ*, 746, 69, doi: [10.1088/0004-637X/746/1/69](https://doi.org/10.1088/0004-637X/746/1/69)
- Genzel, R., Tacconi, L. J., Lutz, D., et al. 2015, *ApJ*, 800, 20, doi: [10.1088/0004-637X/800/1/20](https://doi.org/10.1088/0004-637X/800/1/20)
- Gerhard, O., Kronawitter, A., Saglia, R. P., & Bender, R. 2001, *AJ*, 121, 1936, doi: [10.1086/319940](https://doi.org/10.1086/319940)
- Gerhard, O. E. 1981, *MNRAS*, 197, 179, doi: [10.1093/mnras/197.1.179](https://doi.org/10.1093/mnras/197.1.179)
- Giavalisco, M. 2002, *ARA&A*, 40, 579, doi: [10.1146/annurev.astro.40.121301.111837](https://doi.org/10.1146/annurev.astro.40.121301.111837)
- Glazebrook, K., Schreiber, C., Labbé, I., et al. 2017, *Nature*, 544, 71, doi: [10.1038/nature21680](https://doi.org/10.1038/nature21680)
- Gobat, R., Daddi, E., Onodera, M., et al. 2011, *A&A*, 526, A133, doi: [10.1051/0004-6361/201016084](https://doi.org/10.1051/0004-6361/201016084)
- Gómez-Guijarro, C., Toft, S., Karim, A., et al. 2018, *ApJ*, 856, 121, doi: [10.3847/1538-4357/aab206](https://doi.org/10.3847/1538-4357/aab206)

BIBLIOGRAPHY

- Gonzaga, S., & et al. 2012, The DrizzlePac Handbook
- Greenslade, J., Clements, D. L., Cheng, T., et al. 2018, MNRAS, 476, 3336, doi: [10.1093/mnras/sty023](https://doi.org/10.1093/mnras/sty023)
- Greve, T. R., Bertoldi, F., Smail, I., et al. 2005, MNRAS, 359, 1165, doi: [10.1111/j.1365-2966.2005.08979.x](https://doi.org/10.1111/j.1365-2966.2005.08979.x)
- Griffin, M. J., Abergel, A., Abreu, A., et al. 2010, A&A, 518, L3, doi: [10.1051/0004-6361/201014519](https://doi.org/10.1051/0004-6361/201014519)
- Grogin, N. A., Kocevski, D. D., Faber, S. M., et al. 2011, ApJS, 197, 35, doi: [10.1088/0067-0049/197/2/35](https://doi.org/10.1088/0067-0049/197/2/35)
- Groves, B. A., Schinnerer, E., Leroy, A., et al. 2015, ApJ, 799, 96, doi: [10.1088/0004-637X/799/1/96](https://doi.org/10.1088/0004-637X/799/1/96)
- Guo, Y., McIntosh, D. H., Mo, H. J., et al. 2009, MNRAS, 398, 1129, doi: [10.1111/j.1365-2966.2009.15223.x](https://doi.org/10.1111/j.1365-2966.2009.15223.x)
- Guth, A. H. 1981, Phys. Rev. D, 23, 347, doi: [10.1103/PhysRevD.23.347](https://doi.org/10.1103/PhysRevD.23.347)
- Guth, A. H., & Pi, S.-Y. 1982, Physical Review Letters, 49, 1110, doi: [10.1103/PhysRevLett.49.1110](https://doi.org/10.1103/PhysRevLett.49.1110)
- Hainline, L. J., Blain, A. W., Smail, I., et al. 2011, ApJ, 740, 96, doi: [10.1088/0004-637X/740/2/96](https://doi.org/10.1088/0004-637X/740/2/96)
- Hawking, S. W. 1982, Physics Letters B, 115, 295, doi: [10.1016/0370-2693\(82\)90373-2](https://doi.org/10.1016/0370-2693(82)90373-2)
- Hayashi, M., Tadaki, K.-i., Kodama, T., et al. 2018, ApJ, 856, 118, doi: [10.3847/1538-4357/aab3e7](https://doi.org/10.3847/1538-4357/aab3e7)
- Hayward, C. C., Behroozi, P. S., Somerville, R. S., et al. 2013, MNRAS, 434, 2572, doi: [10.1093/mnras/stt1202](https://doi.org/10.1093/mnras/stt1202)
- Hayward, C. C., Chapman, S. C., Steidel, C. C., et al. 2018, MNRAS, 476, 2278, doi: [10.1093/mnras/sty304](https://doi.org/10.1093/mnras/sty304)
- Helou, G., Soifer, B. T., & Rowan-Robinson, M. 1985, ApJ, 298, L7, doi: [10.1086/184556](https://doi.org/10.1086/184556)
- Hernquist, L. 1989, Nature, 340, 687, doi: [10.1038/340687a0](https://doi.org/10.1038/340687a0)
- Hickox, R. C., Wardlow, J. L., Smail, I., et al. 2012, MNRAS, 421, 284, doi: [10.1111/j.1365-2966.2011.20303.x](https://doi.org/10.1111/j.1365-2966.2011.20303.x)

- Hodge, J. A., Karim, A., Smail, I., et al. 2013, ApJ, 768, 91, doi: [10.1088/0004-637X/768/1/91](https://doi.org/10.1088/0004-637X/768/1/91)
- Hodge, J. A., Swinbank, A. M., Simpson, J. M., et al. 2016, ApJ, 833, 103, doi: [10.3847/1538-4357/833/1/103](https://doi.org/10.3847/1538-4357/833/1/103)
- Holland, W. S., Robson, E. I., Gear, W. K., et al. 1999, MNRAS, 303, 659, doi: [10.1046/j.1365-8711.1999.02111.x](https://doi.org/10.1046/j.1365-8711.1999.02111.x)
- Hopkins, P. F., Somerville, R. S., Hernquist, L., et al. 2006, ApJ, 652, 864, doi: [10.1086/508503](https://doi.org/10.1086/508503)
- Howell, J. H., Armus, L., Mazzarella, J. M., et al. 2010, ApJ, 715, 572, doi: [10.1088/0004-637X/715/1/572](https://doi.org/10.1088/0004-637X/715/1/572)
- Hoyle, F., & Tayler, R. J. 1964, Nature, 203, 1108, doi: [10.1038/2031108a0](https://doi.org/10.1038/2031108a0)
- Hubble, E. 1929, Proceedings of the National Academy of Science, 15, 168, doi: [10.1073/pnas.15.3.168](https://doi.org/10.1073/pnas.15.3.168)
- Hubble, E., & Humason, M. L. 1931, ApJ, 74, 43, doi: [10.1086/143323](https://doi.org/10.1086/143323)
- Hubble, E. P. 1926, ApJ, 64, doi: [10.1086/143018](https://doi.org/10.1086/143018)
- Hunter, J. D. 2007, Computing In Science & Engineering, 9, 90, doi: [10.1109/MCSE.2007.55](https://doi.org/10.1109/MCSE.2007.55)
- Ikarashi, S., Ivison, R. J., Caputi, K. I., et al. 2015, ApJ, 810, 133, doi: [10.1088/0004-637X/810/2/133](https://doi.org/10.1088/0004-637X/810/2/133)
- Ilbert, O., Arnouts, S., McCracken, H. J., et al. 2006, A&A, 457, 841, doi: [10.1051/0004-6361:20065138](https://doi.org/10.1051/0004-6361:20065138)
- Ivison, R. J., Swinbank, A. M., Smail, I., et al. 2013, ApJ, 772, 137, doi: [10.1088/0004-637X/772/2/137](https://doi.org/10.1088/0004-637X/772/2/137)
- Jarvis, M. J., Bonfield, D. G., Bruce, V. A., et al. 2013, MNRAS, 428, 1281, doi: [10.1093/mnras/sts118](https://doi.org/10.1093/mnras/sts118)
- J Jeans, J. H. 1902, Philosophical Transactions of the Royal Society of London Series A, 199, 1, doi: [10.1098/rsta.1902.0012](https://doi.org/10.1098/rsta.1902.0012)
- Jiménez-Andrade, E. F., Magnelli, B., Karim, A., et al. 2018, A&A, 615, A25, doi: [10.1051/0004-6361/201732186](https://doi.org/10.1051/0004-6361/201732186)
- Jin, S., Daddi, E., Liu, D., et al. 2018, ApJ, 864, 56, doi: [10.3847/1538-4357/aad4af](https://doi.org/10.3847/1538-4357/aad4af)
- Jones, G. C., Carilli, C. L., Shao, Y., et al. 2017, ApJ, 850, 180, doi: [10.3847/1538-4357/aa8df2](https://doi.org/10.3847/1538-4357/aa8df2)

BIBLIOGRAPHY

- Joseph, R. D., & Wright, G. S. 1985, MNRAS, 214, 87, doi: [10.1093/mnras/214.2.87](https://doi.org/10.1093/mnras/214.2.87)
- Kartaltepe, J. S., Dickinson, M., Alexander, D. M., et al. 2012, ApJ, 757, 23, doi: [10.1088/0004-637X/757/1/23](https://doi.org/10.1088/0004-637X/757/1/23)
- Kauffmann, G., Heckman, T. M., Tremonti, C., et al. 2003, MNRAS, 346, 1055, doi: [10.1111/j.1365-2966.2003.07154.x](https://doi.org/10.1111/j.1365-2966.2003.07154.x)
- Kaufman, M. J., Wolfire, M. G., & Hollenbach, D. J. 2006, ApJ, 644, 283, doi: [10.1086/503596](https://doi.org/10.1086/503596)
- Kaufman, M. J., Wolfire, M. G., Hollenbach, D. J., & Luhman, M. L. 1999, ApJ, 527, 795, doi: [10.1086/308102](https://doi.org/10.1086/308102)
- Kaviraj, S., Peirani, S., Khochfar, S., Silk, J., & Kay, S. 2009, MNRAS, 394, 1713, doi: [10.1111/j.1365-2966.2009.14403.x](https://doi.org/10.1111/j.1365-2966.2009.14403.x)
- Kennicutt, Jr., R. C. 1998, ARA&A, 36, 189, doi: [10.1146/annurev.astro.36.1.189](https://doi.org/10.1146/annurev.astro.36.1.189)
- Koekemoer, A. M., Aussel, H., Calzetti, D., et al. 2007, ApJS, 172, 196, doi: [10.1086/520086](https://doi.org/10.1086/520086)
- Koekemoer, A. M., Faber, S. M., Ferguson, H. C., et al. 2011, ApJS, 197, 36, doi: [10.1088/0067-0049/197/2/36](https://doi.org/10.1088/0067-0049/197/2/36)
- Kriek, M., Conroy, C., van Dokkum, P. G., et al. 2016, Nature, 540, 248, doi: [10.1038/nature20570](https://doi.org/10.1038/nature20570)
- Krogager, J.-K., Zirm, A. W., Toft, S., Man, A., & Brammer, G. 2014, ApJ, 797, 17, doi: [10.1088/0004-637X/797/1/17](https://doi.org/10.1088/0004-637X/797/1/17)
- Kubo, M., Tanaka, M., Yabe, K., et al. 2018, ApJ, 867, 1, doi: [10.3847/1538-4357/aae3e8](https://doi.org/10.3847/1538-4357/aae3e8)
- Kubo, M., Yamada, T., Ichikawa, T., et al. 2017, MNRAS, 469, 2235, doi: [10.1093/mnras/stx920](https://doi.org/10.1093/mnras/stx920)
- Kurk, J. D., Röttgering, H. J. A., Pentericci, L., et al. 2000, A&A, 358, L1
- Laigle, C., McCracken, H. J., Ilbert, O., et al. 2016, ApJS, 224, 24, doi: [10.3847/0067-0049/224/2/24](https://doi.org/10.3847/0067-0049/224/2/24)
- Lang, P., Wuyts, S., Somerville, R. S., et al. 2014, ApJ, 788, 11, doi: [10.1088/0004-637X/788/1/11](https://doi.org/10.1088/0004-637X/788/1/11)
- Larson, R. B. 1975, MNRAS, 173, 671, doi: [10.1093/mnras/173.3.671](https://doi.org/10.1093/mnras/173.3.671)
- Lee, K.-G., Hennawi, J. F., White, M., et al. 2016, ApJ, 817, 160, doi: [10.3847/0004-637X/817/2/160](https://doi.org/10.3847/0004-637X/817/2/160)

BIBLIOGRAPHY

- Lee, M. M., Tanaka, I., Kawabe, R., et al. 2017, *ApJ*, 842, 55, doi: [10.3847/1538-4357/aa74c2](https://doi.org/10.3847/1538-4357/aa74c2)
- Lemaître, G. 1927, *Annales de la Société Scientifique de Bruxelles*, 47, 49
- . 1931, *MNRAS*, 91, 483, doi: [10.1093/mnras/91.5.483](https://doi.org/10.1093/mnras/91.5.483)
- Leroy, A. K., Bolatto, A., Gordon, K., et al. 2011, *ApJ*, 737, 12, doi: [10.1088/0004-637X/737/1/12](https://doi.org/10.1088/0004-637X/737/1/12)
- Li, Y., Mo, H. J., & Gao, L. 2008, *MNRAS*, 389, 1419, doi: [10.1111/j.1365-2966.2008.13667.x](https://doi.org/10.1111/j.1365-2966.2008.13667.x)
- Liu, D., Daddi, E., Dickinson, M., et al. 2018, *ApJ*, 853, 172, doi: [10.3847/1538-4357/aaa600](https://doi.org/10.3847/1538-4357/aaa600)
- Lonsdale, C. J., Smith, H. E., Rowan-Robinson, M., et al. 2003, *PASP*, 115, 897, doi: [10.1086/376850](https://doi.org/10.1086/376850)
- Lotz, J. M., Jonsson, P., Cox, T. J., et al. 2011, *ApJ*, 742, 103, doi: [10.1088/0004-637X/742/2/103](https://doi.org/10.1088/0004-637X/742/2/103)
- Lotz, J. M., Jonsson, P., Cox, T. J., & Primack, J. R. 2010, *MNRAS*, 404, 575, doi: [10.1111/j.1365-2966.2010.16268.x](https://doi.org/10.1111/j.1365-2966.2010.16268.x)
- Lutz, D., Berta, S., Contursi, A., et al. 2016, *A&A*, 591, A136, doi: [10.1051/0004-6361/201527706](https://doi.org/10.1051/0004-6361/201527706)
- Madau, P., & Dickinson, M. 2014, *ARA&A*, 52, 415, doi: [10.1146/annurev-astro-081811-125615](https://doi.org/10.1146/annurev-astro-081811-125615)
- Magdis, G. E., Rigopoulou, D., Huang, J.-S., & Fazio, G. G. 2010, *MNRAS*, 401, 1521, doi: [10.1111/j.1365-2966.2009.15779.x](https://doi.org/10.1111/j.1365-2966.2009.15779.x)
- Magdis, G. E., Daddi, E., Béthermin, M., et al. 2012, *ApJ*, 760, 6, doi: [10.1088/0004-637X/760/1/6](https://doi.org/10.1088/0004-637X/760/1/6)
- Magdis, G. E., Rigopoulou, D., Daddi, E., et al. 2017, *A&A*, 603, A93, doi: [10.1051/0004-6361/201731037](https://doi.org/10.1051/0004-6361/201731037)
- Magnelli, B., Elbaz, D., Chary, R. R., et al. 2009, *A&A*, 496, 57, doi: [10.1051/0004-6361:200811443](https://doi.org/10.1051/0004-6361:200811443)
- . 2011, *A&A*, 528, A35, doi: [10.1051/0004-6361/200913941](https://doi.org/10.1051/0004-6361/200913941)
- Magnelli, B., Ivison, R. J., Lutz, D., et al. 2015, *A&A*, 573, A45, doi: [10.1051/0004-6361/201424937](https://doi.org/10.1051/0004-6361/201424937)

BIBLIOGRAPHY

- Malhotra, S., Kaufman, M. J., Hollenbach, D., et al. 2001, *ApJ*, 561, 766, doi: [10.1086/323046](https://doi.org/10.1086/323046)
- Man, A. W. S., Zirm, A. W., & Toft, S. 2016, *ApJ*, 830, 89, doi: [10.3847/0004-637X/830/2/89](https://doi.org/10.3847/0004-637X/830/2/89)
- Marchesi, S., Civano, F., Elvis, M., et al. 2016, *ApJ*, 817, 34, doi: [10.3847/0004-637X/817/1/34](https://doi.org/10.3847/0004-637X/817/1/34)
- Marchesini, D., Muzzin, A., Stefanon, M., et al. 2014, *ApJ*, 794, 65, doi: [10.1088/0004-637X/794/1/65](https://doi.org/10.1088/0004-637X/794/1/65)
- Martí-Vidal, I., Vlemmings, W. H. T., Muller, S., & Casey, S. 2014, *A&A*, 563, A136, doi: [10.1051/0004-6361/201322633](https://doi.org/10.1051/0004-6361/201322633)
- Martinache, C., Rettura, A., Dole, H., et al. 2018, *A&A*, 620, A198, doi: [10.1051/0004-6361/201833198](https://doi.org/10.1051/0004-6361/201833198)
- Mauduit, J.-C., Lacy, M., Farrah, D., et al. 2012, *PASP*, 124, 714, doi: [10.1086/666945](https://doi.org/10.1086/666945)
- McCracken, H. J., Milvang-Jensen, B., Dunlop, J., et al. 2012, *A&A*, 544, A156, doi: [10.1051/0004-6361/201219507](https://doi.org/10.1051/0004-6361/201219507)
- McMullin, J. P., Waters, B., Schiebel, D., Young, W., & Golap, K. 2007, in *Astronomical Society of the Pacific Conference Series*, Vol. 376, *Astronomical Data Analysis Software and Systems XVI*, ed. R. A. Shaw, F. Hill, & D. J. Bell, 127
- Meurer, G. R., Heckman, T. M., & Calzetti, D. 1999, *ApJ*, 521, 64, doi: [10.1086/307523](https://doi.org/10.1086/307523)
- Michałowski, M., Hjorth, J., & Watson, D. 2010, *A&A*, 514, A67, doi: [10.1051/0004-6361/200913634](https://doi.org/10.1051/0004-6361/200913634)
- Michałowski, M. J., Dunlop, J. S., Cirasuolo, M., et al. 2012, *A&A*, 541, A85, doi: [10.1051/0004-6361/201016308](https://doi.org/10.1051/0004-6361/201016308)
- Michałowski, M. J., Hayward, C. C., Dunlop, J. S., et al. 2014, *A&A*, 571, A75, doi: [10.1051/0004-6361/201424174](https://doi.org/10.1051/0004-6361/201424174)
- Michałowski, M. J., Dunlop, J. S., Koprowski, M. P., et al. 2017, *MNRAS*, 469, 492, doi: [10.1093/mnras/stx861](https://doi.org/10.1093/mnras/stx861)
- Miettinen, O., Smolčić, V., Novak, M., et al. 2015, *A&A*, 577, A29, doi: [10.1051/0004-6361/201425032](https://doi.org/10.1051/0004-6361/201425032)
- Miettinen, O., Delvecchio, I., Smolčić, V., et al. 2017, *A&A*, 606, A17, doi: [10.1051/0004-6361/201730762](https://doi.org/10.1051/0004-6361/201730762)

BIBLIOGRAPHY

- Mihos, J. C., & Hernquist, L. 1996, *ApJ*, 464, 641, doi: [10.1086/177353](https://doi.org/10.1086/177353)
- Miller, T. B., Chapman, S. C., Aravena, M., et al. 2018, *Nature*, 556, 469, doi: [10.1038/s41586-018-0025-2](https://doi.org/10.1038/s41586-018-0025-2)
- Mo, H., van den Bosch, F. C., & White, S. 2010, *Galaxy Formation and Evolution*
- Momcheva, I. G., Brammer, G. B., van Dokkum, P. G., et al. 2016, *ApJS*, 225, 27, doi: [10.3847/0067-0049/225/2/27](https://doi.org/10.3847/0067-0049/225/2/27)
- Monet, D. G., Levine, S. E., Canzian, B., et al. 2003, *AJ*, 125, 984, doi: [10.1086/345888](https://doi.org/10.1086/345888)
- Muñoz Arancibia, A. M., Navarrete, F. P., Padilla, N. D., et al. 2015, *MNRAS*, 446, 2291, doi: [10.1093/mnras/stu2237](https://doi.org/10.1093/mnras/stu2237)
- Muldrew, S. I., Hatch, N. A., & Cooke, E. A. 2015, *MNRAS*, 452, 2528, doi: [10.1093/mnras/stv1449](https://doi.org/10.1093/mnras/stv1449)
- Murphy, E. J. 2013, *ApJ*, 777, 58, doi: [10.1088/0004-637X/777/1/58](https://doi.org/10.1088/0004-637X/777/1/58)
- Naab, T., Jesseit, R., & Burkert, A. 2006, *MNRAS*, 372, 839, doi: [10.1111/j.1365-2966.2006.10902.x](https://doi.org/10.1111/j.1365-2966.2006.10902.x)
- Naab, T., Johansson, P. H., & Ostriker, J. P. 2009, *ApJ*, 699, L178, doi: [10.1088/0004-637X/699/2/L178](https://doi.org/10.1088/0004-637X/699/2/L178)
- Narayanan, D., Davé, R., Johnson, B. D., et al. 2018, *MNRAS*, 474, 1718, doi: [10.1093/mnras/stx2860](https://doi.org/10.1093/mnras/stx2860)
- Narayanan, D., Turk, M., Feldmann, R., et al. 2015, *Nature*, 525, 496, doi: [10.1038/nature15383](https://doi.org/10.1038/nature15383)
- Negrello, M., Hopwood, R., De Zotti, G., et al. 2010, *Science*, 330, 800, doi: [10.1126/science.1193420](https://doi.org/10.1126/science.1193420)
- Neistein, E., van den Bosch, F. C., & Dekel, A. 2006, *MNRAS*, 372, 933, doi: [10.1111/j.1365-2966.2006.10918.x](https://doi.org/10.1111/j.1365-2966.2006.10918.x)
- Nelson, E., van Dokkum, P., Franx, M., et al. 2014, *Nature*, 513, 394, doi: [10.1038/nature13616](https://doi.org/10.1038/nature13616)
- Newman, A. B., Belli, S., & Ellis, R. S. 2015, *ApJ*, 813, L7, doi: [10.1088/2041-8205/813/1/L7](https://doi.org/10.1088/2041-8205/813/1/L7)
- Newman, A. B., Belli, S., Ellis, R. S., & Patel, S. G. 2018, *ApJ*, 862, 126, doi: [10.3847/1538-4357/aacd4f](https://doi.org/10.3847/1538-4357/aacd4f)

BIBLIOGRAPHY

- Newman, A. B., Ellis, R. S., Bundy, K., & Treu, T. 2012, *ApJ*, 746, 162, doi: [10.1088/0004-637X/746/2/162](https://doi.org/10.1088/0004-637X/746/2/162)
- Niemi, S.-M. 2011, PhD thesis, PhD Thesis, 2011
- Noble, A. G., McDonald, M., Muzzin, A., et al. 2017, *ApJ*, 842, L21, doi: [10.3847/2041-8213/aa77f3](https://doi.org/10.3847/2041-8213/aa77f3)
- Noeske, K. G., Weiner, B. J., Faber, S. M., et al. 2007, *ApJ*, 660, L43, doi: [10.1086/517926](https://doi.org/10.1086/517926)
- Obreschkow, D., Croton, D., De Lucia, G., Khochfar, S., & Rawlings, S. 2009, *ApJ*, 698, 1467, doi: [10.1088/0004-637X/698/2/1467](https://doi.org/10.1088/0004-637X/698/2/1467)
- O'Dea, C. P. 1998, *PASP*, 110, 493, doi: [10.1086/316162](https://doi.org/10.1086/316162)
- Oke, J. B. 1974, *ApJS*, 27, 21, doi: [10.1086/190287](https://doi.org/10.1086/190287)
- Oliver, S. J., Bock, J., Altieri, B., et al. 2012, *MNRAS*, 424, 1614, doi: [10.1111/j.1365-2966.2012.20912.x](https://doi.org/10.1111/j.1365-2966.2012.20912.x)
- Onodera, M., Renzini, A., Carollo, M., et al. 2012, *ApJ*, 755, 26, doi: [10.1088/0004-637X/755/1/26](https://doi.org/10.1088/0004-637X/755/1/26)
- Oser, L., Naab, T., Ostriker, J. P., & Johansson, P. H. 2012, *ApJ*, 744, 63, doi: [10.1088/0004-637X/744/1/63](https://doi.org/10.1088/0004-637X/744/1/63)
- Oteo, I., Ivison, R. J., Dunne, L., et al. 2016, *ApJ*, 827, 34, doi: [10.3847/0004-637X/827/1/34](https://doi.org/10.3847/0004-637X/827/1/34)
- Oteo, I., Ivison, R. J., Negrello, M., et al. 2017, ArXiv e-prints. <https://arxiv.org/abs/1709.04191>
- Oteo, I., Ivison, R. J., Dunne, L., et al. 2018, *ApJ*, 856, 72, doi: [10.3847/1538-4357/aaa1f1](https://doi.org/10.3847/1538-4357/aaa1f1)
- Overzier, R. A. 2016, *A&A Rev.*, 24, 14, doi: [10.1007/s00159-016-0100-3](https://doi.org/10.1007/s00159-016-0100-3)
- Overzier, R. A., Heckman, T. M., Wang, J., et al. 2011, *ApJ*, 726, L7, doi: [10.1088/2041-8205/726/1/L7](https://doi.org/10.1088/2041-8205/726/1/L7)
- Pallottini, A., Ferrara, A., Gallerani, S., et al. 2017, *MNRAS*, 465, 2540, doi: [10.1093/mnras/stw2847](https://doi.org/10.1093/mnras/stw2847)
- Papadopoulos, P. P., van der Werf, P., Xilouris, E., Isaak, K. G., & Gao, Y. 2012a, *ApJ*, 751, 10, doi: [10.1088/0004-637X/751/1/10](https://doi.org/10.1088/0004-637X/751/1/10)
- Papadopoulos, P. P., van der Werf, P. P., Xilouris, E. M., et al. 2012b, *MNRAS*, 426, 2601, doi: [10.1111/j.1365-2966.2012.21001.x](https://doi.org/10.1111/j.1365-2966.2012.21001.x)

- Pavesi, R., Riechers, D. A., Capak, P. L., et al. 2016, *ApJ*, 832, 151, doi: [10.3847/0004-637X/832/2/151](https://doi.org/10.3847/0004-637X/832/2/151)
- Pavesi, R., Riechers, D. A., Sharon, C. E., et al. 2018a, *ApJ*, 861, 43, doi: [10.3847/1538-4357/aac6b6](https://doi.org/10.3847/1538-4357/aac6b6)
- Pavesi, R., Sharon, C. E., Riechers, D. A., et al. 2018b, *ApJ*, 864, 49, doi: [10.3847/1538-4357/aacb79](https://doi.org/10.3847/1538-4357/aacb79)
- Pawlik, A. H., Milosavljević, M., & Bromm, V. 2011, *ApJ*, 731, 54, doi: [10.1088/0004-637X/731/1/54](https://doi.org/10.1088/0004-637X/731/1/54)
- Peng, C. Y., Ho, L. C., Impey, C. D., & Rix, H.-W. 2002, *AJ*, 124, 266, doi: [10.1086/340952](https://doi.org/10.1086/340952)
- Penzias, A. A., & Wilson, R. W. 1965, *ApJ*, 142, 419, doi: [10.1086/148307](https://doi.org/10.1086/148307)
- Pérez-González, P. G., Rieke, G. H., Egami, E., et al. 2005, *ApJ*, 630, 82, doi: [10.1086/431894](https://doi.org/10.1086/431894)
- Perlmutter, S., Aldering, G., Goldhaber, G., et al. 1999, *ApJ*, 517, 565, doi: [10.1086/307221](https://doi.org/10.1086/307221)
- Pettini, M., & Pagel, B. E. J. 2004, *MNRAS*, 348, L59, doi: [10.1111/j.1365-2966.2004.07591.x](https://doi.org/10.1111/j.1365-2966.2004.07591.x)
- Pettini, M., Shapley, A. E., Steidel, C. C., et al. 2001, *ApJ*, 554, 981, doi: [10.1086/321403](https://doi.org/10.1086/321403)
- Planck Collaboration, Ade, P. A. R., Aghanim, N., et al. 2016, *A&A*, 596, A100, doi: [10.1051/0004-6361/201527206](https://doi.org/10.1051/0004-6361/201527206)
- Planck Collaboration, Aghanim, N., Akrami, Y., et al. 2018, arXiv e-prints. <https://arxiv.org/abs/1807.06209>
- Pope, A., Chary, R.-R., Alexander, D. M., et al. 2008, *ApJ*, 675, 1171, doi: [10.1086/527030](https://doi.org/10.1086/527030)
- Popping, G., Puglisi, A., & Norman, C. A. 2017a, *MNRAS*, 472, 2315, doi: [10.1093/mnras/stx2202](https://doi.org/10.1093/mnras/stx2202)
- Popping, G., Somerville, R. S., & Galametz, M. 2017b, *MNRAS*, 471, 3152, doi: [10.1093/mnras/stx1545](https://doi.org/10.1093/mnras/stx1545)
- Popping, G., Decarli, R., Man, A. W. S., et al. 2017c, *A&A*, 602, A11, doi: [10.1051/0004-6361/201730391](https://doi.org/10.1051/0004-6361/201730391)
- Pound, M. W., & Wolfire, M. G. 2008, in *Astronomical Society of the Pacific Conference Series*, Vol. 394, *Astronomical Data Analysis Software and Systems XVII*, ed. R. W. Argyle, P. S. Bunclark, & J. R. Lewis, 654

BIBLIOGRAPHY

- Puglisi, A., Daddi, E., Renzini, A., et al. 2017, *ApJ*, 838, L18, doi: [10.3847/2041-8213/aa66c9](https://doi.org/10.3847/2041-8213/aa66c9)
- R Core Team. 2015, *R: A Language and Environment for Statistical Computing*, R Foundation for Statistical Computing, Vienna, Austria
- Ricciardelli, E., Trujillo, I., Buitrago, F., & Conselice, C. J. 2010, *MNRAS*, 406, 230, doi: [10.1111/j.1365-2966.2010.16693.x](https://doi.org/10.1111/j.1365-2966.2010.16693.x)
- Riechers, D. A., Capak, P. L., Carilli, C. L., et al. 2010, *ApJ*, 720, L131, doi: [10.1088/2041-8205/720/2/L131](https://doi.org/10.1088/2041-8205/720/2/L131)
- Riechers, D. A., Bradford, C. M., Clements, D. L., et al. 2013, *Nature*, 496, 329, doi: [10.1038/nature12050](https://doi.org/10.1038/nature12050)
- Riechers, D. A., Carilli, C. L., Capak, P. L., et al. 2014a, *ApJ*, 796, 84, doi: [10.1088/0004-637X/796/2/84](https://doi.org/10.1088/0004-637X/796/2/84)
- Riechers, D. A., Pope, A., Daddi, E., et al. 2014b, *ApJ*, 786, 31, doi: [10.1088/0004-637X/786/1/31](https://doi.org/10.1088/0004-637X/786/1/31)
- Riechers, D. A., Leung, T. K. D., Ivison, R. J., et al. 2017, *ApJ*, 850, 1, doi: [10.3847/1538-4357/aa8ccf](https://doi.org/10.3847/1538-4357/aa8ccf)
- Riess, A. G., Filippenko, A. V., Challis, P., et al. 1998, *AJ*, 116, 1009, doi: [10.1086/300499](https://doi.org/10.1086/300499)
- Robitaille, T., & Bressert, E. 2012, *APLpy: Astronomical Plotting Library in Python*, Astrophysics Source Code Library. <http://ascl.net/1208.017>
- Romano-Díaz, E., Choi, J.-H., Shlosman, I., & Trenti, M. 2011, *ApJ*, 738, L19, doi: [10.1088/2041-8205/738/2/L19](https://doi.org/10.1088/2041-8205/738/2/L19)
- Romano-Díaz, E., Shlosman, I., Choi, J.-H., & Sadoun, R. 2014, *ApJ*, 790, L32, doi: [10.1088/2041-8205/790/2/L32](https://doi.org/10.1088/2041-8205/790/2/L32)
- Rubin, V. C., Ford, Jr., W. K., & Thonnard, N. 1978, *ApJ*, 225, L107, doi: [10.1086/182804](https://doi.org/10.1086/182804)
- . 1980, *ApJ*, 238, 471, doi: [10.1086/158003](https://doi.org/10.1086/158003)
- Rudnick, G., Hodge, J., Walter, F., et al. 2017, *ApJ*, 849, 27, doi: [10.3847/1538-4357/aa87b2](https://doi.org/10.3847/1538-4357/aa87b2)
- Safarzadeh, M., Hayward, C. C., & Ferguson, H. C. 2017, *ApJ*, 840, 15, doi: [10.3847/1538-4357/aa6c5b](https://doi.org/10.3847/1538-4357/aa6c5b)
- Salim, S., Rich, R. M., Charlot, S., et al. 2007, *ApJS*, 173, 267, doi: [10.1086/519218](https://doi.org/10.1086/519218)

- Sanders, D. B., & Mirabel, I. F. 1996, *ARA&A*, 34, 749, doi: [10.1146/annurev.astro.34.1.749](https://doi.org/10.1146/annurev.astro.34.1.749)
- Sanders, D. B., Soifer, B. T., Elias, J. H., et al. 1988, *ApJ*, 325, 74, doi: [10.1086/165983](https://doi.org/10.1086/165983)
- Sanders, D. B., Salvato, M., Aussel, H., et al. 2007, *ApJS*, 172, 86, doi: [10.1086/517885](https://doi.org/10.1086/517885)
- Santini, P., Merlin, E., Fontana, A., et al. 2019, *MNRAS*, doi: [10.1093/mnras/stz801](https://doi.org/10.1093/mnras/stz801)
- Sargent, M. T., Daddi, E., Béthermin, M., et al. 2014, *ApJ*, 793, 19, doi: [10.1088/0004-637X/793/1/19](https://doi.org/10.1088/0004-637X/793/1/19)
- Schinnerer, E., Carilli, C. L., Scoville, N. Z., et al. 2004, *AJ*, 128, 1974, doi: [10.1086/424860](https://doi.org/10.1086/424860)
- Schinnerer, E., Carilli, C. L., Capak, P., et al. 2008, *ApJ*, 689, L5, doi: [10.1086/595680](https://doi.org/10.1086/595680)
- Schinnerer, E., Groves, B., Sargent, M. T., et al. 2016, *ApJ*, 833, 112, doi: [10.3847/1538-4357/833/1/112](https://doi.org/10.3847/1538-4357/833/1/112)
- Schmidt, M. 1959, *ApJ*, 129, 243, doi: [10.1086/146614](https://doi.org/10.1086/146614)
- Schreiber, C., Pannella, M., Elbaz, D., et al. 2015, *A&A*, 575, A74, doi: [10.1051/0004-6361/201425017](https://doi.org/10.1051/0004-6361/201425017)
- Schreiber, C., Glazebrook, K., Nanayakkara, T., et al. 2018a, *A&A*, 618, A85, doi: [10.1051/0004-6361/201833070](https://doi.org/10.1051/0004-6361/201833070)
- Schreiber, C., Labbé, I., Glazebrook, K., et al. 2018b, *A&A*, 611, A22, doi: [10.1051/0004-6361/201731917](https://doi.org/10.1051/0004-6361/201731917)
- Scoville, N., Aussel, H., Brusa, M., et al. 2007, *ApJS*, 172, 1, doi: [10.1086/516585](https://doi.org/10.1086/516585)
- Scoville, N., Aussel, H., Sheth, K., et al. 2014, *ApJ*, 783, 84, doi: [10.1088/0004-637X/783/2/84](https://doi.org/10.1088/0004-637X/783/2/84)
- Scoville, N., Sheth, K., Aussel, H., et al. 2016, *ApJ*, 820, 83, doi: [10.3847/0004-637X/820/2/83](https://doi.org/10.3847/0004-637X/820/2/83)
- Scoville, N., Murchikova, L., Walter, F., et al. 2017a, *ApJ*, 836, 66, doi: [10.3847/1538-4357/836/1/66](https://doi.org/10.3847/1538-4357/836/1/66)
- Scoville, N., Lee, N., Vanden Bout, P., et al. 2017b, *ApJ*, 837, 150, doi: [10.3847/1538-4357/aa61a0](https://doi.org/10.3847/1538-4357/aa61a0)
- Shapley, A. E., Steidel, C. C., Adelberger, K. L., et al. 2001, *ApJ*, 562, 95, doi: [10.1086/323432](https://doi.org/10.1086/323432)

BIBLIOGRAPHY

- Shen, S., Mo, H. J., White, S. D. M., et al. 2003, MNRAS, 343, 978, doi: [10.1046/j.1365-8711.2003.06740.x](https://doi.org/10.1046/j.1365-8711.2003.06740.x)
- Silva, A., Sajina, A., Lonsdale, C., & Lacy, M. 2015, ApJ, 806, L25, doi: [10.1088/2041-8205/806/2/L25](https://doi.org/10.1088/2041-8205/806/2/L25)
- Simpson, J. M., Swinbank, A. M., Smail, I., et al. 2014, ApJ, 788, 125, doi: [10.1088/0004-637X/788/2/125](https://doi.org/10.1088/0004-637X/788/2/125)
- Simpson, J. M., Smail, I., Swinbank, A. M., et al. 2015, ApJ, 799, 81, doi: [10.1088/0004-637X/799/1/81](https://doi.org/10.1088/0004-637X/799/1/81)
- Simpson, J. M., Smail, I., Wang, W.-H., et al. 2017, ApJ, 844, L10, doi: [10.3847/2041-8213/aa7cf2](https://doi.org/10.3847/2041-8213/aa7cf2)
- Skelton, R. E., Whitaker, K. E., Momcheva, I. G., et al. 2014, ApJS, 214, 24, doi: [10.1088/0067-0049/214/2/24](https://doi.org/10.1088/0067-0049/214/2/24)
- Smail, I., Ivison, R. J., & Blain, A. W. 1997, ApJ, 490, L5, doi: [10.1086/311017](https://doi.org/10.1086/311017)
- Smolčić, V., Capak, P., Ilbert, O., et al. 2011, ApJ, 731, L27, doi: [10.1088/2041-8205/731/2/L27](https://doi.org/10.1088/2041-8205/731/2/L27)
- Smolčić, V., Aravena, M., Navarrete, F., et al. 2012a, A&A, 548, A4, doi: [10.1051/0004-6361/201219368](https://doi.org/10.1051/0004-6361/201219368)
- Smolčić, V., Navarrete, F., Aravena, M., et al. 2012b, ApJS, 200, 10, doi: [10.1088/0067-0049/200/1/10](https://doi.org/10.1088/0067-0049/200/1/10)
- Smolčić, V., Karim, A., Miettinen, O., et al. 2015, A&A, 576, A127, doi: [10.1051/0004-6361/201424996](https://doi.org/10.1051/0004-6361/201424996)
- Smolčić, V., Miettinen, O., Tomičić, N., et al. 2017, A&A, 597, A4, doi: [10.1051/0004-6361/201526989](https://doi.org/10.1051/0004-6361/201526989)
- Smoot, G. F., Bennett, C. L., Kogut, A., et al. 1992, ApJ, 396, L1, doi: [10.1086/186504](https://doi.org/10.1086/186504)
- Solomon, P. M., Downes, D., & Radford, S. J. E. 1992, ApJ, 398, L29, doi: [10.1086/186569](https://doi.org/10.1086/186569)
- Solomon, P. M., Downes, D., Radford, S. J. E., & Barrett, J. W. 1997, ApJ, 478, 144, doi: [10.1086/303765](https://doi.org/10.1086/303765)
- Speagle, J. S., Steinhardt, C. L., Capak, P. L., & Silverman, J. D. 2014, ApJS, 214, 15, doi: [10.1088/0067-0049/214/2/15](https://doi.org/10.1088/0067-0049/214/2/15)

BIBLIOGRAPHY

- Spilker, J. S., Bezanson, R., Marrone, D. P., et al. 2016a, *ApJ*, 832, 19, doi: [10.3847/0004-637X/832/1/19](https://doi.org/10.3847/0004-637X/832/1/19)
- Spilker, J. S., Marrone, D. P., Aravena, M., et al. 2016b, *ApJ*, 826, 112, doi: [10.3847/0004-637X/826/2/112](https://doi.org/10.3847/0004-637X/826/2/112)
- Spitler, L. R., Labbé, I., Glazebrook, K., et al. 2012, *ApJ*, 748, L21, doi: [10.1088/2041-8205/748/2/L21](https://doi.org/10.1088/2041-8205/748/2/L21)
- Stanford, S. A., Eisenhardt, P. R., & Dickinson, M. 1998, *ApJ*, 492, 461, doi: [10.1086/305050](https://doi.org/10.1086/305050)
- Starobinsky, A. A. 1982, *Physics Letters B*, 117, 175, doi: [10.1016/0370-2693\(82\)90541-X](https://doi.org/10.1016/0370-2693(82)90541-X)
- Steidel, C. C., Adelberger, K. L., Dickinson, M., et al. 1998, *ApJ*, 492, 428, doi: [10.1086/305073](https://doi.org/10.1086/305073)
- Steidel, C. C., Giavalisco, M., Pettini, M., Dickinson, M., & Adelberger, K. L. 1996, *ApJ*, 462, L17, doi: [10.1086/310029](https://doi.org/10.1086/310029)
- Straatman, C. M. S., Labbé, I., Spitler, L. R., et al. 2015, *ApJ*, 808, L29, doi: [10.1088/2041-8205/808/1/L29](https://doi.org/10.1088/2041-8205/808/1/L29)
- Strandet, M. L., Weiss, A., Vieira, J. D., et al. 2016, *ApJ*, 822, 80, doi: [10.3847/0004-637X/822/2/80](https://doi.org/10.3847/0004-637X/822/2/80)
- Strandet, M. L., Weiss, A., De Breuck, C., et al. 2017, *ApJ*, 842, L15, doi: [10.3847/2041-8213/aa74b0](https://doi.org/10.3847/2041-8213/aa74b0)
- Strateva, I., Ivezić, Ž., Knapp, G. R., et al. 2001, *AJ*, 122, 1861, doi: [10.1086/323301](https://doi.org/10.1086/323301)
- Strong, A. W., & Mattox, J. R. 1996, *A&A*, 308, L21
- Swinbank, A. M., Simpson, J. M., Smail, I., et al. 2014, *MNRAS*, 438, 1267, doi: [10.1093/mnras/stt2273](https://doi.org/10.1093/mnras/stt2273)
- Szomoru, D., Franx, M., & van Dokkum, P. G. 2012, *ApJ*, 749, 121, doi: [10.1088/0004-637X/749/2/121](https://doi.org/10.1088/0004-637X/749/2/121)
- Tacchella, S., Dekel, A., Carollo, C. M., et al. 2016, *MNRAS*, 457, 2790, doi: [10.1093/mnras/stw131](https://doi.org/10.1093/mnras/stw131)
- Tacconi, L. J., Neri, R., Chapman, S. C., et al. 2006, *ApJ*, 640, 228, doi: [10.1086/499933](https://doi.org/10.1086/499933)
- Tacconi, L. J., Genzel, R., Smail, I., et al. 2008, *ApJ*, 680, 246, doi: [10.1086/587168](https://doi.org/10.1086/587168)
- Tacconi, L. J., Genzel, R., Neri, R., et al. 2010, *Nature*, 463, 781, doi: [10.1038/nature08773](https://doi.org/10.1038/nature08773)

BIBLIOGRAPHY

- Tacconi, L. J., Genzel, R., Saintonge, A., et al. 2018, *ApJ*, 853, 179, doi: [10.3847/1538-4357/aaa4b4](https://doi.org/10.3847/1538-4357/aaa4b4)
- Tadaki, K.-i., Kodama, T., Nelson, E. J., et al. 2017, *ApJ*, 841, L25, doi: [10.3847/2041-8213/aa7338](https://doi.org/10.3847/2041-8213/aa7338)
- Takeuchi, T. T., Yuan, F.-T., Ikeyama, A., Murata, K. L., & Inoue, A. K. 2012, *ApJ*, 755, 144, doi: [10.1088/0004-637X/755/2/144](https://doi.org/10.1088/0004-637X/755/2/144)
- Tal, T., Dekel, A., Oesch, P., et al. 2014, *ApJ*, 789, 164, doi: [10.1088/0004-637X/789/2/164](https://doi.org/10.1088/0004-637X/789/2/164)
- Talia, M., Pozzi, F., Vallini, L., et al. 2018, *MNRAS*, 476, 3956, doi: [10.1093/mnras/sty481](https://doi.org/10.1093/mnras/sty481)
- Tanaka, M., Hasinger, G., Silverman, J. D., et al. 2017, ArXiv e-prints. <https://arxiv.org/abs/1706.00566>
- Thomas, D., Maraston, C., Bender, R., & Mendes de Oliveira, C. 2005, *ApJ*, 621, 673, doi: [10.1086/426932](https://doi.org/10.1086/426932)
- Thomson, A. P., Ivison, R. J., Simpson, J. M., et al. 2014, *MNRAS*, 442, 577, doi: [10.1093/mnras/stu839](https://doi.org/10.1093/mnras/stu839)
- Tisanić, K., Smolčić, V., Delhaize, J., et al. 2019, *A&A*, 621, A139, doi: [10.1051/0004-6361/201834002](https://doi.org/10.1051/0004-6361/201834002)
- Toft, S., Gallazzi, A., Zirm, A., et al. 2012, *ApJ*, 754, 3, doi: [10.1088/0004-637X/754/1/3](https://doi.org/10.1088/0004-637X/754/1/3)
- Toft, S., van Dokkum, P., Franx, M., et al. 2005, *ApJ*, 624, L9, doi: [10.1086/430346](https://doi.org/10.1086/430346)
- . 2007, *ApJ*, 671, 285, doi: [10.1086/521810](https://doi.org/10.1086/521810)
- Toft, S., Smolčić, V., Magnelli, B., et al. 2014, *ApJ*, 782, 68, doi: [10.1088/0004-637X/782/2/68](https://doi.org/10.1088/0004-637X/782/2/68)
- Toft, S., Zabl, J., Richard, J., et al. 2017, *Nature*, 546, 510, doi: [10.1038/nature22388](https://doi.org/10.1038/nature22388)
- Toomre, A. 1977, in *Evolution of Galaxies and Stellar Populations*, ed. B. M. Tinsley & R. B. G. Larson, D. Campbell, 401
- Toomre, A., & Toomre, J. 1972, *ApJ*, 178, 623, doi: [10.1086/151823](https://doi.org/10.1086/151823)
- Tremonti, C. A., Heckman, T. M., Kauffmann, G., et al. 2004, *ApJ*, 613, 898, doi: [10.1086/423264](https://doi.org/10.1086/423264)
- Trujillo, I., Feulner, G., Goranova, Y., et al. 2006, *MNRAS*, 373, L36, doi: [10.1111/j.1745-3933.2006.00238.x](https://doi.org/10.1111/j.1745-3933.2006.00238.x)

- Umehata, H., Tamura, Y., Kohno, K., et al. 2015, *ApJ*, 815, L8, doi: [10.1088/2041-8205/815/1/L8](https://doi.org/10.1088/2041-8205/815/1/L8)
- Valentino, F., Daddi, E., Strazzullo, V., et al. 2015, *ApJ*, 801, 132, doi: [10.1088/0004-637X/801/2/132](https://doi.org/10.1088/0004-637X/801/2/132)
- Valentino, F., Daddi, E., Finoguenov, A., et al. 2016, *ApJ*, 829, 53, doi: [10.3847/0004-637X/829/1/53](https://doi.org/10.3847/0004-637X/829/1/53)
- Valentino, F., Magdis, G. E., Daddi, E., et al. 2018, *ApJ*, 869, 27, doi: [10.3847/1538-4357/aaeb88](https://doi.org/10.3847/1538-4357/aaeb88)
- van de Sande, J., Kriek, M., Franx, M., et al. 2013, *ApJ*, 771, 85, doi: [10.1088/0004-637X/771/2/85](https://doi.org/10.1088/0004-637X/771/2/85)
- van der Wel, A., Bell, E. F., Häussler, B., et al. 2012, *ApJS*, 203, 24, doi: [10.1088/0067-0049/203/2/24](https://doi.org/10.1088/0067-0049/203/2/24)
- van der Wel, A., Franx, M., van Dokkum, P. G., et al. 2014, *ApJ*, 788, 28, doi: [10.1088/0004-637X/788/1/28](https://doi.org/10.1088/0004-637X/788/1/28)
- van Dokkum, P. G., Franx, M., Kriek, M., et al. 2008, *ApJ*, 677, L5, doi: [10.1086/587874](https://doi.org/10.1086/587874)
- van Dokkum, P. G., Bezanson, R., van der Wel, A., et al. 2014, *ApJ*, 791, 45, doi: [10.1088/0004-637X/791/1/45](https://doi.org/10.1088/0004-637X/791/1/45)
- van Dokkum, P. G., Nelson, E. J., Franx, M., et al. 2015, *ApJ*, 813, 23, doi: [10.1088/0004-637X/813/1/23](https://doi.org/10.1088/0004-637X/813/1/23)
- Wagoner, R. V., Fowler, W. A., & Hoyle, F. 1967, *ApJ*, 148, 3, doi: [10.1086/149126](https://doi.org/10.1086/149126)
- Walter, F., Decarli, R., Carilli, C., et al. 2012, *Nature*, 486, 233, doi: [10.1038/nature11073](https://doi.org/10.1038/nature11073)
- Wang, T., Elbaz, D., Daddi, E., et al. 2016, *ApJ*, 828, 56, doi: [10.3847/0004-637X/828/1/56](https://doi.org/10.3847/0004-637X/828/1/56)
- . 2018, *ApJ*, 867, L29, doi: [10.3847/2041-8213/aaeb2c](https://doi.org/10.3847/2041-8213/aaeb2c)
- Wardlow, J. L., Smail, I., Coppin, K. E. K., et al. 2011, *MNRAS*, 415, 1479, doi: [10.1111/j.1365-2966.2011.18795.x](https://doi.org/10.1111/j.1365-2966.2011.18795.x)
- Wardlow, J. L., Cooray, A., De Bernardis, F., et al. 2013, *ApJ*, 762, 59, doi: [10.1088/0004-637X/762/1/59](https://doi.org/10.1088/0004-637X/762/1/59)
- Wardlow, J. L., Simpson, J. M., Smail, I., et al. 2018, *MNRAS*, 479, 3879, doi: [10.1093/mnras/sty1526](https://doi.org/10.1093/mnras/sty1526)

BIBLIOGRAPHY

- Watson, D. 2011, *A&A*, 533, A16, doi: [10.1051/0004-6361/201117120](https://doi.org/10.1051/0004-6361/201117120)
- Wei, A., De Breuck, C., Marrone, D. P., et al. 2013, *ApJ*, 767, 88, doi: [10.1088/0004-637X/767/1/88](https://doi.org/10.1088/0004-637X/767/1/88)
- Whitaker, K. E., Pope, A., Cybulski, R., et al. 2017a, *ApJ*, 850, 208, doi: [10.3847/1538-4357/aa94ce](https://doi.org/10.3847/1538-4357/aa94ce)
- Whitaker, K. E., van Dokkum, P. G., Brammer, G., & Franx, M. 2012, *ApJ*, 754, L29, doi: [10.1088/2041-8205/754/2/L29](https://doi.org/10.1088/2041-8205/754/2/L29)
- Whitaker, K. E., Franx, M., Leja, J., et al. 2014, *ApJ*, 795, 104, doi: [10.1088/0004-637X/795/2/104](https://doi.org/10.1088/0004-637X/795/2/104)
- Whitaker, K. E., Bezanson, R., van Dokkum, P. G., et al. 2017b, *ApJ*, 838, 19, doi: [10.3847/1538-4357/aa6258](https://doi.org/10.3847/1538-4357/aa6258)
- White, S. D. M. 1978, *MNRAS*, 184, 185, doi: [10.1093/mnras/184.2.185](https://doi.org/10.1093/mnras/184.2.185)
- White, S. D. M., & Rees, M. J. 1978, *MNRAS*, 183, 341, doi: [10.1093/mnras/183.3.341](https://doi.org/10.1093/mnras/183.3.341)
- Wiklind, T., Conelice, C. J., Dahlen, T., et al. 2014, *ApJ*, 785, 111, doi: [10.1088/0004-637X/785/2/111](https://doi.org/10.1088/0004-637X/785/2/111)
- Wilkinson, A., Almaini, O., Chen, C.-C., et al. 2017, *MNRAS*, 464, 1380, doi: [10.1093/mnras/stw2405](https://doi.org/10.1093/mnras/stw2405)
- Williams, C. C., Giavalisco, M., Cassata, P., et al. 2014, *ApJ*, 780, 1, doi: [10.1088/0004-637X/780/1/1](https://doi.org/10.1088/0004-637X/780/1/1)
- Xue, Y. Q., Luo, B., Brandt, W. N., et al. 2016, *The Astrophysical Journal Supplement Series*, 224, 15, doi: [10.3847/0067-0049/224/2/15](https://doi.org/10.3847/0067-0049/224/2/15)
- Younger, J. D., Fazio, G. G., Huang, J.-S., et al. 2007, *ApJ*, 671, 1531, doi: [10.1086/522776](https://doi.org/10.1086/522776)
- Younger, J. D., Fazio, G. G., Wilner, D. J., et al. 2008, *ApJ*, 688, 59, doi: [10.1086/591931](https://doi.org/10.1086/591931)
- Yuan, T., Nanayakkara, T., Kacprzak, G. G., et al. 2014, *ApJ*, 795, L20, doi: [10.1088/2041-8205/795/1/L20](https://doi.org/10.1088/2041-8205/795/1/L20)
- Yun, M. S., Reddy, N. A., & Condon, J. J. 2001, *ApJ*, 554, 803, doi: [10.1086/323145](https://doi.org/10.1086/323145)
- Yun, M. S., Aretxaga, I., Gurwell, M. A., et al. 2015, *MNRAS*, 454, 3485, doi: [10.1093/mnras/stv1963](https://doi.org/10.1093/mnras/stv1963)
- Zibetti, S. 2009, ArXiv e-prints. <https://arxiv.org/abs/0911.4956>